Truccolo, Giada (2023) *Synthesis and characterization of multifunctional coordination networks: from structure to properties.* Doctor of Philosophy (PhD) thesis, University of Kent,.

Synthesis and characterization of multifunctional coordination networks: from structure to properties

Giada Truccolo

A thesis submitted to the University of Kent in partial fulfilment of the requirements for the degree of Doctor of Philosophy at University of Kent

October 2022

Declaration

I declare that the work described herein was carried out at the University of Kent between September 2018 and April 2022 under the supervision of Dr. H. J. Shepherd. Unless stated otherwise, all work is my own and has not been submitted previously for a degree at this or any other university.

Giada Truccolo
October 2022

Abstract

This study presents the synthesis of new multifunctional materials, ranging from coordination polymers and metal-organic frameworks, to supramolecular peptide frameworks, and their structural investigation *via* X-ray diffraction techniques in order to correlate their structures to their properties.

Eleven new compounds were synthesised while aiming to construct Hofmann-type networks, six of those exhibiting the expected topology. Their SCO properties were investigated, exhibiting a variety of different behaviours. **AZO-1** and **NICO-1** did not show SCO activity, staying in the HS state between 250 K – 100 K. In compound **ISO-2**, a crystallographic phase transition was detected upon cooling, although no change in the spin state was observed. **BPA-2** exhibited a spin transition within the 200-290 K temperature range, being an interesting case of a SCO active material constructed with a flexible ligand though the topological control of a template ligand. Finally, the two isostructural **PINA-1** and **PINA-2** exhibited respectively an abrupt spin transition with 15 K hysteresis, and a gradual and incomplete transition with no hysteresis. The different SCO behaviours were attributed to the different amount of solvent present within the pores, which causes the transition to be incomplete.

The porosity and host-guest properties of three other distinct materials were then investigated. The crystalline sponge method was used to attempt the incorporation of DASAs in the pores of the MOF material **tptZn·*x*G**, in order to explore the solid-state behaviour of their photoswitching mechanism. Despite the variety of conditions attempted, it was not possible to incorporate the DASA molecules into the network at sufficient levels for analysis *via* single crystal diffraction. Two new porous coordination polymers, compounds **BDTC-1** and **BDTC-2**, were synthesised with lanthanoid ions and the flexible **ppz-bdtc** ligand, representing the first porous compound constructed with this ligand in which **ppz-bdtc**, as well as the framework, form *in situ* by self-assembly. Finally, a new crystalline supramolecular peptide framework with the capability to reversibly collapse and reinflate upon guest inclusion was constructed by self-assembly of a tetraproline helix in the polyproline II conformation.

Statement on impact of COVID-19 and supervisor change

The research presented in this PhD thesis work has been significantly disrupted by two events. Firstly, the change of the primary supervisor that occurred at the beginning of the second year of PhD affected the research path that was chosen. It was necessary to move to a research field that was closer to that of Dr. Helena Shepherd, as Dr. William Gee moved away from the UK. This required time to familiarise with the new research topics and new synthetic methods, as well as to elaborate on the literature relevant to the investigated topics. Secondly, the COVID-19 global pandemic that started just a few months after the change of supervisor, further impacted the practical work that could be undertaken. The inability to conduct practical research for several months due to the University closure, followed by the reduced access to the research facilities for a part-time rotation access, further slowed down the research work. The problems that have been reported above had hence an impact on the scope and quantity of research that could be performed, requiring continuous re-planning of the project.

Publications and presentations

Publications

A reversibly porous supramolecular peptide framework, D. F. Brightwell, G. Truccolo, K. Samanta, E. J. Fenn, S. J. Holder, H. J. Shepherd, C. S. Hawes, A. Palma, *Chemistry – A European Journal,* 2022.

Co-crystallisation as a modular approach to the discovery of spin-crossover materials, L. T. Birchall, G. Truccolo, L. Jackson, H. J. Shepherd, *Chem. Sci*., 2022, **13**, 3176.

Forensic applications of rare earths: Anticounterfeiting materials and latent fingerprint developers, G. Truccolo, R. E. Boseley, S. W. Lewis, W. J. Gee, *Handbook on the Physics and Chemistry of Rare Earths, Elsevier*, 2020.

A Zn(II) metallocycle as platform to assemble a 1D + 1D → 1D polyrotaxane via π···π stacking of an ancillary ligand, M. Rancan, G. Truccolo, A. Carlotto, S. Quici, L. Armelao, *Inorganics*, 2019, **7**, 137.

A Cu(II) metallocycle for the reversible self-assembly of coordination-driven polyrotaxane-like architectures, G. Truccolo, Z. Tessari, J. Tessarolo, S. Quici, L. Armelao, M. Rancan, *Dalton Transactions*, 2018, **47**, 12079.

Presentations

June 2019: poster presentation at the "1st International School on Advanced Porous Materials", Como (Italy).

September 2020: presentation at the School of Physical Sciences Postgraduate Colloquium.

August 2021: flash presentation at the "2B-Switch Symposium" entitled "Investigation of the role of modulators in the synthesis of new Hofmann-type MOFs".

Acknowledgements

I would like to immensely thank my supervisor, Dr Helena Shepherd for accompanying me during this PhD. Working with you has been inspiring, you have motivated me every day to be a better scientist and to never give up. Thank you for your knowledge, your precious time and for always knowing what to say. I will never forget all the support I have received from you and I am deeply grateful for the opportunity that you have given me to achieve the end of my PhD.

I would also like to thank Dr Maria Alfredsson for her support over these years and for all her helpful suggestions, and Dr Aniello Palma and the Palma research group for relying on me during this challenging collaboration. I would also like to thank Dr Marzio Rancan and Professor Lidia Armelao from my master in Padova for helping me grow professionally and for still being by my side after all these years. In particular, thank you to Marzio for always checking on me and for all your support and recommendations that have been priceless during these years of PhD. Finally, thank you to Dr William Gee for giving me the opportunity to undertake this project, as well as the University of Kent and the RSC for funding me during the last three years and seven months.

This adventure has been full of ups and downs and would not have been possible without the support of the people that I have had by my side from my beloved Italy. Thank you to my friends from home, Valentina, Anna R., Francesco (Vigna) and Davide (Bisco) for being there for me during all these years full of changes. The time that I spend with you when I come home probably seems normal for you, but is so precious to me. Thank you also to my friends from Padova, Andrea G., Andrea Z., Federica, Martina and Simone for always changing your plans and driving kilometres just to see me for a few hours. The fun that we had while working together in the teaching laboratories and when living together will always be in my heart.

A lot of people have entered in my life while living in Canterbury, supporting me during all the happy moments as well as the harder moments. Thank you to Anna, Athina and Toby for all the nice time we have spent together, for being there for me and listening to me. My life inside and outside the laboratory would not have been the same without you. Thank you to Wilma for the endless phone calls full of deep existential

conversations that I immensely adore, and for your genuine friendship started at the Durham school. Thank you to all the people that I met in lab 310 during these years, to Alex, Jed, Matt and Aaron for the helpful advises and the fun chats. Thank you to Sally, Geraud and Holly for being part of this journey. Thank you to all the Shepherd research group members for the amazing group chats and drinks. A special thank you to Lee for all his support and advice full of kindness when I needed it, and for the numerous discussions on how to solve crystallography-related issues. Thank you also to Amber for being a perfect, fun housemate, and for surviving all my mood changes while writing the thesis at our place.

Lastly, I would like to thank a few more people that mean the world to me. Thank you to my parents for believing so much in me, always and unconditionally. Thank you for not wanting to spend any day without video calling me, and for always making me feel like I am doing the right thing, even if you know how much I miss being around you. Thank you to my brother Davide, and to my little niece Stella and nephew Simone. Your joy and support have been essential over these years away from you. Thank you to my grandparents Luisa, Gabriella and Giacomo for always being on my side. Finally, thank you to my two angels, Marzia and Howard. Marzia, thank you for being my person. You have been by my side when I did not know where to restart from, you have pushed me to do what's best for me and you have always had my back. Thank you for every little thing that only you and I know, which built up our indestructible friendship. Howard, thank you for rendering this my happy place. Your support and caring encouragement have guided me over the last stressful months. Thank you for believing in me so much and for being there, next to me (and sometimes Daisy) listening to all what I need to say, always.

Ringraziamenti

Vorrei ringraziare immensamente la mia supervisor, Dr. Helena Shepherd per avermi accompagnato durante questo dottorato. Lavorare con te è stato d'spirazione, e mi ha motivato giorno dopo giorno ad essere una scienziata migliore e a non arrendermi mai. Grazie per le tue conoscenze, per il tuo tempo prezioso e per avermi sempre detto la cosa giusta al momento giusto. Non dimenticherò mai tutto il supporto che ho ricevuto da te, e sono profondamente grata per l'opportunità che mi hai dato di raggiungere la fine del mio dottorato.

Vorrei anche ringraziare la Dr Maria Alfredsson per il suo supporto durante questi anni e per i suoi suggerimenti preziosi, e il Dr Aniello Palma e il suo gruppo di ricerca per aver fatto affidamento su di me per questa collaborazione impegnativa. Vorrei anche ringraziare il Dr Marzio Rancan e la Prof. Lidia Armelao dal mio master a Padova per avermi aiutato a crescere professionalmente e per essere ancora al mio fianco dopo tutti questi anni. Grazie in particolare a Marzio per aver sempre controllato che qui tutto andasse bene e per tutto il supporto e i consigli che sono stati inestimabili in questi anni di dottorato. Infine, grazie al Dr William Gee per avermi dato l'opportunità di iniziare questo progetto, e all'University of Kent e alla RSC per avermi finanziata in questi tre anni e sette mesi.

Questa avventura piena di alti e bassi è stata possibile anche grazie a tutte le persone che ho avuto al mio fianco in tutto questo tempo dalla mia amata Italia. Grazie ai miei amici di casa, Valentina, Anna R., Francesco (Vigna) e Davide (Bisco) per essere stati al mio fianco durante tutti questi anni pieni di cambiamenti. Il tempo che passo con voi quando torno a casa può sembrare probabilmente solo la normalità per voi, ma è così prezioso per me. Ringrazio anche ai miei amici di Padova, Andrea G., Andrea Z., Federica, Martina and Simone per cambiare sempre i vostri piani e guidare per chilometri anche solo per vedermi per qualche ora. La gioia che abbiamo provato quando lavoravamo insieme nei laboratori didattici e quando vivevamo insieme sarà sempre nel mio cuore.

Molte persone sono anche entrate a far parte della mia vita quando ho vissuto a Canterbury, supportandomi quotidianamente nei momenti felici, oltre che in quelli difficili. Grazie ad Anna, Athina e Toby per tutto il bel tempo passato insieme, per esserci stati e per avermi ascoltato. La mia vita dentro e fuori il laboratorio non sarebbe stata la stessa senza di voi. Grazie a Wilma per le infinite telefonate piene di profonde conversazioni esistenziali che io adoro immensamente, e per la tua amicizia genuina iniziata alla scuola di Durham. Grazie a tutte le persone che ho incontrato nel laboratorio 310 durante questi anni, ad Alex, Jed, Matt e Aaron per gli utili consigli e per le risate. Grazie a Sally, Geraud e Holly per essere stati parte di questo viaggio. Grazie a tutti i membri del gruppo di Helena per le fantastiche chiacchiere e le uscite di gruppo. Un ringraziamento speciale va a Lee per avermi supportato con consigli pieni di immensa gentilezza quando ne avevo bisogno, e per le numerose discussioni su come risolvere problemi relativi alla cristallografia. Grazie anche ad Amber per essere stata una coinquilina perfetta e divertente, e per essere sopravvissuta ai miei cambiamenti di umore mentre scrivevo la tesi a casa nostra.

Infine, vorrei ringraziare alcune persone che significano il mondo per me. Grazie ai miei genitori per credere così tanto in me, sempre e incondizionatamente. Grazie per non voler passare nemmeno un giorno senza videochiamarmi, e per avermi fatto sempre sentire come se stessi facendo la cosa giusta, anche se sapete quanto mi manca essere lì al vostro fianco. Grazie a mio fratello Davide, e ai miei piccoli nipoti Stella e Simone. La vostra gioia e il vostro supporto sono stati essenziali in questi anni lontani da voi. Grazie ai miei nonni Luisa, Gabriella e Giacomo per essere sempre stati al mio fianco. Infine, grazie ai miei due angeli, Marzia e Howard. Marzia, grazie per essere la mia persona. Sei stata al mio fianco quando non sapevo da dove ripartire, e mi hai spinta a fare il meglio per me, stando sempre dalla mia parte. Grazie per ogni piccola cosa che solo io e te sappiamo, che ha costruito la nostra indistruttibile amicizia. Howard, grazie per aver reso questo il mio posto felice. Il tuo sostegno e i tuoi incoraggiamenti premurosi mi hanno guidato negli ultimi mesi stressanti. Grazie per credere così tanto in me e per essere qui, accanto a me (e a volte a Daisy) ad ascoltare tutto quello che ho bisogno di dire, sempre.

A nonno Diego

A Stella e Simone

Abbreviations

Active pharmaceutical ingredients	APIs
Anisotropic displacement parameters	ADPs
Cambridge crystallographic data centre	CCDC
Carbon disulphide	CS_2
Covalent organic frameworks	COFs
2,3-Dimethyl-2,3-dinitrobutane	DMNB
Dimethylformamide	DMF
2,4-Dinitrotoluene	DNT
Donor-acceptor Stenhouse adducts	DASAs
Energy dispersive X-ray spectroscopy	EDS
High spin	HS
Infrared spectroscopy	IR
International Union of Pure and Applied Chemistry	IUPAC
Isoreticular MOFs	IRMOFs
Lanthanide	Ln
Liquid chromatography-mass spectrometry	LC-MS
Low spin	LS
Metal-organic frameworks	MOFs
Methanol	MeOH
Nitrobenzene	$PhNO_2$
Nuclear magnetic resonance	NMR
Octahedron volume	V_{coord}
Polyproline I	PPI
Polyproline II	PPII
Powder X-ray diffraction	PXRD
Scanning electron microscopy	SEM
Single-crystal X-ray diffraction	SCXRD
Single ion monitoring	SIM
Spin crossover	SCO
Supramolecular organic frameworks	SOFs

Supramolecular peptide frameworks	SPFs
Thermogravimetric analysis	TGA
Toluene	Tol
Triethylamine	NEt_3
2,4,6-Trinitro-toluene	TNT
X-ray diffraction	XRD

Ligands

Ligand name	**Abbreviation**
4,4’-Azopyridine	azo
Benzenedicarboxylate	bdc
4,4’-Biphenyldicarboxylate	bpdc
4,4’-Bipyridine	bipy
1,2-Bipyridylethene	bpee
9,10-Bis(4-((3,5-dicyano-2,6-dipyridyl)dihydropyridyl)phenyl)-anthracene	bdddpa
Bis(4-pyridyl)acetylene	bpac
1,2-Bis(4-pyridyl)ethane	bpa
1,2-Bis(4-pyridyl)ethylene	bpe
1,4-diazabicyclo[2.2.2]octane	dabco
1,2-dibromo-1,2-bis(4-pyridyl)ethane	Br2-bpa
1,2-diisonicotinoylhydrazine	di-iso
Dithiocarbamate	dtc
Isonicotinic acid hydrazide (Isoniazid)	iso
1,4-Naphtalene dicarboxylate	ndc
Nicotinic acid amide (Nicotinamide)	nico
4-phenylazo-pyridine	ph-azo
N-(4-pyridyl)isonicotinamide	pina
N’-(propan-2-ylidene)isonicotinohydrazide	iso-hy
Piperazine-bis-dithiocarbamate	ppz-bdtc
Proline	pro
Pyrazine	pz
Pyridine	py
Pyrimidine	pmd
2,4,6-tris(4-pyridyl)-1,3,5-triazine	tpt

List of sample names

Synthesised samples – order of appearance

$\{Fe(H_2O)_2[Pt(CN)_4]\}\cdot iso\cdot 1.5MeOH\cdot H_2O$	**ISO-1**
$\{Fe(di\text{-}iso)[Pt(CN)_4]\}\cdot 0.5MeOH$	**ISO-2**
$\{Fe(iso\text{-}hy)(H_2O)[Pt(CN)_4]\}\{Fe(H_2O)[Pt(CN)_4]\}$	**ISO-3**
$\{Fe(nico)_2[Pt(CN)_4]\}$	**NICO-1**
$\{Fe(pina)[Pt(CN)_4]\}$	**PINA-1**
$\{Fe(pina)[Pd(CN)_4]\}$	**PINA-2**
$\{Fe(H_2O)_2(pina\text{-}H)_2[Pt(CN)_4]_2\}\cdot 2MeOH$	**PINA-3**
$\{Fe(azo)_2[Ag(CN)_2]_2\}$	**AZO-1**
$\{Fe(bpa)[Ag(CN)_2]_2[Ag(CN)]\}$	**BPA-1**
$\{Fe(bpa)[Ag(CN)_2]_2\}$	**BPA-2**
$[Fe(bpa)(Ag(CN)_2)_2\cdot MeOH]$	**BPA-3**
$[(ZnI_2)_3(tpt)_2]_n$	**TPT-1**
$La(ppz\text{-}bdtc)_{1.5}(DMF)_2\cdot DMF$	**BDTC-1**
$Pr(ppz\text{-}bdtc)_{1.5}(DMF)_2\cdot DMF$	**BDTC-2**
$Fmoc\text{-}(Pro)_4\text{-}NH_2$	**PP_4**

Samples from literature – order of appearance

$\{Fe(py)_2[Ni(CN)_4]\}$	**pyNi**
$\{Fe(pz)[Ni(CN)_4]\}\cdot 2H_2O$	**$pzNi\cdot 2H_2O$**
$\{Fe(pz)[Pd(CN)_4]\}\cdot 2.5H_2O$	**$pzPd\cdot 2.5H_2O$**
$\{Fe(pz)[Pt(CN)_4]\}\cdot 2H_2O$	**$pzPt\cdot 2H_2O$**
$\{Fe(bpac)[Pt(CN)_4]\}$	**bpacPt**
$\{Fe(pz)[Ag(CN)_2]_2\}\cdot pz$	**pzAg·pz**
$\{Fe(bipy)_2[Ag(CN)_2]_2\}$	**bipyAg**
$\{Fe(bpe)_2[Ag(CN)_2]_2\}$	**bpeAg**
$\{Fe(bipy)[Ag_2(CN)_3]_2\}_n$	**bipyAg2**
$\{Fe(bipy)[Ag(CN)_2]_2[AgCN]_2\}_n$	**bipyAgCN**
$\{Fe(pmd)[Ag(CN)_2][Ag_2(CN)_3]\}$	**pmdAg2**
$\{Fe(pmd)\text{-}(H_2O)[Ag(CN)_2]_2\}\cdot H_2O$	**$pmd\text{-}H_2OAg$**

$\{Fe(pmd)\text{-}(H_2O)[Au(CN)_2]_2\}\cdot H_2O$	**pmd-H$_2$OAu**
$[Fe(pmd)\{Ag(CN)_2\}_2]$	**pmdAg**
$[Fe(pmd)\{Au(CN)_2\}_2]$	**pmdAu**
$[Fe(pina)\{Ag(CN)_2\}_2]\cdot x\mathrm{MeOH}$	**pinaAg·*x*MeOH**
$[Fe(pina)\{Ag(CN)_2\}_2]$	**pinaAg**
$[Fe(pina)\{Au(CN)_2\}_2]\cdot x\mathrm{MeOH}$	**pinaAu·*x*MeOH**
$[Fe(pina)\{Au(CN)_2\}_2]$	**pinaAu**
$\{Fe(ph\text{-}azo)_2[Pd(CN)_4]\}$	**ph-azoPd**
$\{Fe(Br2\text{-}bpa)[Pd(CN)_4]\cdot 4H_2O\}$	**Br2-bpaPd**
$\{Fe(Br2\text{-}bpa)[Pt(CN)_4]\cdot 4H_2O\}$	**Br2-bpaPt**
$[Fe(bpa)(Au(CN)_2)_2\cdot MeOH]$	**bpaAu**
$[(ZnI_2)_3(tpt)_2\cdot x(G)]_n$	**tptZn·*x*G**
$(H_3O)[Sm(ppz\text{-}bdtc)_2]\cdot 1.5H_2O\cdot 2.5CH_3NO$	**ppz-bdtcSm**
$Na_2\text{-}ppz\text{-}bdtc\cdot 2H_2O$	**Na2-ppz-bdtc**

Table of contents

Chapter 1: Introduction

1.1 Introduction to metal organic frameworks

1.1.1 Metal organic frameworks

Metal organic frameworks (MOFs) are an important class of materials, widely studied for their structural diversity and tunable chemical and physical properties. They have gained attention in the last decades because of their interesting potential applications in gas sorption and separation,[1,2] heterogeneous catalysis,[3] chemical sensing,[4] energy storage and conversion.[5]

MOFs are defined by IUPAC as coordination networks with organic ligands containing potential voids.[6] A coordination network is a coordination compound extending through repeating coordination entities that develops in 1 dimension and presents cross-links between two or more individual chains, or that develops in 2 or 3 dimensions.[6] The extended structures are constructed with metal cations or clusters of cations connected by multitopic organic linker ions or molecules (**Figure 1**).[7] Like zeolites, MOFs can present high porosity, but unlike zeolites they are not purely inorganic materials.[8] Their hybrid nature, deriving from the interplay between organic and inorganic components, allowed scientists to design a large variety of MOFs, exploiting the vast number of possible combinations between the two moieties (**Figure 1**).

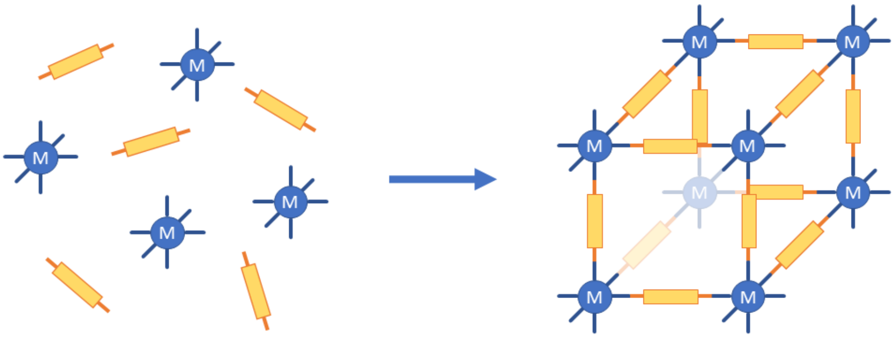

Figure 1: Schematic representation of a general structure of a MOF constructed with metal cations or clusters (blue) that are connected by organic ligands (yellow).

Typically, the most common route to synthesise MOFs is solvothermal synthesis,[9] wherein the precursors are combined after dissolution in polar solvents (usually *N*,*N*-dimethylformamide) and heated in a closed system like a bomb or an autoclave.[10] More recently, other innovative techniques have been explored, such as microwave-assisted synthesis to grow MOFs, with the advantages of reduced particle size, higher efficiency, and greater morphology control; and electrochemical synthesis using anodic and cathodic electrochemical deposition mechanisms, which are mainly used for creating heterogeneous multiphasic and multi-layered MOF thin films and membranes.[9]

Some of the most important characteristics of these materials along with the large internal surface areas and the thermal stability, are the tunable pore sizes and the flexibility of their frameworks. Importance has been given to the rational design of MOFs to impart the final structure with specific desired properties. It is in fact fundamental for a coordination polymer to develop in 2D or 3D in order to be classified as a MOF, unless the single chains are otherwise interconnected. The majority of the metal ions or metal clusters used are transition elements, with preferential coordination geometries that are known *a priori* when choosing the metal, such as linear, square planar, tetrahedral or octahedral geometries.[11] Similarly, the organic linker is most likely either ditopic, tritopic or tetratopic, allowing to form n-dimensional (n = 1, 2 and 3) motifs when mixed together with the inorganic component.[11]

An example of the impact of a rational design in the properties of the final material is the series of isoreticular MOFs (IRMOFs) that can be seen in **Figure 2**. MOF-5 (a.k.a. IRMOF-1) was one of the first MOFs synthesised. It is a 3D porous coordination polymer with formula [Zn_4O(benzene-1,4-dicarboxylate)$_3$], having more than three times the internal surface area of zeolites, the most porous material known at the time it was first reported.[12] The materials classified as IRMOFs have the same cubic topology found in MOF-5, where the vertices of the cube are formed by the octahedral $Zn_4O(CO_2)_6$ cluster (analogous to the core structure of basic zinc acetate), and the edges are formed by the phenylene rings derivatives of the ligands.[13] To synthesise this family of MOFs, ligands with different length and functionalities present in their cores were used. From **Figure 2** it can be seen how an increase in length of the ligand increases the internal void space (drawn as a yellow sphere) of the material, but can also allow interpenetration to occur. Interpenetration refers to when two or more independent networks are intergrown such that they cannot be separated without breaking a chemical bond. However, there are no direct chemical bonds present between frameworks.[14] Finally, the IRMOFs series represents one of the few examples where the level of control in the chemical modification of the organic ligand allowed to obtain this extended variety of isostructural compounds.[13]

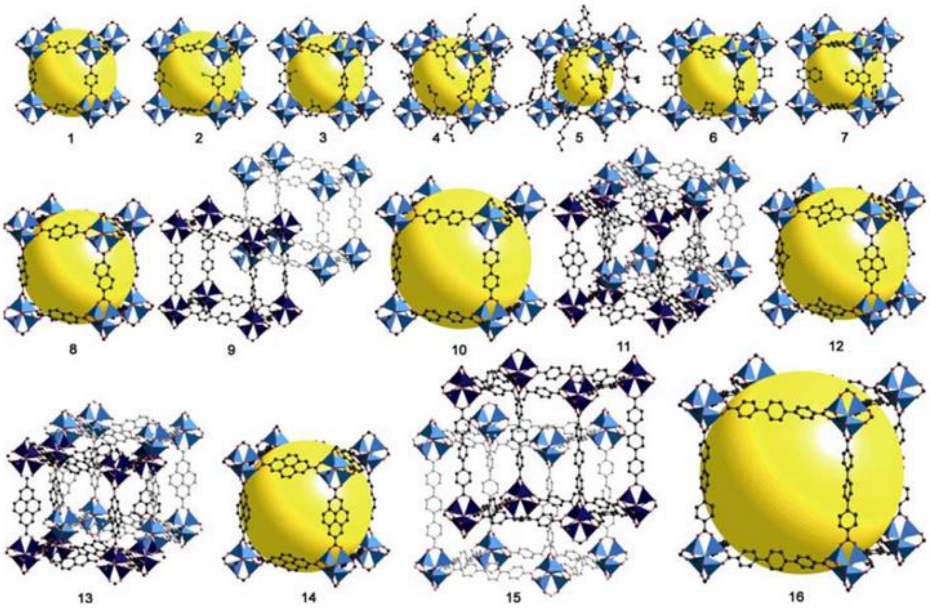

Figure 2: A series of isoreticular metal-organic frameworks (IRMOFs) with formula $Zn_4O(L)_3$ constructed by changing the L rigid dicarboxylate ligand, exhibiting the same cubic topology. Reprinted with permission.[13]

Interpenetration of independent frameworks represents an issue when aiming to synthesise materials with high surface areas and gas storage capacity, and should hence be avoided. Farha and co-workers reported in 2012 two new materials named NU-109 and NU-110 (**Figure 3**) that showed surface areas of 7010 and 7140 m^2/g and void volumes of 3.77 and 4.40 cm^3/g respectively, corresponding to ca. 93% of the structures.[15] These values represented the highest ones found among all the other high-pore volume MOFs reported in the literature before that year.[15] Compound NU-110 is still nowadays one of the materials that exhibits some of the most extraordinary porosity properties. The approach that was used to synthesise NU-109 and NU-110 was to design a topology that would not have allowed interpenetration to occur.[15] Two hexa-carboxylated ligands were used for the two compounds, differing for the number and position of the phenyl rings and alkyne groups. The vertexes of the pores were constructed with Cu^{II}_2 units, which were coordinated by the carboxylates of the ligands that form the edges of the pores.[15] The structure of NU-110 can be seen in **Figure 3**: the connectivity found in this compound develops into a network topology that does not allow the formation of interpenetrated structures, in contrast with the connectivity seen for the cubic topology of MOF-5, and hence favours the formation of a highly-porous material. This demonstrates how the rational design of MOFs with a specific topology allows a material that exhibits the desired properties to be obtained.

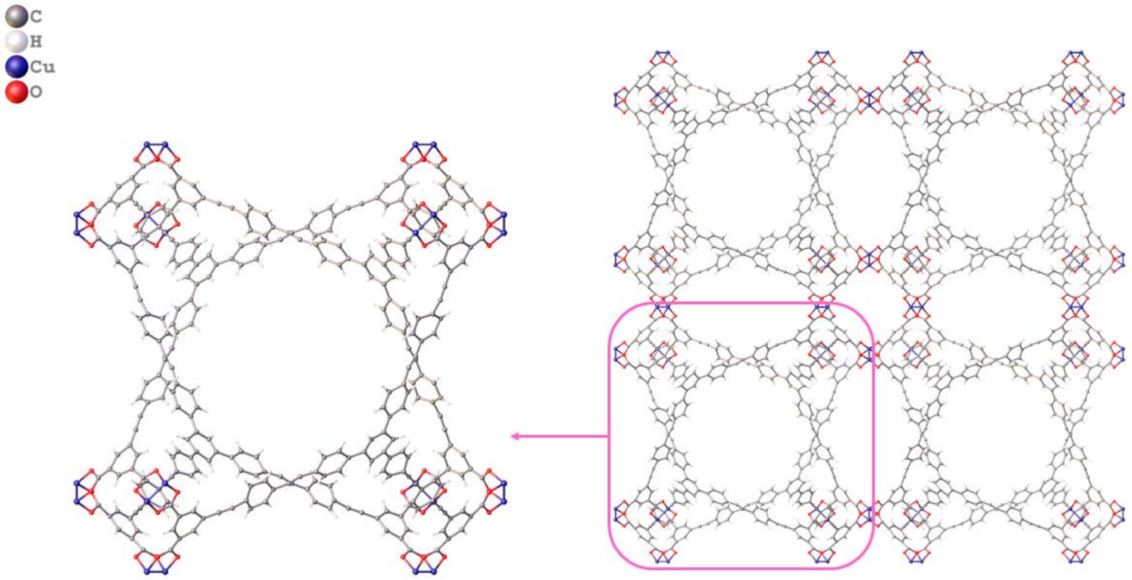

Figure 3: Structural features of NU-110 obtained from SCXRD data representing the packing seen along the *a* axis which shows the channels present in the structure. CCDC N°: 856013.[15]

As already mentioned above, the ability to impart structural control when designing a MOF allowed scientists to develop materials with specific properties, which are usually based on exploiting the space within their pores. Among the plethora of uses that MOFs have because of their pores, highlights include gas storage and separation of small molecules like H_2, CO_2 and CH_4, heterogeneous catalysis, drug delivery, sensing, confined space chemistry and nanoreactors for the synthesis of nanoparticles and other new materials.[16,17] It is therefore essential to be able to construct compounds with specific pore sizes, shapes and environments that are suitable for their functional applications.[16] The ligand choice imparts to the pores a variety of possible sizes that can be tuned from several angstrom to several nanometers.[16] When designing the characteristics of the pores, importance has also been placed upon the chemical functionalities that are present in the ligand: it is possible to tune the hydrophobicity or hydrophilicity of the pores by choosing specific ligands or by functionalizing them in order to allow specific host-guest interactions to occur.[17]

The latter aspect has been used to stabilize and maintain the porosity of the framework when under certain conditions. MOF-5 is unstable in water, exhibiting a structural collapse under humid conditions.[18] However, functionalization of the well-known benzene-1,4-dicarboxylate (**bdc**) ligand in MOF-5 with hydrophobic functional groups, prevents water from coming into close proximity with the metal-linker bond, and hence the material to be stable in water.[18] When grafting a hydrophobic moiety, such as trifluoromethoxy or methyl groups, onto the **bdc** ligand, the stability of the modified material is instead prolonged for several days of exposure to ambient air, with no structural change visible *via* PXRD analysis (**Figure 4**).[19,20,18] This demonstrates how it is possible to control the chemistry of the pores and hence its host-guest interactions, and thus impart specific properties to the MOF.

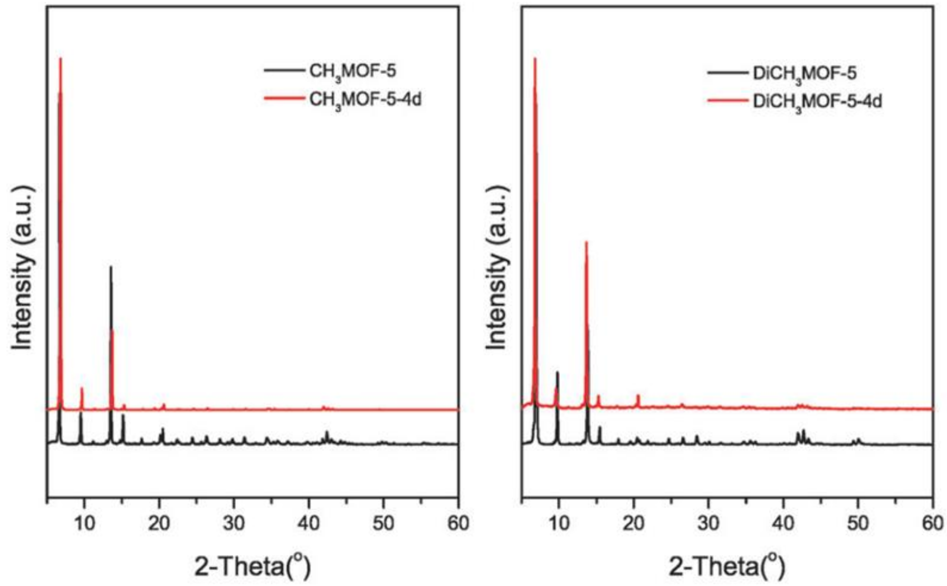

Figure 4: PXRD patterns of the MOF-5 material where the **bdc** ligand was functionalised with a methyl (CH$_3$MOF-5, left) and a dimethyl (DiCH$_3$MOF-5, right) functional group (red) and same materials analysed after 4 days of exposure to ambient air. Reprinted with permission.[19]

This thesis looks at the development of multifunctional MOFs and coordination polymers exhibiting a variety of characteristics and properties. **Chapter 2** and **Chapter 3** focus on the study of switchable frameworks, where the impact of chemical modifications of the ligand (**Chapter 2**) and of the change in topology of the network (**Chapter 3**) in the spin crossover behaviour of the material will be investigated. **Chapter 4** aims to explore the behaviour of photoswitchable molecules within the pores of a known MOF, and hence to exploit the space inside the pores to study the properties of the guest. **Chapter 5** includes the rational design of a ligand and of a metal-ligand system to obtain a porous material with enhanced luminescence properties. Finally, moving beyond MOFs, **Chapter 6** investigates the porosity features of an organic framework where the rational design of organic units through supramolecular interactions rather than via metal coordination was performed. The specific theoretical aspects relating to each chapter will hence be treated in the following sections.

1.1.2 Spin crossover phenomenon in MOFs

As already mentioned, MOFs can exhibit different properties deriving from a degree of rational design, through a specific choice of the building blocks used. Switchable materials are compounds that can switch between two or more states when under the influence of external stimuli, and have attracted attention due to the many potential applications of these materials including in environmental and chemical sensing.[21] Within the many different families of switchable materials, importance has been given to molecular and polymeric coordination compounds exhibiting spin crossover (SCO) activity.[22]

SCO is a phenomenon that can be seen in octahedral metal centres with configuration $3d^4 - 3d^7$ deriving from the reversible change in the electronic configuration of the metal centre between a low-spin (LS) and a high-spin (HS) state.[21] It was first reported by Cambi and co-workers in 1931 in Fe^{III} dithiocarbamate complexes[23] and was rapidly also reported in compounds involving Co^{II}, Co^{III}, Cr^{II}, Mn^{II}, Mn^{III} and Ni^{II} as metals, with the latter case requiring Ni^{II} to be in a tetragonally distorted octahedral environment.[21,24] Despite this, the most common metal used to generate SCO compounds in the modern day is Fe^{II}. This is related to the possibility for this metal ion to be in a diamagnetic LS state with $\mathrm{t_{2g}^{6}e_{g}^{0}}$ electronic configuration, or in a paramagnetic HS state with $\mathrm{t_{2g}^{4}e_{g}^{2}}$ electronic configuration when in a octahedral surrounding (**Figure 5**).[21,25] Most Fe^{II} compounds exhibit either a HS or LS configuration, but when the energy gap between the two states is close to thermal energy ($\Delta E^{\circ}_{\mathrm{HL}} \approx k_{\mathrm{B}}\mathrm{T}$), the SCO phenomenon can occur (**Figure 5**).[25] In this case, the electronic configuration of the metal centre can reversibly switch between the HS and LS states in response to external stimuli like temperature, pressure, light or guest molecules.[25] The temperature change is the one that is most widely used. Looking at the spin transition as a phase transition associated with a change of the Gibbs free energy $\Delta G = \Delta H - T\Delta S$, the thermally induced LS-HS transition is an entropy driven process, leading to the stabilisation of the HS state at high temperatures.[22] Finally, the spin state change is detectable as it induces a change in the magnetic, optical, dielectric and structural properties of the material.[25]

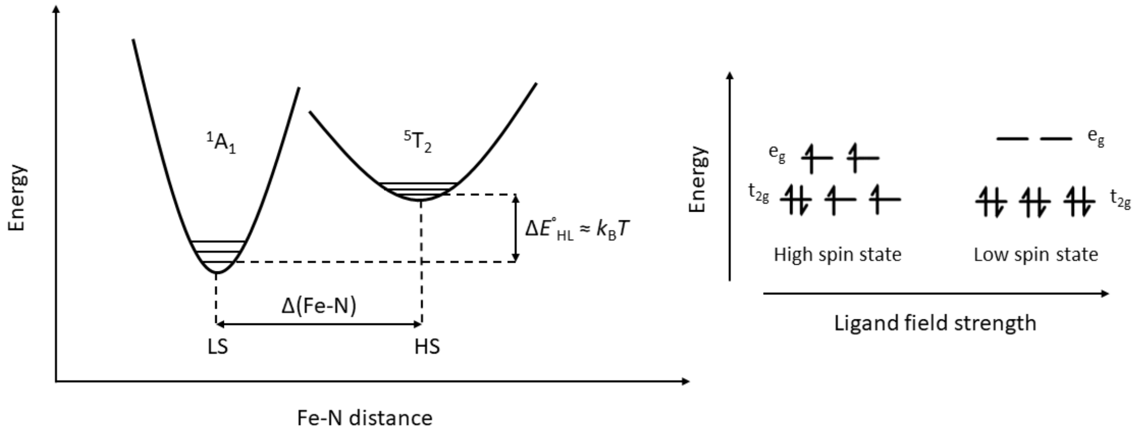

Figure 5: Potential energy level diagram plotted as a function of Fe-N bond distance (left) and distribution of electrons in *d*-orbitals for Fe^{II} in the high spin (HS) and low spin (LS) state (right).

The population and depopulation of the antibonding e_g orbitals that occurs when switching the spin state is responsible for the change in physical and chemical properties of the material.[21,25] More specifically, the population of those orbitals provokes the weakening, and hence the elongation, of the bond between the metal and the ligand (Fe-L), which increases the FeN_6 octahedron volume (V_{coord}).[26] The smaller V_{coord} of the LS state compared to the one of the HS is the responsible of the increase in energy of the HS state when high pressure is applied, stabilising the LS state in these conditions. The HS-LS electronic and structural reorganization results in a change of the colour of the material due to differences in the optical absorption bands between the HS and LS states.[26] Finally, the structural change transmits in the solid state cooperatively from one active site to another through elastic interactions. If the interactions between metal centres are weak, the cooperativity is poor and the spin change is gradual, as illustrated in **Figure 6a**. Strong interactions within the material instead lead to good communication between the active sites and strong cooperativity, resulting in an abrupt change in the magnetic, optical and structural properties (**Figure 6b**), which might also exhibit hysteretic behaviour (**Figure 6c**).[25] Stepped transition (**Figure 6d**) occurs instead when one or more intermediate mixed spin phases are present during the SCO transition.

Finally, another relatively common scenario that can be seen is the incomplete transition (**Figure 6e**), where the compound is unable to reach either the full HS or LS state.

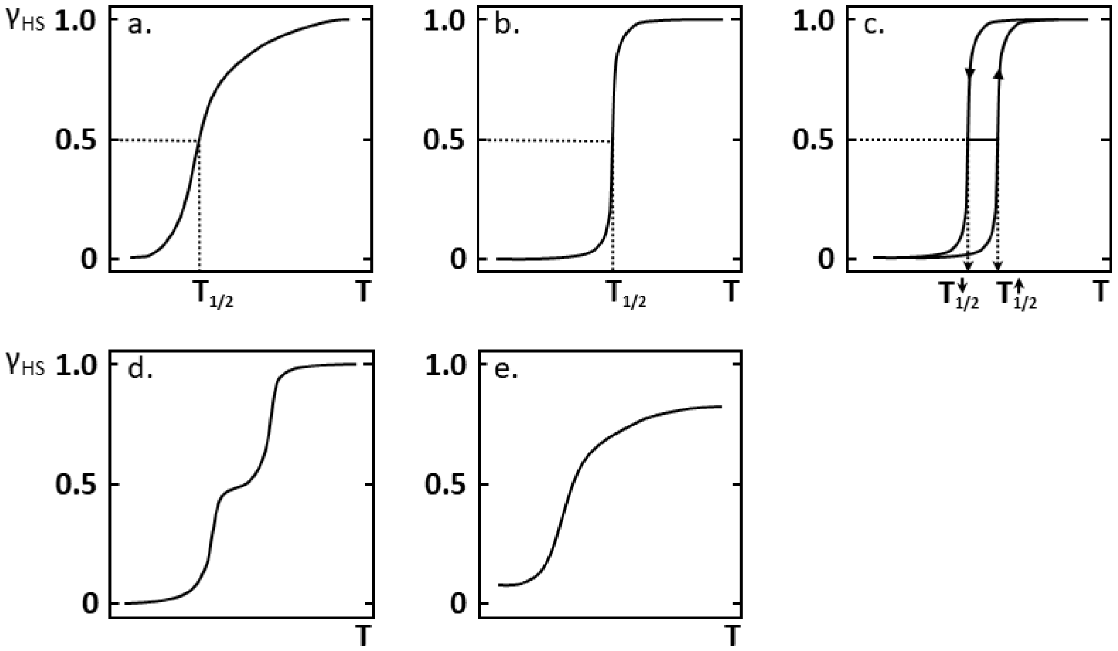

Figure 6: Representation of the principal types of spin transition curves showing the high spin fraction (γ_{HS}) vs temperature (T): **a.** gradual; **b.** abrupt; **c.** with hysteresis; **d.** two-step; **e.** incomplete.

Considering all the characteristics of the SCO phenomenon presented above, a rational design of framework materials, which have the intrinsic advantage of favouring the communication between the Fe^{II} centres through formation of coordination bonds, can allow the development of SCO MOFs with targeted properties. To this regard, attention needs to be given to the ligand used during the synthesis as the SCO behaviour is strongly dependent to the coordination environment surrounding the metal centre.[21] Furthermore, the adsorption of guests inside the pores of a framework can also influence the SCO behaviour. These materials are particularly interesting for applications in the field of sensing because if SCO occurs upon guest adsorption or removal, the change in spin state can be readily detected. In this case, the interactions between the host framework and the guest molecules are fundamental to the switching properties.[27] A well-known class of frameworks that present SCO activity are the Hofmann-type clathrates.

1.1.3 Hofmann-type clathrates

The class of materials known as Hofmann clathrates finds its origin in the compound with formula $\{Ni(NH_3)_2[Ni(CN)_4]\}\cdot 2G$ (with G = guest molecules such as benzene, pyrrole thiophene, furan), whose structure was solved in the 1950s by Powell and Rayner.[28,29] The 2D square grid network of the host involves two distinct Ni(II) ions: the first one is in the square-planar anion $[Ni(CN)_4]^{2-}$, which connect *via* the bridging cyanide components to the second Ni(II), which has an octahedral geometry and its coordination sphere is saturated with four cyanide ions in the equatorial positions and two ammonia molecules in the apical positions of the octahedron. These 2D layers stack together with a separation of 8 Å *ca.* between adjacent layers, which allows the host to include the aromatic guest molecules reported above between the sheets, guests that are hence intercalated within the network.

Modifications of the original network along the years with various divalent metal centres, and the substitution of ammonia with other nitrogen-donor mono- or ditopic ligands, allowed scientists to develop a plethora of 2D and 3D coordination polymers and frameworks, and to investigate their temperature-dependent properties, including SCO behaviour when Fe(II) is incorporated into the network. While the substitution of the octahedral Ni(II) with Fe(II) leads to the formation of the network $\{Fe(NH_3)_2[Ni(CN)_4]\}$ that is isostructural with the original Hofmann-type clathrate (**Figure 7**), the replacement of NH_3 with the pyridine (**py**) ligand forming compound $\{Fe(py)_2[Ni(CN)_4]\}$ (**pyNi**) causes a considerable structural change (**Figure 8**).[30] When NH_3 is coordinated to the apical positions of the Fe(II) ions, the adjacent 2D layers are in an eclipsed stacking, with the NH_3 molecules pointing directly on top of each other (**Figure 7a**). When the larger pyridine ligand is instead coordinated to the Fe(II) centre, the 2D layers become offset such that they reach a more efficient packing within the crystal, leading to the Fe(II) ion of one layer to align vertically with the Ni(II) ion of the adjacent layer (**Figure 8b**).[28] The 2D layers stack with interdigitation of the axial pyridine ligands.

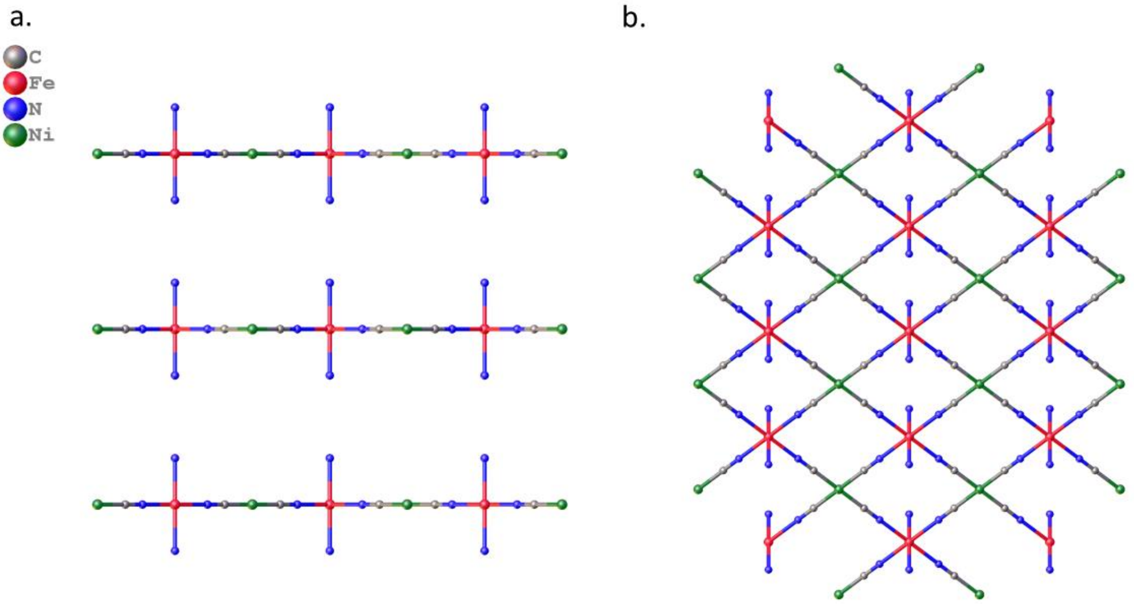

Figure 7: Structure of the Hofmann-type clathrate {Fe(NH_3)$_2$[Ni(CN)$_4$]}[30] that shows how the adjacent 2D layers of the compound arrange in an eclipsed stacking with the ammonia molecules lying directly on top of each other. **a.** View along the *a*-axis and **b.** view along the [011] direction. The hydrogen atoms and the guest benzene molecules have been removed for clarity. CCDC deposition number 1243944.

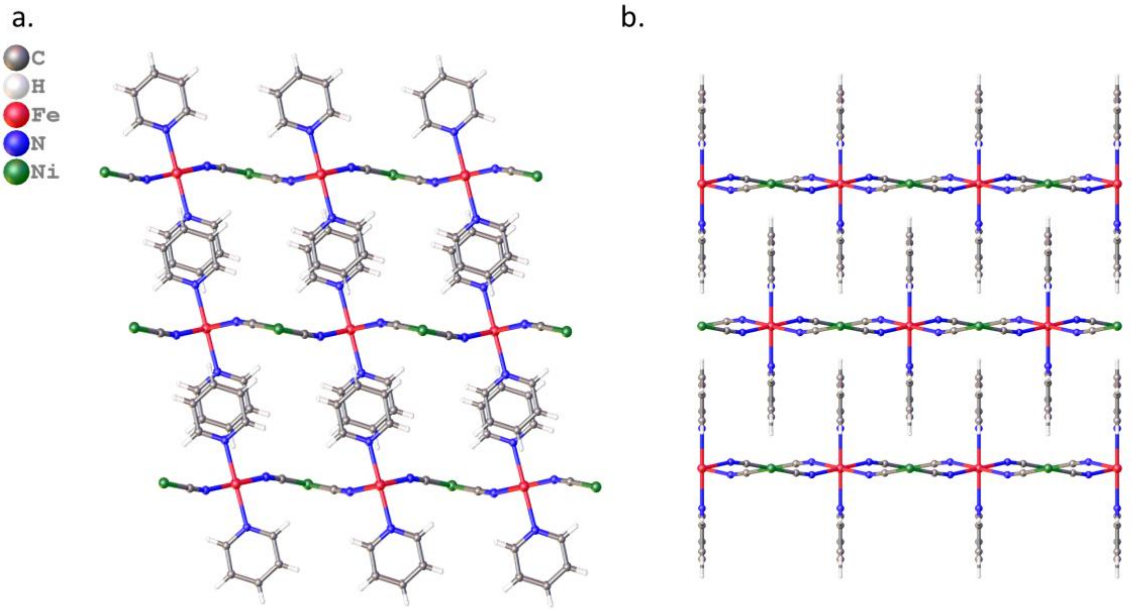

Figure 8: Structure of the Hofmann-type coordination polymer {Fe(py)$_2$[Ni(CN)$_4$]}[30] (**pyNi**) that shows how the adjacent 2D layers of the compound arrange in an interdigitated pattern in the supramolecular packing. **a.** View along the *b*-axis and **b.** view along the *c*-axis. CCDC deposition number 1317951.

The investigation of the temperature-dependent magnetic susceptibility for compound **pyNi** showed a cooperative SCO behaviour with a 9 K hysteresis loop ($T_{1/2}\downarrow$ = 186 K and $T_{1/2}\uparrow$ = 195 K).[31] This material was the first example of a Hofmann-type SCO active coordination polymer and it represented a milestone for a new strategy of designing SCO polymers. This family was in fact quickly expanded with other compounds with structure $\{Fe(L)_x[M^{II}(CN)_4]\}$, with L = mono- (x = 2) or ditopic ligands (x = 1) and M^{II} = Ni(II), Pd(II), Pt(II). In particular, the change from pyridine to pyrazine allowed the formation of the first SCO Hofmann-type clathrate $\{Fe(pz)[M^{II}(CN)_4]\}\cdot xH_2O$ (**pz** = pyrazine; M^{II} = Ni(II), (n = 2), **pzNi·2H$_2$O**; Pd(II), (n = 2.5), **pzPd·2.5H$_2$O**; Pt(II), (n = 2), **pzPt·2H$_2$O**, **Figure 9a**),[32] where the 2D $Fe[M^{II}(CN)_4]$ sheets were connected by the bridging pyrazine ligands.[33] The change in dimensionality from a 2D polymer to a 3D rigid framework had the consequence of increasing the spin transition temperatures and widening the hysteresis loops: for **pzNi·2H$_2$O**, $T_{1/2}\downarrow$ = 280 K and $T_{1/2}\uparrow$ = 305 K; for **pzPd·2.5H$_2$O**, $T_{1/2}\downarrow$ = 233 K and $T_{1/2}\uparrow$ = 266 K; for **pzPt·2H$_2$O**, $T_{1/2}\downarrow$ = 220 K and $T_{1/2}\uparrow$ = 240 K (**Figure 9b**).

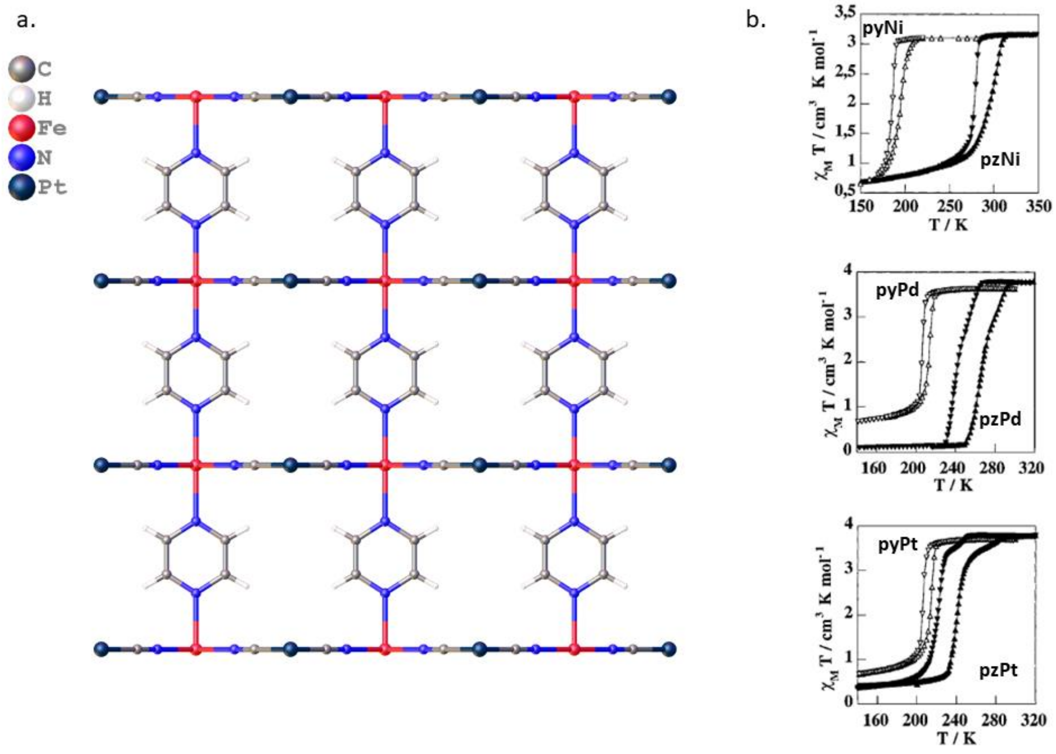

Figure 9: **a.** Structure of the Hofmann-type clathrate $\{Fe(pz)[Pt(CN)_4]\}\cdot 2H_2O$ (**pzPt·2H$_2$O**) seen along the *a*-axis. The guest water molecules have been removed for clarity. CCDC deposition number 660920.[32] **b.** X_MT variation *versus* temperature for compounds **pyNi**, and the isostructural **pyPd** and **pyPt** (grey line, from top down), and **pzNi·2H$_2$O**, **pzPd·2.5H$_2$O** and **pzPt·2H$_2$O** (black line, from top down). Adapted with permission from Ref. [33].

The structural changes in the solid state that a HS to LS transition induces are in fact transmitted cooperatively within the structure through elastic interactions.[25] This is generally interpreted as being mediated by intermolecular interactions such as hydrogen-bonds or van der Waals contacts in molecular SCO materials. In the case of a coordination network where the SCO centres are directly linked together through a bridging, rigid ligand *via* strong interactions such as coordination bonds, the communication between the SCO centres is enhanced, and hence the cooperativity is expected to be stronger.[25] A material with a strong cooperativity displays an abrupt SCO behaviour that can show hysteresis, a characteristic that is preferred for its potential application in switching devises and sensors.[31,34] It is important to point out that the SCO behaviour can also be influenced by other factors like the motion of the ligand. Real, Kitagawa and co-workers reported an interesting study that showed how the switching of the rotation of the **py** ligand in **pyPt** is associated with the change in the spin state of the material: the **py** rings perform in fact a 4-fold rotational motion when in the HS state, while suppression of the motion is seen in the LS state.[35]

It is hence clear how the choice of the building blocks used for synthesizing these materials has a strong influence on their final structure and SCO properties.

Focusing on the organic linker as a building block, it has already been mentioned that by using a monodentate ligand such as **py**, a 2D structure **pyPt** is obtained, while three-dimensionality is achieved in **pzPt** when a bidentate ligand is involved (**Figure 10a-d**). Additionally to the dimensionality, the interest in enhancing the accessible volume for guest molecules opened up the investigation of structures with more extended ligands, such as bis(4-pyridyl)acetylene (**bpac**) (**Figure 10e**). Compound **bpacPt** (**Figure 10f**) crystallizes with H_2O and a guest molecule **G** within the pores, where **G** = bpac, toluene or 2,4,6-trichlorophenol, and has an accessible volume of 293.6 Å^3, corresponding to the 41.7% of the unit cell volume at 120 K.[36] The comparison with the accessible volume reported for the pyrazine derivatives, equal to a 22% of the unit cell volume, proves how the attempt to design a material with enhanced porosity was achieved by using a larger rigid bidentate ligand.

Interest has been given to Hofmann clathrates for their guest-dependent SCO properties. The porosity of the structures serves as a host for adsorbing and desorbing guest molecules that can interact with the host *via* van der Waals, $\pi\cdots\pi$, hydrogen bonding interactions and also coordination bonding. These interactions act to perturb the system and can hence tune the SCO properties of the material.[37]

It has been seen that the desorption and adsorption of guests in Hofmann-clathrates influences the SCO behaviour following the trend in which incorporation of larger guests stabilize the HS state and hence reduces the SCO temperature of the host.[38] The adsorbed guest molecules can not only be solvent molecules, but also molecules of the ligand itself, like in the case of **bpacPt**. This framework showed a guest-dependent SCO behaviour in which a higher quantity of included guest led to a complete and cooperative spin transition, while a low quantity of guest led to an incomplete and less cooperative transition.[39] Finally, a rational design of the framework itself can lead to a controlled modulation of the SCO behaviour. Specific ligands can in fact be chosen to deliberately introduce supramolecular interactions between the host and the guest, an aspect that can both influence the capability of the framework to absorb guest molecules and the extent to which the SCO properties are affected by them.[40]

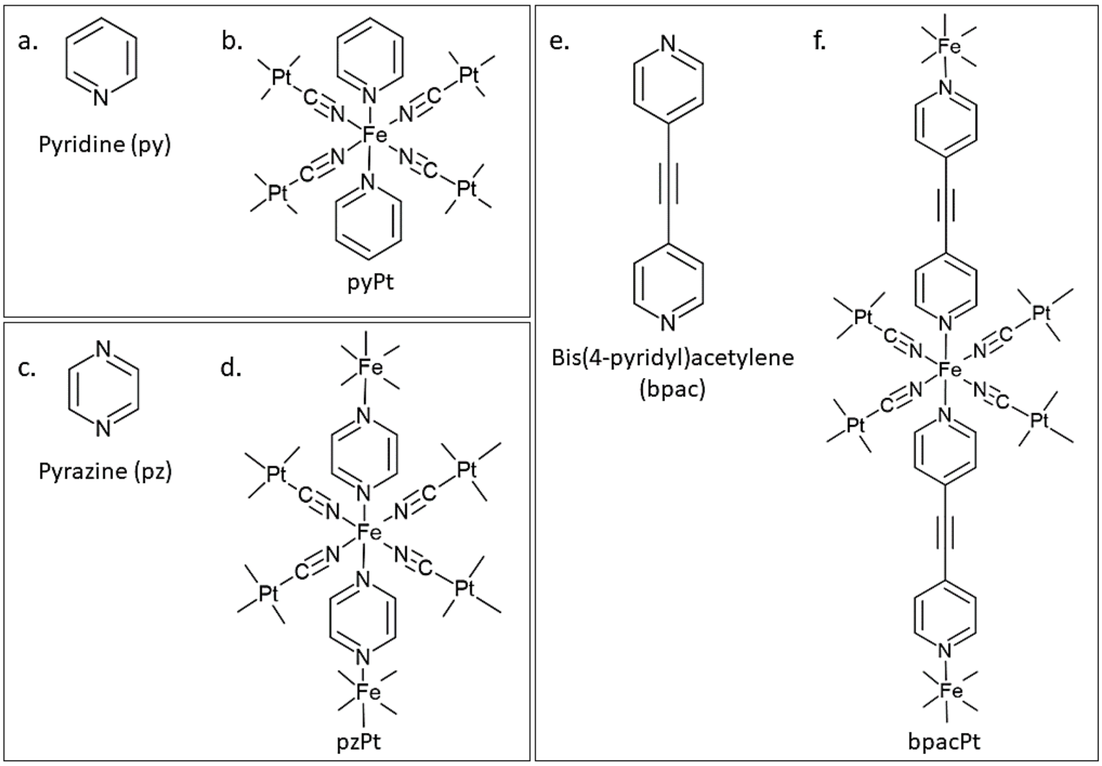

Figure 10: Schematic representation of **a.** pyridine ligand (**py**); **b.** the 2D Hofmann-type network {Fe(py)$_2$[Pt(CN)$_4$]} (**pyPt**); **c.** pyrazine ligand (**pz**); **d.** the 3D Hofmann-type framework {Fe(pz)[Pt(CN)$_4$]} (**pzPt**); **e.** bis(4-pyridyl)acetylene ligand (**bpac**); **f.** the 3D Hofmann-type framework {Fe(bpac)[Pt(CN)$_4$]} (**bpacPt**).

As an alternative to changing the ligand or guest to modify the network properties, the $[M^{II}(CN)_4]^{2-}$ ($M^{II} = Ni^{2+}$, Pd^{2+} or Pt^{2+}) building block can also be substituted by the linear ion $[M^{I}(CN)_2]^{-}$ ($M^{I} = Ag^{+}$, Au^{+} or Cu^{+}). The first cyanide-bridged Fe^{II}-Ag^{I} bimetallic compounds reported in literature are doubly interpenetrated 3D frameworks with formula $\{Fe(L)_x[Ag(CN)_2]_2\}\cdot G$, (L = **pz**, x = 1, G = **pz**, **pzAg·pz**; L = **bipy** = 4,4'-bipyridine, x = 2, **bipyAg**; L = **bpe** = 1,2-Bis(4-pyridyl)ethylene, x = 2, **bpeAg**).[41] The structure of the compounds with the three different ligands differ slightly: the 2D $\{Fe[Ag(CN)_2]_2\}$ sheets are connected through the organic linkers that coordinate to two iron atoms of adjacent layers for the **pz** compound, while an iron-silver coordination is seen in the **bipy** and **bpe** compounds.

Interpenetration takes place for all the three 3D frameworks just discussed, as opposed to what was reported for compounds $\{Fe(pz)[M^{II}(CN)_4]\}\cdot xH_2O$, where no interpenetration occurs. This difference was attributed to the fact that the tetradentate $[M^{II}(CN)_4]^{2-}$ unit forms voids that are four times smaller than the ones formed by the linear $[Ag(CN)_2]^{-}$ ion.[41] The increased void space allows the ligand of a second independent framework to be accommodated within the pores of the first framework, forming an entangled motif that can't be disentangled without disrupting the overall structure. Interestingly, the SCO behaviour seems to be less controllable when the ion $[Ag(CN)_2]^{-}$ is used: the **pz** based compound is in fact in the LS state at room temperature; the **bipy** one is in the HS state and doesn't show a thermally-induced spin transition at ambient pressure; the compound with **bpe** shows instead a cooperative spin transition at the temperature of 120 K with a hysteresis loop of 95 K.[41]

All the observations reported above indicate how small changes in the building blocks used for the synthesis of Hofmann-type clathrates can influence the structure of the resultant framework, and hence the SCO behaviour of the final material. Furthermore, porous SCO MOFs are very sensitive to changes in the presence of guest molecules, making them highly attractive for further exploration of the guests influence on the SCO properties of the host framework.

1.1.4 Metallophilic interactions in coordination compounds

The investigation of the chemistry and of the SCO behaviour of Hofmann-like compounds involving the $[M^{I}(CN)_2]^-$ group, where M^{I} = Cu^{I}, Ag^{I} and Au^{I}, was started in 2002 by Real and co-workers.[41] The group synthesised a new series of doubly interpenetrated 3D bimetallic compounds with formula $\{Fe(pz)[Ag(CN)_2]_2\}\cdot pz$ (**pzAg·pz**), $\{Fe(bipy)_2[Ag(CN)_2]_2\}$ (**bipyAg**) and $\{Fe(bpe)_2[Ag(CN)_2]_2\}$ (**bpeAg**), reporting the first examples of compounds where the ligand bridges an iron and a silver atom in the case of **bipyAg** and **bpeAg**, showing also a cooperative single-step SCO transition in the case of compound **bpeAg**.[41]

The comparison between the **pz**-based Hofmann-like structure constructed with Pt^{2+} and the one constructed with Au^+ that can be seen in **Figure 11**, allows to see how the supramolecular packing can change when the $[M^{II}(CN)_4]^{2-}$ group is substituted by the $[M^{I}(CN)_2]^-$ group. In this specific case, the voids that are generated when the $[Au^{I}(CN)_2]^-$ building block is involved in the synthesis (**Figure 11b**) are four times bigger than the ones formed when the $[Pt^{II}(CN)_4]^{2-}$ group is involved (**Figure 11a**).[42] The increased pore accessible volume generates hence enough space for interpenetration to occur, allowing the second independent network highlighted in light blue that can be seen in **Figure 11b** to accommodate within the pores of another network.[42]

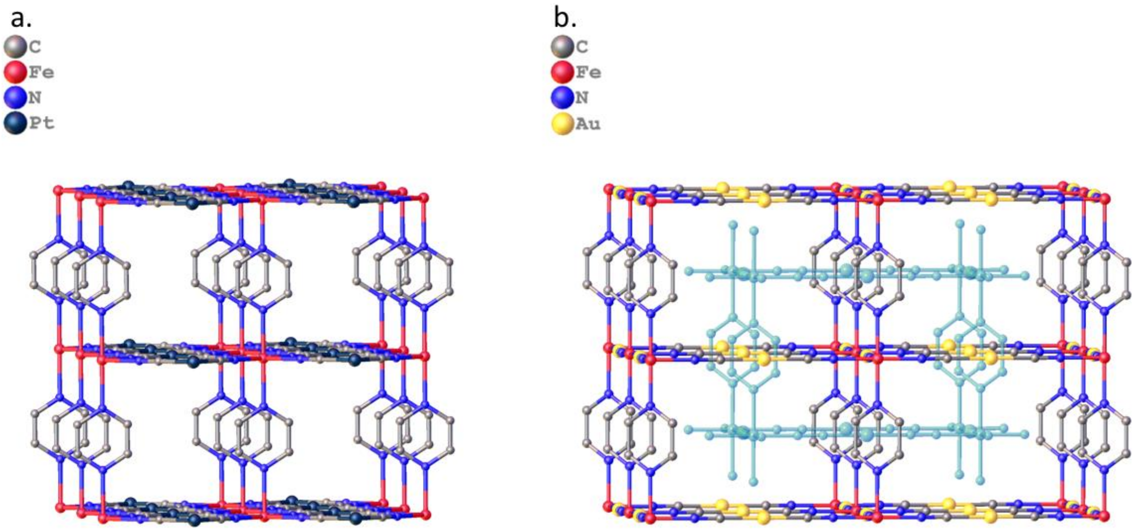

Figure 11: Structures of the **pz**-based Hofmann-type clathrates constructed with **a.** the $[Pt(CN)_4]^{2-}$ group and **b.** the $[Au(CN)_2]^-$ group. The second independent, interpenetrated network formed when the $[Au(CN)_2]^-$ group is used can be seen highlighted in light blue. CCDC deposition number for structure **a.** 660920,[32] for structure **b.** 1422396.[42]

The use of the $[M^I(CN)_2]^-$ group spread rapidly in the SCO community, allowing the impact of metallophilic interactions on the stability of the coordination networks and SCO properties to be investigated. The term “metallophilic” indicates the presence of metal-metal distances within a compound that are shorter than the sum of the van der Waals radii. It is referred to the propensity of d^{10} metals to be attracted to each other, and it arises from the overlap of the filled (n-1)d orbitals with the empty ns and np orbitals.[43] Argentophilic interactions, Ag(I)···Ag(I), are generally weaker than the aurophilic ones, Au(I)···Au(I), and allow a more diverse coordination numbers and geometries compared to the almost solely linear Au(I) compounds.[43] The $[Ag^I(CN)_2]^-$ group has been used more often in the formation of polymeric species compared to the analogous gold(I)-based building block because of the ability for Ag(I) to be 2- or 3-coordinate; however the higher flexibility of $[Ag^I(CN)_2]^-$ when compared to $[Au^I(CN)_2]^-$ renders its chemistry less controllable, and the lower stability of the silver(I)-based group makes it susceptible to dissociation with ligand distribution to form the species $[Ag_2(CN)_3]^-$ *in situ*.[43]

An interesting study showing the structural variety that can be obtained when the $[Ag^I(CN)_2]^-$ group is involved in the synthesis, reports the formation of two compounds with significantly different topology that are obtained when solvothermal conditions are used with a Fe^{II} salt, **bipy** and $K[Ag(CN)_2]$: the interpenetrated 3D compounds $\{Fe(bipy)[Ag_2(CN)_3]_2\}_n$ (**bipyAg2**) and $\{Fe(bipy)[Ag(CN)_2]_2[AgCN]_2\}_n$ (**bipyAgCN**).[44] Interestingly, the coordination environment of the iron centre that can be seen in compound **bipyAg2** is formed by two nitrogen atoms of the **bipy** ligands and by four nitrogen atoms of the cyanide group $[Ag_2(CN)_3]^-$ (**Figure 12a**).[44] The flexibility of this group allows then self-interpenetration of adjacent 3D networks to occur, forming a framework whose stability and rigidity is supported by argentophilic interactions between the interpenetrated networks, where the silver atoms of adjacent frameworks have a distance of 3.318(1) Å (**Figure 12b**).[44] Compound **bipyAgCN** shows instead a doubly interpenetrated Hofmann-like structure where the 2D $\{Fe[Ag(CN)_2]_2\}$ sheets are connected by the bridging **bipy** ligand, with the additional and unexpected formation of a [AgCN] chains along the *b* axis (**Figure 13**). Once again, the presence of the silver atoms in the framework stabilizes the structure *via* argentophilic interactions between the silver atoms of the anionic linker $[Ag(CN)_2]^-$ and of the [Ag(CN)] chains, which have a distance of 2.992(1) Å.[44] The rigidity of the frameworks induced by the Ag···Ag interactions was hypothesised to be the responsible for the quenching of the cooperativity in the two compounds, resulting in the compound being stuck in the HS state.[44]

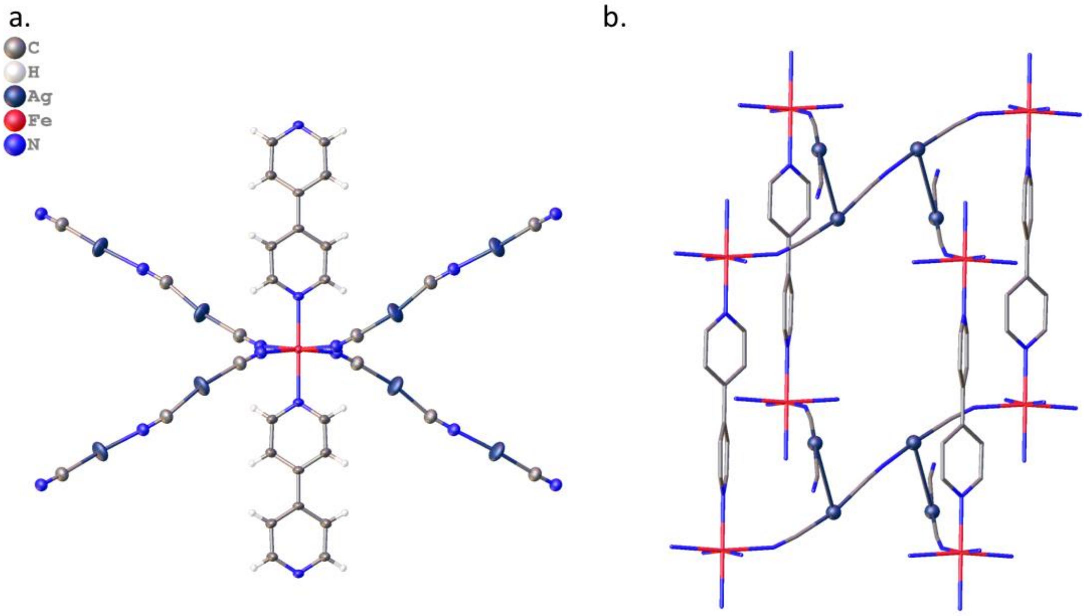

Figure 12: **a.** Structure of compound **bipyAg2** showing the coordination surrounding of the Fe(II) centre and **b.** the interpenetration between adjacent networks highlighting the Ag···Ag interactions. CCDC N°: 1445356.[44]

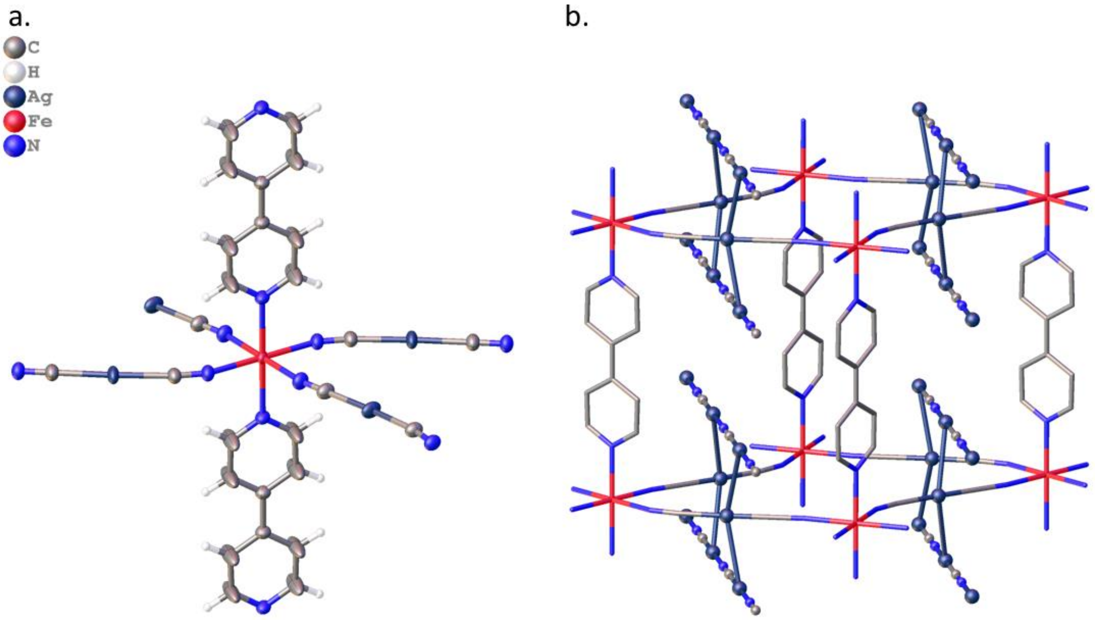

Figure 13: **a.** Structure of compound **bipyAgCN** showing the coordination surrounding of the Fe(II) centre and **b.** the supramolecular packing of the Hofmann-like framework **bipyAgCN** highlighting the Ag···Ag interactions between the 3D network and the 1D [AgCN] chains. CCDC N°: 1445357.[44]

An example of a compound that showed SCO behaviour influenced by argentophilic interactions involves the **pmd** ligand. In this work, Real and co-workers present a thermally and optically switchable coordination polymer with formula {Fe(pmd)[Ag(CN)$_2$][Ag$_2$(CN)$_3$]} (**pmdAg2**).[45] The compound forms an intricate 3D network where the **pmd** ligands bridge two consecutive iron centres in the axial positions, while the [Ag(CN)$_2$]$^-$ and the [Ag$_2$(CN)$_3$]$^-$ groups occupy the equatorial positions of the metal centre coordination sphere. Due to the *meta* (or 1,3) disposition of the nitrogen-donor atoms in the **pmd** ligand, the framework assumes the complex structure that can be seen in **Figure 14**. In this structure, the **pmd** ligand and the [Ag(CN)$_2$]$^-$ and [Ag$_2$(CN)$_3$]$^-$ groups act as three different ligands that form five distinct iron centres, each with a different number of silver anions around it.[45] Strong argentophilic interactions are present between the silver groups, with Ag···Ag distances in the 2.98-3.02 Å range at the temperature of 290 K, where the compound is in the HS state.[45] A two-step spin transition is reported for compound **pmdAg2**, with half of the Fe(II) centres going from the HS to the LS state at 170 K. An analogous behaviour is seen for the argentophilic interactions, which follow this two-step trend during the SCO transition for the Ag···Ag distance values. Finally, a full HS-to-LS transition is observed at 90 K where all the iron atoms are in the LS state, with all the Ag···Ag distances contracting to around 2.94 Å.[45] This compound shows an example of synergy between the metallophilic interactions within a framework and its SCO behaviour.

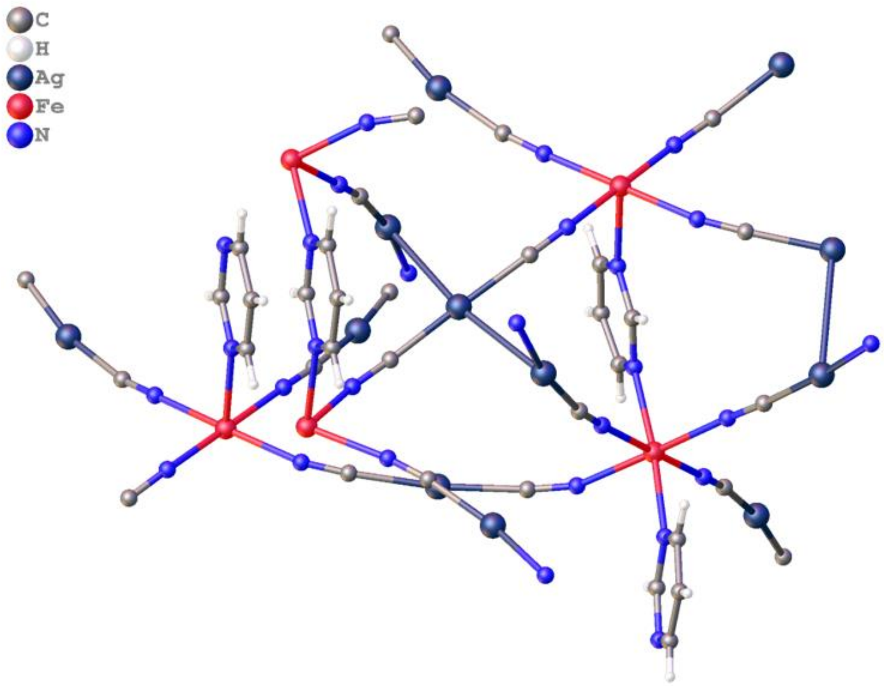

Figure 14: Structure of compound **pmdAg2** showing its intricate asymmetric unit. The structure has been drawn isotropically for clarity. CCDC N°: 249686.[45]

1.1.5 MOFs as crystalline flasks

The space within the pores of crystalline materials has been exploited in recent years to analyse *via* SCXRD guests that do not crystallise easily, but that arrange within the host's cavities in an ordered fashion.[46,47] This idea was developed from the principle that frameworks with large and well-defined interconnected cavities can allow the inclusion of small molecules from a sample solution, and that guests with a suitable size and shape can be trapped in the cavities in an ordered array. This allows them to be analysed using XRD even if they are not in the solid state, and hence to use a framework as a tool to study other materials incorporated within it. Additionally, the fact that the guest molecules are loosely interacting with the walls of the cavities allows them to reversibly bind with it until reaching a minimum of energy, an aspect that further encourages the ordering of the guest to occur.[46] These materials took the name of crystalline sponges or crystalline molecular flasks.[47,48] In 2002, Fujita and co-workers published the structure of a MOF constructed with 2,4,6-tris(4-pyridyl)triazine (**tpt**) ligand and ZnI_2 that exhibited the ability to contract after guest removal and expand after guest readsorption while preserving crystallinity.[47] In 2013, the concept of porous materials as crystalline sponges was then introduced as a method to analyse non crystalline materials *via*

SCXRD.[46] Since then, the method expanded rapidly to many research groups, allowing guests with different characteristics and sizes to be analysed.[49]

The MOF that is still nowadays mostly used as a crystalline sponge is Fujita's framework, which exhibits an extraordinary robustness and yet ability to breathe upon guest inclusion without losing the crystallinity. The framework has formula $[(ZnI_2)_3(tpt)_2 \cdot x(G)]_n$ (**tptZn·*x*G**) and it exhibits some interesting characteristics, such as an appropriate size of pores to accommodate common organic molecules, and multiple sites that favours the formation of supramolecular host-guest interactions. Finally, as it can be seen in **Figure 15**, the framework can adapt to the shape of the guest due to its flexibility, and this renders **tptZn·*x*G** a candidate that is even more suitable to be used as a crystalline sponge.[49]

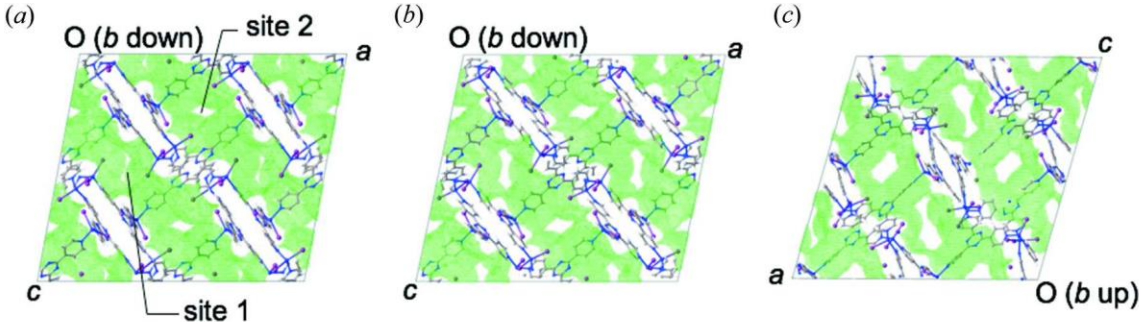

Figure 15: Crystal structure of **tptZn·*x*G** with different guests inside the pores: **a.** cyclohexane, **b.** guaiazulene and **c.** santonin. The walls of the pores are shown in green, presented with semi-transparent van der Waals surfaces. The deformation of site 2 and site 1 can be seen inclusion of different guests. Reprinted with permission.[49]

The method starts with the synthesis of the host framework, which has been optimised by Clardy and co-workers who published in 2015 the synthesis of **tptZn·*x*G** performed from a chloroform-methanol layering rather than a nitrobenzene-methanol one.[50] This change allows to obtain a chloroform-filled crystalline sponge, removing the step of solvent exchange necessary when nitrobenzene is instead inside the pores of the as-synthesised framework. In that latter case, cyclohexane is usually used to replace nitrobenzene, as it is a non-interactive and inert solvent.[49]

The guest soaking is the most important step of the process, and it requires optimization according to the nature of the guest. It can be performed by dipping the crystals of the sponge directly into a solution of the analytes (**Figure 16a**), method that requires a large quantity of analyte, or by using one grain of the sponge crystal that is placed in contact with a few milligrams of the liquid sample (**Figure 16b**), if the target compound is available in a small scale.[49] Another variation to perform the guest inclusion consists in allowing the slow evaporation of the solvent, and hence concentrate the guest solution until reaching the saturation point by equipping the vial lid with a needle (**Figure 16c**). Finally, one or more experimental conditions can be changed: soaking temperature, soaking time, solvent used, concentration of analytes, size of the crystal chosen and evaporation rate.

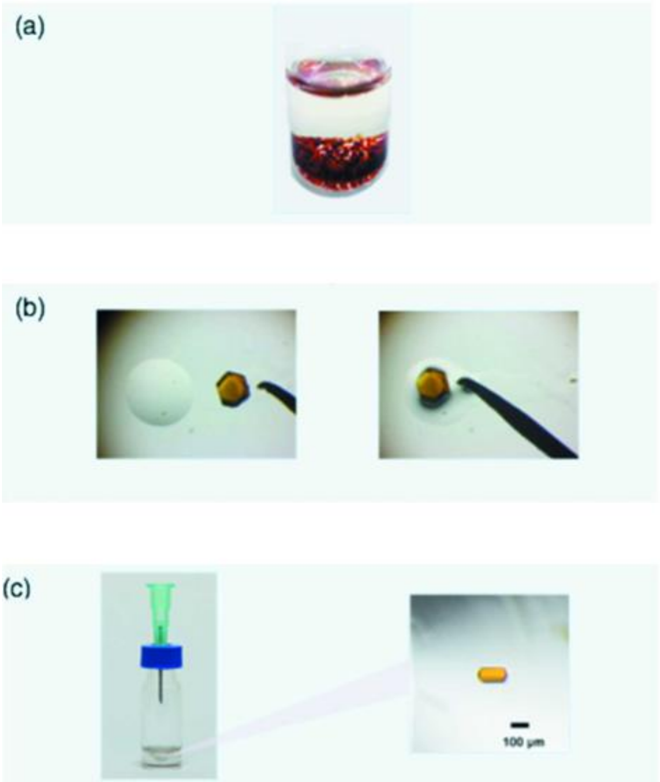

Figure 16: Soaking process methods: **a.** crystals of the sponge are directly dipped into the target solution; **b.** one grain of sponge is placed into contact with a drop of the analyte solution; **c.** the slow-evaporation of the analyte is allowed. Adapted with permission.[49]

The crystallographic analysis is the last step of the process. A good guest occupancy determines a good data quality and hence it is essential to start by finding the soaking conditions that works to incorporate as much of the specific analyte as possible. However, some precautions can be taken during the data collection to enhance the quality of the final data: measuring a sufficient number of reflections with a suitable I/σ value at high angle in order to be able to properly model the guest; using Cu $K\alpha$ radiation that provides a much higher I/σ in the high angle region.[49] In **Figure 17** the molecular structures of some of the guest molecules analysed with the crystalline sponge method is reported. More details about the steps of the method and the data processing can be found in section **4.1.2**.

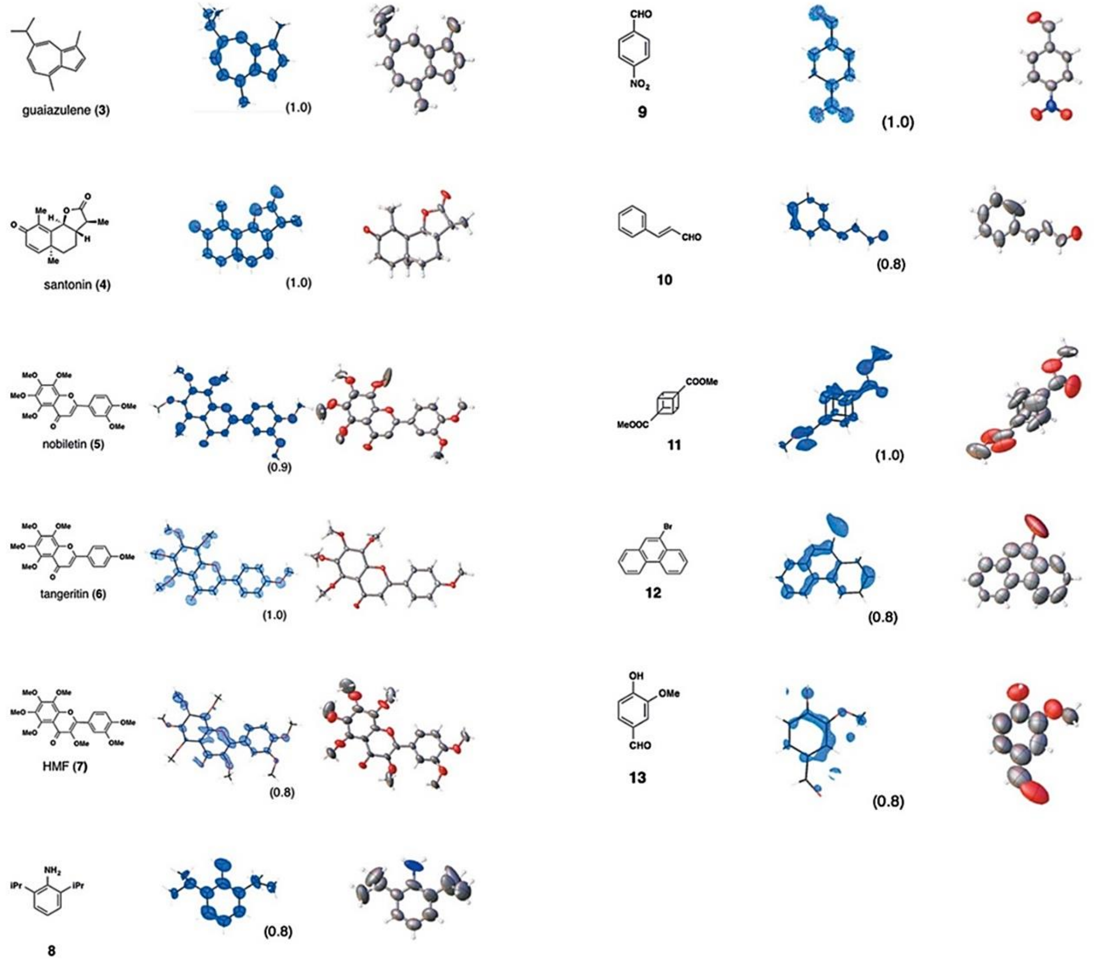

Figure 17: Molecular structure of some of the guests that have been analysed with the crystalline sponge method. Adapted with permission.[49]

The confined space of crystalline sponges, with all its features reported above, does not only allow to analyse the structure of molecules that do not crystallise easily, but it also provides a platform to observe *via* SCXRD dynamic processes occurring within the pores of the framework.[51,52,53] Fujita and co-workers published in 2008 a work in which an unstable imine was produced inside the pores of the **tptZn·*x*G** sponge by the condensation of the amino group of the guest 1-aminotriphenylene with acetaldehyde.[51] In 2011, the same group worked on the incorporation of Diels-Alder reactants (a diene and a dienophile) on the crystalline sponge frameworks, and to the consequent Diels-Alder reaction.[52] They exploited the host-guest interactions to orient the reactants in a precise manner, which allowed to control the reactivity and regioselectivity of the reaction while monitoring it with *in-situ* XRD.[52] Finally, Burrows and co-workers reported in 2016 the first example of the use of a gas-phase reagent to perform a chemical transformation inside the crystalline sponge.[53] The group performed the quantitative cyclization of 1,8-bis(2-phenylethynyl)naphthalene to 7-iodo-12-phenylindeno[2,1-α]phenalene upon exposure to iodine vapours, expanding the utility of the crystalline sponges also to gas-mediated transformations.[53] These examples represent just some of the most interesting works where the use of a crystalline sponge allowed to follow dynamic transformation occurring in the solid-state.

1.1.6 Luminescence and sensing in MOFs

Among all the fascinating properties of MOFs, many studies have been carried out that focus on their photoluminescence behaviour.[54,7,55] This derives from the possibility of harnessing these properties in real-world applications such as chemical- and biological-sensing and detection.[54]

Luminescence is defined as the process in which light is produced by the absorption of energy.[56] There are two types of luminescence: fluorescence, that lasts no more than 10 ns and relates to spin-allowed radiative transitions that involve energy states with the same spin multiplicity; and phosphorescence, that typically lasts between a microsecond and seconds and refers to spin-forbidden radiative transitions, involving the emission of light between states with different spin multiplicity.[57] More details about how this phenomenon generates light can be found in section **5.1.1**.

The tunable pore size of MOFs allows them to selectively recognize small molecules or ions. Additionally, the possibility for rational design in MOFs allowed scientists to easily induce luminescence properties into these materials by choosing specific building blocks or functionalities, enabling a wide range of emissive phenomena to occur.[55] In fact, the sensitivity of luminescent sensing of these materials can be enhanced by introducing functional sites such as Lewis basic or acidic sites and open metal sites to allow differential interactions with the guest molecules. This allows the guests to be in close proximity to the host structure, and interact with the MOF,[57] leading to a perturbation of the system. This perturbation can be detected in several ways as it can include a change in the emission wavelength or a change in the emission intensity. A change in the wavelength of emission occurs when there is a change in the structure of the MOF, which derives from dynamic movements of the framework upon guest inclusion, such as structural breathing behaviour.[58] This phenomenon implies a change in the energy gap between the ground state and the excited state of the system, thus resulting in a difference in the emission wavelength.[58]

Wavelength-based luminescence sensing has however been rarely reported compared to the one that is based on a change in emission intensity, lifetime and/or quantum yield.[58] The latter phenomenon does not imply a structural change and is hence more common, especially in more rigid MOFs. The signal that is seen in this case is the quenching of luminescence upon guest adsorption, and, more rarely, its enhancement.[7] This effect has been exploited to sense several analytes such as organic solvents, aromatics, water and ions.[7] An interesting use of fluorescent MOFs regards the field of sensing of hazardous materials, more particularly explosives.[59,60] Lan and co-workers published in 2009 the synthesis of a luminescent microporous MOF with formula [$Zn_2(bpdc)_2(bpee)$], where **bpdc** = 4,4'-biphenyldicarboxylate and **bpee** = 1,2-bipyridylethene), capable of a very fast and fully reversible detection of 2,4-dinitrotoluene (DNT) and 2,3-dimethyl-2,3-dinitrobutane (DMNB) (**Figure 18**).[59] DNT is an inevitable byproduct in the manufacturing formation of 2,4,6-trinitro-toluene (TNT), and it is much easier to detect because of its higher vapour pressure, and hence it is often used to detect the presence of nitroaromatic explosives.[59] On the other hand, plastic explosives do not contain nitroaromatics, and hence DMNB, a taggant contained in all the commercial plastic explosives as a requirement by law, is used to detect them.[59]

The enhanced luminescence of the framework herein discussed derives from the two organic ligands that were chosen to construct it. Their highly conjugated π-system acts both as a source of luminescence and as a binding site for host-guest interactions to occur.[59] As it can be seen in **Figure 18**, within 10 seconds of exposure to the analytes, the fluorescence quench percentage reaches 85 % and 84 % for respectively DTN and DMNB.[59] Additionally, the luminescence can be reversibly recovered more than one time consecutively, by simply heating the sample at 150 °C for one minute.[59] This crystalline porous material is hence able to detect traces of explosives in the vapour phase, giving a fast response in just a few seconds of exposure, and exhibiting high sensitivity to the analytes investigated.[59] This work represents a remarkable example of how the properties of these multifunctional porous materials can find important applications in solving real-world issues, such as the sensing of explosives.

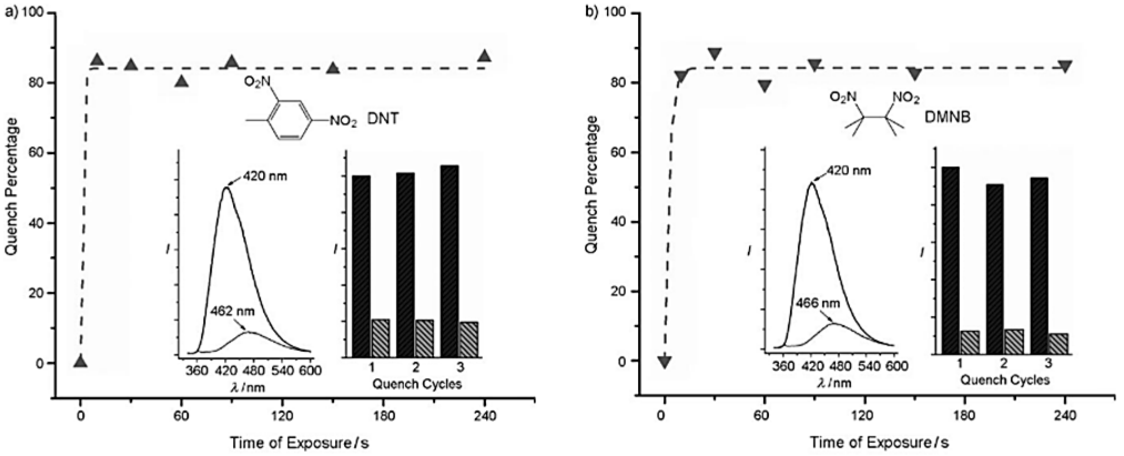

Figure 18: Time-dependent fluorescence quenching induced by the adsorption of **a.** DNT and **b.** DMNB. The insets represent the fluorescence spectra before and after the exposure of the MOF to the analyte for 10 s (left) and the effect of three consecutive quench and regeneration cycles (right). Adapted with permission.[59]

As seen in the example above, the origin of luminescence in emissive MOFs is typically generated from the organic linker.[61] More specifically, organic molecules with extended π-systems used as ligands do not only allow the backbone of the framework to be rigid, but they also are the main contributors to the emissive features of the entire system. In fact, the immobilization of the organic ligands and their ordered arrangement within the framework reduce the non-radiative decay from the excited state, enhancing the quantum yield of the system.[61]

A different way to generate luminescence emission from a MOF is to exploit the emissive nature of lanthanoid ions by incorporating them within the framework. This type of metal-based emission will be the subject of **Chapter 5**, where efforts towards rational design of porous lanthanoid coordination compounds will be described.

1.1.7 Organic-frameworks and SOFs

The family of porous materials contains not only hybrid frameworks constructed with a metal centre and an organic ligand – the well-known MOFs – but also frameworks constructed with only organic moieties, such as covalent organic frameworks (COFs). Both MOFs and COFs have an ordered internal periodicity and have pores with large surface areas.[62] The main difference between the two types of frameworks is that the building blocks self-assemble through robust coordination bonds for MOFs, while dynamic covalent bonds are present in COFs.[62] These products are normally isolated as insoluble crystals or crystalline powders, while the concept of constructing frameworks held together by less robust noncovalent interactions in solution was not introduced until 2013.[63] In this year, Li and co-workers synthesised the first 2D supramolecular organic frameworks (SOFs) soluble in water, which could also maintain its structural periodicity when in the solid state.[64] The interest in studying soluble porous supramolecular frameworks exhibiting periodic porosity arises form the possibility to render porous structures accessible for applications where homogeneity of the materials is essential.[64] This is important especially for biomedical and drug delivery applications, where any phase separation in the body has to be avoided.[64] A full description of the first 2D honeycomb SOF soluble in water mentioned above can be found in section **6.1.1**.[63]

The structure of SOFs are constructed through functional organic molecules that assemble via supramolecular interactions such as hydrogen bonding, π-π stacking, CH···π and van der Waals interactions.[65,66] Similar to MOFs and COFs, the structures of SOFs are periodic, but in contrast with them, they are characterised by a soft and flexible nature deriving from the supramolecular interactions between the organic components.[65] Additionally, most of the MOFs and COFs require harsh solvothermal conditions, while SOFs can be synthesised *via* molecular self-assembly in solution, rendering the conditions quite mild and potentially suitable for mass production.[62]

One limitation of SOFs as porous materials is that in most of the cases they are not stable upon the removal of the included species.[66] This derives from the fact that the structures of SOFs are not robust enough to stop the structural collapse towards a more densely packed structure to occur.[66] In this regard, Schröder and co-workers reported an interesting work where a SOF constructed with 9,10-Bis(4-((3,5-dicyano-2,6-dipyridyl)dihydropyridyl)phenyl)-anthracene (**bdddpa**) as organic moiety having formula **bdddpa·2.5DMF·3MeOH** (**Figure 19**) exhibited an unusually high thermal stability and promising gas adsorption results.[66] More specifically, the adsorption of gases like C_2H_2, CO_2, CH_4 and N_2 within this material showed a type-I isotherm, and their high uptake indicated that **bdddpa·2.5DMF·3MeOH** could potentially be a good candidate for C_2H_2, and natural gas purification and for CO_2 removal.[66] The approach that was used consisted of constructing the SOF with a large organic moiety carrying different functional groups that could act cooperatively to stabilize the supramolecular assembly, while at the same time the polar part of the molecule could remain available for host-guest interactions to occur.[66]

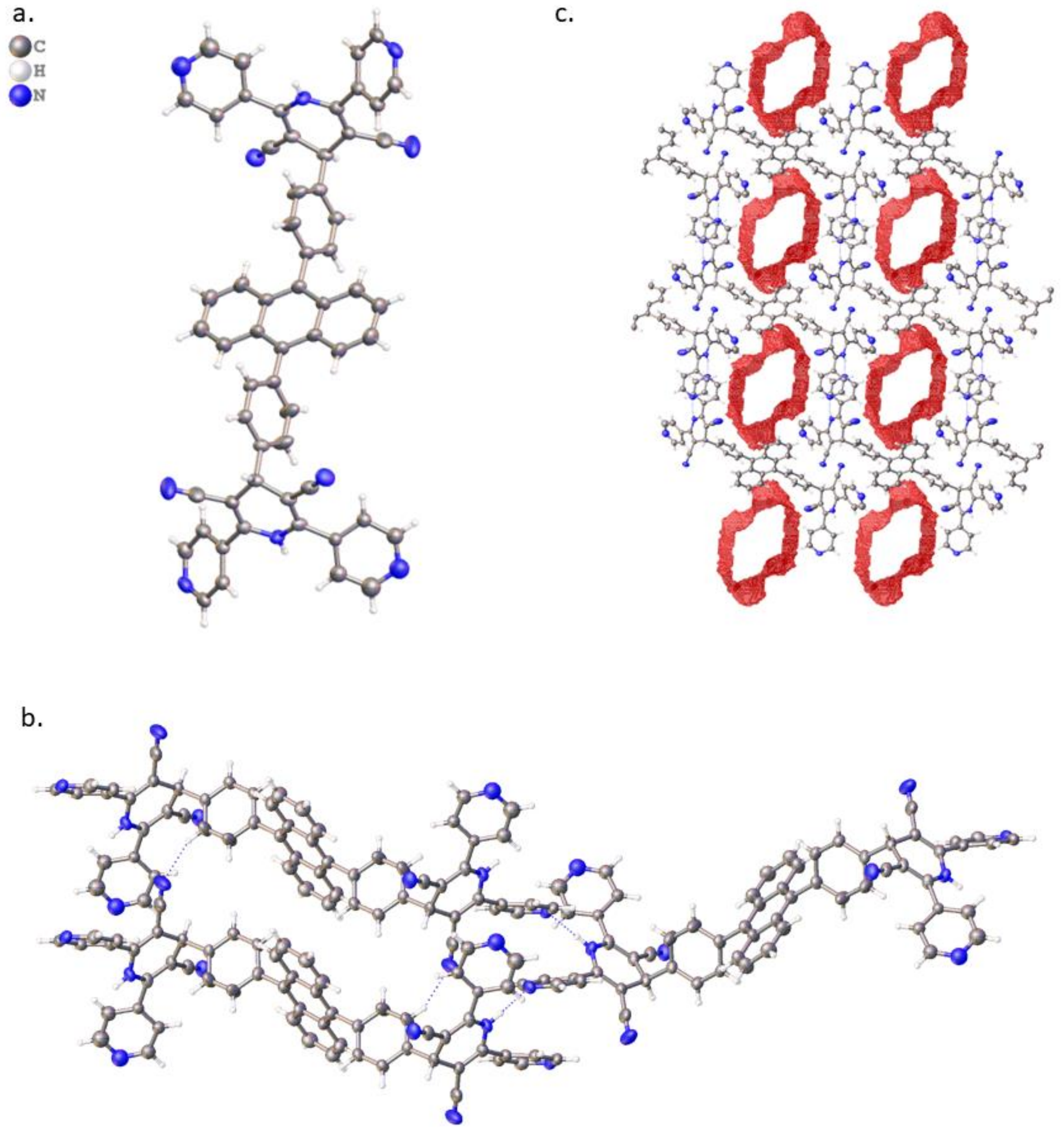

Figure 19: Structure of compound **bdddpa·2.5DMF·3MeOH** showing **a.** the organic moiety of **bdddpa** from SCXRD data, **b.** how the moieties interact in the supramolecular packing, and **c.** the voids that the packing forms. The red surface is obtained by a calculation that considers a sphere with a 1.2 Å^3 radius rolling within the voids of the structure. The white spaces are hence channels present in the structure.

This family of materials shares a lot of advantageous characteristics with the progenitor MOF class, such as periodicity in the solid state, thermal stability, and permanent porosity. SOFs present however some additional advantages, such as a low density deriving from the incorporation of low molecular weight elements in the framework, and enhanced solubility. Therefore, all the aspects herein reported render SOFs good candidates for numerous applications, ranging from catalysis, medicine and molecular sensing, to gas storage and separation.[67]

1.2 Introduction to characterization techniques

1.2.1 Characterization techniques for MOFs

A basic characterization of MOFs materials includes powder X-ray diffraction (PXRD) analysis to establish the crystallinity and purity of a sample, and the analysis of its potential porosity *via* the measurement of N_2 adsorption and desorption isotherms.[68] Additional techniques might be included to further demonstrate other interesting features of the material. For example, thermogravimetric analysis (TGA) can be used to determine the thermal stability of a MOF, with the possibility to also estimate the percentage of solvent (or guest) loss. Scanning electron microscopy (SEM) can be useful to measure the crystal size and morphology, and if equipped with energy dispersive X-ray spectroscopy (EDS), information about the elemental composition and distribution can be achieved.[68] Daily-routine techniques such as NMR can be used to determine the bulk purity and the ligand ratios in mixed ligand MOFs, or IR can be useful to determine the active functional groups in the framework. Finally, single crystal X-ray diffraction (SCXRD) gives essential information regarding the structure of the obtained MOF.[68]

The following sections include a full description of diffraction-based techniques, which are the main characterization techniques that will be used within this work.

1.2.2 Fundamentals of X-ray diffraction

Among all the characterization techniques used in the field of chemistry, crystallography is one of the most powerful ones that allows details about the structure of a material to be obtained. More specifically, information about the relative position of the atoms and the molecules in the solid state can be determined and used to understand the properties of those materials.[69] Crystallography is the study of crystalline matter using diffraction, and it includes single crystal X-ray diffraction (SCXRD), powder X-ray diffraction (PXRD), and neutron and electron diffraction both on single crystals or powders. Although each of these techniques gives invaluable information by its own, SCXRD and PXRD are by far the most common techniques used to perform the study of the structure of a crystalline solid.[69]

X-ray diffraction (XRD) experiments are performed on crystalline materials, which can be present in the form of a single crystal or of a crystalline powder. A perfect crystalline solid material is constructed from the repetition of a large number of identical structural units, which are arranged in a precise regular way in all the directions, to form a highly ordered structure.[70] Each of the structural units that are present in the crystal, called a unit cell, is always related to the others by translation. There are often additional symmetry elements within the unit cell that relate different parts of the unit cell to each other. The unique part of the unit cell is known as the asymmetric unit. It is hence possible to generate the contents of the unit cell from the asymmetric unit *via* symmetry operations, and then generate the rest of the crystal through translation of the unit cell.[70] The unit cell is a parallelepiped defined by three vectors **a**, **b** and **c** (**Figure 20**) with length *a*, *b* and *c*, and forming angles α, β and γ between them.[71] These six values define hence the unit cell parameters.

Before understanding the geometry of diffraction, it is useful to define Miller planes. These are imaginary planes within the crystal and are defined as the reciprocal of the fractional intercepts between the plane and the crystallographic axes (**Figure 20**). They are identified by a set of three integer numbers *h*, *k*, *l*, which refers to an infinite number of planes parallel to each other, separated by a spacing, *d*.[72]

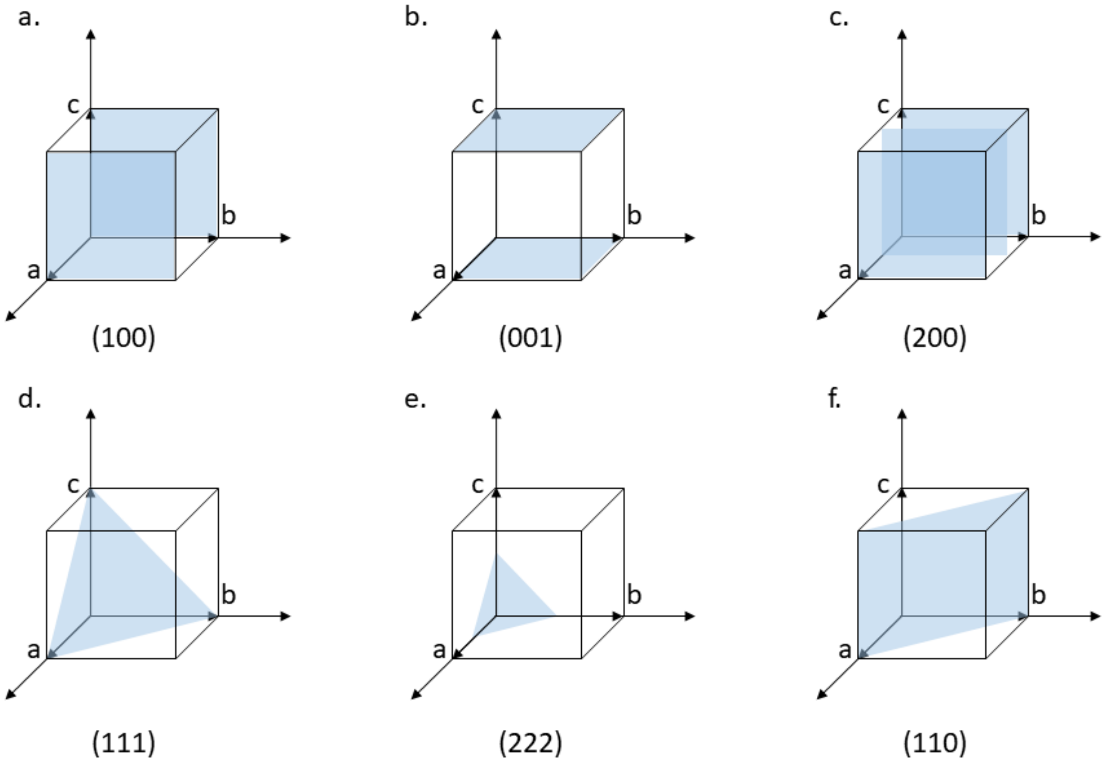

Figure 20: Graphic representation of the Miller planes representing **a.** the planes (100); **b.** the planes (001); **c.** the planes (200); **d.** the plane (111); **e.** the plane (222); **f.** the plane (110). For clarity, the parallel set of planes is shown for **a.**, **b.** and **c.**, while only one plane was shown in the remaining examples.

1.2.3 Single crystal and powder X-ray diffraction

When performing a SCXRD experiment, a single crystal of a sample is hit by a beam of monochromatic X-rays. The interactions between the electrons of the atoms of the crystal and the incident X-ray beam causes scattering of X-rays in all the directions.[72] Elastic scattering occurs when the incident radiation is not absorbed by the sample, but is deviated from the interaction with it, maintaining the same energy. Each atom can be seen as a point that acts hence as a source of scattering (**Figure 21a**).

The diffraction of X-rays from a crystals lattice come from all the Miller set of planes of the crystal, giving rise to a discrete diffraction pattern.[72] The diffraction pattern obtained from a single crystal can be explained using Bragg's law.[72] Looking at **Figure 21b** it can be seen that in a crystal lattice, the set of planes are located at a distance of *d*, which is also known as *d*-spacing.[72] When a beam of parallel X-rays impinges with an incident angle, θ, on a set of planes separated by *d*, the X-rays are hence scattered.

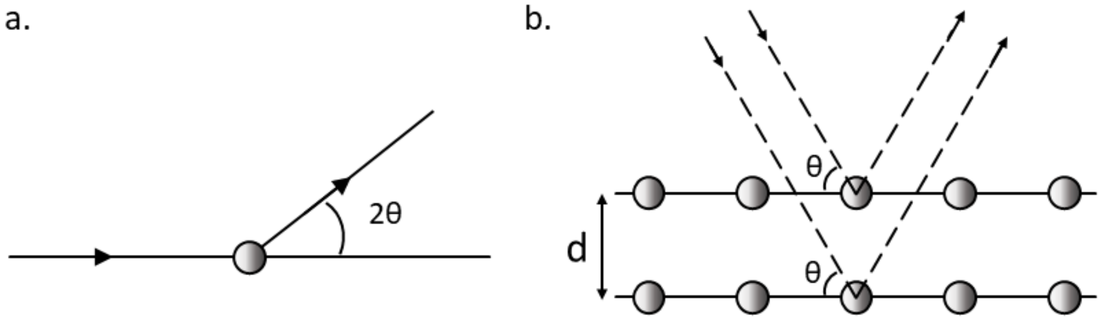

Figure 21: **a.** Generic scattering of a single X-ray from an atom that acts as a point of diffraction. **b.** Schematic representation of an array of atoms, two of which scatter the two incident X-rays having identical wavelength and phase.

Bragg's law (**Equation 1**) is an equation that describes the conditions under which constructive interference, and hence a diffracted beam, can be observed,[71] as shown in **Figure 21b.** The path difference between the two X-ray beams is equal to $2d\sin(\theta)$, and this value must be an integer multiple of the wavelength λ in order for the scattered X-rays to interact constructively.[71] On the contrary, when Bragg's law is not respected, the scattered X-rays will interfere destructively and no diffraction will be seen.

$$n\lambda = 2d\sin(\theta)$$

Equation 1: Bragg's law, where *n* is an integer number, λ is the wavelength of the radiation used, *d* is the distance between two consecutive planes and θ is the angle between the incident ray and the plane of the crystal.

It is important to notice that the schematic representation reported above for Bragg's law assumes that the material is formed from discrete planes of atoms. In reality, a single crystal is composed of many intersecting sets of planes with different orientations. Bragg intensities are measured from a large number of these planes, each of which contributes to the diffraction pattern. These intensities, that are measured from the diffracting planes with Miller indices *hkl*, are proportional to the square of the amplitudes of the structure factors F_{hkl} that are defined as:[69]

$$F_{hkl} = \sum_{i=1}^{n} f_i T_i \exp\left(2\pi i(hx_i + ky_i + lz_i)\right)$$

Equation 2: Structure factor formula. *hkl* are the Miller indices; n are the atoms in a unit cell; f_i are the scattering factors of the atoms in the unit cell; T_i is the temperature factor; x_i, y_i, z_i are the fractional atomic coordinates.

The summation includes all the atoms in the unit cell (n), each having a scattering power given by the scattering factor f_i and having fractional atomic coordinates x_i, y_i, z_i.[69] From **Equation 2** it is clear that the temperature factor term T_i, which takes into consideration the thermal motion of each atom, influences the structure factors. More specifically, $T_i = 1$ if the atoms are considered still, while atoms that move will have $T_i < 1$.[69] As a consequence, T_i reduces the scattering power due to lattice vibrations, which are reduced when the temperature is reduced.[69] The temperature used during the data collection is hence an important factor that influences the intensity of the diffracted beams, and for this reason using a lower temperature is usually preferred to overcome this issue.

The scattering power is also dependent on the scattering angle. Considering the hypothetical case in which the electrons of an atom were situated in one point, the atomic scattering factor would be equal to the atomic number (*Z*) of the atom itself. The electrons are however spread in a finite volume having the same order of magnitude of the X-rays wavelength, and hence there will be a difference in the path of X-rays that are scattered from different electrons belonging to the same electron cloud.[69] For low angle data, the path difference is very small and the atomic scattering factors will be close to the *Z* value. The increase of 2θ increases instead this path difference, enhancing the chance to have destructive interference between the scattered beams, and rendering f_i < < *Z*.[69] The latter situation is further aggravated by higher temperatures, as this enhances even further the motion of electrons producing a larger smear of electron density.[69] In this case, the decrease of scattering power is more abrupt compared to when the crystal is at a lower temperature, when instead this decrease is gradual. Therefore, using a lower temperature allows for more scattering contribution in the high angle region, which is the one that contains higher resolution data.

Another aspect that can be influenced by the temperature is disorder. Crystals are periodic structures with long range order of atoms and molecules.[73] Real crystals however are not perfect, presenting several types of lattice defects, including disorder. Disorder occurs when the orientation of some atoms differs in different unit cells.[73] As the structure determined from the diffraction pattern is an average over all the crystal and over the time of the experiment, this defect will result in the two (or more) orientations of the structure being observed at once, each with a fraction of the total occupancy of the disordered unit.[74] There are two different types of positional disorder, defined as the case in which one atom appears to occupy more than one site: static disorder and dynamic disorder. Dynamic disorder describes motion of atoms in the solid state, and it occurs when there is sufficient energy for the unit to rotate or oscillate in the crystal lattice. Imagining each of the unit cells being a soldier, this case can be seen as if the soldiers were continuously shaking their heads unable to decide whether to look right or left, rather than all looking to the right.[73] This type of disorder can occur when organic side chains, or groups that can be free to rotate like the *tert*-butyl group are present in the molecule, or when free solvent molecules are located within pores of the crystal lattice.[73] Static disorder arises instead when the molecule can possess two, or rarely more, well-defined conformations that are energetically similar.[73] In this case, some soldiers look to the right, some look instead to the left.[73] The two conformers can in fact crystallize in the same packing during the process of crystallization, but they cannot interconvert without re-dissolution.[74] While dynamic disorder can be reduced by collecting the data at a lower temperature as this reduces the movement of atoms, static disorder shows instead no temperature dependence.[73] In the latter case, the disorder arises during the growth of the crystal, and hence lowering the temperature during this step rather than during the data collection might make the difference in stabilizing one of the two energetically similar orientations.[73] For these reasons, performing variable temperature measurements can help in distinguishing between the two types of disorder.

The phenomenon of SCO can be seen as a special case of dynamic disorder, where the spin transition, and hence the movement of the atoms within the crystal, is reversibly dependent on the temperature. The LS state of a material observed at low temperatures, and the HS state formed at higher temperatures differ in their magnetic, optical and indeed structural properties. It appears hence clear how fundamental it is to perform structural studies of the different states at different temperatures in order to fully understand the mechanism of the transition.[69] From **Figure 22a** it can be seen how the structure of a SCO active material changes between the two states: when going from the HS state (blue structure) to the LS state (pink structure), the average Fe-N distances of compound [Fe(phen)$_2$(NCS)$_2$] are reduced from 2.122(5) Å to 1.983(5) Å, and consequently the FeN_6 octahedron volume (V_{coord}) highlighted in **Figure 22b** is reduced from 12.71(2) Å^3 to 10.327(10) Å^3.

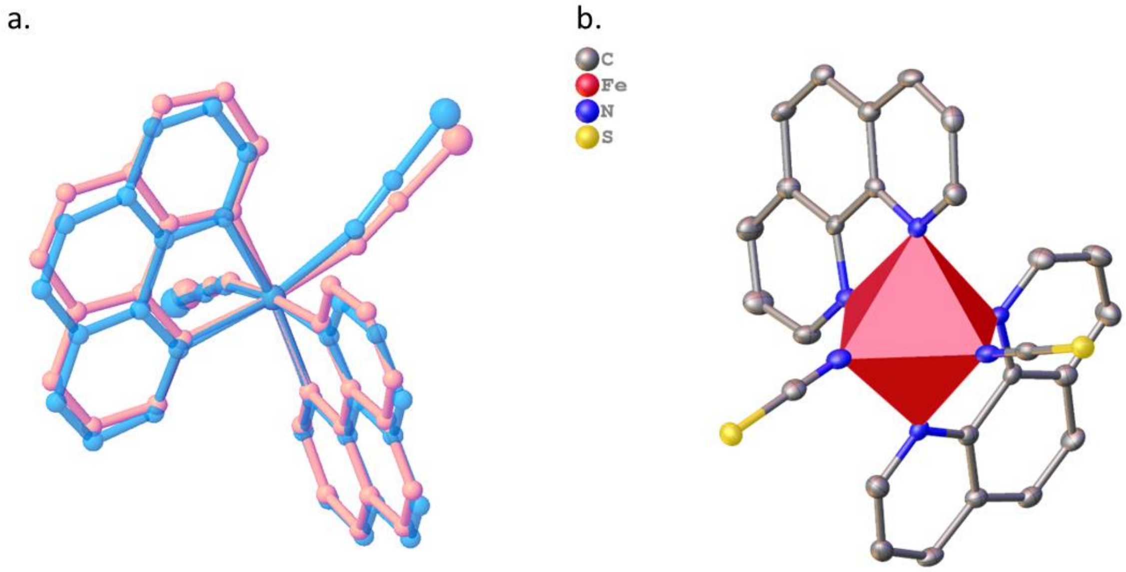

Figure 22: **a.** Overlay of the structures of compound $[Fe(phen)_2(NCS)_2]$ in the HS state (blue structure) and in the LS state (pink structure) and **b.** graphic illustration of the FeN_6 octahedron volume V_{coord} for the compound in the LS state.[69]

So far, the focus has been given to diffraction obtained from a single crystal, which forms diffraction spots following the Bragg's law, as explained above. In order to measure the intensities of all reflections up to a desired resolution, it is essential to rotate the single crystal during data collection.[68] In the case of a crystalline powder material, many single crystals of the same compound are oriented randomly. Each of them gives its own diffraction pattern which are overall superimposed.[68] Diffraction occurs once again when the Bragg equation is fulfilled, but in this case a particular reflection is generated by individual crystals at different times (when the Bragg equation is satisfied).[68] More specifically, the Bragg angle and the intensity of the diffracted beams will be the same, but their direction will vary.[68] This forms a diffraction pattern with concentric circles, rather than the discrete one seen from single crystal. These circles have radii dictated by the Bragg's law, and hence contain information about the unit cell geometry.[68] The powder diffraction data is usually presented by showing the intensities of the diffracted beams, I, recorded as a function of the scattering angle 2θ, and it gives important information about the crystallinity of a sample and about its phase purity.

PXRD is a rapid method to identify crystalline compounds, it is non-destructive and the sample does not require complex preparation. For this reason, it is a very common technique used in variety of fields of research, ranging from chemistry, forensic science, and mineralogy, to pharmaceutical and biological sciences. On the other hand, more detailed information regarding the crystal structure, such as bond-lengths and bond-angles are more easily measurable through a SCXRD experiment. This especially applies to the case of a low symmetry or to materials with a large unit cell volume, as it will be discussed in the following chapters. This technique has however the limitation of requiring the sample to be a good-quality single crystal, and this often implies that time needs to be spent in the sample preparation to find the best crystallisation conditions. Additionally, while in PXRD the diffraction pattern represents the bulk composition of the crystalline material, in a SCXRD experiment the pattern is obtained from one single crystal, which doesn’t necessarily represent the composition of the overall material.

1.3 Aims

This work aims to expand the structural diversity of coordination polymers and framework materials by using ligands that are less frequently reported in the literature, and to determine how this aspect affects their properties. Ligands with different chemical functionalities and conformational flexibility will be investigated, aiming to construct new materials exhibiting SCO activity. Furthermore, ligands with the ability to self-assemble *in-situ* will be explored to obtain porous luminescent materials with potential applications in the field of sensing, as well as to construct SCO materials.

The porosity of these compounds will also be exploited to observe dynamic processes, and to modify the properties of the materials themselves. A porous crystalline MOF will be investigated as a tool to study the dynamic mechanism of photoswitching in DASAs materials. Additionally, the host-guest properties of SCO materials will be explored to investigate how the guest influences their SCO behaviour.

Finally, a newer class of porous materials that uses supramolecular interactions rather than the directional metal-ligand coordination bonds will be studied to construct robust networks that are capable as well to allow dynamic processes to occur.

1.4 Experimental details of SCXRD and PXRD

Single crystal XRD data were collected on a Rigaku Oxford Diffraction SuperNova A S2 single crystal diffractometer using a Cu or a Mo radiation source. Sample specific details can be found in the crystallographic tables. Sample temperature was controlled using an Oxford Cryosystems 800 series Cryostream.

Using the software Olex2,[75] the structures were solved with the ShelXT structure solution program using Intrinsic Phasing method and refined with the ShelXL refinement package using Least Squares minimisation.[76,77,78]

Powder XRD data were collected on a Rigaku Miniflex 600 using a Cu radiation source and measurements were performed at room temperature.

1.5 References

1 J.-R. Li, Y. Ma, M. C. Mccarthy, J. Sculley, J. Yu, H.-K. Jeong, P. B. Balbuena and H.-C. Zhou, *Coord. Chem. Rev.*, 2011, **255**, 1791–1823.

2 J. Long, O. Yaghi, J.-R. Li, R. J. Kuppler and H.-C. Zhou, *Chem. Soc. Rev*, 2009, **38**, 1477–1504.

3 J. Lee, O. K. Farha, J. Roberts, K. A. Scheidt, S. T. Nguyen and J. T. Hupp, *Chem. Soc. Rev.*, 2009, **38**, 1450–1459.

4 B. Chen, S. Xiang and G. Qian, *Acc. Chem. Res.*, 2010, **43**, 1115–1124.

5 S. George K. H., T. Jared M. and K. SiRim, *Science*, 2013, **341**, 354–355.

6 S. R. Batten, N. R. Champness, X. Chen, J. Garcia-martinez, S. Kitagawa, L. Öhrström, M. O. Keeffe, M. P. Suh and J. Reedijk, *Pure Appl. Chem.*, 2013, **85**, 1715–1724.

7 L. E. Kreno, K. Leong, O. K. Farha, M. Allendorf, R. P. Van Duyne and J. T. Hupp, *Chem. Rev.*, 2012, 112, 1105–1125.

8 C. Janiak and J. K. Vieth, 2010, **34**, 2337–2684.

9 Y. Sun and H.-C. Zhou, *Sci. Technol. Adv. Mater.*, 2015, **16**, 1–11.

10 J. L. C. Rowsell and O. M. Yaghi, *Microporous Mesoporous Mater.*, 2004, **73**, 3–14.

11 M. Alhamami, H. Doan and C. H. Cheng, *Materials (Basel).*, 2014, 7, 3198–3250.

12 H. Li, M. Eddaoudi, M. O'Keeffe and O. M. Yaghi, *Nature*, 1999, **402**, 276–279.

13 J. L. C. Rowsell and O. M. Yaghi, *Microporous Mesoporous Mater.*, 2004, **73**, 3–14.

14 Y. N. Gong, D. C. Zhong and T. B. Lu, *CrystEngComm*, 2016, 18, 2596–2606.

15 O. K. Farha, I. Eryazici, N. C. Jeong, B. G. Hauser, C. E. Wilmer, A. A. Sarjeant, R. Q. Snurr, S. T. Nguyen, A. Ö. Yazaydin and J. T. Hupp, *J. Am. Chem. Soc.*, 2012, **134**, 15016–15021.

16 H.-L. Jiang and Q. Xu, *Chem. Commun.*, 2011, **47**, 3351.

17 T. R. Cook, Y.-R. Zheng and P. J. Stang, *Chem. Rev.*, 2013, **113**, 734–777.

18 X. Zhang, Z. Chen, X. Liu, S. L. Hanna, X. Wang, R. Taheri-Ledari, A. Maleki, P. Li and O. K. Farha, *Chem. Soc. Rev.*, 2020, 49, 7406–7427.

19 J. Yang, A. Grzech, F. M. Mulder and T. J. Dingemans, *Chem. Commun.*, 2011, **47**, 5244–5246.

20 T. Wu, L. Shen, M. Luebbers, C. Hu, Q. Chen, Z. Ni and R. I. Masel, *Chem. Commun.*, 2010, **46**, 6120–6122.

21 O. I. Kucheriv, I. O. Fritsky and I. A. Gural'skiy, *Inorg. Chim. Acta*, 2021, **521**, 120303.

22 P. Gütlich and H. A. Goodwin, Springer, Berlin, Heidelberg, 2012, pp. 1–47.

23 L. Cambi and L. Szegö, *Berichte der Dtsch. Chem. Gesellschaft (A B Ser.*, 1931, **64**, 2591–2598.

24 C. J. Ballhausen and A. D. Liehr, *J. Am. Chem. Soc.*, 1959, **81**, 538–542.

25 M. C. Muñoz and J. A. Real, *Coord. Chem. Rev.*, 2011, 255, 2068–2093.

26 E. Collet and P. Guionneau, *Comptes Rendus Chim.*, 2018, 21, 1133–1151.

27 J. Cirera, *Rev. Inorg. Chem.*, 2014, 34, 199–216.

28 Y. Garcia, V. Niel, M. Carmen Muñoz and J. A. Real, *Top. Curr. Chem.*, 2004, **233**, 229–257.

29 J. H. Rayner and H. M. Powell, *J. Chem. Soc.*, 1952, 319–328.

30 T. Kitazawa, Y. Gomi, M. Takahashi, M. Takeda, M. Enomoto, A. Miyazaki and T. Enoki, *J. Mater. Chem.*, 1996, **6**, 119–121.

31 Z. P. Ni, J. L. Liu, M. N. Hoque, W. Liu, J. Y. Li, Y. C. Chen and M. L. Tong, *Coord. Chem. Rev.*, 2017, **335**, 28–43.

32 M. Ohba, K. Yoneda, G. Agusti, M. C. Muñoz, A. B. Gaspar, J. A. Real, M. Yamasaki,

H. Ando, Y. Nakao, S. Sakaki and S. Kitagawa, *Angew. Chemie - Int. Ed.*, 2009, **48**, 4767–4771.

33 V. Niel, J. M. Martinez-Agudo, M. C. Muñoz, A. B. Gaspar and J. A. Real, *Inorg. Chem.*, 2001, **40**, 3838–3839.

34 W. Liu, L. Wang, Y. J. Su, Y. C. Chen, J. Tucek, R. Zboril, Z. P. Ni and M. L. Tong, *Inorg. Chem.*, 2015, **54**, 8711–8716.

35 J. A. Rodríguez-Velamazán, M. A. González, J. A. Real, M. Castro, M. C. Muñoz, A. B. Gaspar, R. Ohtani, M. Ohba, K. Yoneda, Y. Hijikata, N. Yanai, M. Mizuno, H. Ando and S. Kitagawa, *J. Am. Chem. Soc.*, 2012, **134**, 5083–5089.

36 C. Bartual-Murgui, N. A. Ortega-Villar, H. J. Shepherd, M. C. Muñoz, L. Salmon, G. Molnár, A. Bousseksou and J. A. Real, *J. Mater. Chem.*, 2011, **21**, 7217–7222.

37 Z. P. Ni, J. L. Liu, M. N. Hoque, W. Liu, J. Y. Li, Y. C. Chen and M. L. Tong, *Coord. Chem. Rev.*, 2017, 335, 28–43.

38 P. D. Southon, L. Liu, E. A. Fellows, D. J. Price, G. J. Halder, K. W. Chapman, B. Moubaraki, K. S. Murray, J. F. Létard and C. J. Kepert, *J. Am. Chem. Soc.*, 2009, **131**, 10998–11009.

39 C. Bartual-Murgui, L. Salmon, A. Akou, N. A. Ortega-Villar, H. J. Shepherd, M. C. Muñoz, G. Molnár, J. A. Real and A. Bousseksou, *Chem. - A Eur. J.*, 2012, **18**, 507–516.

40 M. Meneses-Sánchez, R. Turo-Cortés, C. Bartual-Murgui, I. Da Silva, M. C. Muñoz and J. A. Real, *Inorg. Chem.*, 2021, **60**, 11866–11877.

41 V. Niel, M. C. Muñoz, A. B. Gaspar, A. Galet, G. Levchenko and J. A. Real, *Chem. Eur. J.*, 2002, **8**, 2446–2453.

42 I. A. Gural'skiy, B. O. Golub, S. I. Shylin, V. Ksenofontov, H. J. Shepherd, P. R. Raithby, W. Tremel and I. O. Fritsky, *Eur. J. Inorg. Chem.*, 2016, **2016**, 3191–3195.

43 M. J. Katz, K. Sakai and D. B. Leznoff, *Chem. Soc. Rev.*, 2008, **37**, 1884–1895.

44 Z. Setifi, A. Addala, J. Tao, N. Wannarit, C. Glidewell, F. Setifi and S. Youngme,

Inorg. Chem. Commun., 2016, **68**, 80–84.

45 V. Niel, A. L. Thompson, A. E. Goeta, C. Enachescu, A. Hauser, A. Galet, M. C. Muñoz and J. A. Real, *Chem. - A Eur. J.*, 2005, **11**, 2047–2060.

46 P. Stallforth and J. Clardy, *Nature*, 2013, **495**, 456–457.

47 K. Biradha and M. Fujita, *Angew. Chemie - Int. Ed.*, 2002, **41**, 3392–3395.

48 Y. Inokuma, M. Kawano and M. Fujita, *Nat. Chem.*, 2011, **3**, 349–358.

49 M. Hoshino, A. Khutia, H. Xing, Y. Inokuma and M. Fujita, *IUCrJ*, 2016, **3**, 139–151.

50 T. R. Ramadhar, S. L. Zheng, Y. S. Chen and J. Clardy, *Acta Crystallogr. Sect. A Found. Crystallogr.*, 2015, **71**, 46–58.

51 T. Haneda, M. Kawano, T. Kawamichi and M. Fujita, *J. Am. Chem. Soc.*, 2008, **130**, 1578–1579.

52 K. Ikemoto, Y. Inokuma and M. Fujita, *J. Am. Chem. Soc.*, 2011, **133**, 16806–16808.

53 J. V. Knichal, H. J. Shepherd, C. C. Wilson, P. R. Raithby, W. J. Gee and A. D. Burrows, *Angew. Chemie - Int. Ed.*, 2016, **55**, 5943–5946.

54 Y. Zhang, S. Yuan, G. Day, X. Wang, X. Yang and H.-C. Zhou, *Coord. Chem. Rev.*, 2018, **354**, 28–45.

55 M. D. Allendorf, C. A. Bauer, R. K. Bhakta and R. J. T. Houk, *Chem. Soc. Rev.*, 2009, **38**, 1330–1352.

56 Y. Cui, Y. Yue, G. Qian and B. Chen, *Chem. Rev.*, 2012, **112**, 1126–1162.

57 Z. Hu, B. J. Deibert and J. Li, *Chem. Soc. Rev*, 2014, **43**, 5815–5840.

58 X. L. Lv, L. H. Xie, B. Wang, M. Zhao, Y. Cui and J. R. Li, *J. Mater. Chem. C*, 2018, **6**, 10628–10639.

59 A. Lan, K. Li, H. Wu, D. H. Olson, T. J. Emge, W. Ki, M. Hong and J. Li, *Angew. Chemie - Int. Ed.*, 2009, **48**, 2334–2338.

60 S. Pramanik, C. Zheng, X. Zhang, T. J. Emge and J. Li, *J. Am. Chem. Soc.*, 2011, **133**,

4153–4155.

61 W. P. Lustig, S. Mukherjee, N. D. Rudd, A. V Desai, J. Li and S. K. Ghosh, *Chem. Soc. Rev.*, 2017, 46, 3242–3285.

62 S. Y. Jiang and X. Zhao, *Chinese J. Polym. Sci. (English Ed.*, 2019, 37, 1–10.

63 K. Da Zhang, J. Tian, D. Hanifi, Y. Zhang, A. C. H. Sue, T. Y. Zhou, L. Zhang, X. Zhao, Y. Liu and Z. T. Li, *J. Am. Chem. Soc.*, 2013, **135**, 17913–17918.

64 J. Tian, L. Chen, D. W. Zhang, Y. Liu and Z. T. Li, *Chem. Commun.*, 2016, **52**, 6351–6362.

65 J. Lü, C. Perez-Krap, M. Suyetin, N. H. Alsmail, Y. Yan, S. Yang, W. Lewis, E. Bichoutskaia, C. C. Tang, A. J. Blake, R. Cao and M. Schröder, *J. Am. Chem. Soc.*, 2014, **136**, 12828–12831.

66 W. Yang, A. Greenaway, X. Lin, R. Matsuda, A. J. Blake, C. Wilson, W. Lewis, P. Hubberstey, S. Kitagawa, N. R. Champness and M. Schröder, *J. Am. Chem. Soc.*, 2010, **132**, 14457–14469.

67 J. Lü, C. Perez-Krap, F. Trousselet, Y. Yan, N. H. Alsmail, B. Karadeniz, N. M. Jacques, W. Lewis, A. J. Blake, F. X. Coudert, R. Cao and M. Schröder, *Cryst. Growth Des.*, 2018, **18**, 2555–2562.

68 A. J. Howarth, A. W. Peters, N. A. Vermeulen, T. C. Wang, J. T. Hupp and O. K. Farha, *Chem. Mater.*, 2017, 29, 26–39.

69 A. E. Goeta and J. A. K. Howard, *Chem. Soc. Rev.*, 2004, **33**, 490–500.

70 W. Clegg, *X-ray Crystallogr.*, 2015, 33–70.

71 D. D. Le Pevelen, *Encycl. Spectrosc. Spectrom. (Second Ed.*, 2010, 2559–2576.

72 L. Ooi, *Principles of X-ray Crystallography*, Oxford University Press, 2010.

73 P. Müller, R. Herbst-Irmer, A. L. Spek, T. R. Schneider and M. R. Sawaya, *Crystal Structure Refinement: A Crystallographer's Guide to SHELXL*, 2010, vol. 9780198570.

74 B. Dittrich, *IUCrJ*, 2021, **8**, 305–318.

75 O. V. Dolomanov, L. J. Bourhis, R. J. Gildea, J. A. K. Howard and H. Puschmann, *J. Appl. Crystallogr.*, 2009, **42**, 339–341.

76 G. M. Sheldrick, *Acta Crystallogr. Sect. A Found. Crystallogr.*, 2008, 64, 112–122.

77 G. M. Sheldrick, *Acta Crystallogr. Sect. A Found. Crystallogr.*, 2015, **71**, 3–8.

78 G. M. Sheldrick, *Acta Crystallogr. Sect. C Struct. Chem.*, 2014, **71**, 3–8.

Chapter 2: Exploring spin-crossover metal-organic-frameworks and coordination polymers

2.1 Introduction

2.1.1 Dynamic processes in Hofmann-type networks

An example of a structure-property relationship in a Hofmann-type SCO material was studied by Real and co-workers in the early 2000s, where the role of water molecules coordinated to Fe(II) ions in Hofmann-like networks was investigated.[1] In particular, their work presented the first example of a reversible conversion from a triply interpenetrated 3D spin-crossover network {Fe(pmd)-(H_2O)[$M^I(CN)_2$]$_2$}·H_2O (**pmd-H_2OM^I**) (**pmd** = pyrimidine; M^I = Ag(I), **pmd-H_2OAg**; M^I = Au(I), **pmd-H_2OAu**) into a single 3D network [Fe(pmd){$M^I(CN)_2$}$_2$] (**pmdM^I**, M^I = Ag(I), **pmdAg**; M^I = Au(I), **pmdAu**) upon removal of both coordinated and guest water molecules.

The structure of compounds **pmd-H_2OM^I** presents the 2D Fe[$M^I(CN)_2$]$_2$ layers typical of the Hofmann clathrates, with the Fe(II) ions connected through the [$M^I(CN)_2$]$^-$ entities in their equatorial positions. However, each layer contains two distinct Fe(II) ions: Fe(1) has two pyrimidine ligands coordinated in the apical positions of the octahedron, while two water molecules coordinate to the apical positions of Fe(2) (**Figure 23c**). The supramolecular packing shows two other equivalent and interpenetrated networks that interact *via* metallophilic interactions (Ag···Ag or Au···Au) and *via* hydrogen bonds between the water molecules coordinated to Fe(2) and the uncoordinated nitrogen atom of the pyrimidine ligand that is bonded to Fe(1).[1] The conversion from compounds **pmd-H_2OM^I** (**Figure 23d**) to compounds **pmdM^I** (**Figure 23e**) is hence possible thanks to the strategic position of the pyrimidine ligand of a network to the Fe(2) ion of the adjacent network: the removal of the coordinated water molecules from Fe(2) leaves two unsaturated sites in the metal coordination sphere that are promptly saturated by the adjacent pyrimidine free nitrogen atom (**Figure 23d**). This topochemical reaction that occurs is reversible, meaning that compounds **pmd-H_2OM^I** can be regenerated upon exposure to water vapours or by simply leaving it open to atmospheric moisture.

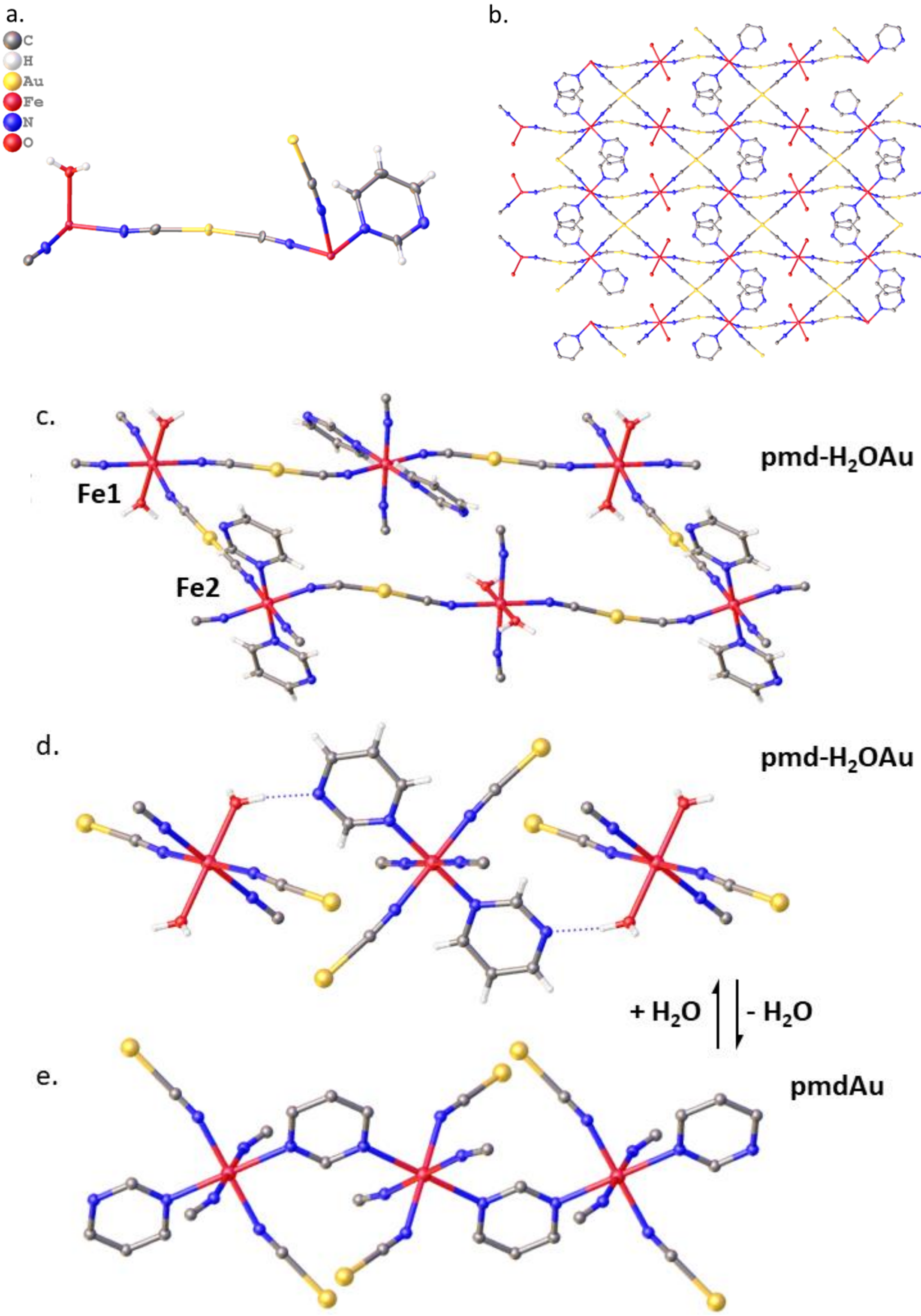

Figure 23: **a.** Asymmetric unit of compound **pmd-H_2OAu**; **b.** Supramolecular packing seen along the *c*-axis showing the 3D structure of compound **pmd-H_2OAu**; **c.** Structure of compound **pmd-H_2OAu** showing a portion of a 2D layer with three pairs of the two distinct Fe(II) ions forming a rectangular motif; **b.** Interactions between three adjacent networks of compound **pmd-H_2OAu** that allow the topochemical reaction to occur. The guest water molecules have been removed for clarity. CCDC deposition number 209795. **c.** Structure of compound **pmdAu** after the topochemical reaction occurred. CCDC deposition number 1278362.[1]

The SCO properties of both the materials with Ag show that compounds **pmd-H₂OAg** and **pmdAg** undergo a first order SCO transition upon cooling at 218 K and 125 K respectively. Similarly, compound **pmd-H₂OAu** exhibits the same SCO behaviour, going from the HS state to the LS state at the temperature of 165 K, while for compound **pmdAu** no spin transition was detected in the range 50 K – 200 K. The $X_M T$ values go from 3.7 to 1.8 cm^3 K mol^{-1} for **pmd-H₂OAg**, from 3.6 to 1.7 cm^3 K mol^{-1} for **pmd-H₂OAu** and from 3.6 to 1.9 cm^3 K mol^{-1} for **pmdAg**, proving that Fe(1) undergoes the HS to LS transition, while Fe(2) stays in the HS, as expected for an iron ion with coordinating water molecules.[1] These compounds represent hence an example of how a combination of events within a framework can induce dynamic processes in the solid state, and how the dynamicity can influence the electronic properties of the obtained materials.

2.1.2 Choice of the ligands

It has already been discussed how the choice of the ligand influences the structure and the properties of the final material. A monodentate ligand can form a 2D Hofmann-type coordination polymer, with the interdigitation of adjacent $\{Fe(L)_2[M^{II}(CN)_4]\}$ networks. Three-dimensionality can be obtained instead when a bidentate ligand is used, where the 2D layers are connected through the bridging ligands, leading to the formation of $\{Fe(L)[M^{II}(CN)_4]\}$ frameworks. In addition to the coordination geometry of the ligand, other characteristics such as its flexibility and reactivity has to be considered when designing a new material. These aspects can in fact influence the structure, the SCO properties of the material, as well as its possible applications.

The ligands investigated in this chapter are isoniazid (**iso**), nicotinamide (**nico**) and N-(4-pyridyl)isonicotinamide (**pina**) (**Figure 24**). The following section examines some of the materials containing these ligands that have been reported in the literature and highlights the motivations behind using these ligands in SCO Hofmann-type clathrates.

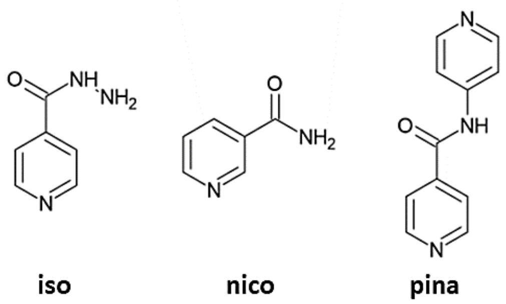

Figure 24: Schematic representation of the organic ligands used in this chapter and abbreviations.

2.1.2.1 Iso ligand

Isoniazid (**iso**) is one of the active pharmaceutical ingredients (APIs) used for treating tuberculosis,[2] an infectious disease that still nowadays presents one of the major causes of death worldwide.[3] Its important role as a drug has led to several studies in the past decades to investigate its stability. Concerns were raised due to the degradation behaviour of the drug when exposed to thermal stress and the possibility of it to undergo hydrolysis, oxidation and photolysis reactions.[4,5] **Figure 25** shows some of the degradation products that are known in literature for **iso**. In particular, the condensation of **iso**, with the elimination of hydrazine to form isonicotinic acid N'-(pyridyl-4-carbonyl)-hydrazide can be catalysed in solution state by divalent metal ions such as Zn^{2+}, Cu^{2+} and Mn^{2+}.[6] Furthermore, irradiation of **iso** with UV light leads to the formation of several of the degradation products reported below due to the possibility of both N-N and N-C (carbon from the carbonyl group) cleavage.[7]

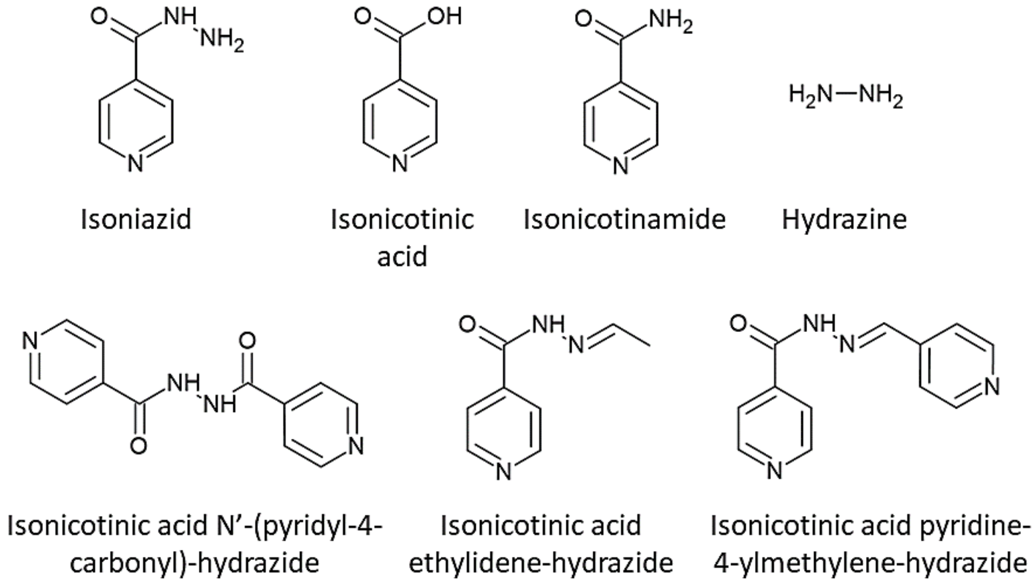

Figure 25: Schematic representation of some of the known degradation products of **iso**.[5]

One of the possible solutions to the instability of **iso** in the solid state is reported to be the incorporation of the drug in a cocrystal, where the molecule of interest is stabilised by supramolecular interactions with synthons that are pharmaceutically acceptable.[3,8] More recently, with the expansion of the field of drug delivery, biocompatible MOFs such as MIL-100(Fe) were investigated for this application. More specifically, adsorption and release studies have been performed for **iso** onto MIL-100(Fe), showing that the aforementioned MOF could be a promising candidate for a controlled release of the **iso** drug.[9]

These discoveries find their origin in the supramolecular interactions that the structure of **iso** allows: the flat and conjugated pyridine ring is suitable for π-π stacking; the hydrazide group acts as a hydrogen-bond donor and acceptor, and can moreover coordinate metal ions as a mono- or bidentate ligand through the nitrogen and oxygen atoms; finally, the nitrogen atom of the pyridine ring acts as a coordination site for building up stable metal-organic supramolecular structures.[10]

Literature reports several examples in which the **iso** ligand is coordinated to divalent metal centres, such as Co^{2+} and Zn^{2+}, both with the nitrogen atoms of the pyridine ring, and with the oxygen and terminal nitrogen atoms of the hydrazide group (**Figure 26a**), forming 1D, 2D or 3D coordination polymers (**Figure 26b**).[11,12,13]

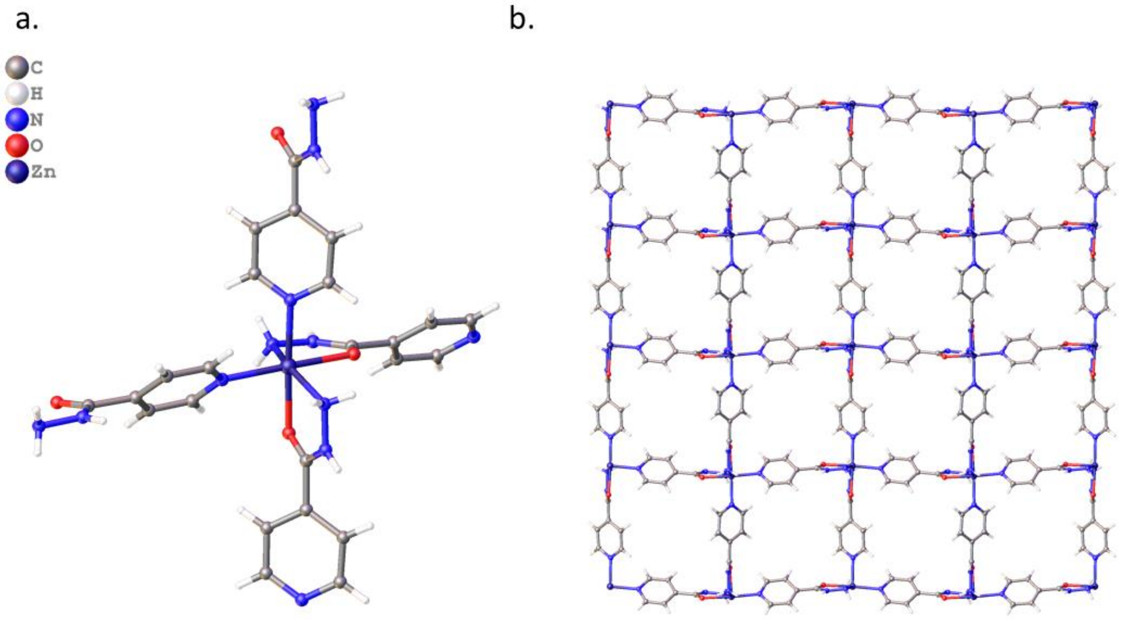

Figure 26: Structure of compound [Zn(iso)$_2$](ClO$_4$)$_2$·6H$_2$O[13] showing **a.** the coordination sphere of Zn^{2+} with the four **iso** molecules coordinated to each metal centres as mono- and bidentate ligands; **b.** Supramolecular packing forming the 2D coordination polymer. The perchlorate counterions and the guest water molecules have been removed for clarity. CCDC deposition number 811749.

In addition to its various coordination modes, and hence architectures that can be obtained with **iso**, this ligand was also of interest for the reactivity of the hydrazide group. An example of this aspect was found in literature, which reports a condensation reaction that occurred between the ketones used as solvents (acetone and 2-butanone) and **iso** ligand while performing a co-crystallization, leading to the formation of the new imine N=C covalent bond seen in the product in **Figure 27**.[14]

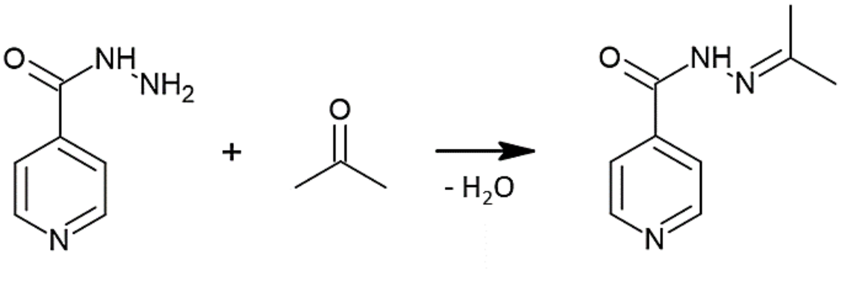

Figure 27: Schematic representation of the condensation reaction between **iso** and acetone.

The variety of structures that it is possible to obtain with **iso** as a mono- or bidentate ligand, along with the reported reactivity of hydrazides with aldehydes and ketones, raise the possibility of performing *in-situ* post-synthetic modifications on a Hofmann-type framework built with **iso**, by exposing it to acetone vapours or solution, and to monitor how these changes might affect the SCO behaviour. Additionally, as described above, the structure of the **iso** ligand allows a variety of supramolecular interactions (*π*-*π* stacking, hydrogen-bond donor and acceptor) that, added to the reactivity of the hydrazide functional group, can be exploited to explore the possibility to self-assemble multiple ligands in a one-pot synthesis.

2.1.2.2 Nico ligand

Nicotinamide (**nico**) is the amide derivative of nicotinic acid, also known as niacin, two molecules that added to nicotinamide riboside represent the three different molecular forms of vitamin B_3.[15] **Nico** is an active pharmaceutical ingredient used for various therapeutic applications such as pellagra, arthritis, ischaemia, stroke and neurodegenerative conditions.[16] A recent study has developed a water-stable and biosafe Fe-based MOF that can encapsulate the drug and control its release on specific target sites on skin, representing an advanced cutaneous therapy to treat skin disorders.[17] Interest has also been given to **nico** for the possibility to use this drug to preserve the beta-cell regeneration, which is fundamental to prevent the development of Type I diabetes mellitus complications especially in high-risk and first-grade relatives.[18,19]

The structure of **nico** is characterised by a pyridyl ring suitable for *π*-*π* stacking, with an amide functionality in the *meta* position having the ability to hydrogen-bond. Literature reports that it can act both as a monodentate or as a bidentate ligand. **Figure 28a** shows a structure of a cobalt-based complex, where the **nico** ligand binds to the metal centre as a monodentate ligand through the pyridyl nitrogen atom. At the same time, **nico** also acts as a platform for hydrogen bonding, leading to the development of a network that offers sites that can stabilise the inclusion of guest molecules though supramolecular interactions, in this case **nico** itself.[16] **Figure 28b** shows instead an example of a compound where **nico** coordinates as a bidentate ligand through both the pyridyl nitrogen atom and the carbonyl oxygen atom. The **nico** molecules thus act as bridging ligands between two adjacent metal centres, defining the centrosymmetric dimeric unit reported in **Figure 28b**.

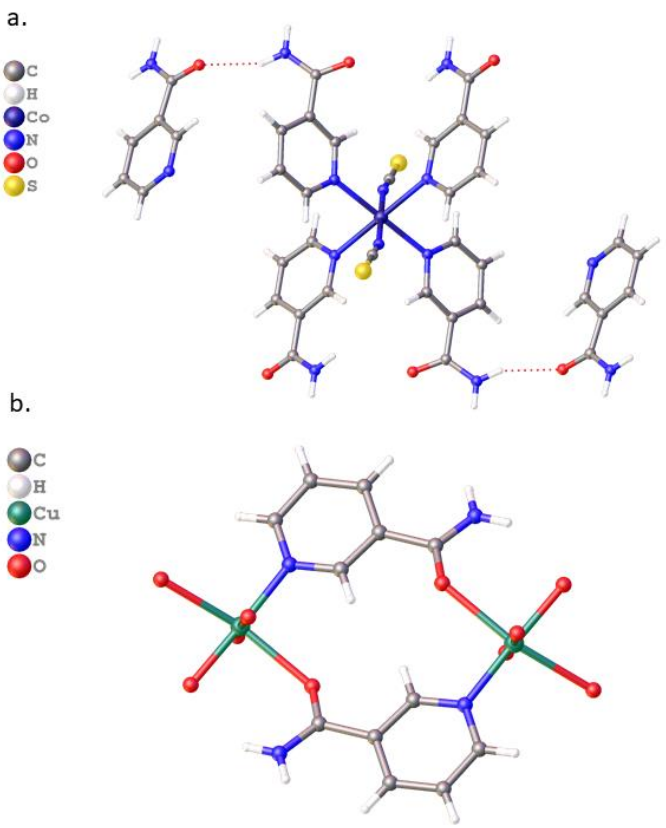

Figure 28: Structure of two **nico**-based compounds showing **a.** the possibility for **nico** to coordinate through the pyridyl nitrogen atom as a monodentate ligand, showing at the same time hydrogen-bonding interaction with the guest **nico** molecules; **b.** the possibility for **nico** to coordinate as a bidentate ligand through the pyridyl ring and the oxygen atom of the amide group. CCDC deposition numbers: **a.** 2059714;[16] **b.** 790579.[20]

These structures show how versatile **nico** can be in constructing materials with different architectures and how the supramolecular packing can be influenced by the intermolecular interactions that **nico** can form with its surrounding environment. The rigidity of the conjugated system that characterises **nico**, added to the peculiarities that have just been presented, make it a good candidate for the investigation of new **nico**-based Hofmann-type networks. Furthermore, interest is raised in understanding the role of the supramolecular interactions in the propagation of the SCO phenomenon. This area has in fact only briefly been investigated in an Fe(II) coordination polymer constructed with the **nico** derivative *N,N'*-diethylnicotinamide,[21] but no SCO active compounds involving **nico** have to date been discovered.

2.1.2.3 Pina ligand

N-(4-pyridyl)isonicotinamide (**pina**) is a ditopic organic linker with distinctive characteristics. The backbone of the ligand is composed of two rigid pyridyl rings that represent a platform for π-π interactions, connected by an amide group, which allows hydrogen bonding interactions.[22] As a consequence, when the **pina** ligand is incorporated into a network, the amide moiety in between the two pyridyl rings adds a possible interaction site for potential guest molecules and a cross-linking site for coordination-based networks.[22]

Literature reports that in the solution state the amide functional group spacer allows the ligand to adopt both the *cis* and the *trans* conformation.[23] However, investigation of the solid state behaviour of the **pina** molecule in the Cambridge Structural Database (CSD) shows that all the structures deposited with it report the **pina** ligand in a *trans* conformation, with the two coordination vectors pointing at angles that shifts more or less from 180°, and with an offset that can be seen in **Figure 29**.

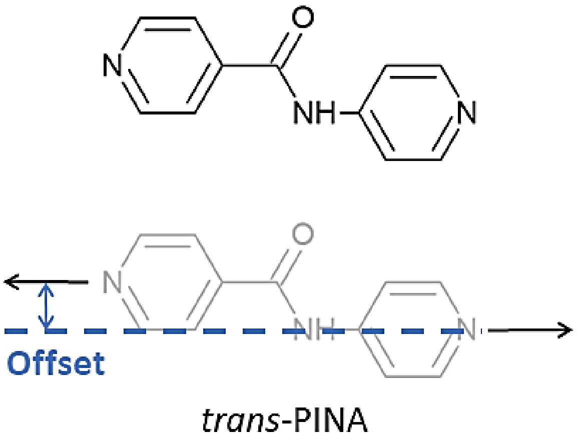

Figure 29: The structure of **pina** in the *trans*, linear conformation, showing the offset present between the two coordination vectors.

Three examples of deposited structures that present some of the possible forms that the ligand can assume are reported in **Figure 30**. It is important to clarify that none of the crystallographic data considered presented disorder in the ligand core. For each structure, α and β are also calculated from SCXRD data in order to evaluate how the offset is influenced, defining α as the angle between the two planes normal to the plane formed by the pyridyl rings highlighted in pink and blue in **Figure 30**, and β as the angle formed by the vectors passing through the C_{amide}-$N_{pyridyl}$ and N_{amide}-$N_{pyridyl}$ atoms.

In the case of a structure with the ligand lying almost completely on the same plane seen in **Figure 30A**, the offset is further increased by the two coordination vectors that shift from linearity by 9.412°, forming a β angle of 170.588°. **Figure 30B** and **C** instead show **pina** having β values close to linearity (respectively β = 178.560° and β = 178.782°), but where the offset is dictated in case **B** by the orientation of the amide group, that lies perpendicular to the planes formed by the pyridyl rings, while in case **C** is dictated by the misalignment of the pyridyl planes, that are rotated of an α angle of 68.509°.

These examples show how the structure obtained in the solid state can be influenced by the possible supramolecular interactions that **pina** can have. In particular, to avoid having the oxygen atom of the amide group and the hydrogen atom of the pyridyl ring in close proximity one from the other, either the amide geometry must deviate from the ideal linearity (case **A**), the amide group must rotate and orient out of the way of the pyridyl rings (case **B**), or one of the pyridyl rings must twist out of the way of the amide group (case **C**).

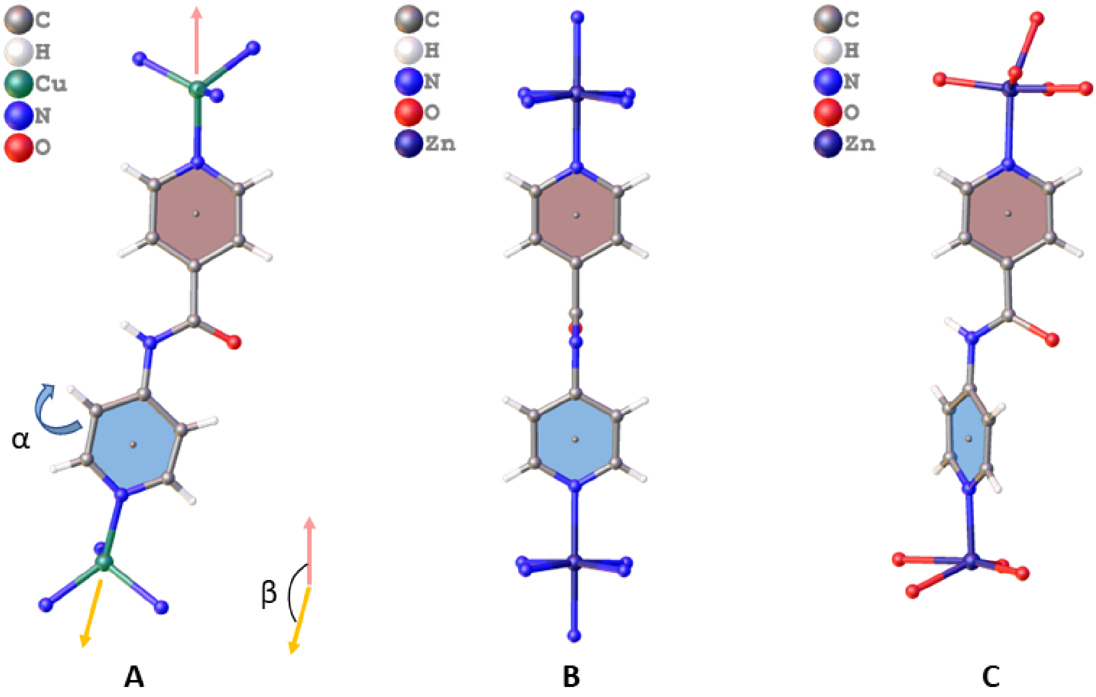

α = 9.915°   α = 2.147°   α = 68.509°

β = 170.588°   β = 178.560°   β = 178.782°

Figure 30: Crystalline structures reported in literature for three compounds involving **pina** showing the different possible forms that the ligand can assume. CCDC deposition numbers for **A**: 1822226;[24] **B**: 823867;[25] **C**: 1401562.[26] α = angle between the two planes normal to the plane formed by the pyridyl rings (pink and blue). β = angle formed by the vectors passing through the C_{amide}-$N_{pyridyl}$ and N_{amide}-$N_{pyridyl}$ atoms.

Literature reports several studies regarding the use of **pina** for synthesising SCO materials.[27,28] An interesting work was recently published involving this ligand in the synthesis of Hofmann-type clathrates constructed with the $[M^{I}(CN)_2]^-$ moiety, with M^I = Ag^+, Au^+.[29] More specifically, Real and co-workers synthesised the doubly interpenetrated 3D compounds with formula $[Fe(pina)\{Ag(CN)_2\}_2]\cdot x$MeOH (**pinaAg·*x*MeOH**) and $[Fe(pina)\{Au(CN)_2\}_2]\cdot x$MeOH (**pinaAu·*x*MeOH**, x = 0 – 5), and investigated the impact of the guest molecules on the SCO properties of these compounds by comparing them with their desolvated forms **pinaAg** and **pinaAu**.[29]

Compound **pinaAg·*x*MeOH** is in the HS state until the temperature of 245 K, where X_MT starts to decrease showing a two-step transition, reaching 0.1 cm^3 K mol^{-1} at 150 K, consistent with the material being in the LS state (**Figure 31a**). The narrow hysteresis loop of ~5 K for **pinaAg·*x*MeOH** further narrows down to ~3 K for the desolvated compound **pinaAg**, which shows an almost complete, but more gradual thermal HS to

LS transition within the temperature range investigated.[29] Compound **pinaAu·*x*MeOH** (**Figure 31b**) shows instead an almost complete four-step spin transition corresponding to the formation of various mixed spin states between the temperatures of 210 K and 142 K upon cooling, with a similar SCO behaviour reported upon heating. Similarly to compound **pinaAg**, the desolvated compound **pinaAu** presents a gradual thermal transition without marked steps, reporting a very different SCO behaviour compared to the equivalent solvated **pinaAu·*x*MeOH**. The readsorption of MeOH molecules was attempted for both the compounds, but the process has been shown to be reversible only in the case of **pinaAu·*x*MeOH**.[29]

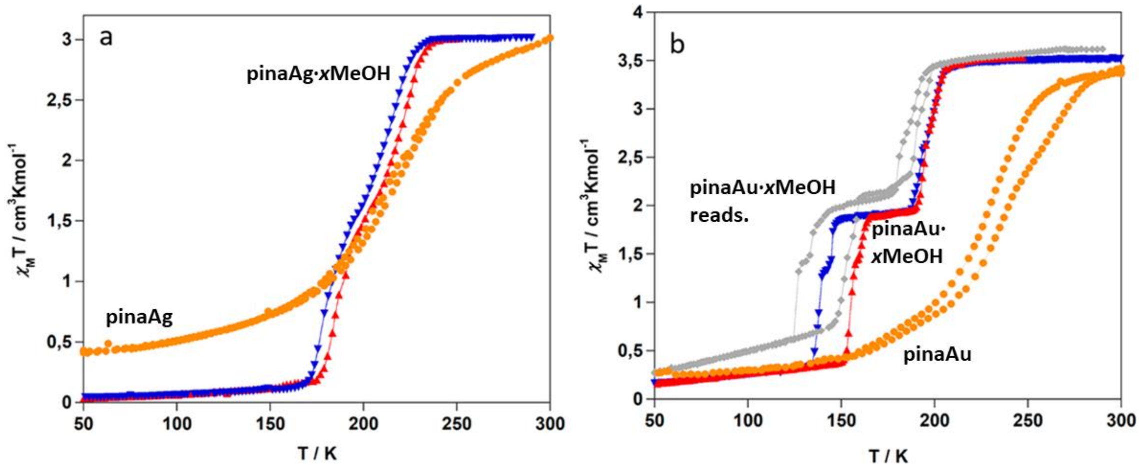

Figure 31: $X_M T$ variation *versus* temperature for **a.** compounds **pinaAg·*x*MeOH** and the equivalent desolvated **pinaAg**; **b.** compounds **pinaAu·*x*MeOH**, the equivalent desolvated **pinaAu** and compound **pinaAu·*x*MeOH** after readsorption. Blue points: cooling process; red points: heating process; orange points: heating and cooling for desolvated compounds; grey points: heating and cooling for readsorbed compound. Adapted with permission from Ref. [29].

The different SCO behaviour seen between the solvated and the desolvated compounds, was attributed to the presence of the various supramolecular interactions within the framework. The cooperativity of the two-step and four-step spin transitions of **pinaAg·*x*MeOH** and **pinaAu·*x*MeOH** may in fact be promoted by both hydrogen-bonding interactions between the intercalated MeOH molecules present along the channels, and by the interframework C=O···HC interaction between adjacent **pina** molecules, allowing an efficient transmission of the structural changes (**Figure 32**).[29]

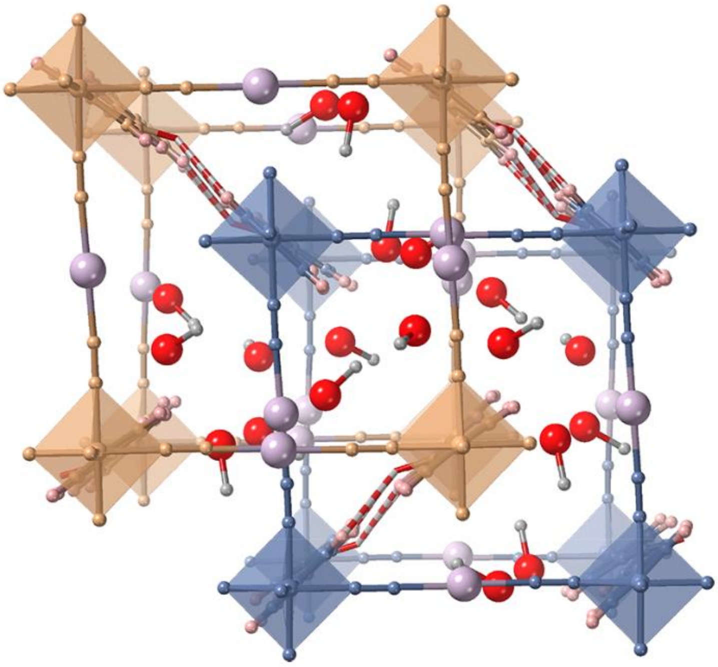

Figure 32: Supramolecular packing of the two interpenetrated frameworks of compound **pinaAg·xMeOH** showing the C=O···HC interactions (red and white dashed lines) and the MeOH molecules present as guests. Reprinted with permission from Ref. [29].

The bridging **pina** ligand is an organic linker characterised by a variety of interesting features. The flexibility of the amide functional group and the possibility of the pyridyl rings to rotate from planarity, allow the ligand to assume a plethora of different forms and to optimize the supramolecular interactions in the solid state. These interactions can influence the propagation of the SCO behaviour within the crystalline structure, an interesting phenomenon that opens up to further investigation on new **pina**-based materials.

2.1.3 Aims

The aims of this chapter are the synthesis and the structural investigation of new Hofmann-like frameworks and coordination polymers that are constructed with the organic linkers **iso**, **nico** and **pina**. These three ligands have in common the rigid, conjugated pyridyl ring core, along with the presence of a carbonyl functionality in the hydrazide (**iso**) or amide group (**nico** and **pina**), which represent sites for various supramolecular interactions that add possible cross-linking sites to change the topology or supramolecular interactions of the coordination networks. In addition, they can all act as bidentate ligands, with **iso** and **nico** having the possibility to also act as monodentate ligands, and **iso** being known for its reactivity that can lead to an *in-situ* modification of the ligand itself, opening up to the possibility to obtain a variety of new 2D and 3D structures.

This chapter thus aims to explore the solid-state behaviour of Hofmann-type materials involving the ligands described above, in order to exploit the versatility of the ligands to influence the structure of the frameworks and hence potentially influence the SCO behaviour of the final material. Particular interest will be addressed to the investigation of the spin state and spin changes of these compounds when varying the temperature, changes that will be monitored by using SCXRD analysis.

2.2 Results and discussion

2.2.1 Iso-based materials

From the layering reaction between $K_2[Pt(CN)_4]$, $Fe(BF_4)_2{\cdot}6H_2O$ and the **iso** ligand, the cyanide-based bimetallic coordination polymer $\{Fe(H_2O)_2[Pt(CN)_4]\}{\cdot}iso\cdot1.5MeOH{\cdot}H_2O$ (**ISO-1**) was obtained. The compound crystallises in the monoclinic $P2_1/n$ space group and is in the HS state at 250 K, with an Fe-L_6 coordination volume (V_{coord}) of 13.12(2) Å^3. The four equatorial positions of the iron octahedron are coordinated by $[Pt(CN)_4]^{2-}$ groups, forming the 2D $Fe[Pt(CN)_4]$ sheets that are typical of Hofmann-type compounds (**Figure 33**). Two water molecules coordinate to the iron centre in its apical positions, while one **iso** molecule, 1.5 methanol molecules and one water molecule *per* asymmetric unit intercalate between adjacent layers of the coordination polymer (**Figure 33**).

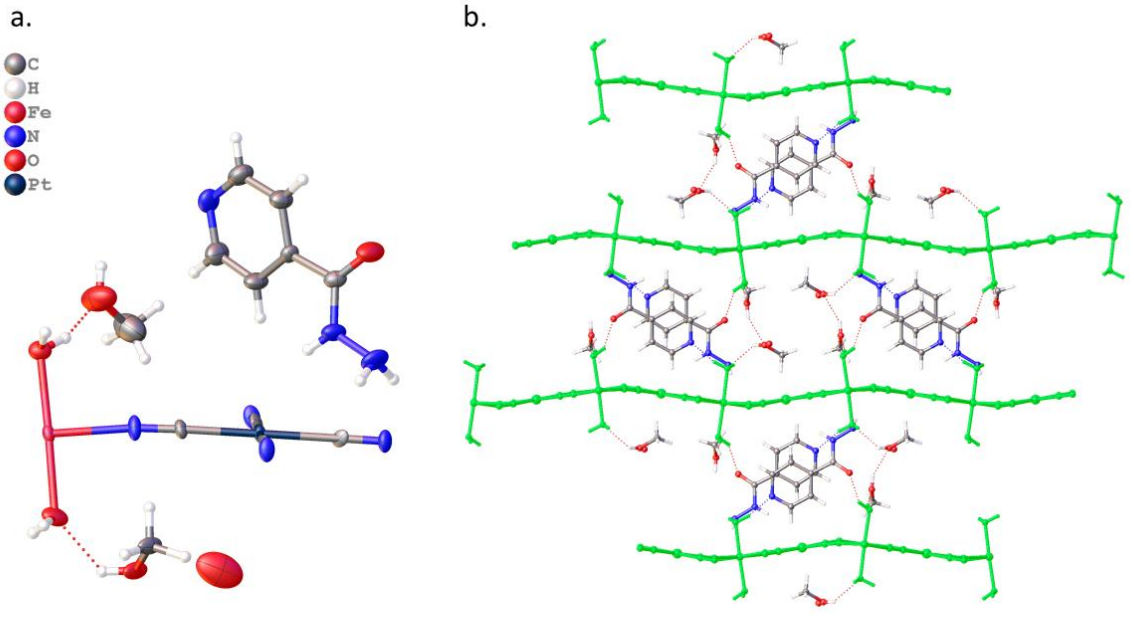

Figure 33: **a.** Asymmetric unit of **ISO-1** at 250 K. Atomic displacement parameters are drawn at 50 % probability; **b.** Supramolecular packing along the *a*-axis. The 2D $\{Fe[Pt(CN)_4]\}$ layers are highlighted in green to simplify the visualisation of the guest molecules and the structure has been drawn isotropically for clarity.

Literature reports that it is possible for dynamic processes to occur within a network, such as in the case reported by Real and co-workers (**2.1.1**) that shows that a pyrimidine ligand bonded as a monodentate ligand, can switch to being a bidentate ligand when a water molecule coordinated to the adjacent Fe(II) centre is removed.[1] In an effort to explore the possibility of similar dynamic processes in compound **ISO-1**, its structure has been investigated upon heating. By contrast, the low temperature range was not considered as no SCO transition is expected when water molecules saturate the coordination sphere of the Fe(II) centre[30] and dynamic processes are significantly less likely as temperature is reduced. It was hypothesised that if a similar dynamic change in coordination environment is observed in **ISO-1** as that seen in compounds **pmd-H_2OM^I** and **pmdM^I**, then it may be possible to obtain an FeN_6 coordination environment capable of SCO.

The crystal was hence gradually heated to 400 K at a rate of 300 K/h, in order to evaluate the possibility for thermally-induced reorganisation of the chemical connectivity. Degradation of the crystal started to occur at 330 K, suggesting that the removal of the guest methanol molecules may play an important role in the stability of the structure. This aspect can be confirmed by looking at the interactions that take place between the 2D {Fe[Pt$(CN)_4$]} sheets: each water molecule that coordinates to the iron centres is hydrogen bonded to a methanol molecule that lies within the pores, which is in-turn hydrogen bonded to the water-methanol system of the adjacent layer (**Figure 34**). Additional N-H and O-H interactions are present between the layers of the coordination polymer and the **iso** ligand that is hence stabilised as a guest molecule instead of being coordinated to the Fe(II) metal centres (**Figure 34**).

The crystalline structure data for compound **ISO-1**, along with the observations of the crystal degradation upon heating, led to the conclusion that either the methanol removal or the great structural rearrangement needed to coordinate the intercalated ligand, may cause the crystalline structure to collapse.

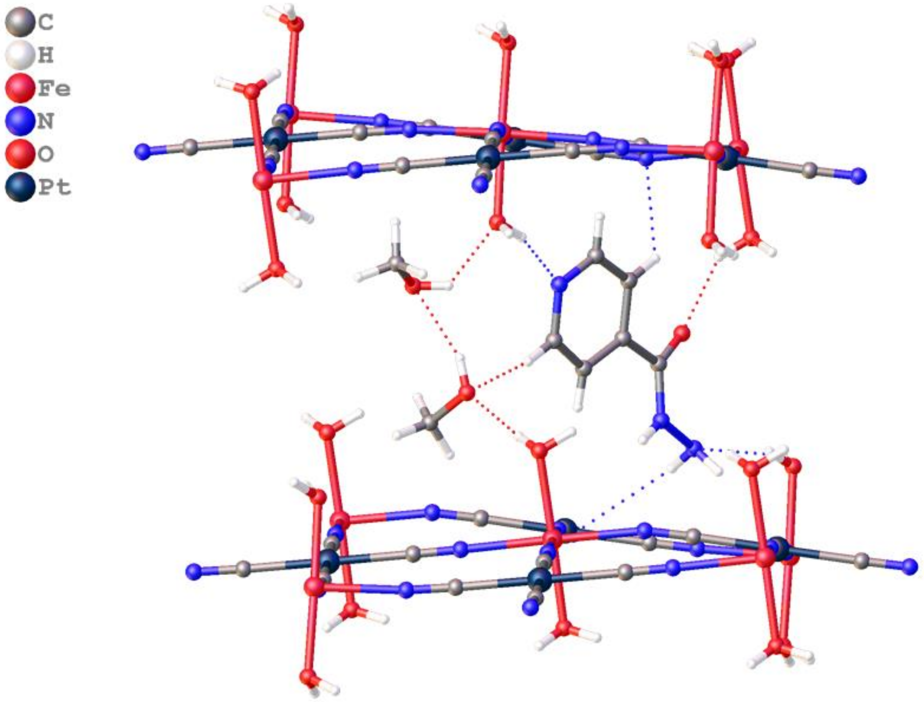

Figure 34: Interactions between two adjacent 2D {Fe[Pt(CN)$_4$]} sheets and the two methanol and isoniazid ligand molecules intercalated between the layers in **ISO-1**. The guest water molecules have been removed for clarity.

Layering of $K_2[Pt(CN)_4]$, $Fe(BF_4)_2{\cdot}6H_2O$ and the **iso** ligand led also to the Hofmann clathrate with the dimerised **di-iso** ligand (1,2-diisonicotinoylhydrazine) that we hypothesised having the formula {Fe(di-iso)[Pt(CN)$_4$]}·0.5MeOH (**ISO-2**). The framework crystallises in the monoclinic space group *P2/m* and is in the HS state at 250 K (V_{coord} = 13.61(2) Å^3). As shown in **Figure 35**, the organic ligand has undergone a condensation reaction from **iso** to 1,2-diisonicotinoylhydrazine with hydrazine elimination, as discussed in section **2.1.2.1**. The asymmetric unit (**Figure 35a**) presents half of the dimer ligand, with the oxygen and nitrogen atoms of the hydrazide component disordered over two positions with the other half generated by symmetry. The 2D {Fe[Pt(CN)$_4$]} sheets are connected through the dimeric ligand that coordinates the iron centres of two adjacent layers in their apical positions, leading to the formation of the 3D metal-organic framework **ISO-2**. Extended channels are present along the *a*-axis, which contains half a molecule of disordered methanol *per* asymmetric unit (**Figure 35**).

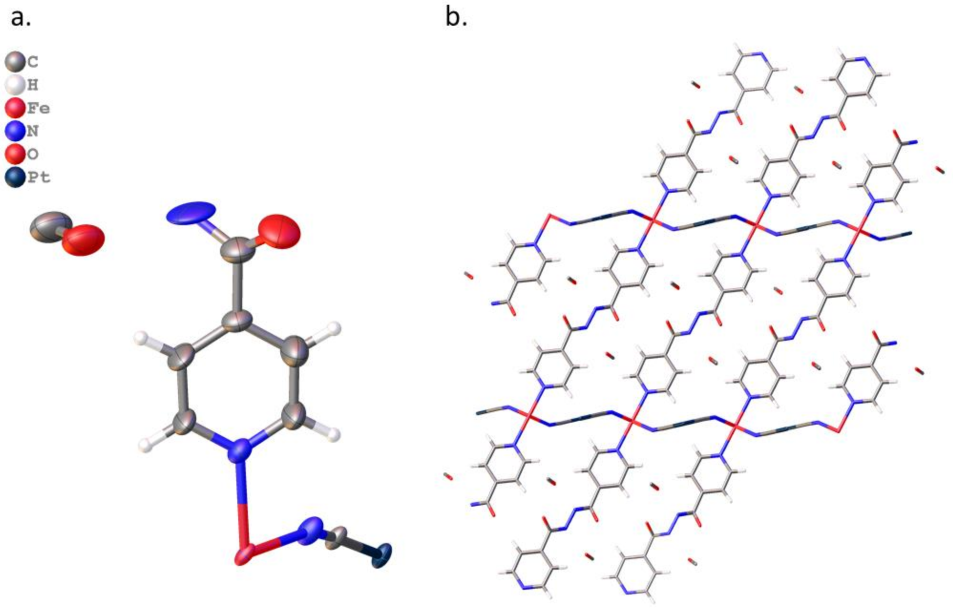

Figure 35: **a.** Asymmetric unit with atomic displacement parameters drawn at 50 % probability and **b.** supramolecular packing for compound **ISO-2** at 250 K.

In order to support the hypothesis that the interconversion reaction that occurred to the **iso** ligand was catalysed in solution state by the presence of the divalent metal ion Fe^{2+} (**2.1.2.1**), liquid chromatography mass spectrometry (LC-MS) was performed on a pure ligand solution in MeOH and on a ligand solution upon addition of $Fe(BF_4)_2 \cdot 6H_2O$, aiming to reproduce the synthetic conditions used. The mass spectrum obtained in the positive mode for the **iso** ligand solution showed a single peak at a retention time of 4.44 minutes with a *m/z* value of 138.2 and no other fragmentations, coherent with the presence of the protonated form of the pure **iso** ligand (**Figure 36a**). Similarly, a single peak at a retention time (RT) of 4.30 minutes was also found when the Fe(II) salt was added to the solution, with a *m/z* value of 138.2 correspondent again to **iso** ligand, but also showing other fragments that might be attributed to the presence of other species in solution with a lower concentration. The data analysis performed in Single Ion Monitoring (SIM) mode allowed to search for the presence or absence of the peak corresponding to the protonated form of the dimer 1,2-diisonicotinoylhydrazine, expected to have a *m/z* value of 243.0. This peak was found at a RT of 6.01 minutes with a m/z value of 243.1 in the solution containing both the ligand and the Fe(II) salt (**Figure 37**), but was not contained in the pure ligand solution (**Figure 36b**), proving that the formation of the dimer occurred after the addition of the metal salt.

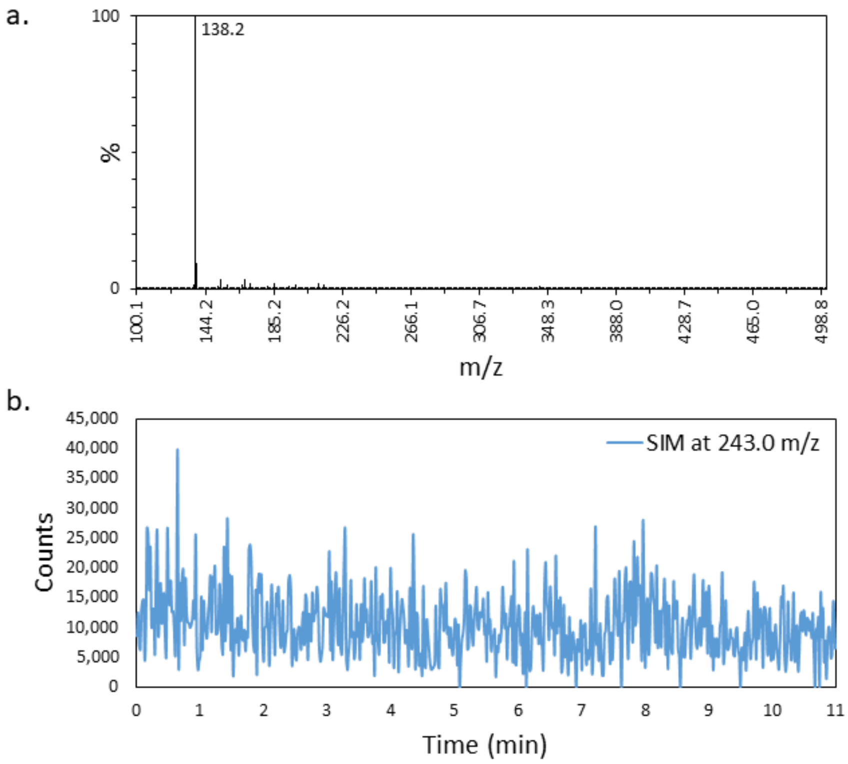

Figure 36: **a.** Mass spectrum obtained in the positive mode at a retention time of 4.44 minutes and **b.** chromatogram in SIM for 243.0 m/z for the **iso** ligand solution.

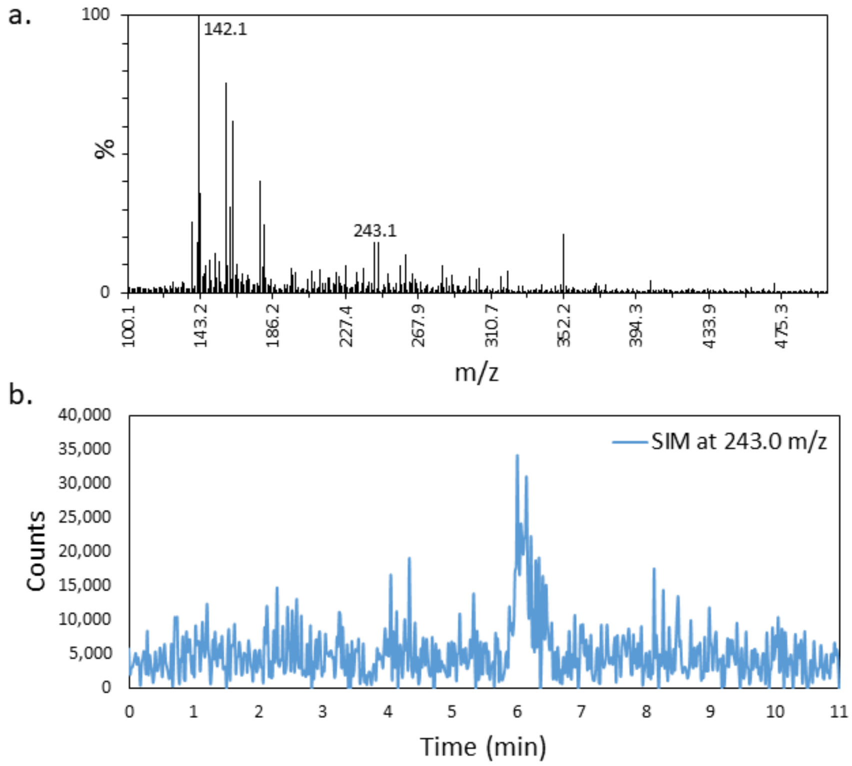

Figure 37: **a.** Mass spectrum obtained in the positive mode at a retention time of 6.01 minutes from the SIM peak and **b.** chromatogram in SIM for 243.0 m/z for the solution of **iso** ligand upon addition of the Fe(II) salt.

Compound **ISO-2** was analysed upon cooling and heating in order to investigate its spin crossover properties. The spin state of the iron centre did not change on cooling up until the temperature of 170 K (**Figure 38**), when a phase transition was detected within the 150 K – 110 K temperature range from the appearance of twin domains (**Figure 39**), rendering it impossible to measure the coordination volume and the unit cell parameters reliably. The data measured at 110 K showed the presence of four domains and a phase transition from the monoclinic space group *P2/m* to the triclinic space group *P-1*. Despite the poor data quality, the molecular model obtained at this temperature allowed to confirm that the phase transition did not lead to a change in the spin state of the metal centre, as a Fe-L$_6$ coordination volume of 13.72(12) Å^3 was obtained at the temperature of 110 K. Finally, the phase transition was shown to be reversible: upon heating, the space group of the compound returns back to the original monoclinic *P2/m* at the temperature of 170 K, with the disappearance of the twined domains (**Figure 39**). From **Figure 38** it is possible to see that the compound stays in the HS state within the 250 K – 170 K temperature range.

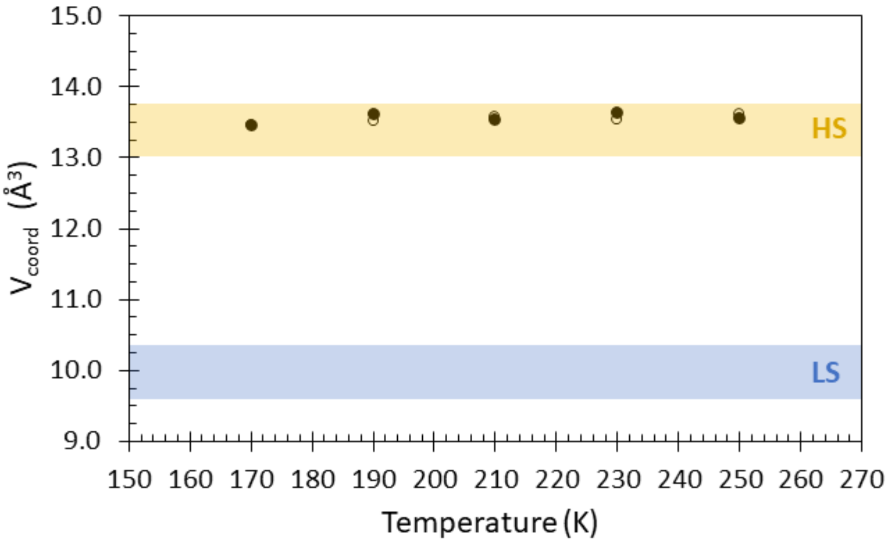

Figure 38: Graph showing the variation of the Fe-L$_6$ coordination volume (V$_{coord}$) within the 250 K – 170 K temperature range for compound **ISO-2**. The hollow points represent the values upon cooling, the solid points represent the values upon heating.

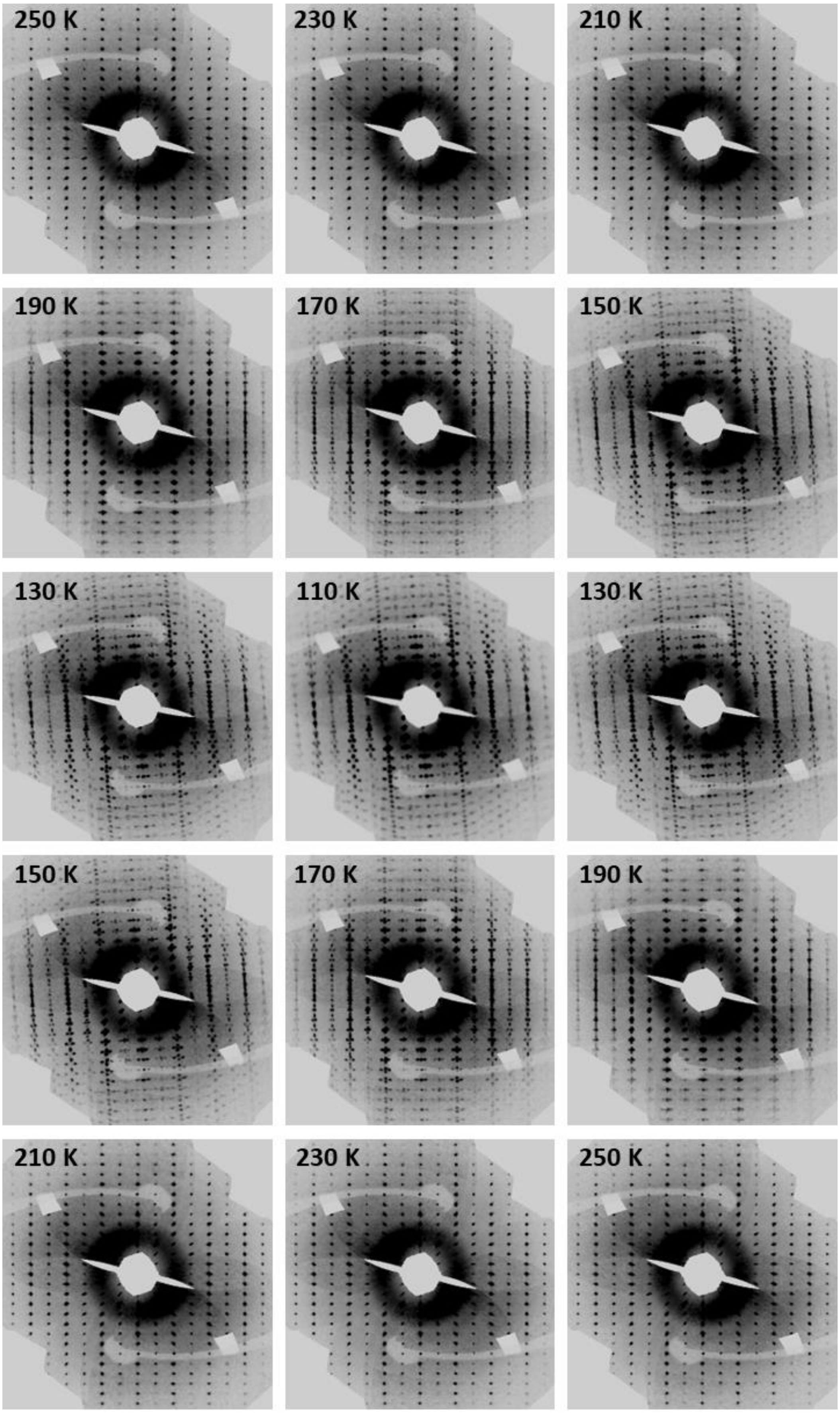

Figure 39: Reconstructed images of the (0kl) reciprocal lattice plane at different temperatures showing the appearance of the twin domains at low temperature.

To further investigate the reactivity of the **iso** ligand and to exploit its potential to perform *in-situ* modification, a layering analogous to the previous one was set up adding acetone in the layer of pure MeOH and H_2O. The structure that was obtained, shows the formation of a 2D coordination polymer with formula {Fe(iso-hy)(H_2O)[Pt(CN)$_4$]}{Fe(H_2O)[Pt(CN)$_4$]} (**ISO-3**) (**Figure 40**), where a condensation reaction occurred between the **iso** ligand and acetone molecule during the crystallization process. This phenomenon is already reported in literature[14] (section **2.1.2.1**) and led to the formation of a new imine N=C covalent bond in the ligand *N'*-(propan-2-ylidene)isonicotinohydrazide (**iso-hy**) (**Figure 27**).

The coordination polymer crystallises in the monoclinic space group $P2_1$ and is in the HS state at 150 K (V_{coord} = 13.54(10) Å^3). An H_2O molecule and an **iso-hy** ligand molecule are coordinated to the apical position of the Fe(II) centre of the {Fe[Pt(CN)$_4$]} sheets, which develops in two dimensions forming discrete layers. Each of these layers are then alternated with a {Fe(H_2O)[Pt(CN)$_4$]} layer that is situated in between, rendering the supramolecular packing optimal. The dataset showed a severe two-component twin, making it possible to obtain a stable structural model only by modelling the atoms with isotropic displacement parameters. Additionally, a rapid degradation of the crystal attributed to solvent loss with consequent worsening of the diffraction quality was detected when mounting the crystal at 250 K. The data collection was hence performed at the temperature of 150 K to avoid the crystal deterioration.

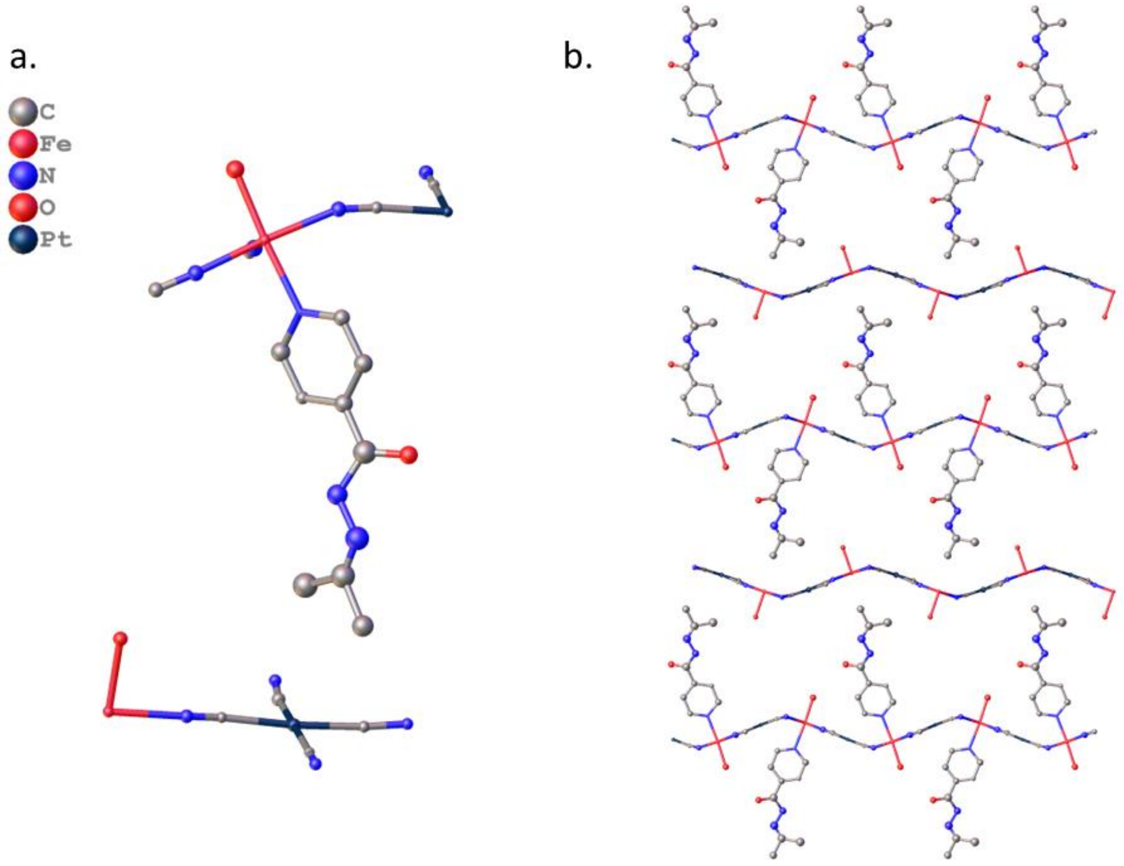

Figure 40: **a.** Asymmetric unit and **b.** supramolecular packing for compound **ISO-3** at 150 K.

The three different compounds presented in this work involving **iso** clearly show how versatile this ligand can be. The potential for undergoing dynamic processes in the solid state has been investigated in compound **ISO-1**, while the reactivity of the ligand has been exploited in compound **ISO-2** to explore the possibility for **iso** to self-assemble, and in compound **ISO-3** to perform *in-situ* modifications of the ligand. A variety of structures were obtained, ranging from 2D coordination polymers to a 3D Hofmann-type framework, with the organic linker acting as a guest that intercalate within the networks, or undergoing chemical reactions that modified its coordination sites and hence coordination numbers. Even though none of these compounds has shown any SCO transition, the variety of structures that it is possible to obtain with **iso** and the potential to functionalise the ligand *in-situ*, and hence to potentially influence the SCO properties of the material, makes the **iso** ligand a suitable candidate to be further employed in the synthesis of new SCO active compounds.

2.2.2 Nico-based materials

From the layering crystallisation of $K_2[Pt(CN)_4]$, $Fe(BF_4)_2{\cdot}6H_2O$ and the **nico** ligand, the 2D Hofmann clathrate $\{Fe(nico)_2[Pt(CN)_4]\}$ (**NICO-1**) was obtained. The framework is in the triclinic space group *P-1* at both 250 K and 100 K. The Fe-L_6 coordination volume (V_{coord}) varies from 13.7284(9) Å^3 to 13.516(16) Å^3 respectively for the measurements at 250 K and 100 K, showing that the compound stays in the HS state within this temperature range. **Figure 41** shows that each Fe(II) ion is coordinated by two **nico** molecules that act as a monodentate ligand. The 2D $\{Fe(nico)_2[Pt(CN)_4]\}$ sheets are hence connected through intermolecular interactions between the **nico** molecules of two adjacent layers, forming the stable 2D network **NICO-1**.

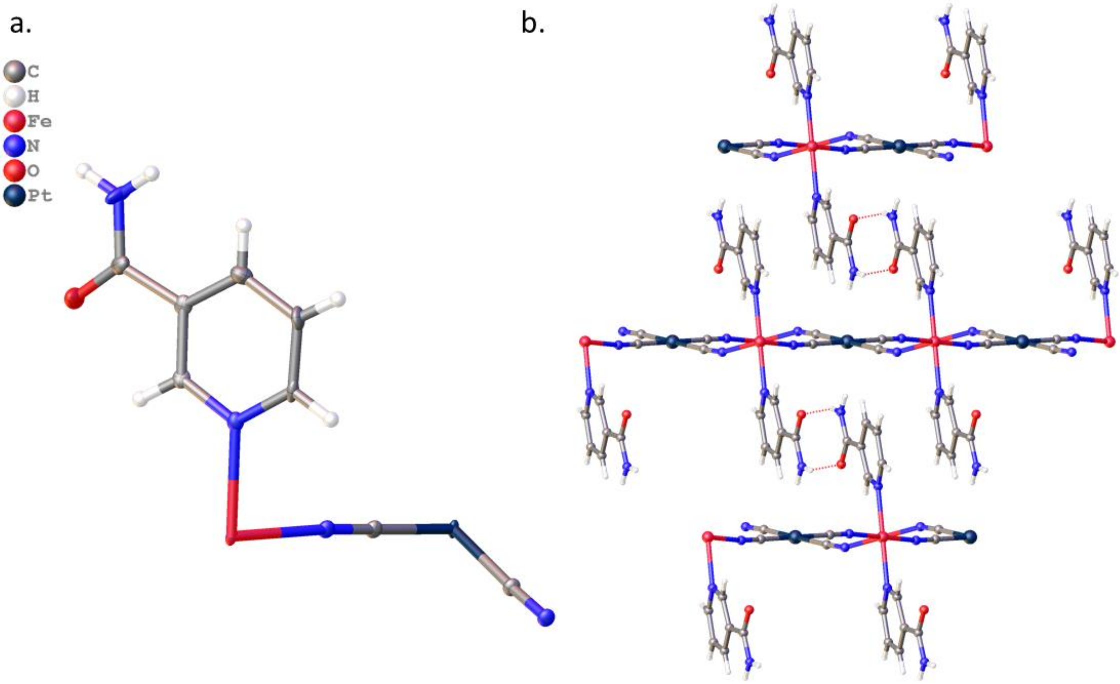

Figure 41: **a.** Asymmetric unit of **NICO-1** at 100 K. Atomic displacement parameters are drawn at 50 % probability; **b.** Supramolecular packing along the *a*-axis. The structure has been drawn isotropically for clarity.

As seen in **Figure 42**, interdigitation occurs between consecutive layers like in the analogous 2D coordination polymer **pyNi** (section **1.1.3**). By looking at the supramolecular packing, it is possible to see that the presence of the amide functional group in **nico** directs the rotation of the ligand molecules in a way that orients the amide groups of two adjacent 2D sheets to interact, leading to the formation of a pseudo 3D framework held together by supramolecular interactions. The relatively strong hydrogen bonding between the oxygen atom of a **nico** molecule and the -NH_2 hydrogen of the amide of the adjacent **nico** molecule can in fact be classified by looking at the O···N distance ($d_{O\cdots N}$) measured from the SCXRD data: a $d_{O\cdots N}$ of 2.943(6) Å was measured from the structure of **NICO-1**, which is within the 2.5-3.2 Å range and is hence coherent with a *moderate* hydrogen bonding, and corresponds to a bond with energy in the range 4-15 kcal/mol.[31]

This compound shows an example of crystal engineering in which the introduction of synthons that favour hydrogen bonding can be relevant for the formation of a network whose structural arrangement is dictated not only by coordination bonds, like in the case of **pyNi**, but also by supramolecular interactions. Cooperativity is generally lowered when going from a 3D to a 2D network, because the communication between the Fe(II) centres is not as efficient as when adjacent layers are connected *via* bridging ligands through coordination bonds. However, the structure of **NICO-1** represents a 2D system with enhanced interactions between the adjacent layers that interact *via* hydrogen bonding, forming a pseudo 3D network. Even though this structure didn't show a SCO transition within the temperature range analysed, the aspects here discussed could potentially be crucial to increase the cooperativity and hence to tune the SCO behaviour of related materials. This approach can in fact be used as an alternative to using ditopic bridging ligands, but further studies need to be carried out in order to obtain other pseudo 3D networks that exhibit a SCO behaviour.

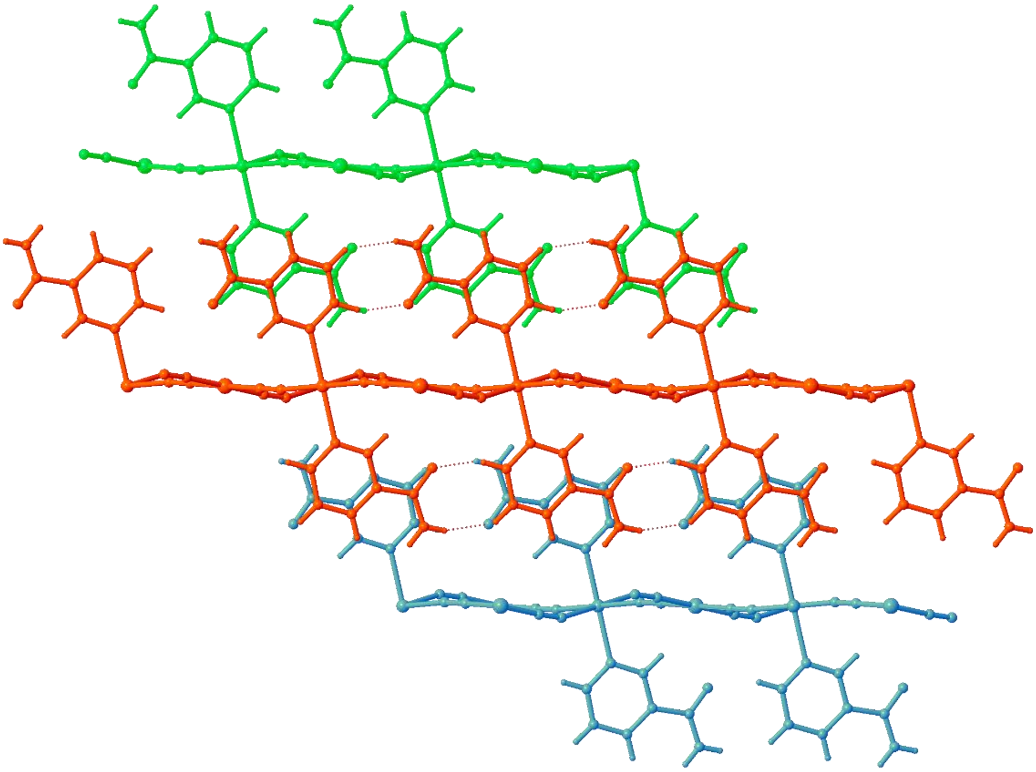

Figure 42: Supramolecular packing for **NICO-1** seen along the *b*-axis showing the hydrogen-bonds and π-π interactions between three adjacent 2D {Fe(nico)$_2$[Pt(CN)$_4$]} layers. Each layer is highlighted in a different colour (green, red and light blue) to simplify the visualisation.

2.2.3 Pina-based materials

Layering of a $K_2[Pt(CN)_4]$ solution with a $Fe(BF_4)_2·6H_2O$ and **pina** ligand solution, led to the formation of the 3D Hofmann clathrate {Fe(pina)[Pt(CN)$_4$]} (**PINA-1**). The framework crystallises in the monoclinic space group $P2_1/c$ and is in the HS state at 230 K (V_{coord} = 13.3622(8) Å^3). The asymmetric unit presents one ligand molecule coordinated to the {Fe[Pt(CN)$_4$]} fragment (**Figure 43a**). This fragment develops in a plane forming 2D sheets that are connected by the pillar **pina** ligands that bridge two iron ions of two consecutive layers, leading to a 3D Hofmann clathrate structure (**Figure 43b**).

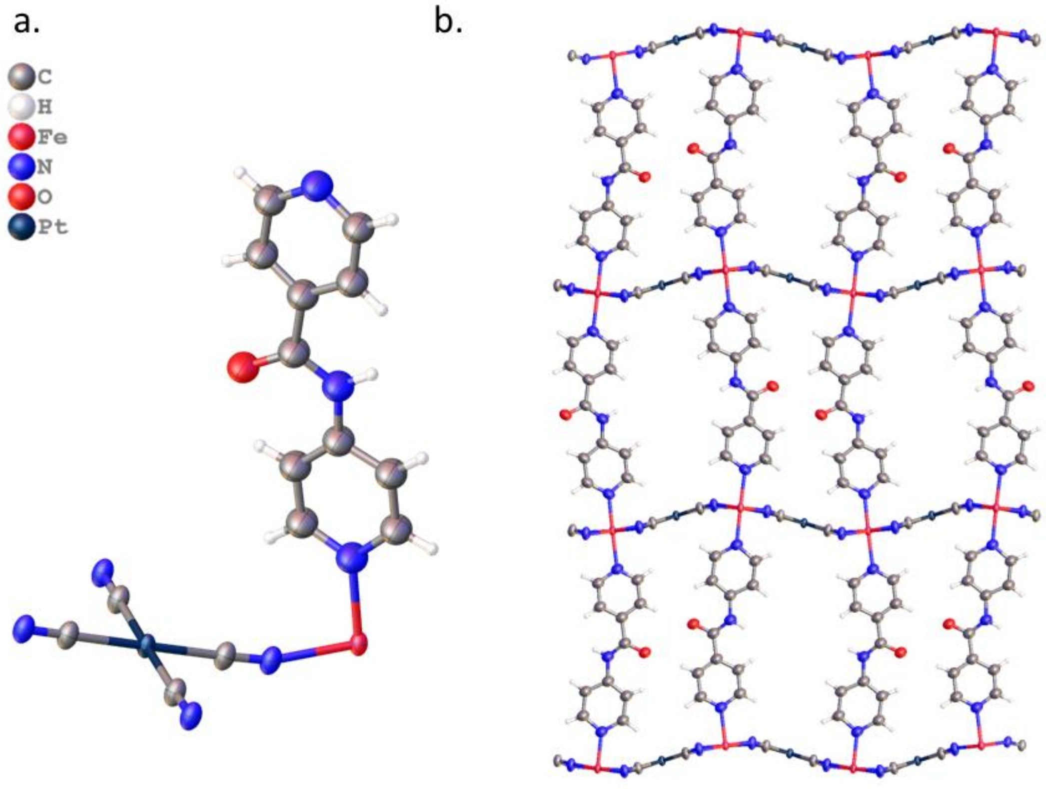

Figure 43: **a.** Asymmetric unit of **PINA-1** at 230 K. Atomic displacement parameters are drawn at 50 % probability; **b.** Supramolecular packing along the *a*-axis.

The supramolecular packing for **PINA-1** shows how the 2D sheets are slightly distorted from planarity seen in the progenitor compound **pzPt·2H$_2$O** (section **1.1.3**), which is attributed to the distortion from linearity of the two pyridyl rings of **pina** (**Figure 43b**). Similarly to case **A** reported in section **2.1.2.3**, the ligand lies almost completely on the same plane, with an α angle of 6.290°, so the offset is dictated by the two coordination vectors that form a β angle of 168.120°, shifting from linearity by 11.880°. Finally, the ligand molecules are present in the framework in an antiparallel motif: adjacent ligands situated in between the same two 2D layers lay on the same plane, with the amide oxygen atoms pointing at the pyridyl ring of the neighbouring ligand molecule (**Figure 43b**).

The SCO behaviour of the material was investigated upon cooling to 170 K. The SCXRD data collected for each of the explored temperatures, allowed the evaluation of the Fe-L$_6$ V_{coord}. From **Figure 44** it is possible to see that the HS state was maintained until 200 K, with a V_{coord} = 13.2047(10) Å^3. After this temperature, an abrupt spin-transition occurred until reaching a V_{coord} = 10.3597(9) Å^3 at 170 K, where the full LS state is achieved. SCXRD data was also collected upon heating on the same crystal. The LS state is in that case maintained until 225 K, followed by a more gradual LS to HS transition with a hysteresis loop of 15 K. Finally, the HS state is re-gained at the temperature of 220 K, with a V_{coord} = 13.1621(15) Å^3.

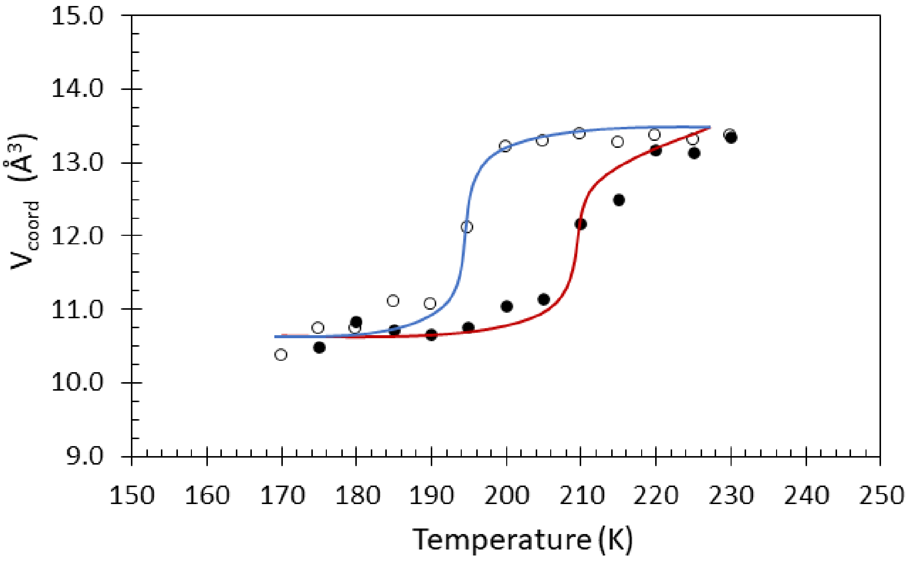

Figure 44: Graph showing the variation of the Fe-L$_6$ coordination volume (V_{coord}) upon cooling down from the temperature of 230 K up until 170 K for **PINA-1**. The blue line (cooling) and the red line (heating) have been drawn as a guide to the eye and do not represent a fit.

With the interest of obtaining the analogous compound with Pd(II) and to study its SCO properties, a layering with the same conditions reported for **PINA-1** was set up by substituting the Pt(II) solution with a $K_2[Pd(CN)_4]$ solution, leading to the formation of compound $\{Fe(pina)[Pd(CN)_4]\}$ (**PINA-2**) shown in **Figure 45**.

The structure of **PINA-2**, isostructural with **PINA-1**, crystallises in the monoclinic space group $P2_1/c$ and is in the HS state at 250 K (V_{coord} = 13.79(4) Å^3). The asymmetric unit again presents one ligand molecule coordinated to the $\{Fe[Pt(CN)_4]\}$ fragment (**Figure 45a**). This fragment forms extended 2D layers that are then connected by the bridging **pina** ligands (**Figure 45b**). The 3D Hofmann clathrate that forms in these conditions is characterised once again by an almost planar ligand, showing two slightly more twisted pyridyl rings compared to **PINA-1**, forming an α angle of 11.070°. The offset is however mostly influenced by the shift from linearity of the two coordination vectors by 11.903°, that form a β angle of 168.097°.

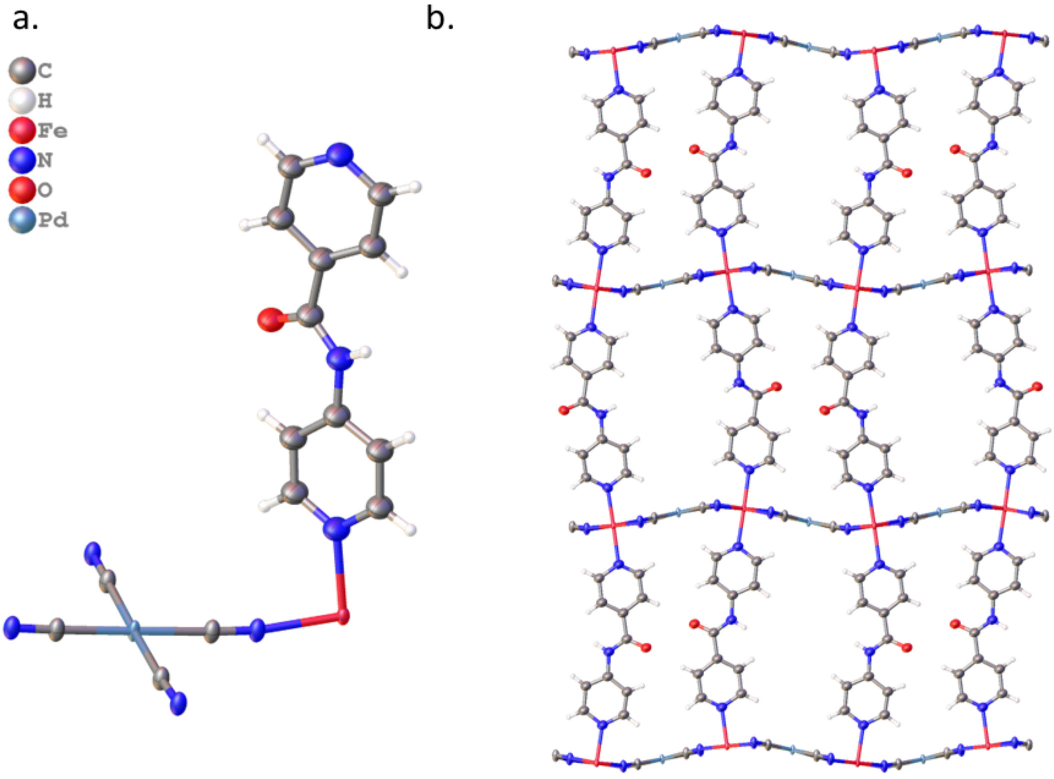

Figure 45: **a.** Asymmetric unit of **PINA-2** at 250 K. Atomic displacement parameters are drawn at 50 % probability; **b.** Supramolecular packing along the *a*-axis.

An investigation of the SCO behaviour of this material was carried out within the 250-150 K range by evaluating the V_{coord} values obtained from the SCXRD data collected. As seen in **Figure 46**, compound **PINA-2** maintains the HS state upon cooling for a wider range of temperatures compared to the isostructural **PINA-1**, with a V_{coord} of 13.4540(7) Å^3 at 190 K, indicating that **PINA-2** is still in the full HS state at this temperature. After this temperature, a more gradual spin-transition occurs within the 180-160 K range, until reaching a V_{coord} of 11.3209(6) Å^3 at 150 K. This coordination volume value is coherent with an incomplete transition from the HS state to the LS state. The SCXRD data obtained upon heating shows a very narrow hysteresis loop, with the two sets of points obtained upon cooling and heating almost overlapping. The full HS state is finally re-gained already at the temperature of 190 K, with a V_{coord} = 13.3562(7) Å^3.

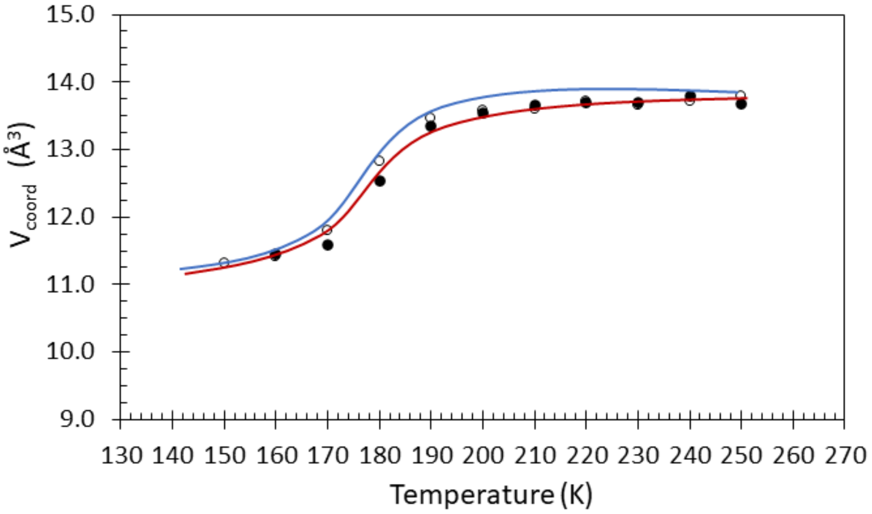

Figure 46: Graph showing the variation of the Fe-L_6 coordination volume (V_{coord}) upon cooling down from the temperature of 250 K up until 150 K for **PINA-2**. The blue line (cooling) and the red line (heating) have been drawn as a guide to the eye and do not represent a fit.

The SCO behaviour obtained for **PINA-1** and for **PINA-2** present significant differences, which is generally expected for compounds that are isostructural, but are constructed with different metal centres. This can be seen for example by looking at the different spin transition temperatures of compounds **pzM** and **pyM** (**M** = Ni, Pd or Pt) that can be found in section **1.1.3**.[32] Another aspect that can influence the SCO curve is also the different amount of solvent that is present within the pores of the material. This is especially important for highly porous materials like MOFs, as already discussed in section **2.1.2.3** where the work of Real and co-workers was presented.[29] For this reason, an analysis of the volume that is accessible by the solvent was carried out for the two structures.

By considering the SCXRD data collected at the temperature of 230 K for the two data sets, a total solvent accessible volume *per* unit cell of 1564.1 Å^3 and 1602.1 Å^3, corresponding to the 53.5% and 54.1% of the unit cell volume, was calculated respectively for compounds **PINA-1** and **PINA-2**. Interestingly, while the volumes of the voids are slightly different, but comparable between the two structures, the total electron count that was calculated to be present within the pores *per* unit cell varies drastically from 217.3 to 419.0 electrons respectively for **PINA-1** and **PINA-2**, indicating that the voids of the two compounds contain a considerably different amount of solvent. By considering that the solvents used in the crystallizations, water and methanol, carry respectively 10 and 18 electrons and that the **pina** ligand carries 104 electrons, it has been calculated that **PINA-1** may contain 12 molecules of methanol, or two **pina** molecules and one water molecule *per* unit cell, while **PINA-2** may contain 22 molecules of methanol and 2 molecules of water, or four **pina** molecules *per* unit cell. These considerations clearly show the differences in solvent uptake between the two compounds analysed. It is also important to point out that this is just an estimation of the solvent content based on the known species that took part in the synthesis, but a more accurate analysis using TGA would give a more reliable estimate of solvent content.

In contrast with Real's work, where desolvation and aging of the crystals led to incomplete SCO behaviour,[29] for the structures obtained in this work with the **pina** ligand, an incomplete SCO transition was seen in compound **PINA-2** where a higher solvent occupancy was calculated. These results support even further the conclusion that different amounts of solvent that are present within the channels of a porous material can significantly influence its SCO behaviour.

The vial containing crystals of **PINA-1** was screened again 25 days after the crystallization was set up. By looking at this batch under the microscope, it was observed that the yellow block-shaped crystals of **PINA-1** presented signs of deterioration that could potentially be related to loss of guest. As seen above, **PINA-1** and **PINA-2** present a high amount of guest molecules inside their pores that could play an important role in the stabilization of the framework. The loss of guest content over time in crystalline materials with enhanced porosity can hence lead to the disruption of the framework and the consequent loss of crystallinity, leading to the noticeable worsening of the diffraction quality that was detected. Yellow, plate crystals were instead observed in the walls of the vial, from which the structure of the discrete complex $\{Fe(H_2O)_2(pina\text{-}H)_2[Pt(CN)_4]_2\}\cdot 2MeOH$ (**PINA-3**) was obtained. The compound crystallises in the triclinic space group *P-1* and is in the HS state at 150 K, with a V_{coord} of 13.501(14) Å^3. Half of the complex **PINA-3** forms the asymmetric unit that can be seen in **Figure 47**, where each iron centre has a water molecule, a $[Pt(CN)_4]^{2-}$ group and a protonated **pina-H** ligand coordinated to it. One methanol molecule *per* asymmetric unit crystallises with the complex, further stabilised by hydrogen bonding interactions with the amide proton of the ligand.

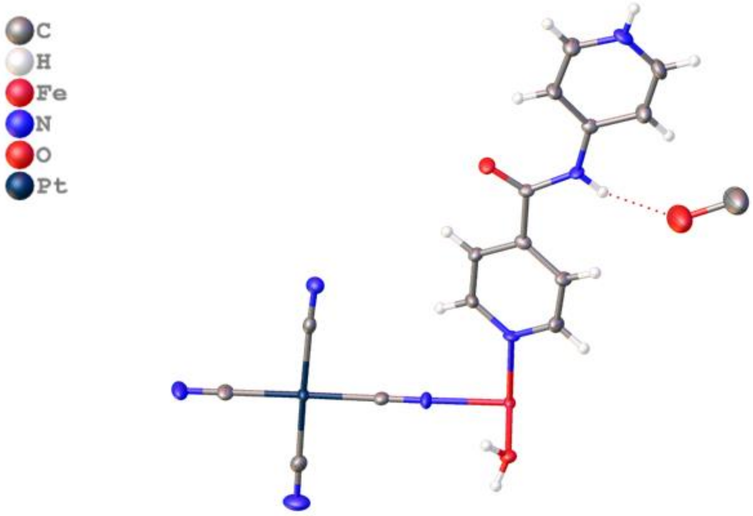

Figure 47: Asymmetric unit of **PINA-3** at 150 K. Atomic displacement parameters are drawn at 50 % probability.

By looking at the interactions that the **pina-H** ligand establishes in the supramolecular packing, it is possible to see that its pyridyl proton interacts *via* hydrogen bond with the nitrogen atom of the $[Pt(CN)_4]^{2-}$ group that is in close proximity, forming an infinite hydrogen bonded chain (**Figure 48a**). Each chain packs very closely, in a slightly staggered manner: **Figure 48b** shows that the water molecules coordinated to the iron centre of the light blue chain interact *via* hydrogen bond with the nitrogen atoms of the $[Pt(CN)_4]^{2-}$ groups of the green and red chains, that are respectively above and below the light blue one.

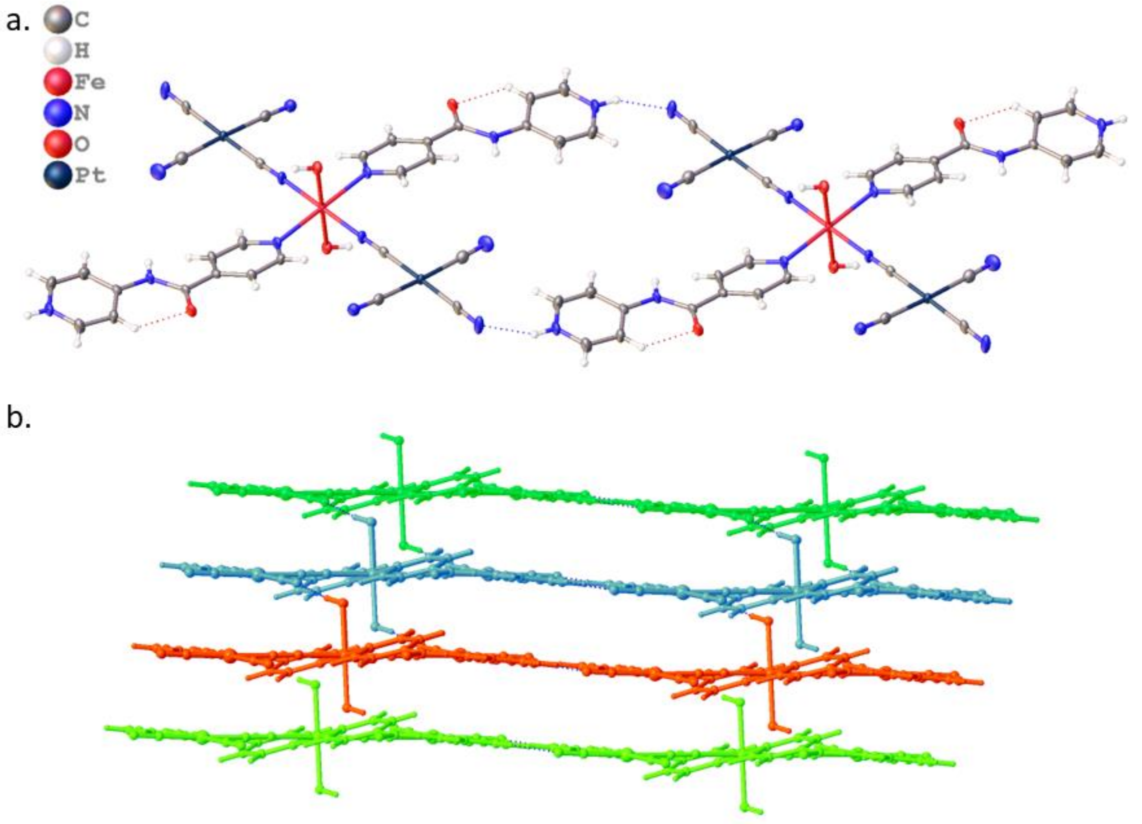

Figure 48: **a.** Supramolecular interactions between two adjacent {$Fe(H_2O)_2(pina\text{-}H)_2[Pt(CN)_4]_2$} fragments and **b.** supramolecular packing showing how the chains formed by the complex pack together. Each chain is highlighted in a different colour (green, light blue and red) to simplify the visualisation. The atoms are drawn isotropically for clarity. The methanol molecules were removed for clarity.

The three compounds herein presented involving the **pina** ligand show the variety of structures that it is possible to obtain with this ligand and how the SCO properties of a material can be influenced by its structure. The two isostructural Hofmann clathrates obtained with Pt(II) (**PINA-1**) and Pd(II) (**PINA-2**) showed distinctly different SCO curves, leading to an incomplete HS to LS transition in the presence of a higher amount of solvent within the pores in the case of **PINA-2**. The complex with the protonated ligand **PINA-3** forms instead when the vial is left for a longer period of time. This is most likely to be due to a ligand decomposition from a bidentate to a monodentate ligand over time in solution rather than a dynamic process in the solid state from **PINA-1** to **PINA-3**. The latter case would require a change in stoichiometry (from a Fe:**pina**:Pt ratio of 1:1:1 present in **PINA-1**, to a 1:2:2 in **PINA-3**) and a drastic structural rearrangement.

2.3 Experimental

2.3.1 Materials

The chemicals isonicotinic acid, triethylamine, propyl chloroformate, 4-aminopyridine, potassium carbonate, $Fe(BF_4)_2{\cdot}6H_2O$, $K_2[Pt(CN)_4]$, $K_2[Pd(CN)_4]$, the **iso** ligand, the **nico** ligand, THF, diethyl ether, MeOH, formic acid and acetone were obtained commercially (Sigma-Aldrich, Fisher Chemical, Alfa Aesar and Thermo Scientific) and used as received.

The **pina** ligand was synthesised by Lee Birchall following the procedure here reported. Isonicotinic acid (1.0 g, 8.12 mmol) and triethylamine (1.1 mL, 8.12 mmol) were dissolved in THF (80 mL) and stirred for 10 minutes. Propyl chloroformate (1 mL) was then added dropwise, forming a white solution. A solution of 4-aminopyridine (0.63 g, 6.76 mmol) in THF (20 mL) was added to the stirred solution, resulting in a colour change from white to cream. The solution was left to stir overnight, and changed colour from cream to white. The solvent was removed under vacuum, yielding an off-white solid. The crude product was washed with a potassium carbonate solution (10 % wt, 100 mL), water (2 x 25 mL) and diethyl ether (25 mL), leading to a white powder of **pina** ligand.

2.3.2 Synthesis of compound ISO-1 and ISO-2

A solution of $Fe(BF_4)_2{\cdot}6H_2O$ (30.4 mg, 0.09 mmol) in MeOH (1 mL) was added to a solution of the **iso** ligand (24.7 mg, 0.18 mmol) dissolved in MeOH (2 mL). A solution of $K_2[Pt(CN)_4]$ (38.8 mg, 0.09 mmol) in H_2O (1 mL) was placed at the bottom of a sample vial and layered with the solution of the Fe(II) salt and ligand described above. A buffer solution containing a 1:1 ratio of MeOH/H_2O (4 mL) was placed between the two layers. The vial was sealed and after a few days, light yellow, iridescent plate crystals of **ISO-1** suitable for X-ray diffraction analysis formed on the walls of the vial.

From the same crystallisation conditions, light yellow block crystals of **ISO-2** formed in the same vial and were analysed by X-ray diffraction.

2.3.3 Preparation of LC-MS samples

A solution of **iso** ligand (1.1 mg, 0.008 mmol) was prepared in MeOH with 0.1 % of formic acid (HPLC grade, 1 mL) and was placed in a vial for LC-MS.

The analysis was performed using a Thermo Scientific Ultimate 3000 LC coupled with MSQ Plus System mass spectrometer, equipped with a C18 analytical column (Hypersil DBS C18 4.6 mm I.D. × 150 mm; Shandon HPLC). The mobile phase consisted of 0.1 % HCOOH in H_2O (A) and 0.1 % HCOOH in acetonitrile (B), all solvents were HPLC grade or higher. Isocratic elution was programmed: 0-11 min 4 % solvent B. The total run time was 11 min at a flowing rate of 0.50 mL/min and an injection volume of 1.0 µL. Mass spectrometer was operated in positive mode with electrospray ionization (ESI) source with the following parameters: cone voltage: 75 V, probe temperature: 350°C, ion source gas (N_2) 75 psi. Chromeleon software version 7 (Dionex, USA) was used for system control, data acquisition, and processing.

The LC-MS analysis was also performed using the same conditions on a solution containing the **iso** ligand (1.1 mg, 0.008 mmol) and $Fe(BF_4)_2{\cdot}6H_2O$ (5.0 mg, 0.015 mmol) dissolved in MeOH with 0.1 % of formic acid (HPLC grade, 1 mL).

2.3.4 Synthesis of compound ISO-3

A solution of $Fe(BF_4)_2{\cdot}6H_2O$ (30.4 mg, 0.09 mmol) in MeOH (1 mL) was added to a solution of the **iso** ligand (24.7 mg, 0.18 mmol) dissolved in MeOH (2 mL). A solution of $K_2[Pt(CN)_4]$ (38.8 mg, 0.09 mmol) in H_2O (1 mL) was placed at the bottom of a sample vial and layered with the solution of the Fe(II) salt and ligand described above. A buffer solution containing 1 mL of H_2O, 1 mL of MeOH and 2 mL of acetone was placed between the two layers. The vial was sealed and after a few days, yellow plate crystals of **ISO-3** suitable for X-ray diffraction analysis formed on the walls of the vial.

2.3.5 Synthesis of compound NICO-1

A solution of $Fe(BF_4)_2{\cdot}6H_2O$ (30.4 mg, 0.09 mmol) in MeOH (1 mL) was added to a solution of the **nico** ligand (22.0 mg, 0.18 mmol) dissolved in MeOH (2 mL). A solution of $K_2[Pt(CN)_4]$ (38.8 mg, 0.09 mmol) in H_2O (1 mL) was placed at the bottom of a sample vial and layered with the solution of the Fe(II) salt and ligand described above. A buffer solution containing a 1:1 ratio of MeOH/H_2O (4 mL) was placed between the two layers. The vial was sealed and after a few days, colourless, iridescent plank crystals of **NICO-1** suitable for X-ray diffraction analysis formed on the walls of the vial.

2.3.6 Synthesis of compound PINA-1

A solution of $Fe(BF_4)_2·6H_2O$ (30.4 mg, 0.09 mmol) in MeOH (1 mL) was added to a solution of the **pina** ligand (17.9 mg, 0.09 mmol) dissolved in MeOH (2 mL). A solution of $K_2[Pt(CN)_4]$ (38.8 mg, 0.09 mmol) in H_2O (1 mL) was placed at the bottom of a sample vial and layered with the solution of the Fe(II) salt and ligand described above. A buffer solution containing a 1:1 ratio of MeOH/H_2O (4 mL) was placed between the two layers. The vial was sealed and after a few days, yellow block crystals of **PINA-1** suitable for X-ray diffraction analysis formed on the walls of the vial.

2.3.7 Synthesis of compound PINA-2

A solution of $Fe(BF_4)_2·6H_2O$ (30.4 mg, 0.09 mmol) in MeOH (1 mL) was added to a solution of the **pina** ligand (17.9 mg, 0.09 mmol) dissolved in MeOH (2 mL). A solution of $K_2[Pd(CN)_4]$ (26.0 mg, 0.09 mmol) in H_2O (1 mL) was placed at the bottom of a sample vial and layered with the solution of the Fe(II) salt and ligand described above. A buffer solution containing a 1:1 ratio of MeOH/H_2O (4 mL) was placed between the two layers. The vial was sealed and after a few days, yellow plate crystals of **PINA-2** suitable for X-ray diffraction analysis formed on the walls of the vial.

2.3.8 Synthesis of compound PINA-3

The layering set up for **PINA-1** led to the formation of yellow plate crystals of **PINA-3** suitable for X-ray diffraction analysis after a month time.

2.4 Conclusions

A series of new Hofmann-like frameworks, coordination polymers and complexes that are comprised of the organic linkers **iso**, **nico** and **pina** were investigated in this chapter. In particular, seven new compounds were synthesised *via* the layering technique and their structural investigation was carried out with SCXRD analysis.

The ligands explored in this work include some interesting aspects that differ when comparing them to the ligands involved in the synthesis of the progenitors Hofmann-clathrates, such as the dipyridyl **bipy** or **bpac**. The rigid, conjugate pyridyl ring core is still present, but the addition of the carbonyl functionality of the hydrazide group in **iso**, or of the amide group in **nico** and **pina**, further adds coordination sites and sites for various supramolecular interactions to occur, characteristics that can influence the topology of the coordination networks obtained and hence potentially their SCO properties. The presence of multiple heteroatoms and functional groups opens up also to the possibility for the ligands to assume different coordination modes and to the possibility to perform *in-situ* modification of the ligand such as dimerization or functionalization, making them potential "multifunctional ligands" compared to the progenitor dipyridyl ones.

The different possible coordination modes that the investigated ligands can assume allowed in fact the formation of a variety of 2D and 3D structures. When the bidentate ligands **pina** and **di-iso** were used, the 3D Hofmann-clathrates **PINA-1**, **PINA-2** and **ISO-2** were formed. The ligands **iso-hy**, **nico** and **pina-H** acted instead as monodentate ligands, forming the 2D coordination networks **ISO-3**, **NICO-1** and **PINA-3**, with the latter structure obtained as a consequence of the protonation of **pina** that hence went from a mono- to a bidentate ligand. An additional variation was seen in compound **ISO-1**, where the **iso** ligand takes part only as a guest intercalated between the 2D layers.

The reactivity of the hydrazide group in the **iso** ligand allowed two structures to be obtained in which the ligand had undergone an *in-situ* chemical modification: the Hofmann-clathrate **ISO-2** and the 2D coordination polymer **ISO-3**. On one hand, the self-assembly of two **iso** ligand molecules that occurs in solution in the presence of a metal salt, led to the unexpected formation of the dimeric **di-iso** ligand in **ISO-2**. This phenomenon further increases the diversity of possible outcomes when using **iso**, but renders the rational design of specific architectures more complicated. On the other hand, the known reactivity of the amide group of the ligand towards ketones was used to modify the ligand *in-situ* to form the **iso-hy** ligand in **ISO-3**, proving the ability of **iso** to also undergo chemical reactions in a more controlled way.

With particular focus on the investigation of the solid-state behaviour of Hofmann-type compounds, four of the seven structures presented in this chapter belong to this family of materials. With regards to the **nico** ligand, the only structure that formed was the 2D Hofmann-clathrate **NICO-1**. The compound represented an interesting example of a network which extents *via* both coordination bonds and supramolecular interactions, in this specific case hydrogen bonding. This concept can potentially have a role in the effectiveness of the transmission of the structural changes that occur during a SCO transition. The **iso** ligand formed instead a 3D Hofmann-clathrate only when its dimerization led to the formation of the bidentate **di-iso** ligand, and consequently of compound **ISO-2**. The material showed a phase transition from the monoclinic space group *P2/m* to the triclinic space group *P-1* upon cooling, but no SCO activity was detected for any of these two compounds. Finally, the **pina** ligand led to the most interesting results in terms of SCO properties, with the two isostructural 3D Hofmann-clathrates **PINA-1** and **PINA-2** being SCO active. A different amount of solvent within the pores of the two compounds led to significantly different SCO curves: an abrupt transition with 15 K hysteresis when a lower amount of solvent was present in the pores (**PINA-1**); a more gradual and incomplete transition with no hysteresis when the amount of solvent was higher (**PINA-2**).

In conclusion, seven new compounds have been synthesised and their solid-state behaviour has been explored in order to elucidate structure-property correlations. The Hofmann-clathrates **PINA-1** and **PINA-2** showed a SCO transition within the temperature range analysed. However, the variety of structures that has been presented here, along with the potential to functionalize ligands *in-situ*, or to tune the 3D packing by introducing synthons to induce supramolecular interactions, renders these multifunctional ligands interesting candidates to further investigate their use in the field of SCO materials.

2.5 References

1 V. Niel, A. L. Thompson, M. C. Muñoz, A. Galet, A. E. Goeta and J. A. Real, *Angew. Chemie - Int. Ed.*, 2003, **42**, 3760–3763.

2 M. D. Iseman, in *European Respiratory Journal, Supplement*, 2002, vol. 20, pp. 87s-94s.

3 B. Swapna, D. Maddileti and A. Nangia, *Cryst. Growth Des.*, 2014, **14**, 5991–6005.

4 M. G. Smith and A. Lemmerer, *J. Mol. Struct.*, 2019, **1179**, 132–144.

5 H. Bhutani, S. Singh, S. Vir, K. K. Bhutani, R. Kumar, A. K. Chakraborti and K. C. Jindal, *J. Pharm. Biomed. Anal.*, 2007, **43**, 1213–1220.

6 A. Koppenhöfer, U. Hartmann and H. Vahrenkamp, *Chem. Ber.*, 1995, **128**, 779–785.

7 H. -C Chiang and L. -J Lin, *J. Chinese Chem. Soc.*, 1978, **25**, 125–130.

8 A. Lemmerer, J. Bernstein and V. Kahlenberg, *CrystEngComm*, 2010, **12**, 2856–2864.

9 M. A. Simon, E. Anggraeni, F. E. Soetaredjo, S. P. Santoso, W. Irawaty, T. C. Thanh, S. B. Hartono, M. Yuliana and S. Ismadji, *Sci. Rep.*, 2019, **9**, 1–11.

10 Y. A. Tyula, A. Zabardasti, H. Goudarziafshar, M. Kucerakova and M. Dusek, *Appl. Organomet. Chem.*, 2018, **32**, e4141.

11 F. B. De Almeida, F. H. E Silva, M. I. Yoshida, H. A. De Abreu and R. Diniz, *Inorganica Chim. Acta*, 2013, **402**, 60–68.

12 F. B. de Almeida, M. S. Cunha, H. A. De Abreu and R. Diniz, *ChemistrySelect*, 2016, **1**, 3770–3776.

13 M. C. R. Freitas, J. M. S. António, R. L. Ziolli, M. I. Yoshida, N. A. Rey and R. Diniz, *Polyhedron*, 2011, **30**, 1922–1926.

14 A. Lemmerer, J. Bernstein and V. Kahlenberg, *CrystEngComm*, 2010, **12**, 2856–

2864.

15 M. H. Stipanuk and M. A. Caudill, *Biochemical, Physiological, and Molecular Aspects of Human Nutrition*, 2013.

16 M. M. Wicht, L. Mevoe Obiang and L. R. Nassimbeni, *Polyhedron*, 2021, **202**, 115202.

17 S. D. Taherzade, S. Rojas, J. Soleimannejad and P. Horcajada, *Nanomaterials*, 2020, **10**, 1–20.

18 M. Knip, I. F. Douek, W. P. T. Moore, H. A. Gillmor, A. E. M. McLean, P. J. Bingley and E. A. M. Gale, *Diabetologia*, 2000, 43, 1337–1345.

19 A. Ghorbani, R. Rashidi and R. Shafiee-Nick, *Biomed. Pharmacother.*, 2019, **111**, 947–957.

20 M. Perec, R. F. Baggio, O. Peña, R. P. Sartoris and R. Calvo, *Inorganica Chim. Acta*, 2011, **373**, 117–123.

21 I. Ondrejkovičová, S. Galková, J. Mroziński, J. Kłak, T. Lis and Z. Olejnik, *Inorganica Chim. Acta*, 2008, **361**, 2483–2490.

22 M. Kondo, A. Asami, H.-C. Chang and S. Kitagawa, *Cryst. Eng.*, 1999, **2**, 115–122.

23 S. Shanmugaraju, D. Samanta, B. Gole and P. S. Mukherjee, *Dalt. Trans.*, 2011, **40**, 12333–12341.

24 C. Mugenzi, D. R. Powell, N. N. Gerasimchuk and L. Yang, *Polyhedron*, 2018, **154**, 39–46.

25 X. Chen, H. Zhou, Y. Y. Chen and A. H. Yuan, *CrystEngComm*, 2011, **13**, 5666–5669.

26 D. De, S. Neogi, E. C. Sañudo and P. K. Bharadwaj, *Chem. - A Eur. J.*, 2015, **21**, 17422–17429.

27 T. M. Ross, S. M. Neville, D. S. Innes, D. R. Turner, B. Moubaraki and K. S. Murray, *Dalt. Trans.*, 2010, **39**, 149–159.

28 C. Lochenie, W. Bauer, A. P. Railliet, S. Schlamp, Y. Garcia and B. Weber, *Inorg.*

Chem., 2014, **53**, 11563–11572.

29 F. J. Valverde-Muñoz, C. Bartual-Murgui, L. Piñeiro-López, M. C. Muñoz and J. A. Real, *Inorg. Chem.*, 2019, **58**, 10038–10046.

30 Y. Garcia, V. Niel, M. Carmen Muñoz and J. A. Real, *Top. Curr. Chem.*, 2004, **233**, 229–257.

31 T. Steiner, *Angew. Chemie-International Ed.*, 2002, **41**, 48.

32 V. Niel, J. M. Martinez-Agudo, M. C. Muñoz, A. B. Gaspar and J. A. Real, *Inorg. Chem.*, 2001, **40**, 3838–3839.

Chapter 3: Investigation of the role of modulators in the synthesis of new Hofmann-type networks

3.1 Introduction

3.1.1 Coordination modulators

The concept of a coordination modulator was first introduced by Kitagawa *et al.* in 2009 with the aim of understanding and controlling the process of crystal growth in framework materials.[1] The idea behind this concept was based on the introduction of a second ligand in the reaction mixture, called capping reagent or modulator (**Figure 49**), having the same chemical functionality of the organic linker used to synthesise the material in order to modulate the metal-ligand interactions, known as the coordination equilibria.[1] The competitive situation generated by the presence of two compounds (linker and modulator) that can potentially both coordinate to the metal centre, can in fact break the coordination balance in the process of crystal growth and influence the self-assembly of the building blocks that form the network.[2] More specifically, the presence of the modulator impedes the immediate coordination of the linker to the metal centre regulating the rate of the framework formation and hence influencing the size, the morphology and the crystallinity of the final material.[1]

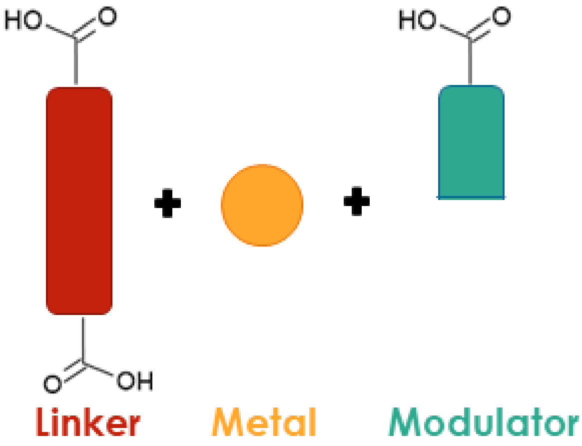

Figure 49: Schematic refiguration of an example of a carboxylic acid-based coordination modulator.

Interest was mostly given at first to the use of carboxylic acid-based modulators because the majority of MOFs present in the literature were constructed with organic linkers carrying this functionality. The first example reported in literature that used the term "coordination modulator" shows however a Cu-based MOFs constructed both with a N-donor and a dicarboxylate ligand, the $[Cu_2(ndc)_2(dabco)]_n$ MOF (**ndc** = 1,4-naphthalene dicarboxylate; **dabco** = 1,4-diazabicyclo[2.2.2]octane).[1] In that work, focus was given only to the use of a monocarboxylic acid-based modulator, more specifically acetic acid, which led to the growth of crystalline nanorods.[1] A few years after, the use of pyridine as a N-donor modulator, and the simultaneous use of pyridine and acetic acid as modulators were investigated, leading respectively to the formation of nanosheets and nanocubes of the MOF of interest.[3] The mechanism of regulation of the morphology of the MOF is mostly related to the orientation in the space of the Cu-**ndc** and Cu-**dabco** coordination bonds: the Cu-**ndc** connectivities develop in fact in the (*h*00) and (0*k*0) facets, while the Cu-**dabco** ones develop in the (00*l*) facets. Hence, when acetic acid and pyridine are both used, their functionality compete respectively with **ndc** and with **dabco** ligands, and the linker coordination is impeded in the [100] and [001] direction, leading to the formation of nanocubes.[3]

The concept of a modulator is related to the one of a template. The latter is however used more broadly than just with MOFs, including for other porous materials such as zeolites. Both terms were developed from the idea that rational design when synthesising a material, in this case a MOF, is essential to obtain a structure that exhibits specific pore size, pore chemistry and topology. The term “template molecule” specifically refers to a species that interacts with the MOF building blocks *via* weak interactions, and that assembles together with them into specific building units that then form the final framework structure.[4] This approach can open up new topologies that are not accessible by direct mixing of the starting precursors, as the addition of a template molecule can dictate a specific spatial arrangement of the building units that wouldn’t be achieved without the template itself. These template molecules are usually solvent or guest molecules that influence the building units spatial arrangement with their polarity, size and host-guest interactions, inducing the formation of specific defined spaces in the framework like cavities or channels.[4]

The concepts of modulators and templates show how the simple approach of introducing an additional chemical species can be used to control the growth of the crystalline material and how it is possible to rationalise the use of the modulator or a template to obtain a specific morphology.

3.1.2 Host-guest properties in Hofmann-type MOFs

Hofmann-type compounds are not only known for their interesting SCO properties, but also for their ability to incorporate guest molecules, two characteristics that belong to these materials and that are not independent one from the other. Real, Kitagawa and co-workers reported in 2009 an interesting work where the SCO properties of compound **pzPt** were analysed when in presence of different guest molecules.[5] The analysed compound has a spin transition at 285 K upon cooling and 309 K upon heating when no guest is included. Three different classes were identified for the guests analysed, according to the different SCO properties that **pzPt** was exhibiting when incorporating them within the room temperature region. The gas molecules N_2, O_2 and CO_2 showed no effect on the spin state of **pzPt**.[5] Molecules of H_2O, alcohols, acetone and five- or six-membered ring ones stabilised the HS state, while CS_2 stabilised the LS state.[5] Size and shape of the guests, along with the interactions that these molecules have with the host framework were considered to be the responsible for the different SCO behaviours seen in **pzPt**. Interestingly, the compound showed chemical and thermal memory. Compound **pzPt·CS$_2$** is in the LS state within the 2-330 K temperature range, spin state that is maintained when the CS_2 molecules are removed at 298 K under vacuum due to the memory effect.[5] Similarly, compound **pzPt·bz** (**bz** = benzene) is paramagnetic at all temperatures, hence benzene adsorption in the LS compound allows a transition to the HS state, which once again is retained after guest desorption under vacuum.[5]

This example shows how the SCO properties of porous materials such as Hofmann-type networks can be influenced by the guest uptake and hence how it is possible to tune the SCO behaviour of a compound according to the guest used. It is also important to point out that a rational design of the framework can impart specific host-guest characteristics to the material, such as a more extended ligand can increase the solvent accessible volume or supramolecular interactions between the framework and the guest’s network can be induced by introducing building blocks that can favour their formation.

3.1.3 Choice of the ligands

The ligands used for the synthesis of new Hofmann-like networks that are investigated in this chapter are the bidentate nitrogen-donor ligands 4,4'-azopyridine (**azo**) and 1,2-bis(4-pyridyl)ethane (**bpa**) that are reported in **Figure 50**. Both of them are bridging ligands that are characterised by a backbone composed of two rigid pyridyl rings, and differ for the spacer situated in between the two rings.

Three-dimensional structures are generally obtained when a bidentate ligand is used to construct Hofmann-like networks, but other factors such as a different degree of flexibility of the ligand core, and hence different possible coordination geometries available, can considerably influence the structure and properties of the final material. The following section examines the main characteristics of these ligands, and analyses the structures and the properties of the most important materials that are present in the literature that involve the **azo** and the **bpa** ligand.

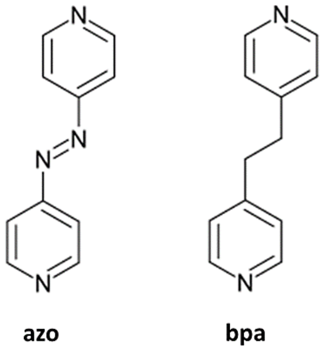

Figure 50: Schematic representation of the organic ligands used in this chapter and abbreviations.

3.1.3.1 Azo ligand

The ligand 4,4'-azopyridine (**azo**) is a dipyridyl ligand characterised by an extended conjugated π-system. The two pyridyl rings are separated by the rigid N=N group, rendering **azo** a good candidate for the construction of metal-organic compounds where phenomena like electron transport, intramolecular photoinduced electron transfer and energy transfer processes can occur.[6,7] Investigation of the *trans*-*cis*-isomerization of azo-functionalities incorporated into MOF structures has also attracted attention in the last few decades, allowing the switching mechanism to be followed and tuned in a controlled way.[8]

The **azo** ligand has already been used in the field of SCO materials to synthesise Hofmann-like compounds. An interesting work by Real and co-workers presented the synthesis of a polycrystalline compound with formula $\{Fe(azo)[M^{II}(CN)_4]\}\cdot nH_2O$ (M^{II} = Ni^{II}, Pd^{II} and Pt^{II}, **azoM**) both as a bulk material and as a nanopatterned thin film deposited on a gold substrate.[9] The material exhibits the typical structure of a Hofmann-clathrate, where the pillar **azo** ligand bridges two iron ions of consecutive 2D $\{Fe[M^{II}(CN)_4]\}$ layers, forming 3D frameworks that are isostructural to the **pz** ones. However, the use of the more extended **azo** ligand compared to the shorter **pz**, increases the separation between the $\{Fe[M^{II}(CN)_4]\}$ layers. The values go from ca. 7.3 Å for the **pz**-based networks to ca. 13.5 Å for the **azo**-based ones, with the consequent increase of the solvent accessible volume from ca. 131 $Å^3$ to 286 $Å^3$.[9] The less rigid nature of the **azo** ligand compared to the **pz** ligand appears to be the responsible for a smaller cooperativity seen for the **azoM** family of materials, that similarly to the **pz**-based ones still exhibit a SCO behaviour near room temperature.[9]

Another work present in the literature reports the use of the analogous **azo**-benzene form of the **azo** ligand, the monodentate 4-phenylazo-pyridine (**ph-azo**) ligand, which has been used to prepare the 2D Hofmann-like compound $\{Fe(ph\text{-}azo)_2[Pd(CN)_4]\}$ (**ph-azoPd**) that can be seen in **Figure 51**.[10] The coordination environment of each Fe(II) in compound **ph-azoPd** is in fact composed of two molecules of the monodentate **ph-azo** ligand coordinated in the apical position of the metal centre, and the $[Pd(CN)_4]^{2-}$ fragment bridging adjacent Fe(II) ions through their equatorial positions forming an infinite 2D layer (**Figure 51a**). Each of the adjacent layers are then interdigitated forming the closely packed, non-porous coordination network that can be seen in **Figure 51b**. The compound undergoes an abrupt and hysteretic spin transition with transition temperatures of $T_{1/2}\downarrow$ = 233 K and $T_{1/2}\uparrow$ = 250 K respectively upon cooling and heating, and a 17 K hysteresis loop.[10]

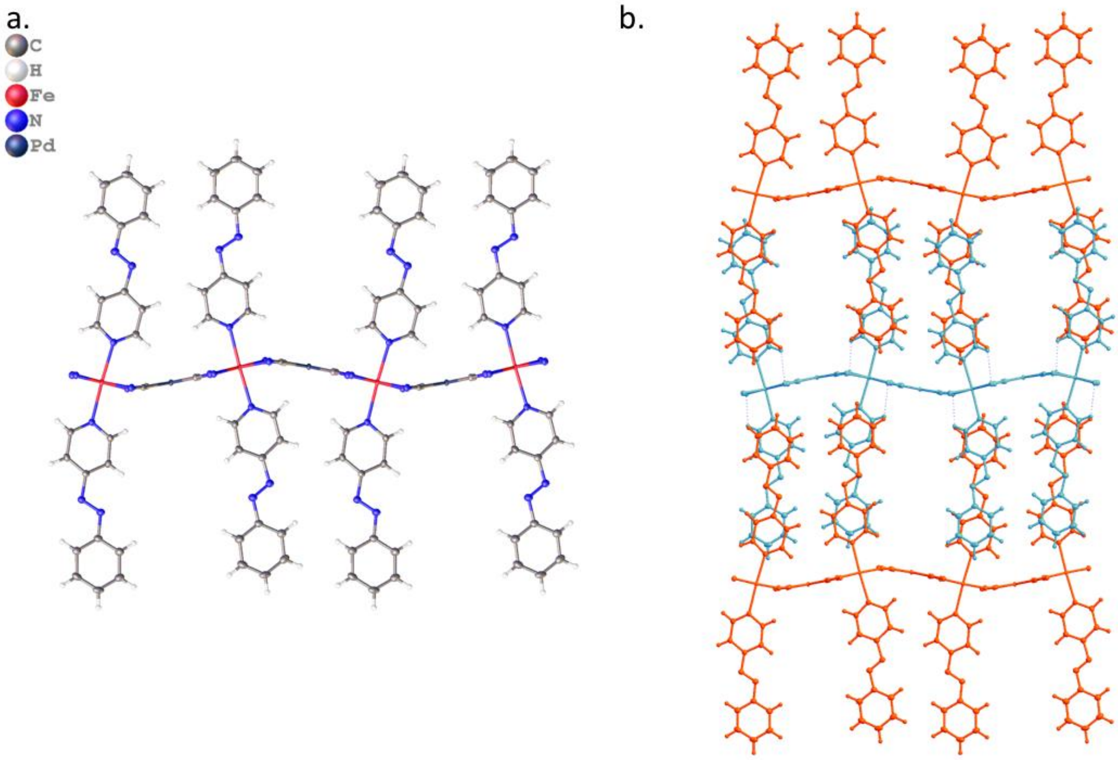

Figure 51: **a.** One 2D layer of compound **ph-azoPd** seen along the *a*-axis and **b.** supramolecular packing for compound **ph-azoPd** where each layer is highlighted in a different colour (red and light blue) to simplify the visualisation. CCDC N°: 993492.[10]

The reported interesting characteristics of the **azo** ligand deriving from its conjugated backbone, such as its capability to allow electron transfer between bridging metal centres, raised the interest of including it in the synthesis of SCO materials. More specifically, the Hofmann-like compounds that are present in the literature with **azo** and the **azo**-derivative **ph-azo** ligand, and their interesting SCO properties, renders it a good candidate to further extend this family also to clathrate structures constructed with the $[M^{I}(CN)_2]^-$ fragment and to analyse their structure-to-properties correlations.

3.1.3.2 Bpa ligand

The organic linker 1,2-bis(4-pyridyl)ethane (**bpa**) is a bidentate ligand constructed with two rigid pyridyl rings that are separated by the flexible bridging alkyl group. Interest has been given to the investigation of the different possible supramolecular isomers that can be obtained when using **bpa** because of its flexible core. Different structures can be constructed by self-assembly of the same few components, when the ligand itself can assume different isomers: Nakashima and co-workers reports an example where a 1D complex, a 2D grid-based compound and an interpenetrated structure, and hence three completely different isomers, are obtained by reacting **bpa**, a Fe(II) salt and a building block containing the $^-$NCS unit, demonstrating a distinctive structural variety.[11]

The **bpa** ligand has been investigated in the field of SCO materials by the group of Kitagawa, who reported in 2013 the synthesis of the Hofmann-type 3D porous coordination polymer with formula {Fe(bpa)[Pt(CN)$_4$]·G·nH$_2$O} (G = **bpa**, bibenzyl (**bbz**) and stilbene (**stb**)), where the **bpa** ligand bridges two Fe(II) ions of two adjacent 2D {Fe[Pt(CN)$_4$]} sheets.[12] The structural characterization of the clathrate framework was performed on a microcrystalline powder, while single crystals of the material were not obtained from the slow-diffusion technique attempted. The compound exhibits different SCO behaviour according to the type of guest molecule present in the pores. A three-step spin transition within the temperature range of 180-240 K is seen for the compound with **bpa** as guest, with the same SCO behaviour retained after dehydration. For the compound having **bbz** as guest, a more gradual three-step spin transition in the 80-200 K temperature range is reported, while the framework containing **stb** molecules as guest shows instead an abrupt spin transition with T_c = 163 K.[12] The fact that the TGA, the elemental analysis and the PXRD showed that the amount of guest molecules and the structure of the framework are essentially the same in all the cases, proves that the guest molecules are essential to stabilize the porous and flexible network.[12] Additionally, the SCO inactivity after guest removal supports the fact that the they have an important impact in the communication between adjacent metal centres and hence in the SCO properties of the final material.[12]

The data presented so far regarding the Pt-based Hofmann-type framework constructed with the **bpa** ligand is obtained from crystalline powders. A full structural analysis *via* SCXRD of porous materials with enhanced flexibility seems in fact to be less easy to obtain. In addition, when single crystals grow, issues with severe disorder of the flexible part of the structure can be encountered while solving and refining the structures. An example of the latter case are the 3D networks synthesised with the ligand 1,2-dibromo-1,2-bis(4-pyridyl)ethane (**Br2-bpa**), which are the only Hofmann-type structures constructed with a **bpa**-derivative ligand that are present in the literature reporting structural data from SCXRD analysis. The **Br2-bpa** ligand has the analogous structure of the **bpa** ligand with the exception of having the flexible CHBr-CHBr group as a spacer between the two rigid pyridyl rings instead of the alkyl CH_2-CH_2 group. The two networks with formula {Fe(Br2-bpa)[$M^{II}(CN)_4$]·$4H_2O$} (M^{II} = Pd^{II} and Pt^{II}, **Br2-bpaPd** and **Br2-bpaPt** respectively) have the typical structure of a Hofmann-clathrate, where the 2D {Fe[$M^{II}(CN)_4$]} layers are pillared by the flexible organic linker **Br2-bpa**.[13] As it can be seen from **Figure 52**, the ligand in the structure is severely disordered.[13]

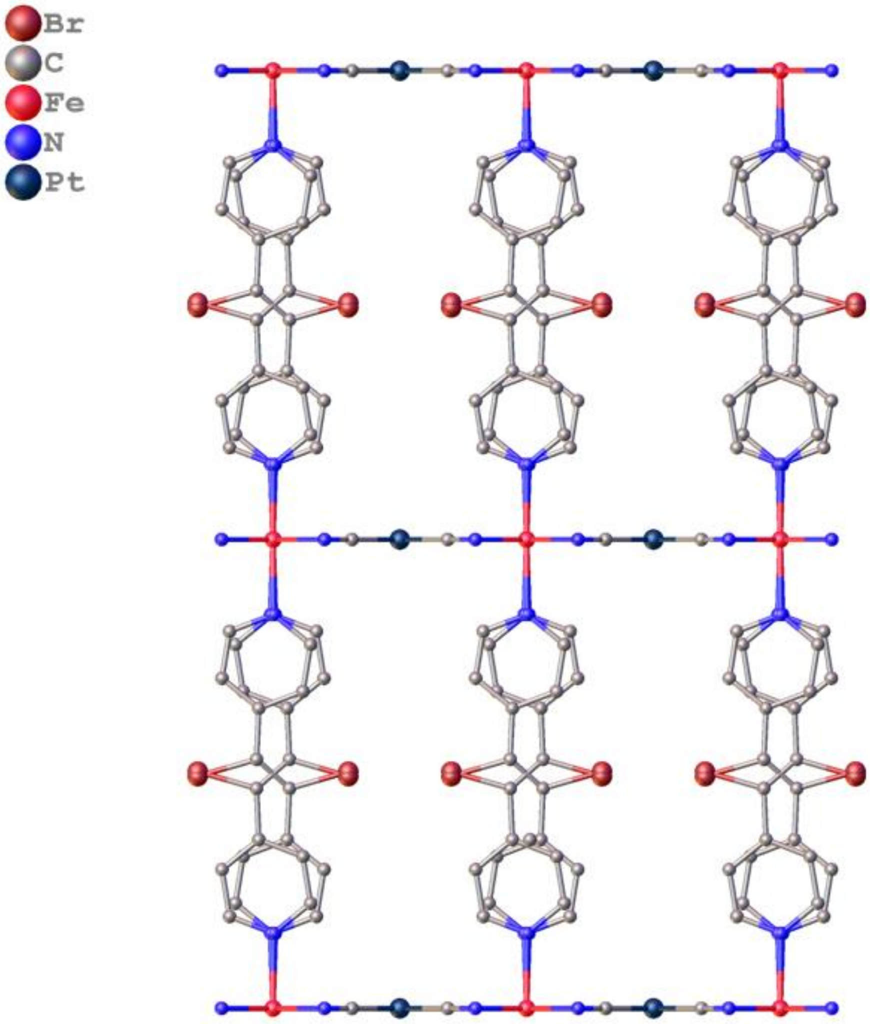

Figure 52: Structure of compound **Br2-bpaPt** showing the supramolecular packing along the *a*-axis and the two components of the disordered organic linker **Br2-bpa**. The structure has been drawn isotropically for clarity. CCDC N°: 2023229.[13]

Compounds **Br2-bpaPt** and **Br2-bpaPd** have a similar SCO behaviour showing an incomplete one-step spin transition below 200 K when at ambient pressure.[13] Interestingly, the application of hydrostatic pressure to compound **Br2-bpaPt** leads to higher transition temperature values that shift from 185 to 298 K, and hence closer to room temperature, and to the broadening of the hysteresis loop to 13-25 K which was not present at ambient pressure.[13]

To date, no structures of Hofmann-type compounds constructed with the $[M^I(CN)_2]^-$ fragment and the **bpa** ligand are present in the literature. However, the structure of an interesting two-dimensional polyrotaxane net constructed with **bpa**, the $[M^I(CN)_2]^-$ fragment and a Fe(II) salt was reported in 2010 by Sato and co-workers.[14] The compound with formula $[Fe(bpa)(Au(CN)_2)_2 \cdot MeOH]$ (**bpaAu**) is composed of **bpa** ligands that are bent and that bridge two adjacent Fe(II) ions. Each metal centre has hence two coordination sites occupied by the ligand, three coordination sites occupied by the $[Au(CN)_2]^-$ fragment and the last available one occupied by the oxygen atom of a methanol molecule, forming the 2D coordination polymer. Finally, the $Fe_2(bpe)_2$ rings of a 2D network interpenetrate with the $[Au(CN)_2]^-$ fragments of a second independent 2D sheets stabilised by aurophilic interactions, forming a doubly interpenetrated polyrotaxane structure. Even though the compound did not exhibit any SCO behaviour, remaining in the HS state from room temperature until the temperature of 50 K,[14] it still represents a very interesting structure from the point of view of the self-assembly of the building blocks that are used to construct Hofmann-type compounds.

Most of the Hofmann-type materials that are present in the literature are constructed with rigid linkers. The only flexible non-**bpa** derivative that has been previously used to construct a Hofmann-like compounds is the ligand 4,4'-di(pyridylthio)methane (**dpsme**), which forms a network that exhibits a unique three-step SCO transition.[15] The materials presented above involving **bpa** are really promising both for the different SCO behaviour that were illustrated and for the structural variety that can be obtained when using a more flexible ligand. However, the flexibility of the ligand seems to impart a lower predictability in the structures that forms, which is an advantage when looking at structural variety, but can become a disadvantage when trying to construct a material with specific properties deriving from its specific structure. Nevertheless, the structural variety, added to the fact that only one Hofmann-clathrate is present in the literature with a flexible ligand, raised our interest in investigating frameworks belonging to this family of materials constructed with **bpa** and the $[M^I(CN)_2]^-$ fragment aiming to expand the clathrate family with new SCO active materials.

3.1.4 Aims

The aims of this chapter are to synthesise new Hofmann-like networks and coordination polymers constructed with the **azo** and the **bpa** ligands using the $[M^{I}(CN)_2]^-$ fragment and to perform their structural characterization *via* SCXRD. These two ditopic ligands are interesting building blocks to be involved in the synthesis of this family of materials because of their structural variety. The rigid spacer between the pyridyl rings of **azo** and the flexible one of **bpa** allow the two ligands to assume different possible conformations: while the trans **azo** ligand can only assume the linear conformation, **bpa** has access both to the linear and to the bent conformation. Additionally, the possibility for the pyridyl rings to rotate increases even further our interest in performing a structural investigation of these materials and in studying the correlation between their structures and their properties, such as the SCO behaviour.

To date, the vast majority of the Hofmann-type materials reported in the literature are constructed with rigid ligands as building blocks rather than flexible ligands. It is in fact more complicated to impart a topological control to structures that involve building blocks that can have more than one conformation, like the **bpa** ligand, or more than one coordination mode, like the $[Ag(CN)_2]^-$ fragment. The use of flexible building blocks is however an interesting aspect to explore when aiming to build porous networks. The construction of a structure that has the ability to breathe as a consequence of the flexibility of its building blocks can in fact help with the guest uptake by creating more space for the guest itself, an aspect that can then influence the SCO behaviour.

This chapter therefore aims to investigate the solid-state behaviour of Hofmann-type materials constructed with the $[M^{I}(CN)_2]^-$ group and the ligands above described, aiming to understand how the different characteristics of the two ligands can influence the structure of the final material. More specifically, the structures obtained when the rigid **azo** ligand, the flexible **bpa** ligand and both of the two ligands are used will be explored in order to compare the solid-state behaviour of the designed materials. Finally, interest will be given to the study and investigation of their SCO behaviour with the aim to further expand our understanding of the structure-property correlations of these materials.

3.2 Results and discussion

3.2.1 Azo-based materials

The layering crystallization performed using $K[Ag(CN)_2]$, $Fe(BF_4)_2 \cdot 6H_2O$ and the **azo** ligand, led to the formation of the doubly interpenetrated 3D $\{Fe(azo)_2[Ag(CN)_2]_2\}$ (**AZO-1**). The compound crystallises in the monoclinic *$P2_1/n$* space group and is in the HS state within the temperature range investigated, with an Fe-L$_6$ V_{coord} of 13.841(10) Å^3 and 13.729(10) Å^3 at 290 K and 80 K respectively. The two interpenetrated 3D networks consist of parallel 2D layers of $\{Fe[Ag(CN)_2]_2\}$ where the **azo** ligands bridge two adjacent layers coordinating to two Fe-Ag atoms (**Figure 53**).

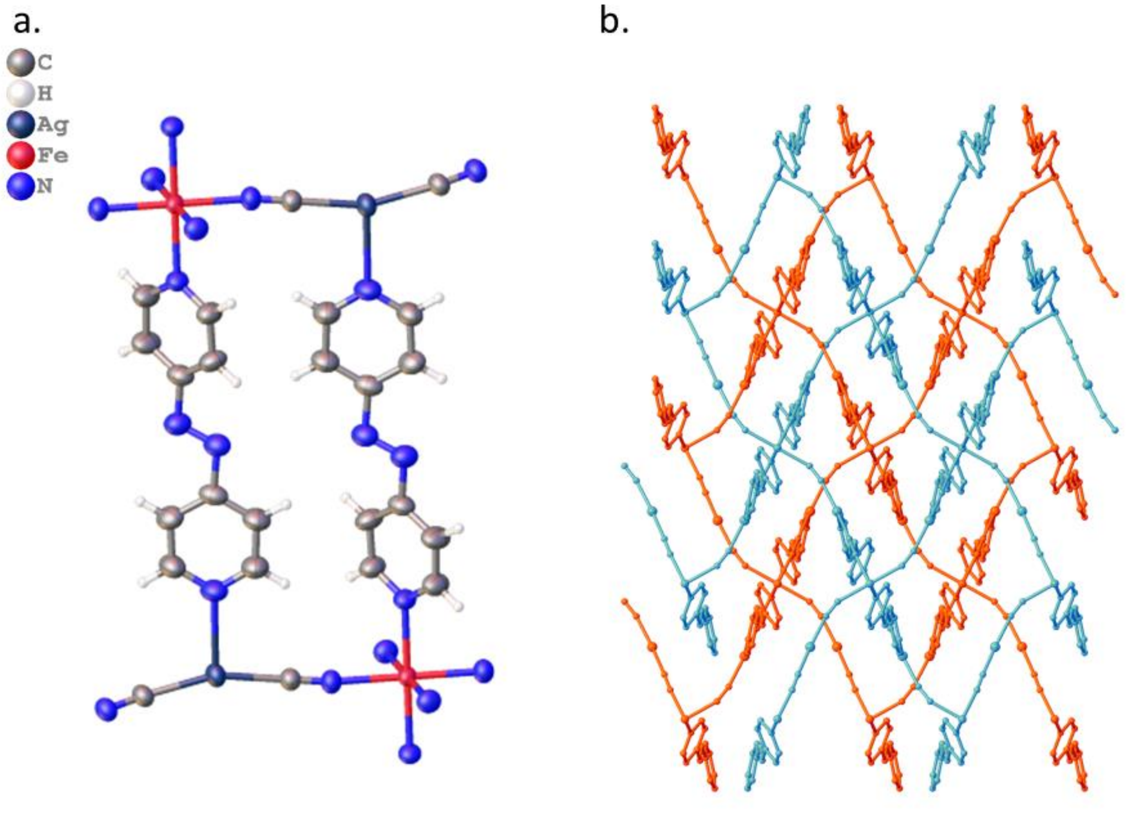

Figure 53: **a.** Fragment of the structure of **AZO-1** at 290 K. Atomic displacement parameters are drawn at 50 % probability; **b.** Supramolecular packing seen from the [101] plane. Independent 3D networks of **AZO-1** are highlighted in blue and orange to simplify the visualisation and the structure has been drawn isotropically for clarity.

The coordination motif of the bidentate ligand bridging an iron and a silver atom differs significantly from the one that is usually seen in the original Hofmann-clathrates, where the ligand bridges instead two iron atoms. This unusual coordination is however already reported in the literature for the analogous compounds constructed with the **bipy** (**bipyAg**) and the **bpe** (**bpeAg**) ligands.[16] As no analogous crystal structures are deposited in the literature constructed with the rigid **azo** ligand and the $[M^{I}(CN)_2]^-$ fragment, our initial interest was to perform a crystallization with these building blocks in order to try to obtain a structure exhibiting the original Hofmann-type coordination motif. However, compound **AZO-1** proved to be isostructural with compound **bpeAg**, exhibiting the less common coordination motif reported above. Additionally, two correlated structural aspects that are common to this family of materials led the networks to be interpenetrated: the first is the flexibility of the $[Ag(CN)_2]^-$ group, which allowed the C-Ag-C' fragment in **AZO-1** to go from linear to bent [C-Ag-C' = 160.8654(6)°], and hence the coordination of the ligand to an iron and a silver atom to occur; the second is the fact that the voids that are generated when going from the $[M^{II}(CN)_4]^{2-}$ to the $[Ag(CN)_2]^-$ group are bigger,[16] leaving space for the **azo** ligand of the adjacent network to be accommodated. Finally, no argentophilic interactions are observed, as expected for these specific structures where the packing is such that the coordination sphere of the Ag(I) ions is occupied by either the CN^- group or by the **azo** ligand itself.

Compound **AZO-1** did not show any SCO activity within the 290 K - 80 K temperature range that was investigated. By looking at the Hofmann-type compounds that are present in the literature and that involve the unusual Fe-**azo**-Ag coordination motif, it is possible to see that the less common coordination mode of the organic linker is not the cause of the SCO inactivity. Despite the presence this coordination motif, compound **bpeAg** shows a cooperative single-step SCO transition at about 95 K,[16] proving that in that case the communication between adjacent metal centres is still efficient. It should be noted that considering the low transition temperature for the only known SCO active compound with the unusual Fe-**azo**-Ag coordination, compound **bpeAg**, it is possible for **AZO-1** to exhibit a SCO transition below 80 K, the minimum temperature examined. It is however important to point out that the correlation between the obtained structures and the SCO properties of the materials seems to be less controllable when the $[Ag(CN)_2]^-$ group is used: as reported in section **1.1.4**, compounds **pzAg·pz** and **bipyAg** are respectively in the LS state and HS state at room temperature, with **bipyAg** not showing any transition at ambient pressure within the temperature range analysed, while compound **bpeAg** shows SCO activity, as reported below.[16]

The different SCO behaviour reported for the various Ag-based Hofmann-type compounds present in the literature, added to the results obtained with the rigid **azo** ligand in compound **AZO-1** demonstrate that a variety of magnetic behaviours are accessible when the $[M^{I}(CN)_2]^-$ fragment is used. Compound **AZO-1** has the structure of a Hofmann-type compound that does not have the same structural motif of the original Hofmann-clathrates. Further studies are hence necessary in order to be able to control the self-assembly of the building blocks when using this fragment, and to clarify the structure-to-property correlation for this family of materials.

3.2.2 Bpa-based materials

Layering of a $K_2[Ag(CN)_2]$ solution with a $Fe(BF_4)_2{\cdot}6H_2O$ and a **bpa** ligand solution, led to the formation of the doubly interpenetrated 2D compound $\{Fe(bpa)[Ag(CN)_2]_2[Ag(CN)]\}$ (**BPA-1**) (**Figure 54**). The framework crystallises in the monoclinic space group *C2/c* and is in the HS state at 290 K (V_{coord} = 14.02(3) Å^3). The unit cell of the framework was measured every 20 K upon cooling until reaching the temperature of 80 K, but no change in the cell parameters or in the colour of the yellow crystal was observed, suggesting that the compound is in the HS state within this temperature range.

From **Figure 54a** it can be seen that the flexible **bpa** ligand assumes a bent conformation in **BPA-1**, bridging between two adjacent Fe(II) ions of the same 2D network, rather than following the coordination motif seen in the typical Hofmann-type compounds where the ligand bridges between 2D adjacent layers. As already mentioned in section **3.1.3.2**, the bent coordination conformation for the **bpa** ligand has already been seen in the literature in the structure of the polyrotaxane **bpaAu**. However, the unusual structural motif that can be seen in **BPA-1** further supports the idea that a ligand that is more flexible and has more rotational freedom renders the structure of the final material less predictable compared to when a more typical rigid bridging ligand is used. In the structure of compound **BPA-1**, each Fe(II) ion has hence two coplanar coordination sites occupied by different **bpa** ligands, while other two are occupied by the $[Ag(CN)_2]^-$ ion that bridges consecutive Fe(II) centres, and the last two by the [Ag(CN)] fragment, forming a 2D network seen in **Figure 54b**. The distinct, consecutive 2D networks are independent from the others and they interpenetrate in the supramolecular packing, forming the motif reported in **Figure 54c** which is significantly different compared to the structure of a Hofmann-clathrate.

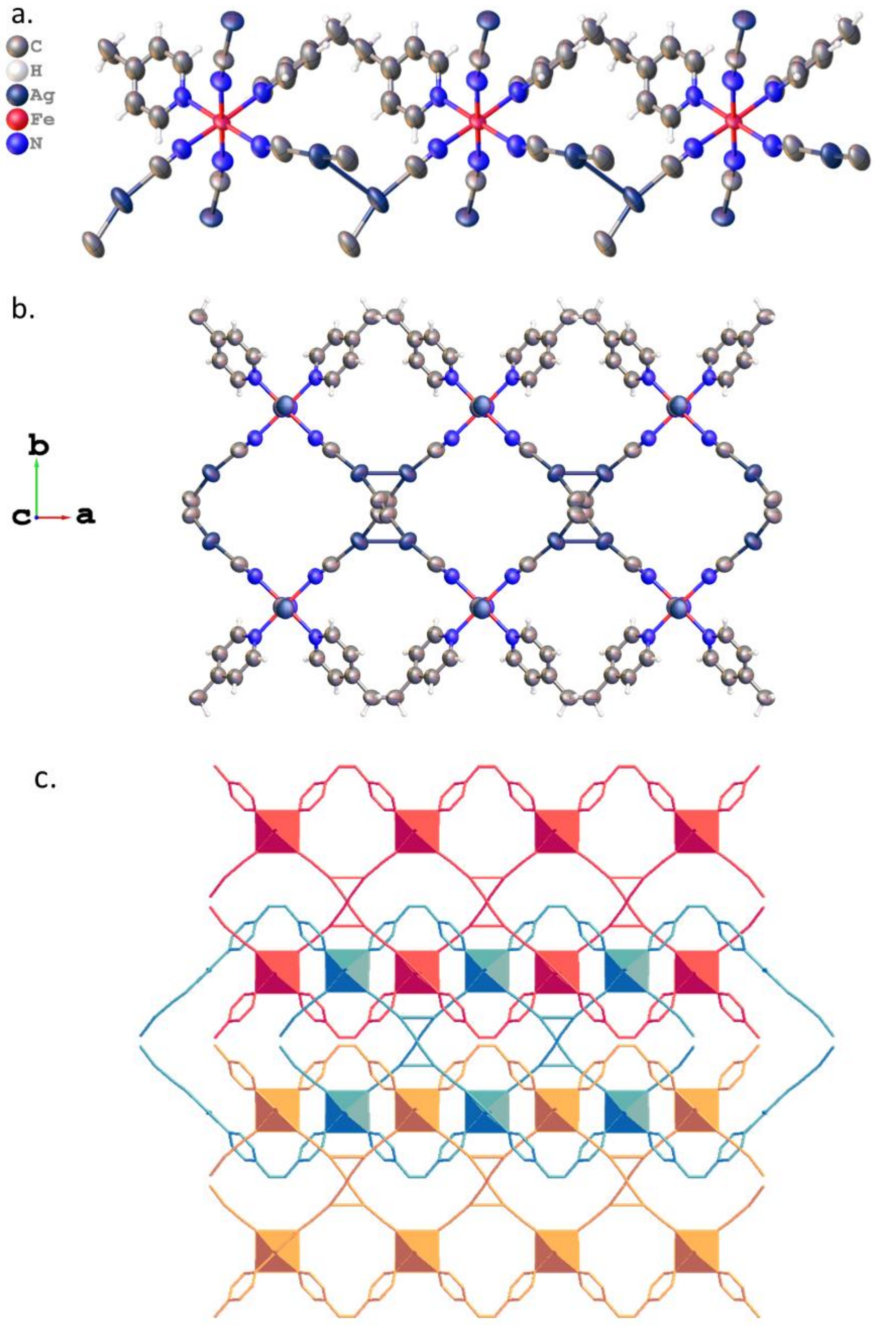

Figure 54: **a.** Fragment of the structure of **BPA-1** at 290 K. Atomic displacement parameters are drawn at 50 % probability; **b.** Supramolecular packing seen from the [001] plane showing a single 2D network, which extends infinitely in the *a* direction; **c.** Supramolecular packing seen from the [001] plane. Independent 3D networks of **BPA-1** are highlighted in red, blue and orange to simplify the visualisation and the structure has been drawn isotropically for clarity.

The bridging **bpa** ligand was disordered in the structure herein reported. The whole ligand was hence split over two positions (**Figure 55**), with the two components having a total occupancy of 1. Each of the parts was then freely refined, leading to a percentage of occupancy for the two components of 56.4(13) % and 43.6(13) %, which means that the electron density of the ligand is almost split equally between the two components.

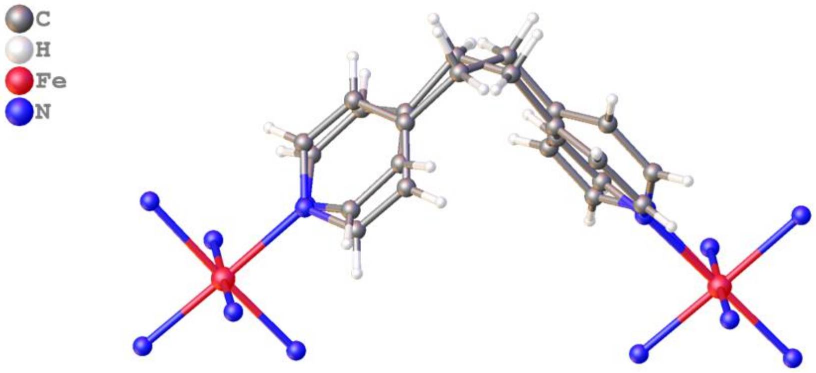

Figure 55: Fragment of the structure of **BPA-1** showing the disordered **bpa** ligand split into the two components. The structure has been drawn isotropically for clarity.

The voids that are generated from the use of the $[Ag(CN)_2]^-$ group allowed once again to form a doubly interpenetrated structure. Additionally, argentophilic interactions that contribute to the stability of the structure are present between adjacent [Ag(CN)] fragments within the same 2D network, with a Ag···Ag distance that was measured to be 3.273(3) Å.

3.2.3 (Azo-bpa)-based materials

The layering crystallization performed using $K[Ag(CN)_2]$, $Fe(BF_4)_2·6H_2O$ and a solution containing both the **azo** and **bpa** ligands in a 1:1 ratio, led to the formation of the doubly interpenetrated 3D Hofmann-clathrate $\{Fe(bpa)[Ag(CN)_2]_2[AgCN]_3\}$ (**BPA-2**). The compound crystallises in the orthorhombic *Pbca* space group, and the V_{coord} values for the two Fe-L_6 octahedra of 10.20(6) Å^3 and 10.41(7) Å^3 suggest that it is in the low spin state at 200 K. The structure of the 3D network consists of parallel 2D layers of $\{Fe[Ag(CN)_2]_2\}$ that are connected through the bridging **bpa** ligand, which coordinates two Fe(II) centres of adjacent layers forming the classical Hofmann-type motif (**Figure 56a**). The coordination motif in **BPA-2** is in fact remarkably different compared to the one in **BPA-1**, where the **bpa** ligand is bent, or the one in **AZO-1**, where the linear ligand bridges a Fe(II) and a Ag(I) ion of adjacent layers.

Two crystallographically distinct **bpa** ligands are present in the structure, coordinating to the metal centres with two different geometries: in one ligand, the rotational angle between the two rigid pyridyl rings is 89.22(3)°, meaning that they are almost perpendicular one to the other; the second half of the other ligand is instead generated by symmetry and hence the two pyridyl rings are fully planar. The voids generated from the four Fe(II) centres, the four bridging **bpa** ligands and the eight $[Ag(CN)_2]^-$ fragments that can be seen in **Figure 57a**, allow to accommodate a second, independent equivalent network and hence interpenetration to occur (**Figure 57b**). It is important to point out that the **azo** ligand is not present in the structure of the framework **BPA-2**, despite the fact that it was included in the synthesis. Finally, chains of [Ag(CN)] develop along the *b* axis, as can be seen from the view of the [010] plane in **Figure 56b**, stabilised by argentophilic interactions with the framework of the clathrate.

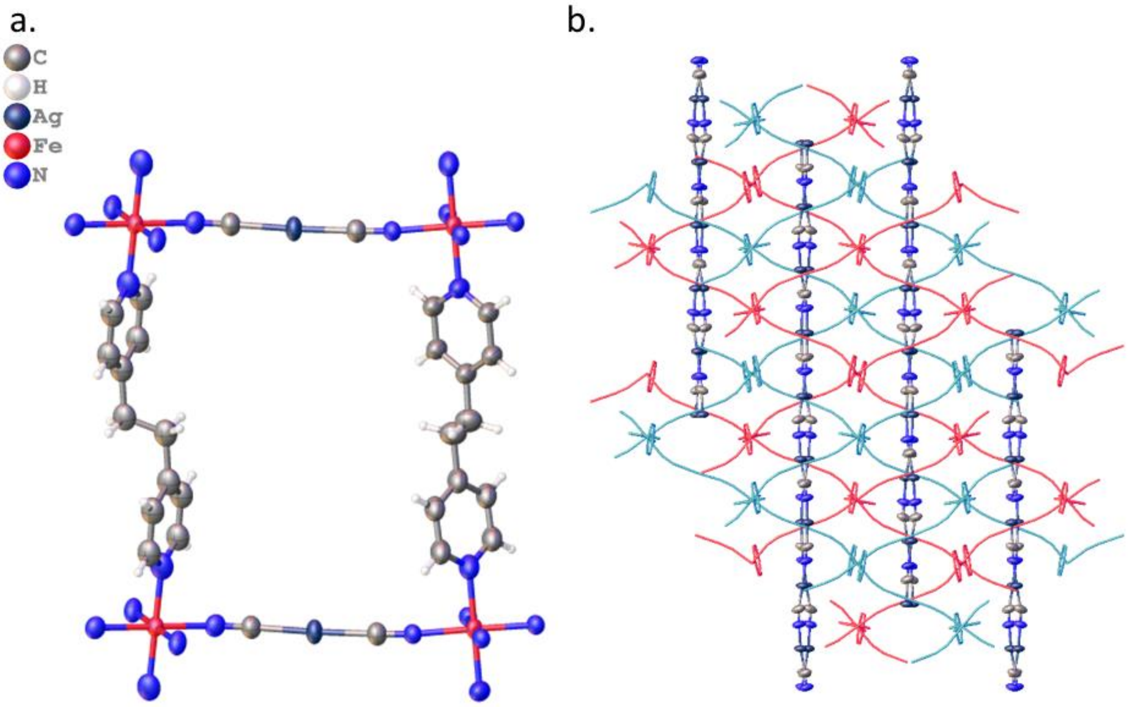

Figure 56: **a.** Fragment of the structure of **BPA-2** at 200 K. Atomic displacement parameters are drawn at 50 % probability; **b.** Supramolecular packing seen from the [010] plane. Independent 3D networks of **BPA-2** are highlighted in red and blue to simplify the visualisation.

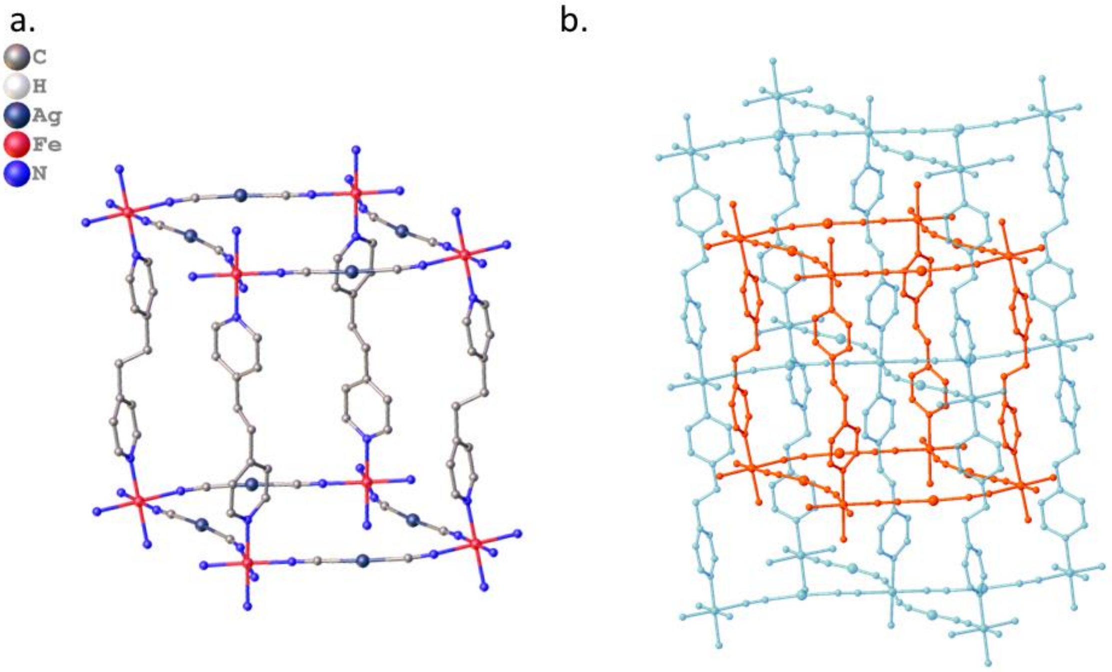

Figure 57: **a.** Fragment of the structure of **BPA-2** at 200 K showing a void generated from four Fe(II) ions, four bridging bpa ligands and the eight [Ag(CN)$_2$]$^-$; **b.** Two independent, interpenetrated 3D networks of **BPA-2** that have been highlighted in different colours (red and light blue) to simplify the visualisation. The structure has been drawn isotropically for clarity.

The presence of the **bpa** ligand in the framework, rather than **azo** was confirmed by inspection of the bond distances of the atoms in between the two pyridyl rings of the ligand, called $d_{x\text{-}x}$. The values of $d_{x\text{-}x}$ = 1.41(5) Å and $d_{x\text{-}x}$ = 1.40(7) Å were measured from the SCXRD data of **BPA-2**. An investigation of the distribution of the C-C and N=N bond distances of all the structures deposited in the CSD with **bpa** and **azo** ligands was then carried out. From these crystallographic data it was possible to obtain a range of bond distances that the carbon atoms of **bpa** ($d_{C\text{-}C}$) and the nitrogen atoms of **azo** ($d_{N=N}$) have within the crystal structures: these ranges are approximately 1.34 Å < $d_{C\text{-}C}$ < 1.61 Å for the C-C distances, and 1.16 Å < $d_{N=N}$ < 1.26 Å for the N=N distances (**Figure 58**). As expected, the N=N distances are significantly smaller as a consequence of the presence of a double bond in **azo** (N=N) rather than the single bond in **bpa** (C-C). The distinctly different values here reported allowed to establish that the $d_{x\text{-}x}$ obtained experimentally are within the range of the C-C bond length, confirming the presence of **bpa** in the framework. It is important to point out that the evaluation of the $d_{x\text{-}x}$ distances from the crystal structure is the only way to reliably state whether the ligand present in the network is **bpa** or **azo**. The location of the protons that should be present in the alkyl fragment of **bpa** is not obvious when heavy elements like Ag(I) and Fe(II) are present in a crystal structure. This parameter cannot hence be used to understand which ligand builds the framework. Additionally, a second investigation of all the deposited structures present in the CSD with **bpa** and **azo** ligands was carried out focusing on the geometry of the ligands to try to use this as a parameter for their differentiation. However, most of these structures show a rotational angle between the two rigid pyridyl rings of the ligand that is within the 0-5° range both for the structures with **bpa** and with **azo**, suggesting that in most of the cases both the ligands will present planarity between the two rings (**Figure 59**). While deviations from planarity are more common for the **bpa** ligand as would be expected, it is not sufficient to draw conclusions as to the identity of the ligand in **BPA-2** using this geometrical information alone.

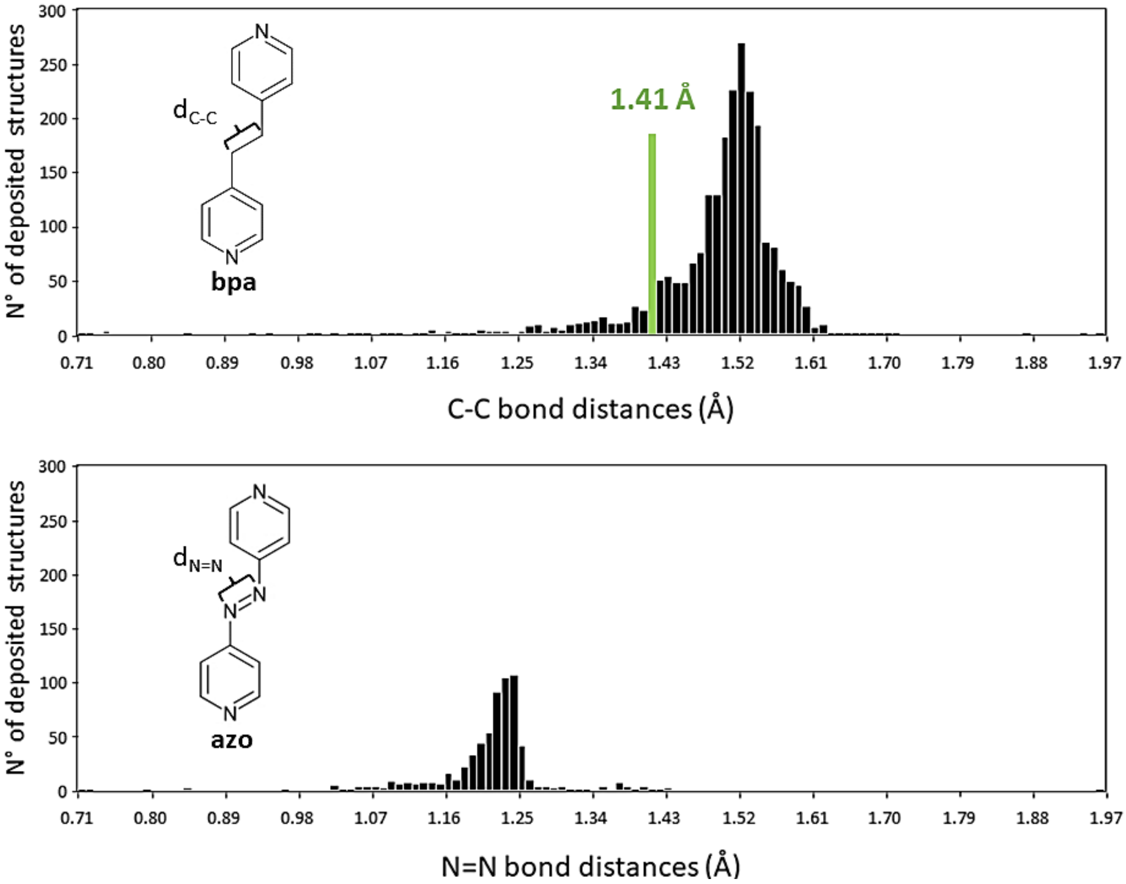

Figure 58: C-C and N=N bond distance distributions for the deposited structures involving **bpa** (top) and **azo** (bottom) ligands and structures of the two ligands involved in this synthesis that highlights the investigated distances: d_{C-C} for **bpa** and $d_{N=N}$ for **azo**.

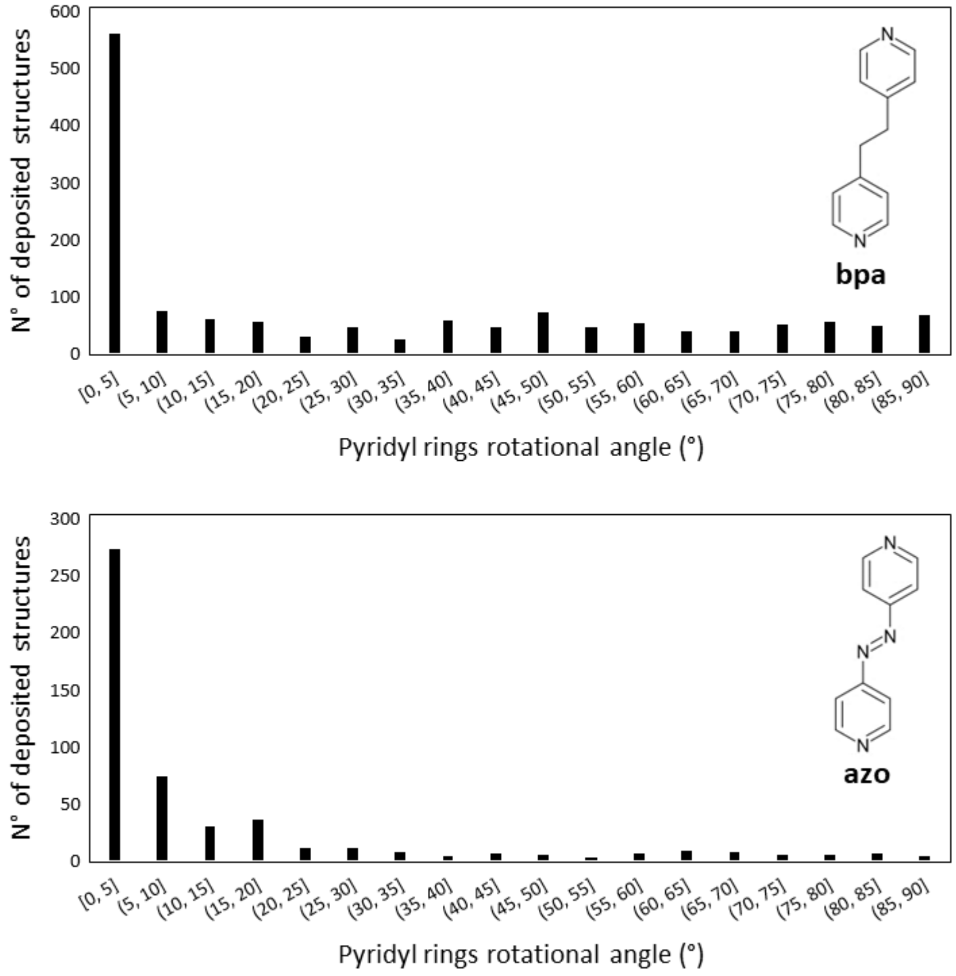

Figure 59: Distribution of the values for the rotational angle between the pyridyl rings for the structures deposited involving **bpa** (top) and **azo** (bottom) ligands with the corresponding structures of the ligands.

As already mentioned above, the evaluation of the $d_{x\text{-}x}$ distances obtained from the crystallographic data was used to establish that the ligand that is present in the network is the **bpa** ligand. The **azo** ligand is hence not observed in the final framework, raising the hypothesis that it might act as a modulator or template. As seen in structure **AZO-1**, the **azo** ligand acts as a bridging bidentate ligand that coordinates to the metal centres with a linear conformation. As a consequence, it is possible that the presence of the linear **azo** ligand in solution during the self-assembly acted as a template, leading to a structure in which the **bpa** ligand is linear, favouring the formation of the network **BPA-2**, rather than network **BPA-1** where the ligand is bent.

In the attempt to analyse the SCO properties of compound **BPA-2**, a variable temperature measurement was set up upon heating from the temperature of 200 K, as the compound was in the LS state at that temperature. The crystal quality decreased over the time, rendering it necessary to reattempt the measurement on a different crystal. A second data collection was performed at 290 K, showing that at that temperature the compound **BPA-2**$_{\mathbf{290\ K}}$ is in the HS state, with a V_{coord} value for the Fe-L_6 octahedron of 13.39(4) Å^3. **BPA-2**$_{\mathbf{290\ K}}$ is isostructural with **BPA-2** and it is in the same orthorhombic *Pbca* space group that hence does not change within the 200-290 K temperature range where the spin transition occurs. As it can be seen in **Figure 60**, the pyridyl rings of the **bpa** ligands are severely disordered and were split over two positions. Additionally, in order to be able to model the ligand, the AFIX constraint had to be applied to render each pyridyl ring planar and the anisotropic displacement parameters of the ligand were set to be equivalent. Upon removal of the AFIX constraints, no stable structural model for the ligand was obtained. Due to the severe disorder of the structure, the $d_{x\text{-}x}$ distances were not considered in that specific case because the value would be strongly affected by the constraints that were applied to refine the structure. Moreover, the ring rotation could be the responsible for the SCO behaviour that was seen: the structure at 200 K did not show the same degree of disorder, raising the hypothesis that while cooling down from 290 K to 200 K, the ring rotation could be locked in one specific orientation and consequently allow the SCO to occur; conversely a second hypothesis could be that the SCO is instead the cause of the stabilization of the ligand to a specific conformation.[17]

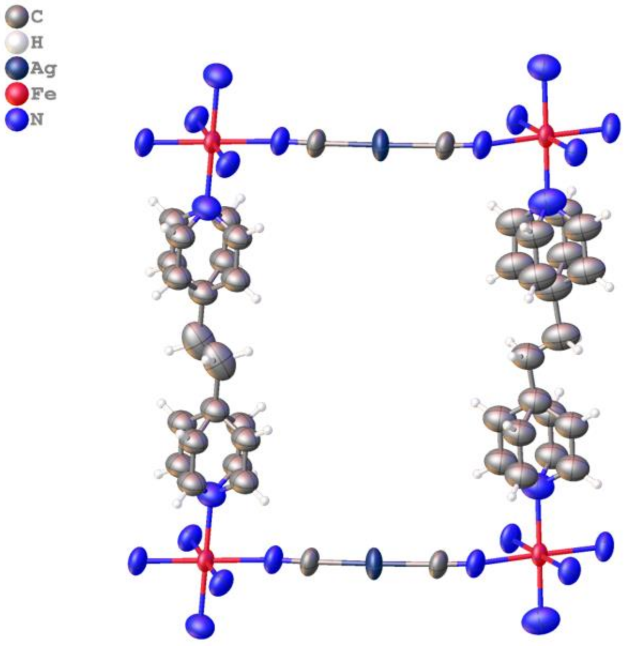

Figure 60: Fragment of the structure of **BPA-2$_{290\,K}$** at 290 K. Atomic displacement parameters are drawn at 50 % probability;

Unfortunately, due to the poor quality of the diffraction from crystals of compound **BPA-2**, that was most likely affected from the disorder present in the structure, and due to the long exposure times needed to obtain a good data collection, the full SCO curve in this case was not obtained. Additionally, another compound was also obtained from a batch that was set up with similar conditions, raising the hypothesis that more than one species could be forming by the self-assembly of the used building blocks. Compound [Fe(bpa)(Ag(CN)$_2$)$_2$·MeOH] (**BPA-3**) was in fact synthesised from the same mixed ligand layering crystallisation performed for compound **BPA-2** with a slight excess of **bpa**, where a 0.6:0.4 **bpa**:**azo** ratio for the two ligands was used instead of the 0.5:0.5 **bpa**:**azo** where **BPA-2** was obtained from. The compound crystallises in the triclinic *P-1* space group and presents a V$_{coord}$ value for the Fe-L$_6$ octahedron of 13.621(10) Å^3 confirming that it is in the HS state at 290 K. This result was expected as **BPA-3** is isostructural with the compound **bpaAu** that is already reported in the literature and was introduced in section **3.1.3.2**, which stays in the HS state within the 50-290 K range of temperature analysed.[14] The structure of the 2D polyrotaxane **BPA-3** presents a bent **bpa** ligand bridging two adjacent Fe(II) ions, with other three coordination sites of the metal occupied by the [Ag(CN)$_2$]$^-$ fragment and the last one occupied by the oxygen atom of a methanol molecule (**Figure 61a**). The 2D coordination polymer that forms and that can be seen in **Figure 61b** is then interpenetrated to a second equivalent and independent network *via* a polyrotaxane motif: the $Fe_2(bpe)_2$ rings of a 2D network interpenetrate with the $[Ag(CN)_2]^-$ fragments of a second independent 2D sheets stabilised by argentophilic interactions, forming a doubly interpenetrated polyrotaxane structure (**Figure 61c**).

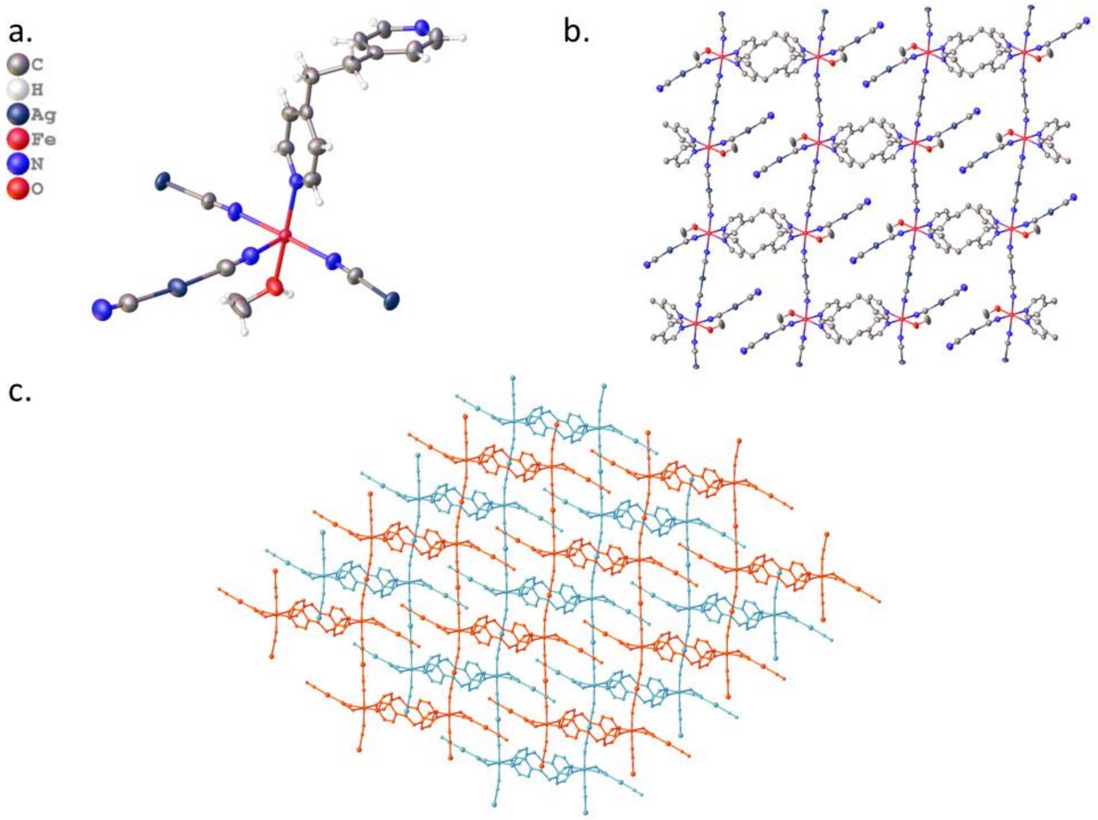

Figure 61: **a.** Asymmetric unit for compound **BPA-3**; **b.** Supramolecular packing for **BPA-3** showing a single 2D network; **c.** Supramolecular packing for **BPA-3** showing the interpenetration that occurs in the structure that forms a polyrotaxane motif.

It should be pointed out that the latter structure reported above represents an example of a limitation of the characterization technique used in this work. The fact that the structure of **BPA-3** was obtained from similar conditions to the ones of **BPA-2** does not necessarily mean that **BPA-2** did not form, but that the crystal selected for the single-crystal experiment has the structure of **BPA-3**. Similarly, when the mixed-ligand reaction was set up with the ligands **bpe** and **bpa**, most of the crystals analysed were the ones of the network **bpeAg**. Once again, this only means that the reaction yielded primarily to compound **bpeAg**, but does not exclude the fact that other crystal might have formed and might present a different structure. Unfortunately, a full structural analysis *via* PXRD was not possible due to the instability of the crystals when outside the solution.

3.3 Experimental

3.3.1 Materials

The chemicals $Fe(BF_4)_2\cdot6H_2O$, $K[Ag(CN)_2]$, the **azo** ligand, the **bpa** ligand and MeOH were obtained commercially (Sigma-Aldrich, Fisher Chemical and Alfa Aesar) and used as received.

3.3.2 Synthesis of compound AZO-1

A solution of $Fe(BF_4)_2\cdot6H_2O$ (30.4 mg, 0.09 mmol) in MeOH (1 mL) was added to a solution of the **azo** ligand (16.6 mg, 0.09 mmol) dissolved in MeOH (2 mL). A solution of $K[Ag(CN)_2]$ (35.8 mg, 0.18 mmol) in H_2O (1 mL) was placed at the bottom of a sample vial and layered with the solution of the Fe(II) salt and ligand described above. A buffer solution containing a 1:1 ratio of MeOH/H_2O (4 mL) was placed between the two layers. The vial was sealed and after a few days, dark blue block crystals of **AZO-1** suitable for X-ray diffraction analysis formed on the walls of the vial.

3.3.3 Synthesis of compound BPA-1

A solution of $Fe(BF_4)_2\cdot6H_2O$ (30.4 mg, 0.09 mmol) in MeOH (1 mL) was added to a solution of the **bpa** ligand (16.6 mg, 0.09 mmol) dissolved in MeOH (2 mL). A solution of $K[Ag(CN)_2]$ (35.8 mg, 0.18 mmol) in H_2O (1 mL) was placed at the bottom of a sample vial and layered with the solution of the Fe(II) salt and ligand described above. A buffer solution containing a 1:1 ratio of MeOH/H_2O (4 mL) was placed between the two layers. The vial was sealed and after a few days, light yellow plate crystals of **BPA-1** suitable for X-ray diffraction analysis formed on the walls of the vial.

3.3.4 Synthesis of compound BPA-2

A solution of $Fe(BF_4)_2\cdot6H_2O$ (30.4 mg, 0.09 mmol) in MeOH (1 mL) was added to a solution containing the **azo** ligand (8.3 mg, 0.045 mmol) and the **bpa** ligand (8.3 mg, 0.045 mmol) dissolved in MeOH (2 mL). A solution of $K[Ag(CN)_2]$ (35.8 mg, 0.18 mmol) in H_2O (1 mL) was placed at the bottom of a sample vial and layered with the solution of the Fe(II) salt and ligand described above. A buffer solution containing a 1:1 ratio of

$MeOH/H_2O$ (4 mL) was placed between the two layers. The vial was sealed and after a few days, light yellow plate crystals of **BPA-2** suitable for X-ray diffraction analysis formed on the walls of the vial.

3.3.5 Synthesis of compound BPA-3

A solution of $Fe(BF_4)_2{\cdot}6H_2O$ (30.4 mg, 0.09 mmol) in MeOH (1 mL) was added to a solution containing the **azo** ligand (6.63 mg, 0.036 mmol) and the **bpa** ligand (9.95 mg, 0.054 mmol) dissolved in MeOH (2 mL). A solution of $K[Ag(CN)_2]$ (35.8 mg, 0.18 mmol) in H_2O (1 mL) was placed at the bottom of a sample vial and layered with the solution of the Fe(II) salt and ligand described above. A buffer solution containing a 1:1 ratio of $MeOH/H_2O$ (4 mL) was placed between the two layers. The vial was sealed and after a few days, light yellow, iridescent plate crystals of **BPA-3** suitable for X-ray diffraction analysis formed on the walls of the vial.

3.4 Conclusions

This chapter presented the structural investigation of a new series of materials constructed with the organic ligands **azo** and **bpa**. Three new compounds were synthesised *via* the layering technique, one of which was derived from a mixed ligand crystallization, and their structural characterization was performed with SCXRD analysis.

The two ligands used in this work present a small structural difference that has however a huge influence in the structure of the final material: the spacer between the two pyridyl rings that are present in both the ligands is composed of the rigid N=N group in **azo** and of the flexible CH_2-CH_2 group in **bpa**. As a consequence, the rigid spacer of **azo** renders it a linear ligand, while the flexibility of the alkyl group in **bpa** allows it to assume either a linear or a bent conformation. The presence in the literature of structural data from crystalline powders of Hofmann-type compounds involving the $[M^{II}(CN)_4]^{2-}$ fragment and the ligand **azo** or **bpa**, added to the structural data from single crystal of the same family of materials constructed with **azo** or **bpa** derivatives, raised our interest to expand the structural investigation to analogous materials constructed with the $[M^{I}(CN)_2]^{-}$ group and to study their SCO behaviours.

Compound **AZO-1** is obtained when only the **azo** ligand is involved in the synthesis and presents the structure of a Hofmann-type network, with the only variation that sees the linear **azo** ligand bridging to a Fe(II) and a Ag(I) ion rather than to two Fe(II) ions. When only the **bpa** ligand is involved in the synthesis, the doubly interpenetrated 2D network **BPA-1** is obtained, where the **bpa** ligand assumes a bent conformation. The synthesis performed when both the **azo** and the **bpa** ligands are present in solution leads instead to the Hofmann-type framework **BPA-2** where only the **bpa** ligand is seen in the crystal structure and it assumes a linear conformation. These structural results allowed to raise the hypothesis that even if the **azo** ligand is not seen in the final structure, it might have a fundamental role in the growth of the network acting as a template. The **bpa** ligand could in fact assume either the linear or the bent conformation when forming compound **BPA-2**, but the fact that **azo** is present in solution during the self-assembly of the building blocks might have formed a template structure for the **bpa** ligand to be linear rather than bent. It seems, however, that structural control is less easy and predictable when flexible building blocks are involved, as seen for **BPA-3**, which shows a polyrotaxane motif that was not expected when the synthesis of these Hofmann-like networks was designed.

In regards to the SCO properties, the only compound that showed a SCO behaviour is **BPA-2**, which exhibited a spin transition within the 200-290 K temperature range. The compound is in the LS state at 200 K and in the HS state at 290 K. The structure of **BPA-2$_{290\ K}$** collected at the temperature of 290 K clearly shows a severe disordered ligand which might be the responsible for the poor quality of the crystals. Heavy restraints were in fact necessary in order to be able to obtain a structural model at that temperature, while no disorder was found in the structure at 200 K. This observation made us raise the hypothesis that the pyridyl rings rotation in **bpa** might be related to the SCO properties reported.

In conclusion, three new compounds were synthesised in this chapter and their structures were characterised *via* SCXRD. Interesting observations were found when comparing the synthesis with only the **bpa** ligand and the one with both **azo** and **bpa** ligand, suggesting that the secondary ligand that does not take part in the synthesis might still play an important role in the structural growth, acting as a template. To date, the vast majority of the structures of Hofmann-type compounds that are reported in the literature involve a rigid ligand rather than a flexible one like **bpa**, aspect that is most likely related to the difficulty in obtaining the designed structure when more coordination conformations are available. The results presented in this chapter represent a potential powerful tool to control the topology of the final material during the self-assembly process by using a template. This approach might overcome the problems related to flexibility of the building blocks, providing a design strategy that can potentially open up to the incorporation of a wider number of flexible ligands that could not be used before. Additionally, this work showed how the use of a template allowed to go from a structure involving the flexible **bpa** ligand that did not show any SCO behaviour, **BPA-1**, to a structure with the same ligand that exhibited a spin transition within the 200-290 K temperature range, **BPA-2**, supporting the fact that this method could be used to tune the SCO properties of a material.

Even if more work still needs to be done, the results herein reported are a fundamental achievement that potentially further extends the family of Hofmann-type compounds constructed with the $[M^{I}(CN)_2]^-$ group to other unexplored flexible ligands. Finally, the ability to impart a structural control through the use of a template that has been presented above represents a powerful tool that can allow novel SCO-active materials to be obtained.

3.5 References

1 T. Tsuruoka, S. Furukawa, Y. Takashima, K. Yoshida, S. Isoda and S. Kitagawa, *Angew. Chemie - Int. Ed.*, 2009, **48**, 4739–4743.

2 D. Jiang, C. Huang, J. Zhu, P. Wang, Z. Liu and D. Fang, *Coord. Chem. Rev.*, 2021, **444**, 214064.

3 M. H. Pham, G. T. Vuong, F. G. Fontaine and T. O. Do, *Cryst. Growth Des.*, 2012, **12**, 3091–3095.

4 X. Guo, S. Geng, M. Zhuo, Y. Chen, M. J. Zaworotko, P. Cheng and Z. Zhang, *Coord. Chem. Rev.*, 2019, 391, 44–68.

5 M. Ohba, K. Yoneda, G. Agusti, M. C. Muñoz, A. B. Gaspar, J. A. Real, M. Yamasaki, H. Ando, Y. Nakao, S. Sakaki and S. Kitagawa, *Angew. Chemie - Int. Ed.*, 2009, **48**, 4767–4771.

6 Z. Zhuang, J. Cheng, X. Wang, Y. Yin, G. Chen, B. Zhao, H. Zhang and G. Zhang, *J. Mol. Struct.*, 2006, **794**, 77–82.

7 M. D. Ward, *Chem. Soc. Rev.*, 1995, 24, 121–134.

8 A. Modrow, D. Zargarani, R. Herges and N. Stock, *Dalt. Trans.*, 2011, **40**, 4217–4222.

9 G. Agustí, S. Cobo, A. B. Gaspar, G. Molnár, N. O. Moussa, P. Á. Szilágyi, V. Pálfi, C. Vieu, M. Carmen Muñoz, J. A. Real and A. Bousseksou, *Chem. Mater.*, 2008, **20**, 6721–6732.

10 F. Ragon, K. Yaksi, N. F. Sciortino, G. Chastanet, J. F. Létard, D. M. D'Alessandro, C. J. Kepert and S. M. Neville, *Aust. J. Chem.*, 2014, **67**, 1563–1573.

11 T. Morita, Y. Asada, T. Okuda and S. Nakashima, *Bull. Chem. Soc. Jpn.*, 2006, **79**, 738–744.

12 R. Ohtani, M. Arai, A. Hori, M. Takata, S. Kitao, M. Seto, S. Kitagawa and M. Ohba, *J. Inorg. Organomet. Polym. Mater.*, 2013, **23**, 104–110.

13 Y. Li, Q. R. Kong, Y. Guo and Z. Tang, *Dalt. Trans.*, 2021, **50**, 1384–1389.

14 H. Xu, G. Juhász, K. Yoshizawa, M. Takahashi, S. Kanegawa and O. Sato, *CrystEngComm*, 2010, **12**, 4031–4034.

15 N. F. Sciortino, K. R. Scherl-Gruenwald, G. Chastanet, G. J. Halder, K. W. Chapman, J. F. Létard and C. J. Kepert, *Angew. Chemie - Int. Ed.*, 2012, **51**, 10154–10158.

16 V. Niel, M. C. Muñoz, A. B. Gaspar, A. Galet, G. Levchenko and J. A. Real, *Chem. Eur. J.*, 2002, **8**, 2446–2453.

17 J. A. Rodríguez-Velamazán, M. A. González, J. A. Real, M. Castro, M. C. Muñoz, A. B. Gaspar, R. Ohtani, M. Ohba, K. Yoneda, Y. Hijikata, N. Yanai, M. Mizuno, H. Ando and S. Kitagawa, *J. Am. Chem. Soc.*, 2012, **134**, 5083–5089.

Chapter 4: The crystalline sponge method as a tool to analyse photo-switchable materials

4.1 Introduction

4.1.1 The origins of the crystalline sponge method

The use of advanced methods to perform a structural characterization of a newly-synthesised compound is essential to obtain reliable information on its structure. Nowadays there are numerous techniques that are commonly used for daily structural analysis: nuclear magnetic spectroscopy (NMR), mass spectrometry (MS) and infrared spectroscopy (IR) allow scientists to obtain the molecular formulas of the analysed molecule, along with the functional groups and bond connectivity within it.[1] However, single-crystal X-ray diffraction (SCXRD) is the only routine method that can give direct and unique structural information at the atomic level, such as the types and the arrangements of atoms, molecules, or ions within a crystal, the bond lengths and angles, and the packing interactions.[2] This powerful characterization technique has on the other hand the intrinsic limitation of needing the sample to be a crystal, resulting in it being impossible for powders, liquids, oils or volatile compounds. Growing crystals is not always possible as the quantity of analyte available may not be enough – at least one milligram is necessary – or simply because the sample is difficult to crystallize.[3] A technique that can circumvent this problem has been reported by Prof. M. Fujita and co-workers in 2013,[4] and named only later as "the crystalline sponge method".[5]

Crystalline sponges are porous metal complexes that exists in the crystalline form and that are able to absorb and orient an analyte – in solution or gaseous state – into their pores in specific and ordered positions, making it observable by conventional SCXRD analysis.[6] The idea behind the crystalline sponges is based on the concept that hollow structures can act as crystalline flasks that can trap and align molecules into their cavities by exploiting the high degree of molecular recognition that the framework can have.[7] Each flask represents in that way a confined space where molecules can accommodate, or reactants can potentially allow solution-state reactions to be transferred into crystalline state *via* a single-crystal-to-single-crystal modification (**Figure 62**).[7]

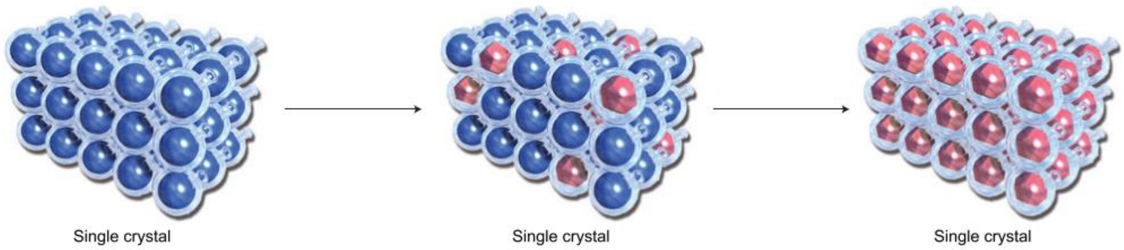

Figure 62: a crystalline sponge seen as a single crystal made of an ordered array of flasks. The change of colour of the flask from blue to pink indicates that its confined space has been modified for example by accommodating a molecule inside the pores, but the crystallinity of the framework has been maintained. Reprinted with permission.[7]

The original method has been matter of controversies for the poor data quality of the trapped guest,[8] and additional optimizations have been necessary to develop a reliable protocol suitable for a wider range of molecules.[6] Even if there still isn't a unique protocol that is valid for every compound, scientists have nowadays reached a deep understanding of this method at the point that it is used not only to determine the structure of new compounds, but also to observe transient intermediates, to visualize chemical reactions and to study the binding sites of host-guest interactions.[1]

The crystalline sponge method has some important and fascinating advantages, but it presents also some weaknesses. One of its most positive aspects is the fact that it gives structural information of analytes that are inaccessible to crystallographic methods, such as liquids or gases. Interestingly, some volatile compounds that have been recently structurally characterised using this process are the molecules that are responsible for the fragrance of fresh wasabi, dishwashing detergents, fresh garlic, cypress essential oil and peppermint oil.[9] Another important advantage of the method is the small quantity of analyte that is required to be able to analyse it: an amount of guest that is on the nano-to-microgram order is in fact sufficient for the soaking process to occur, allowing this technique to be used for valuable and low available compounds.[6]

On the other hand, it is important to note that the crystalline sponges have some important practical and experimental limitations. The host structure presents, in fact, large pores that can reach the size of 5 × 8 Å, making the refinement of the framework often not straightforward, and sometimes requiring the use of restraints and constraints to be able to model the guest.[6] In addition to this, the data quality depends on all the steps of the method, which includes the sponge synthesis, the solvent exchange, the guest soaking, the data collection and the data refinement: each step must be deeply analysed and adjusted according to the nature of the sample and based on the types of information it is intended to achieve.

4.1.2 Steps of the method

The first step of the method is the sponge synthesis. Nowadays the MOF that is most commonly used as crystalline sponge is compound $[(ZnI_2)_3(tpt)_2 \cdot x(G)]_n$ (**tptZn·*x*G**), where **tpt** = 1,3,5-tris(4-pyridyl)triazine and G represents the guest or solvent molecules. The conventional synthesis of the framework consists of the diffusion of a ZnI_2 solution in MeOH into a **tpt** ligand solution in $PhNO_2$/MeOH (*v/v* = 4/1) at room temperature.[10] This method however takes a significant amount of time: the crystals need 7 days to grow and another 7 days are required for the solvent to be exchanged. The solvent exchange is in fact the second step of the method and it is fundamental to replace the solvent nitrobenzene, which fills the pores of the as-synthesised sponge, with a solvent that can easily be exchanged with the guest of interest. Nitrobenzene is in fact a good guest for the framework as it has high affinity to the pores, and for this reason it has to be replaced with a non-interactive solvent before being able to perform the guest-inclusion. Cyclohexane is typically used as a non-interacting solvent, while pentane is used when the soaking process is performed at low temperatures.[6] To avoid the solvent exchange step and reduce the synthetic times, Clardy and co-workers reported a synthesis of the sponge deriving from layering a methanolic solution of ZnI_2 into a $CHCl_3$ solution of the **tpt** ligand, which allows crystals of the sponge to be obtained in only 3 days.[11]

The guest soaking step is the third step of the method and is the most crucial one that determines whether the method works or not, or whether the data quality is good or bad. The single-crystal-to-single-crystal solvent exchange is the most common guest soaking method and consists in dipping the MOFs crystals into the target solution containing the guest of interest.[6] The guest then exchanges with the solvent molecules present within the pores and occupies the cavities of the sponge. This is an easy method to perform the analyte inclusion, but it requires a large amount of the target compound to be available.[6] A soaking method that can be used when instead a small amount of target analyte is available or when the target is valuable is the a-grain-of-crystal method, which consists in adding a few mg of liquid target to one grain of the MOF.[6] Finally, the slow evaporation as soaking method consists in using a vial equipped with a needle where the diluted solution of the target guest is added along with one MOF crystal.[6] The slow evaporation of the solvent favour the gradual concentration of the guest in solution, reaching the point of saturation that forces the guest to diffuse inside the sponge.[6] This soaking method allows also the potential to explore different conditions such as temperature, analyte concentration, evaporation rate, solvents used and soaking time. A lot of aspects need to be taken into consideration when choosing the soaking conditions. For example, higher temperatures favour a faster absorption of the guest, but lower temperatures seem to lead to a more concentrated and ordered guest.[6] Additionally, while longer soaking times allow the guest site occupancy to be enhanced, but the MOF crystals can deteriorate over the time, rendering it impossible to be analysed.

The last two steps of the crystalline sponge method are the data collection and data refinement. For the data collection, attention should be given in collecting enough data and have suitable I/σ (> 10) at high-angle. This derives from the fact that in this region the reflections of light molecules like the guests are much weaker than the one of the host.[6] Additionally, as the framework itself is weakly diffracting compared to other MOFs constructed with metals because of the quantity of solvent molecules present in the pores, the Cu $K\alpha$ radiation is suggested in order to have higher I/σ.[6] Regarding the data refinement, it is suggested to start with a full refinement of the host framework, including the disorder of the flexible ZnI_2 moiety, if present.[6] The guest or solvent molecules should then appear in the difference electron density map from which the full model can be solved with the application of constraints and restraints, if necessary.[6]

4.1.3 Crystalline sponge as a confined molecular vessel for photoswitching molecules

Photoswitchable molecules are responsive materials that can reversibly undergo changes in their physical properties upon irradiation with visible light. Donor-acceptor Stenhouse adducts (DASAs) are photoswitchable molecules that switch from a conjugated, coloured and hydrophobic form to a ring-closed, colourless and zwitterionic form upon exposure to visible light.[12] Their behaviour in solution has been so far widely studied, showing that the solvent used can dramatically influence the form that is mostly present in solution. Generally, halogenated solvents stabilize in fact the open form when in visible light, while a linear to cyclic equilibrium is observed when protic solvents such as water or methanol are used.[13] However, the exact switching mechanism between the two forms is still not proven and only mechanistic hypotheses are present in the literature.[14] For this reason, structural data would help with determining the photoswitching mechanism. Unfortunately, no solid-state switching has yet been reported.

An interesting work published in 2019 reports a Pd^{II}_8 molecular vessel that is used to stabilize and store the open form of DASAs in an aqueous medium.[15] According to that work, the hydrophobic interactions present between the cavity and the coloured, open form of DASAs are the responsible for reversing the equilibrium towards the open form.[15] There are some important host-guest interactions that must be considered when looking at the crystalline sponge **tptZn·*x*G** as a confined molecular vessel. The **tpt** ligand offers flat and electron-deficient binding sites suitable for stacking with aromatic compounds and for CH-π interactions.[6] Additionally, the cavity of the crystalline sponge is hydrophobic, favouring in this way the binding of the most common organic molecules.[6] Finally, the pyridyl protons of the **tpt** ligand are hydrogen-bond donors and the iodine atoms of the ZnI_2 component are hydrogen-bond acceptors.[6]

4.1.4 Choice of the guests

As already mentioned above, DASAs are a class of visible light activated photochromes that can switch from an extended, coloured triene form to a compact, colourless cyclopentenone form when irradiated with visible light **Figure 63**.[12,14]

The structure of DASAs is composed of a donor amine moiety that is connected to an acceptor moiety, which can be either Meldrum's acid or 1,3-dimethyl barbituric acid.[14] The use of a dialkylamine as a donor forms the first generation DASAs, which present a zwitterionic closed-ring structure upon irradiation with light. The second generation of DASAs is instead characterised by the use of *N*-alkyl anilines as donors, forming a neutral closed-ring form, while the third generation presents the use of different acceptor groups.[14]

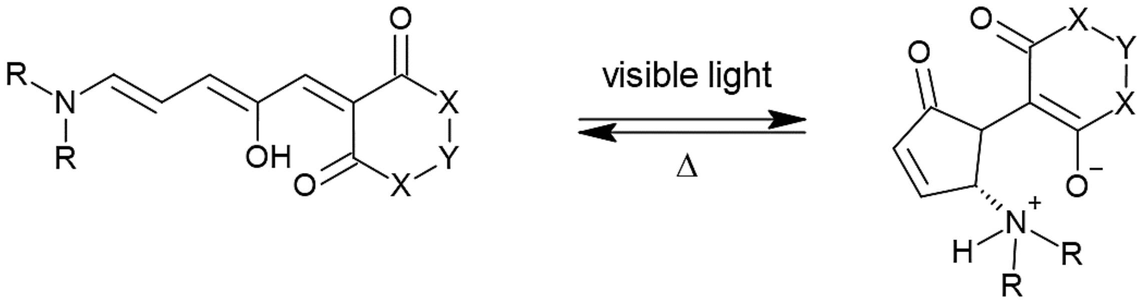

Figure 63: General representation of the photoswitching reaction of a first generation DASA. R = alkyl group; when Meldrum's acid is used as acceptor, X = $-O^{2-}$, Y = $-C(CH_3)_2$; when 1,3-dimethyl barbituric acid is used as acceptor, X = $-N(CH_3)$, Y = -C=O.

The DASAs that are used in this work are reported in **Figure 64**. With the interest of analysing how different DASAs and their different forms interact with the sponge framework, a variety of DASAs presenting diverse donors and acceptors groups, and DASAs from the first and the second generation were investigated. Interest has been given to choosing guest molecules that could potentially interact with the framework *via* hydrogen-bonding and π-stacking, making them more easily observable through SCXRD. Additionally, those interactions could potentially be essential for stabilizing preferentially one of the two forms of the DASAs molecules, either the open or the closed form: the sponge framework could act as a molecular vessel that could stabilize a form that might instead be present only as a small fraction when in solution.

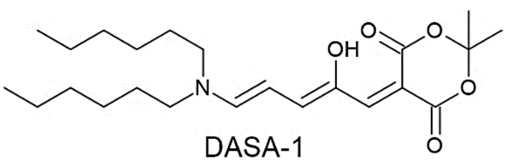
DASA-1

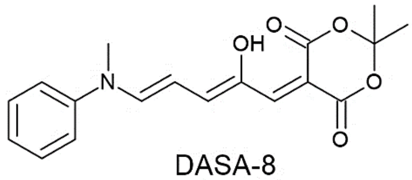
DASA-8

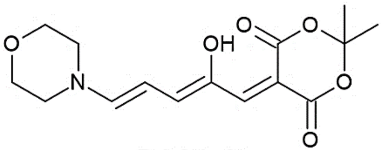
DASA-2

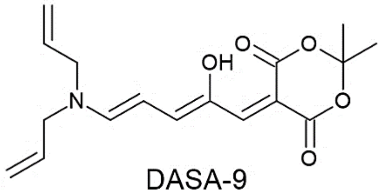
DASA-9

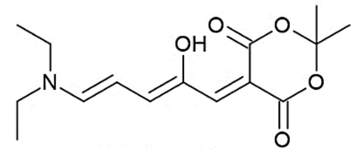
DASA-3

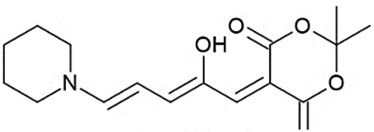
DASA-10

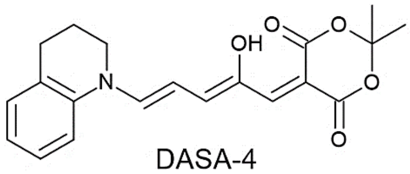
DASA-4

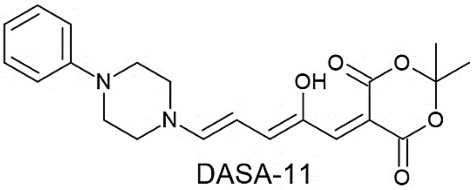
DASA-11

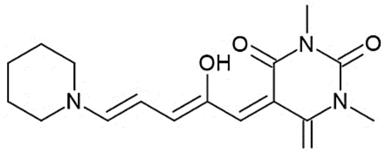
DASA-5

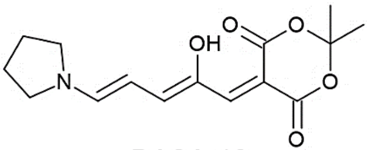
DASA-12

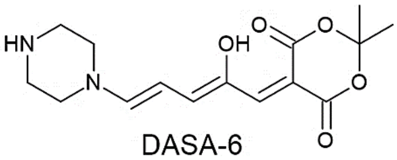
DASA-6

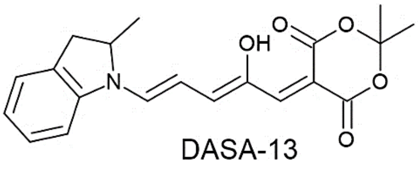
DASA-13

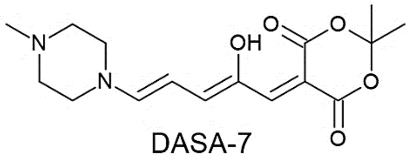
DASA-7

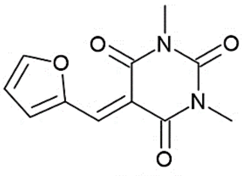
INT-1

Figure 64: Guest molecules used to perform the soaking process. DASA molecules and intermediate that have been synthesised by Sean Connolly and Tom Hitchings.

4.1.5 Aims

The crystalline sponge method is a powerful technique that can be used to obtain crystallographic data of compounds that cannot be easily characterised *via* SCXRD. The well-known Fujita's sponge **tptZn·*x*G** has already been widely used to study these molecules.

DASAs are a class of photoswitchable molecules, that switch from a conjugated, coloured form to a ring-closed, colourless structure through irradiation with visible light. So far, their behaviour in solution has been investigated thoroughly, but the solid-state photoswitching mechanism has not been reported, yet.

The aim of this chapter is to study the solid-state behaviour of the photoswitching process in DASAs by incorporating these molecules in the crystalline sponge framework as a molecular vessel. Different aspects will be exploited to favour the inclusion of the guests, such as the intermolecular interactions between the donor moiety of the DASAs and the framework sponge, or the different interactions that the conjugated, open and nonpolar form of the DASAs can induce with respect to the closed, zwitterionic and polar one. The idea is to use this method to follow *via* SCXRD the switching mechanism, using a multifunctional MOF material to study the properties of these dynamic molecules and obtaining in this way fundamental data regarding both their existing forms.

4.2 Results and discussion

4.2.1 Synthesis of the sponge framework

The synthesis of the framework has been performed following Clardy's procedure in order to reduce the time required to grow the crystals of the framework and to get rid of the solvent exchange step.[11] The layering of a methanolic solution of ZnI_2 into a $CHCl_3$ solution of the **tpt** ligand allowed crystals of the framework $[(ZnI_2)_3(tpt)_2{\cdot}x(CHCl_3)]_n$ (**tptZn·*x*CHCl₃**) to be obtained in only 3 days (0.182 x 0.231 x 0.289 mm in size). Even though the crystallization was set up both with ZnI_2 and $ZnCl_2$ as metal salts, it has been seen that when $ZnCl_2$ was used, the crystals obtained were very small, so less suitable for the purpose of the method (0.034 x 0.039 x 0.091 mm in size).

The initial single-crystal screening was hence performed on some of the crystals obtained from the synthesis with ZnI_2. The guest molecules present inside the pores are more likely to be disordered and so a good model of the framework needs to be obtained as first. It is important in fact to find the ideal conditions that lead to good crystallographic data for the framework itself before starting with the soaking process. The data quality of most of the crystals from $CHCl_3$ was however not ideal, with low percentage of observed reflections fitting the expected unit cell of the sponge framework (29 %), and poor intensity at high angle. Nevertheless, a good crystal was found with higher percentage of fitting (65 %) and was analysed with SCXRD, giving the structure of the expected sponge framework **tptZn·*x*CHCl₃**. As seen in **Figure 65**, the asymmetric unit presents three ZnI_2 fragments connected through two molecules of the **tpt** ligand, and two molecules of the solvent $CHCl_3$ are present within the pores. The framework crystallises in the monoclinic *C2/c* space group. Even though the data collection was performed at 150 K, the iodine atoms of almost all the ZnI_2 fragments and the zinc atom of one of these fragments are disordered and were split over two positions. The framework develops in three dimensions *via* the tridentate **tpt** ligand and interpenetrates with another equivalent, independent 3D framework as reported in **Figure 66**.

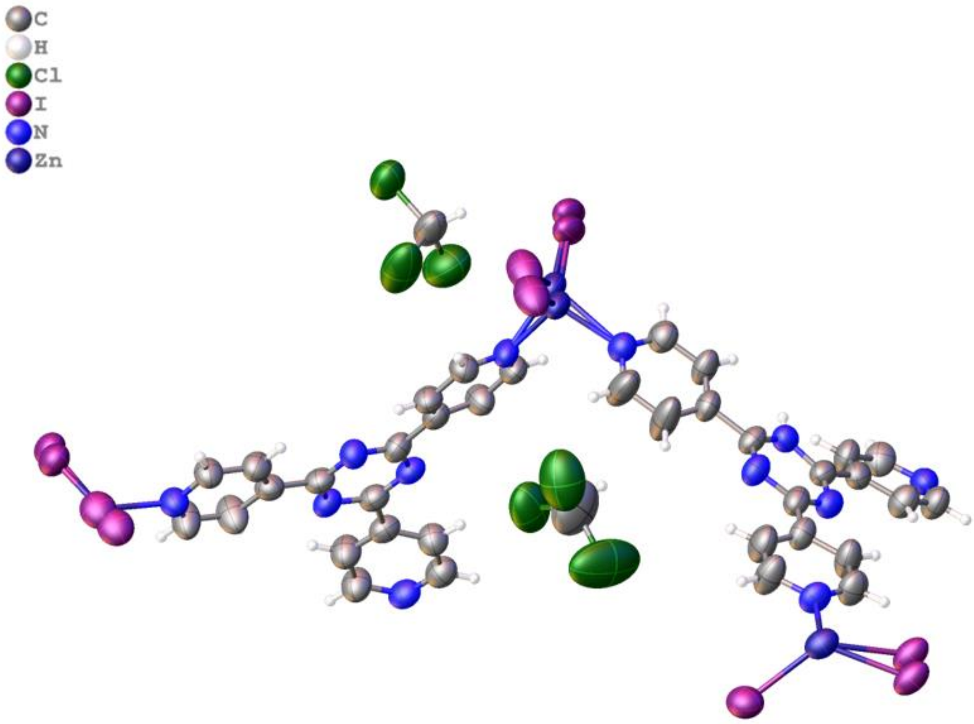

Figure 65: Asymmetric unit of the crystalline sponge framework **tptZn·*x*CHCl$_3$** obtained in CHCl$_3$ at the temperature of 150 K. Atomic displacement parameters are drawn at 50 % probability.

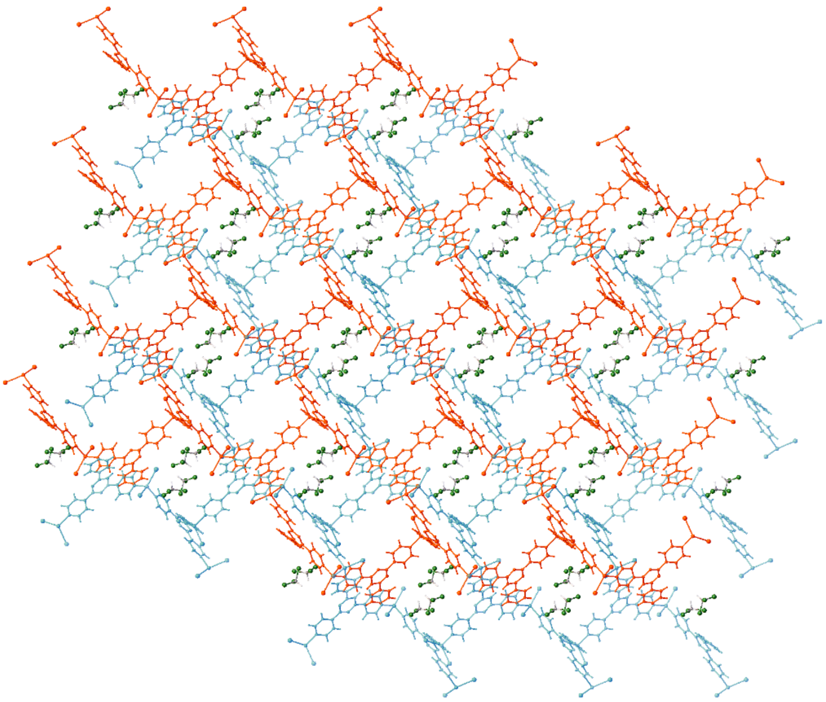

Figure 66: Supramolecular packing of the crystalline sponge framework **tptZn·*x*CHCl$_3$** seen along the *b* axis. The structure has been drawn isotropically for clarity. Each framework is highlighted in a different colour (red and light blue) to simplify the visualisation.

The DASAs that are used in this work are reported in **Figure 64**. In order to ensure that the volume within the pores of the framework was sufficient to accommodate DASA molecules, a calculation of the solvent accessible volume was performed. A total solvent accessible volume of 8049.4 Å^3 *per* unit cell was obtained from this calculation, corresponding to the 50.2% of the volume of the unit cell. Two sets of channels were found along the [010] and [101] directions, which can be seen respectively in **Figure 67a** and in **Figure 67b**. The channels are hence perpendicular one from the other, and the fact that they are not fully independent, but are instead interconnected, forms two crystallographically equivalent void spaces within the same unit cell. Therefore, each void space presents a volume of 4024.7 Å^3. The DASA with the higher number of atoms is DASA-1 (**Figure 64**), with a total number of non-hydrogen atoms of 29. Considering that in typical organic and organometallic species, including most porous MOF materials, each non-hydrogen atom occupies an average volume of 18 Å^3,[16] an indicative volume of 522 Å^3 is needed to incorporate the DASAs inside the pores of the framework. The volume of the voids that is present in the sponge framework is hence sufficient to accommodate the DASA molecules.

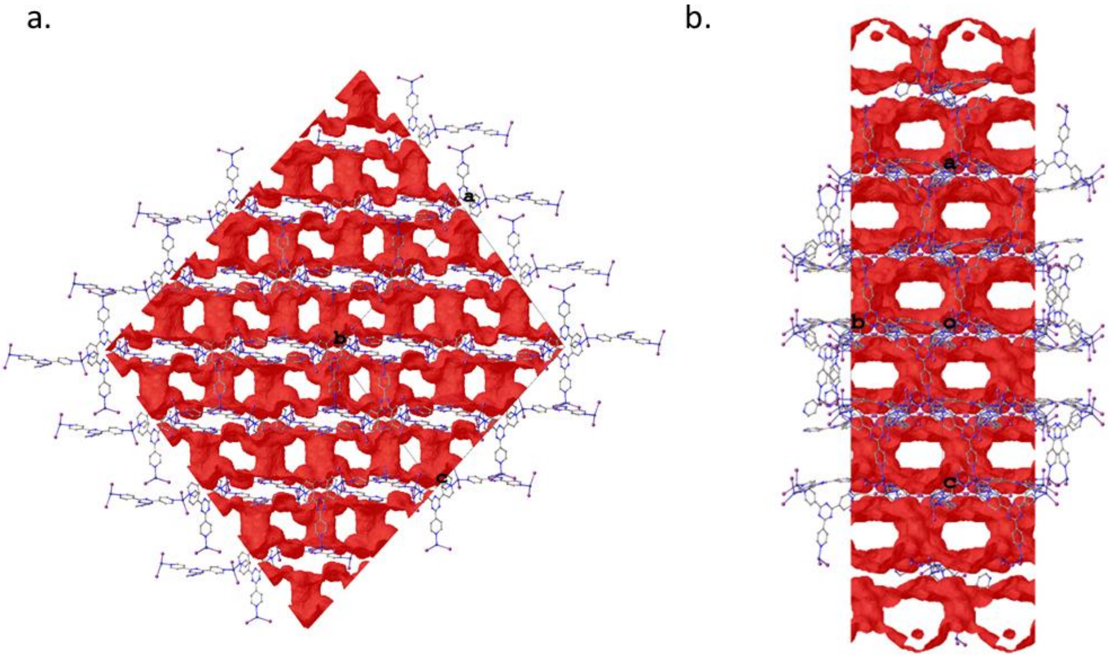

Figure 67: Solvent accessible voids seen along the **a.** [010] and **b.** [101] direction for the framework **tptZn·*x*CHCl$_3$**. The red surface is obtained by a calculation that considers a sphere with a 1.2 Å^3 radius rolling within the voids of the structure. The white spaces are hence channels present in the structure.

The framework **tptZn·*x*CHCl₃** was successfully synthesised, but it has been seen that even small changes in the synthetic procedure can influence the structure of the obtained framework. In fact, by simply adding a layer of ca. 1 ml of pure MeOH between the ligand and the salt solutions to further slow-down the diffusion of the reactants, or by leaving the vials at a temperature that is higher than 25°C, the structure of a packed coordination polymer $[(ZnI_2)_3(tpt)_2]_n$ (**TPT-1**) was obtained. The compound is isostructural with the analogous bromine-derivative reported in the literature although this iodine-containing compound has not been previously reported.[17] As can be seen in **Figure 68**, the asymmetric unit presents a **tpt** ligand coordinated to two ZnI_2 fragments, and a molecule of the solvent $CHCl_3$. The network of **TPT-1** develops in one dimension along the *c* axis, forming 1D chains with the coordination motif seen in **Figure 69a**. This coordination motif differs massively compared to the one seen in **tptZn·*x*CHCl₃**, where the framework develops instead in 3D forming a doubly interpenetrated framework. As a consequence, the 1D chains of **TPT-1** then closely pack in the supramolecular packing forming the coordination polymer reported in **Figure 69b**. This coordination motif does not allow enough space within the pores for DASAs to be hosted and hence these crystals could not be used to perform the crystalline sponge method.

The compound crystallises in the orthorhombic *Pnma* space group and even in this case, despite the fact that the data collection was performed at 150 K and hence at relatively low temperature, disorder of the iodine atoms, zinc atom and of one pyridyl rings was seen. As it can be seen in **Figure 68**, the disordered atoms were split over two positions and the ADP of the split iodine atoms were fixed to be equivalent. Similarly, the ADPs were fixed also for the carbon atoms belonging to the disordered pyridyl ring fragment in which the AFIX66 constraint was also applied in order to fix the distances within the ring to form a regular hexagon.

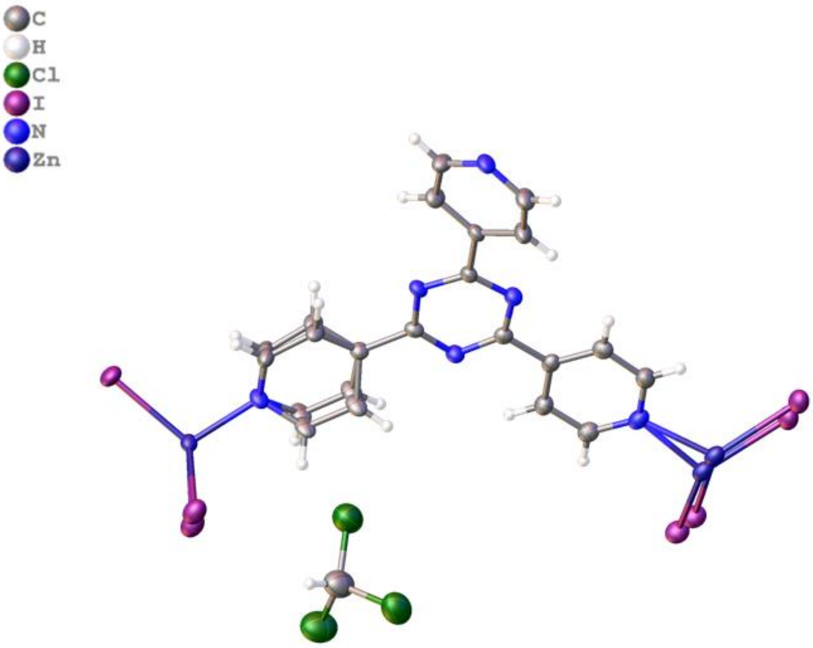

Figure 68: Asymmetric unit for compound **TPT-1** at 150 K. Atomic displacement parameters are drawn at 50 % probability.

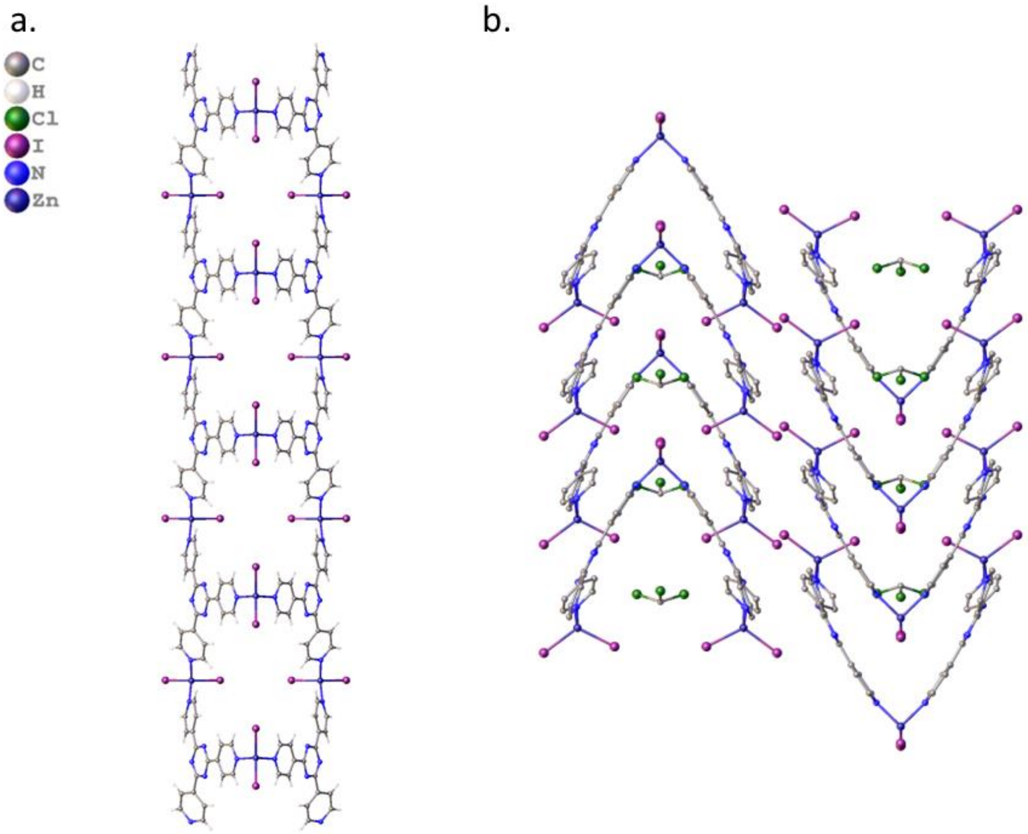

Figure 69: **a.** 1D chains seen along the *a* axis and **b.** supramolecular packing seen along the *c* axis for compound **TPT-1** showing how the 1D chains are packed. The structure has been drawn isotropically for clarity.

4.2.2 The soaking process

The successful synthesis of the sponge framework **tptZn·*x*CHCl$_3$** allowed to proceed with the next step of the crystalline sponge method which is the soaking process. In general, the soaking process starts by quickly transferring some crystals of the framework in small vials with some CHCl$_3$. The crystals were always kept covered in the solvent and never allowed to dry, as their crystallinity is rapidly lost when exposed to air. Some tests were performed to determine in which other solvents the crystals were stable and it was seen that their crystallinity is maintained also in toluene and cyclohexane.

As a starting point, solutions of the guests DASA-2, DASA-3 and DASA-4 (**Figure 64**) in CHCl$_3$ were prepared and added to the vials after decanting most of the solvent to try not to alter too much the concentration of the guest solution. The different DASA molecules were chosen in order to test different donor moieties that can potentially have different interactions with the framework, such as hydrogen-bonding and π-stacking, and hence influence the host-guest properties of the system: in this specific case, DASAs with a morpholine, a diethylamine and a 1,2,3,4-tetrahydroquinoline donor moieties were respectively used. For similar reasons, a soaking process was also set up with DASA-5 (**Figure 64**) in toluene, a DASA that presents an acceptor deriving from barbituric acid rather than from Meldrum's acid like in the other DASAs used. The vials were sealed and left at room temperature. The guest uptake was monitored *via* SCXRD for several weeks, but only structures with CHCl$_3$ or toluene molecules as guests (**tptZn·*x*Tol**) were obtained. As can be seen in **Figure 70**, the asymmetric unit of **tptZn·*x*Tol** at 150 K includes four molecules of toluene. The solvent molecules were severely disordered and an occupancy of 0.5 was assigned to each of them. As expected, the channels where the guest solvent molecules are situated are along the [010] and [101] directions (**Figure 71**).

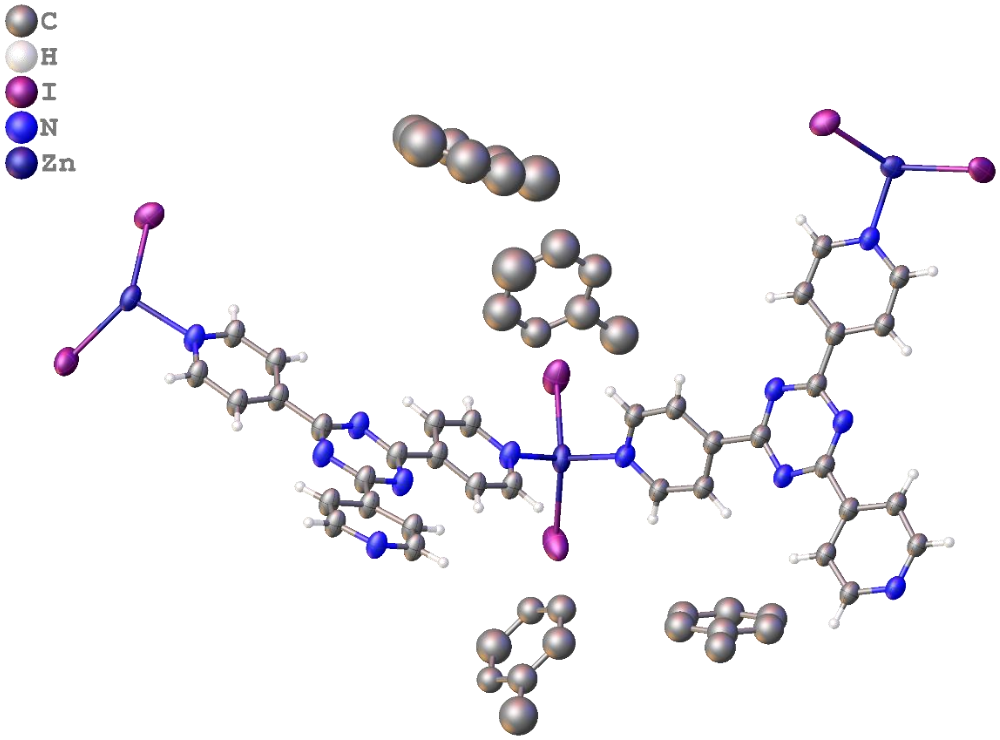

***Figure 70**:* Asymmetric unit of the crystalline sponge framework **tptZn·*x*Tol** in toluene. Atomic displacement parameters are drawn at 50 % probability. The molecules of toluene were kept isotropic during the refinement.

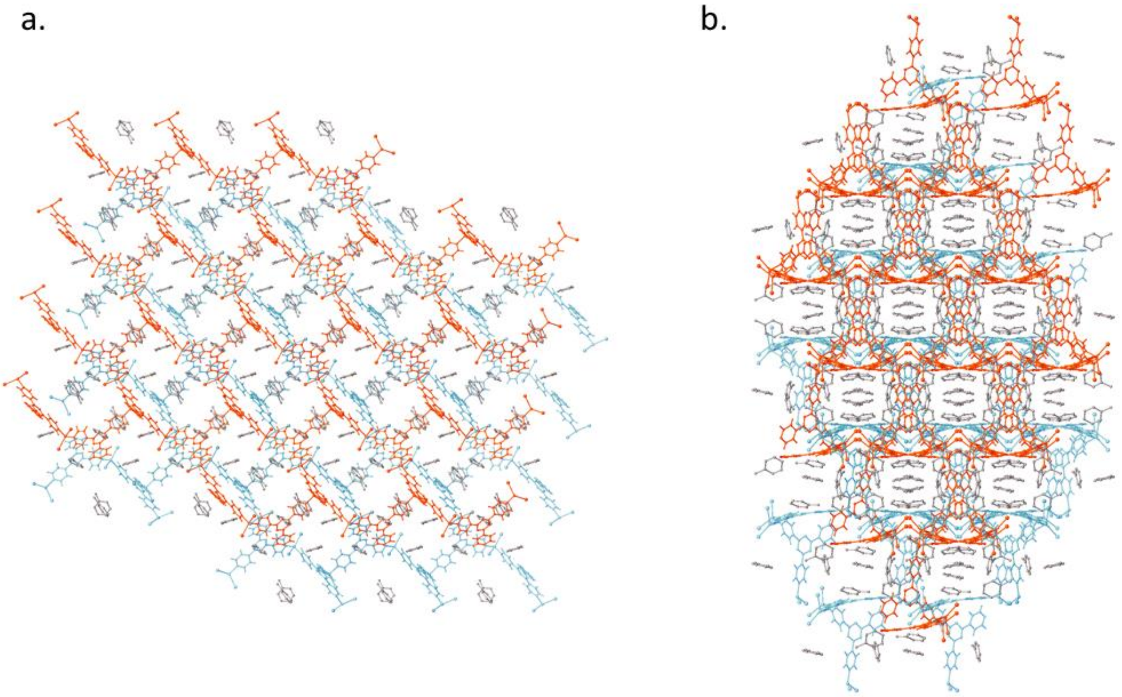

Figure 71: Channels seen along the **a.** [010] and **b.** [101] direction for the framework **tptZn·*x*Tol**.

In order to investigate different conditions for the soaking process to occur, new DASAs were used as guests, aiming to further expand the investigation to guests that can induce different interactions with the framework. In particular, DASA-6 and DASA-7 were used, both presenting a Meldrum's acid acceptor moiety and two similar piperazine derivative donor moieties differing in the addition of a methyl group in the free nitrogen atom in DASA-7. Additionally, as the crystals of the sponge framework were stable in cyclohexane, solubility tests were performed on the DASAs to investigate their behaviour in this solvent. Only DASA-1 was soluble in cyclohexane, forming a fuchsia coloured solution. Two soaking processes were hence set up with DASA-1, both at room temperature and at 5 °C. Some other DASAs led instead to the formation of a turbid solution when trying to dissolve them in cyclohexane (DASA-2, DASA-7, DASA-3, DASA-4, DASA-1, DASA-8 and DASA-9), showing that they are not soluble in this solvent. These DASAs were hence not used to attempt the soaking process in cyclohexane.

Even though different experimental conditions were attempted, such as the use of different solvents or different temperatures (5 °C, room temperature and 50 °C) or the attempt to perform the slow evaporation of the solvent as a soaking process, the method did not seem successful. Unfortunately, none of the soaking conditions used allowed the guests to be modelled inside the pores of the framework. It was in fact not possible to see the electron density of the DASAs after the full refinement of the framework, meaning that either the guest was not incorporated, its occupancy was too low, or it was highly disordered. It is important to point out that a visual observation of the colour of the crystals cannot be used to state whether the guest inclusion occurs or not. The lack of colouration of the crystals may in fact mean that the guest has not been incorporated, but it may also mean that the framework stabilises the closed, colourless form of the DASAs. As a consequence, SCXRD analysis is necessary to prove the incorporation of the guests into the sponge framework.

Three other approaches were hence investigated in order to perform the guest inclusion. Firstly, the DASAs formation was attempted directly inside the pores of the sponge framework; a second attempt involved the guest addition during the synthesis of the framework; finally the third one, used a smaller scale soaking procedure that was found in the literature for compounds that are similar to DASAs.[18]

4.2.3 Attempt to synthesise the DASA inside the sponge framework pores

The last step of the standard synthesis of DASAs consists of opening the activated furan core of the intermediate by reacting it with a nitrogen nucleophile through a series of rearrangements.[14] This aspect opened up the possibility to attempt the synthesis of the DASA directly inside the pores of the framework: by including at first the amine in the sponge framework pores and then adding a solution of the intermediate, or alternatively performing the addition of the intermediate first followed by the amine ones, the formation of the DASA can be induced to occur directly inside the sponge framework.

In an initial attempt, methylpiperazine was added to a vial containing a batch of the sponge framework crystals in $CHCl_3$. It was noticed that the crystals degraded quickly and lost their crystallinity, becoming white and opaque. The same procedure was hence performed with other amines, but using increasingly dilute concentrations. The other amines used, 2-methylindoline and pyrrolidine, again led to the rapid degradation of the crystals with the same behaviour as that seen for methylpiperazine. In addition to this, in the case of pyrrolidine, where more dilute concentrations were used, the framework completely dissolved after being left for some hours in the basic solution.

The inclusion of the intermediate INT-1 (**Figure 64**) as first step was already attempted while setting up the soaking processes with other DASAs. As already mentioned above, the soaking conditions used did not allow any of the guests to be modelled inside the pores of the framework. Additionally, as the crystals of the framework either dissolve or lose their crystallinity when basic conditions are used, the chosen approach did not seem the ideal one.

4.2.4 Attempt to include the DASA during the synthesis of the framework

Another approach to perform the guest inclusion inside the pores of the host framework involved the addition of the guest molecules while synthesising the framework itself. Most of the DASAs are in fact highly soluble in $CHCl_3$, solvent used to dissolve the **tpt** ligand that is involved in the synthesis of the sponge framework. The addition of the DASAs in the solution of the ligand in $CHCl_3$ used for the sponge synthesis could hence be a good approach to incorporate the guest while forming the host.

The procedure performed is very similar to the original one for the synthesis of the framework, and it differs only for the addition of a DASA solution in $CHCl_3$ to the solution of the **tpt** ligand. This reaction was performed with all the DASAs that dissolve in $CHCl_3$. In particular, the vials containing a coloured solution of DASA-10, DASA-3, DASA-1, DASA-11, DASA-12 and DASA-9 were sealed and left at room temperature for 3 days. The guests DASA-2, DASA-7, DASA-4, DASA-8 and DASA-13, showed instead the switching from the coloured to the colourless form in $CHCl_3$ when under an intense source of visible light. That colour change represents more specifically the switching between the open triene (coloured) and the closed cyclopentanone (colourless) forms of the DASAs molecules, forms that might have different interactions with the building blocks of the framework and hence might be differently stabilised within its pores.

Despite the fact that this procedure was attempted with a variety of DASAs as guests, only crystalline structures containing $CHCl_3$ were collected, revealing that these might not be the ideal conditions for the guest to be structurally analysed.

4.2.5 Attempt to include the DASA via soaking in dimethoxyethane

The last approach that was tried to perform the guest incorporation was inspired by Rosenberger's work, which is based on reducing the scale of the experiment.[18] This method was replicated with the only difference that the framework including the ZnI_2 moiety was used instead of the one with $ZnCl_2$. Despite the fact that different conditions were attempted to synthesise crystals of the sponge framework deriving from $ZnCl_2$, their quality was not good enough to perform an in-house measurement: the diffraction was weaker compared to the analogous deriving from ZnI_2 and in this case the use of synchrotron radiation would have been beneficial for the data collection.[19]

The crystals were covered in small quantities of cyclohexane (20-50 µl) and placed on the bottom of a small vial. Even smaller quantities of the DASAs solutions in dimethoxyethane were used (1-2 µl), and the syringe needle on the lids further enhanced the chance for inclusion to occur by slowly increasing the concentration of the guests in solution as the solvent evaporates. Initially, a clearly visible change in colour of the sponge framework crystals from pale yellow to pink (or blue, depending on the DASA used) was observed immediately after the addition of the guest solutions. This seemed an interesting observation that could have indicated that the guest inclusion took place. However, when the crystals were cut in a half under the microscope, they all appeared pale yellow in the middle, indicating that probably the DASAs were only deposited on the surface of the crystals, with little penetration into the centre. This hypothesis was supported by the SCXRD data collected that showed again that only molecules of solvent could be modelled inside the pores of the framework.

4.3 Experimental

4.3.1 Materials

The chemicals ZnI_2, $ZnCl_2$, $CHCl_3$, methylpiperazine, 2-methylindoline, pyrrolidine, MeOH, toluene, cyclohexane, dimethoxyethane were obtained commercially (Fisher Chemical, Alfa Aesar and Acros Organics) and used as received.

The **tpt** ligand was synthesised by Dr. William Gee following the procedure reported in the literature.[20]

4.3.2 Synthesis of tptZn·*n*$CHCl_3$

A solution of **tpt** ligand (6.3 mg, 0.02 mmol) was prepared in $CHCl_3$ (4.2 ml). In order to maximise the dissolution of the solid, the mixture was heated, sonicated, and then filtered before being transferred to a vial. A solution of ZnI_2 (9.58 mg, 0.03 mmol) was then prepared in MeOH (1 ml) and carefully layered on the top of the $CHCl_3$ solution. The interphase became slightly opaque. The vial was sealed and left at room temperature for 3 days, leading to the formation of pale yellow block crystals of **tptZn·*n*$CHCl_3$** on the walls of the vial, suitable for X-ray diffraction analysis. A variant of this synthesis consisted of leaving the vial in the fridge for 3 days instead of at room temperature to further slow-down the diffusion of the reactants.

The crystals were then gently transferred from the sides of the vial to smaller multiple vials with 0.5 ml *ca.* of $CHCl_3$ and washed multiple times with pure $CHCl_3$, making sure not to allow them to dry. The same reaction was performed with $ZnCl_2$.

4.3.3 Soaking process conditions

The DASAs (**Figure 64**) were dissolved in either $CHCl_3$, toluene or cyclohexane. The quantity of powder that has been used varied according to the solubility of each DASA.

The solutions obtained were added to the vials with the sponge framework crystals and different soaking methods were used. The single-crystal-to-single-crystal solvent exchange method was performed by simply sealing the vials having the crystals of the sponge framework dipped into the target solution and leaving to soak for several days.

A variant of this method includes a change of temperature: the vials were left in the oven at 50 °C or in the fridge at 5 °C for several days before being analysed. The second method that has been used is the slow evaporation method. In this case, the vials with the sponge framework crystals and the DASAs solutions were equipped with a needle to allow the slow evaporation of the solvent, and the consequent enhancement of the concentration of the target guest. A variant of this method includes performing the slow evaporation under a light source to maximise the quantity of the closed, colourless form of the DASAs.

4.3.4 Amine inclusion in the MOF framework

Some sponge framework crystals deriving from the synthesis of the framework (**4.3.2**) were dipped into pure $CHCl_3$ (1 ml *ca.*) and methylpiperazine (6 drops *ca.*) was added to the vial. The crystals quickly became white and lost their crystallinity. The same procedure has been repeated in two different vials using respectively 2-methylindoline (3 drops *ca.*) and pyrrolidine (1 drops *ca.*). In both the cases, the crystals lost their crystallinity almost instantaneously becoming white, and when pyrrolidine was used complete dissolution of the sponge framework has been observed after some hours.

4.3.5 Inclusion of DASA molecules during the synthesis of the sponge framework

A solution of **tpt** ligand (6.3 mg, 0.02 mmol) was prepared in $CHCl_3$ (4.2 ml). In order to maximise the dissolution of the solid, the mixture was heated, sonicated and then filtered before being transferred to a vial. A solution of the guest (0.0025 mol) in $CHCl_3$ (0.5 ml *ca.*) was then added and carefully layered with the solution of ZnI_2 (9.58 mg, 0.03 mmol) in MeOH (1 ml). The vials containing DASA-10, DASA-3, DASA-1, DASA-11, DASA-12 and DASA-9 as guests were sealed and left at room temperature for 3 days. The vials containing DASA-2, DASA-7, DASA-4, DASA-8 and DASA-13, guests that switch from coloured to colourless in $CHCl_3$, were sealed and left under an intense source of light at room temperature for 3 days. A variant of this synthesis consisted of leaving the sealed vials in the fridge at 5 °C for 3 days.

4.3.6 Inclusion of DASA using dimethoxyethane

Some sponge framework crystals derived from the synthesis of the framework (**4.3.2**) were dipped into pure cyclohexane (50 µl) placed on the bottom of a small vial. The guest's solutions were prepared with a concentration of 1 mg/ml in dimethoxyethane. Each solution was added to a different vial (1 µl) which was sealed with a lid and pierced with a syringe needle to allow the slow evaporation of the solvent during the guest inclusion. The crystals of the framework became coloured almost instantaneously and they were left at 25 °C for 1 day. A variant of this procedure consisted of using different quantities of pure cyclohexane and different quantities of the guest solution, maintaining constant its concentration: 2 µl of DASAs solution were added to 50 µl of pure cyclohexane, 1 µl of DASAs solution was added to 20 µl of pure cyclohexane and 2 µl of DASAs solution were added to 40 µl of pure cyclohexane. An additional variant consisted of removing the needle from the lid or even sealing the vial with a lid without hole to further slow-down the evaporation of the solvent.

4.3.7 Guest molecules

All the DASAs and the intermediate INT-1 used in this work to perform the soaking processes have been kindly synthesised by Sean Connolly and Tom Hitchings. **Figure 64** represents all the guest molecules used.

4.4 Conclusions

In the current work, the crystalline sponge method was studied to investigate the solid-state behaviour of the photoswitching mechanism of DASAs *via* SCXRD. Unfortunately, despite the variety of attempts that were performed to be able to analyse the DASAs as guests, only the structure of the framework including different solvents and a packed coordination polymer isostructural to the bromine-derivative present in the literature were obtained.

There are many variables that can be tried to favour the inclusion of the target guest. Several conditions were changed, starting from the temperature, the concentration of the guest in solution, the soaking time, the evaporation rate and the DASA used. Different approaches were also investigated, like the inclusion of the intermediate that forms the DASA, which is significantly smaller than the DASA itself, and the consequent addition of the amine to form the guest directly inside the pores, or the inclusion of the guest in the ligand solution while synthetising the framework. The process of finding the ideal conditions to analyse the guest did not seem immediate and straightforward.

It is important to point out that characterisation methods that are alternative to SCXRD are not suitable to test the DASA incorporation. Techniques like Raman or IR would in fact give information about the composition of the surface of the crystals rather than the core, and hence they would not work for this specific purpose. Similarly, the use of solid-state UV-vis would be altered by any surface colouration that might give false results. Additionally, the aim of this work was to perform a structural investigation of the photoswitching phenomenon in the solid-state of DASAs and hence to look at their structural behaviour: if the DASAs cannot be seen *via* SCXRD analysis, it is probably not useful to even have a small incorporation of them as guests. What can be said so far from these results is that if the guest incorporation occurred through some of the attempted guest soaking processes, the incorporation did not occur in a way that allowed to study the effect of the confinement on the DASAs switching *via* SCXRD.

4.5 References

1 Q. Du, J. Peng, P. Wu and H. He, *TrAC - Trends Anal. Chem.*, 2018, **102**, 290–310.

2 L. Ooi, *Principles of X-ray Crystallography*, Oxford University Press, 2010.

3 P. Stallforth and J. Clardy, *Nature*, 2013, **495**, 456–457.

4 Y. Inokuma, S. Yoshioka, J. Ariyoshi, T. Arai, Y. Hitora, K. Takada, S. Matsunaga, K. Rissanen and M. Fujita, *Nature*, 2013, **495**, 461–466.

5 E. V. Vinogradova, P. Müller and S. L. Buchwald, *Angew. Chemie*, 2014, **126**, 3189–3192.

6 M. Hoshino, A. Khutia, H. Xing, Y. Inokuma and M. Fujita, *IUCrJ*, 2016, **3**, 139–151.

7 Y. Inokuma, M. Kawano and M. Fujita, *Nat. Chem.*, 2011, **3**, 349–358.

8 H. Ledford, *Nature*, 2015, 1–2.

9 H. Sato and A. Yamano, *Rigaku J.*, 2019, **35**, 1–4.

10 K. Biradha and M. Fujita, *Angew. Chemie - Int. Ed.*, 2002, **41**, 3392–3395.

11 T. R. Ramadhar, S. L. Zheng, Y. S. Chen and J. Clardy, *Acta Crystallogr. Sect. A Found. Crystallogr.*, 2015, **71**, 46–58.

12 S. Helmy, F. A. Leibfarth, S. Oh, J. E. Poelma, C. J. Hawker and J. R. De Alaniz, *J. Am. Chem. Soc.*, 2014, **136**, 8169–8172.

13 S. Helmy, S. Oh, F. A. Leibfarth, C. J. Hawker and J. Read De Alaniz, *J. Org. Chem.*, 2014, **79**, 11316–11329.

14 M. M. Lerch, W. Szymański and B. L. Feringa, *Chem. Soc. Rev.*, 2018, **47**, 1910–1937.

15 R. Saha, A. Devaraj, S. Bhattacharyya, S. Das, E. Zangrando and P. S. Mukherjee, *J. Am. Chem. Soc.*, 2019, **141**, 8638–8645.

16 William Clegg, *X-ray crystallography*, Oxford University Press, Second., 2015.

17 H. Ohtsu and M. Kawano, *Dalt. Trans.*, 2016, **45**, 489–493.

18 L. Rosenberger, C. Von Essen, A. Khutia, C. Kühn, K. Urbahns, K. Georgi, R. W. Hartmann and L. Badolo, *Drug Metab. Dispos.*, 2020, **48**, 587–593.

19 T. R. Ramadhar, S. L. Zheng, Y. S. Chen and J. Clardy, *Chem. Commun.*, 2015, **51**, 11252–11255.

20 A. Herrera, R. Martínez-Alvarez, P. Ramiro, M. Chioua and R. Chioua, *Synthesis*, 2004, **4**, 503–505.

Chapter 5: Lanthanide-based piperazine-bis-dithiocarbamate MOFs

5.1 Introduction

5.1.1 Rare earth elements and their emissive nature

The lanthanide series includes the elements from lanthanum (57) to lutetium (71), taking the name of “rare earths” when scandium and yttrium are also added.[1] The first applications of lanthanides that are related to lighting date back to the 1880s, when the Austrian scientist Carl Auer von Welsbach invented the incandescent gas mantle (or Welsbach mantle) and the mischmetal, an alloy of rare earth elements used as ignition device. Along the years, lanthanides found applications in devices such as lasers, optical fibres, computer and television displays, in biomedical analysis for diagnosis and cell imaging, and in counterfeiting tags and inks. Most of the interest for these elements derives from their optical properties that are outstanding and unique.

In lanthanide (Ln) elements, the f orbitals start to be progressively filled along the series because of their abrupt decrease in energy.[1] An important property of 4f orbitals derives from the fact that they are close to the nucleus of the metal, and hence they are shielded from the ligand by the filled 5s, 5p and 6s sub-shells that are outer shells. As a consequence, the ligand-field effects are really small for 4f orbitals and this generates emission spectra with extremely narrow bands in the visible and near infrared region that are characteristic for each element.[2] Along with the narrow bands and the fact that the position in the spectra of the f-f transitions are almost independent of the host matrix, lanthanides are widely suited to luminescence also for their emission wavelengths that, in some cases, match the human eye sensitivity (e.g. Eu^{3+} and Tb^{3+}).[3]

The most stable lanthanide ion is the trivalent Ln^{3+}, with an electronic configuration of $[Xe]4f^n$ (n = 0-14), and almost all of them are luminescent. The term luminescence includes both fluorescence and phosphorescence. Using the definition given by IUPAC, fluorescence is a spin-allowed radiative transition, while phosphorescence is a spin-forbidden radiative transition.[4] In general, a spin-allowed transition involves states with the same spin multiplicity (typically $S_1 \rightarrow S_0$), instead a spin-forbidden transition implies a change in the spin multiplicity (typically $T_1 \rightarrow S_0$).

One problem that lanthanides face is that they have a very low molar absorption coefficient (typically < 3 M^{-1} s^{-1}) because of the parity-forbidden nature of 4f-4f transitions.[2] The selection rules can be relaxed by orbital mixing when reaching high atomic numbers, like in lanthanides, but this effect is still too small and sensitization must be used.[5] In general, the sensitization process consists in a donor-acceptor energy transfer, that in coordination compounds is more likely to be from the ligand to the metal centre. This process is also called indirect excitation or antenna effect, and is divided in three steps: light is absorbed by the organic ligand that is attached to the Ln^{3+} ion; secondly the energy is transferred onto one excited state of the metal ion, which finally emits light.[2]

5.1.2 Luminescent MOFs as sensors

The intrinsically porous structures of MOFs can be exploited to capture guest molecules within their pores. MOFs are compounds that present large surface areas, adjustable pore sizes and controllable surface properties, rendering them good candidates for applications like selective gas adsorption, gas storage and gas separation.[6] An additional and correlated way to exploit the porosity of these versatile materials is to use them as sensors. Nowadays there is the need for sensitive and selective detection of gas analytes in a variety of fields, such as industrial process management, chemical threat detection and environmental monitoring.[7] A MOF needs however to exhibit a specific behaviour in order to be used as a sensor. In fact, there must be a change in some measurable property of the material, such as the visible colour or the emission properties, in response to an interaction with a specific analyte, and this change must be detectable. In addition to this, the reversibility of this response is usually preferred, but not required in all the cases.[8]

Luminescence in MOFs is often exploited as a signal in sensing. There are different ways to generate luminescence emission in porous materials like MOFs. Linker-based emission occurs when the material possesses a well-defined spatial arrangement of lumophores, which are luminescent groups that absorb in the UV and visible region and are usually composed of conjugated organic molecules.[8] This also includes the charge transfer between the metal and the ligand and it is generally intense because it benefits from the immobilization and separation of these components within the crystal lattice.[9] The metal-based emission is another way to generate luminescence emission in MOFs, widely observed in lanthanoid-based MOFs through the so-called "antenna effect". It is generated by the proximity of an organic fluorophore to the metal centre that can allow an energy transfer from the organic moieties to the metal ones, increasing the luminescence intensity.[8] Finally, lumophore guests that are hence luminescent molecules can be hosted in the nanopores of a non-emissive MOF or vice-versa the absorption of a guest can quench or enhance the luminescence of an emissive framework.[8] The quenching of luminescence is the most common phenomenon in luminescent MOFs that follows the guest adsorption, and more rarely its enhancement.[7] This phenomenon is stronger when there is an electron-donor/electron-acceptor orbital overlap between the host and the guest. It is therefore easier to detect analytes that are good electron donors or acceptors.[7] Examples of acceptor analytes widely studied nowadays are nitroaromatics, a class of molecules that includes explosives and explosive-like molecules.

5.1.3 Choice of the ligand

The synthesis of coordination polymers most commonly involves nitrogen and oxygen donor ligands. Despite the fact that this area is still expanding to other functionalities, organic ligands with sulphur coordination sites have so far received little attention.[10] The ligand piperazine-bis-dithiocarbamate (**ppz-bdtc**) is a chelating sulphur-donor ligand that can be seen in **Figure 72a**. Its structure is similar to the one of the 1,4-benzenedicarboxylate (**bdc**) ligand (**Figure 72b**), widely used for synthesising MOFs and coordination polymers. The main differences between the two ligands are the donor moieties and the fact that the piperazine core of **ppz-bdtc** allows it to adopt various coordination modes thanks to the possible resonance forms available (**Figure 72c**). A special feature of dithiocarbamate (**dtc**) ligands is in fact the additional π-electron flow from the nitrogen atom to the sulphur atoms. This results from a resonance form with a strong electron donation capacity (**Figure 72c-3**) that, if stabilised, could be used for applications such as carbon dioxide capture (**Figure 72d**). Additionally, the switching from a rigid benzene core of **bdc** to a flexible piperazine core of **ppz-bdtc** opens up the possibility of imparting different properties to the final material: the **ppz-bdtc** ligand can be linear or bent, and so has the potential to allow the framework itself to be highly flexible and to breathe when accommodating guest molecules.

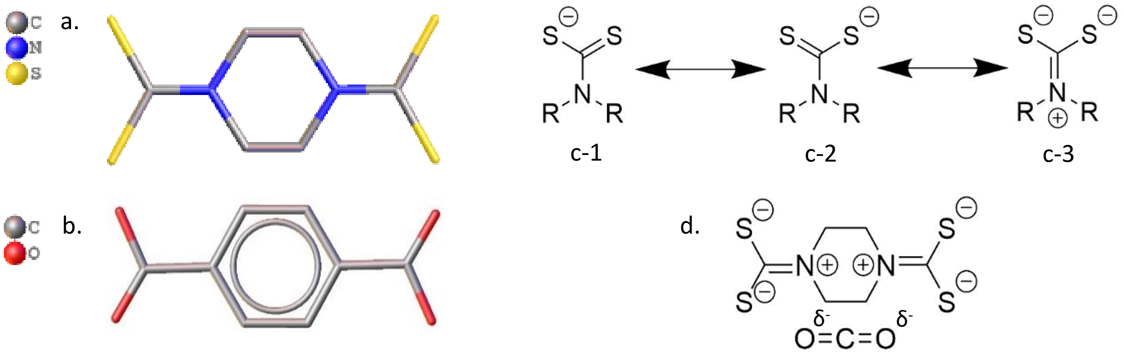

Figure 72: **a.** Structure of the **ppz-bdtc** ligand; **b.** Structure of the **bdc** ligand; **c.** Possible resonance forms of a general dithiocarbamate; **d.** Possible application of the **ppz-bdtc** ligand for CO_2 capture. The hydrogen atoms were omitted for clarity.

The ligand **ppz-bdtc** has been only relatively recently used to construct porous three-dimensional rare earth frameworks. Wang and co-workers reported in 2015 the structure of a Nd-based compound constructed by reacting the sodium salt of the **ppz-bdtc** ligand in water with a $Nd(NO_3)_3 \cdot H_2O$ solution in formamide.[11] The group expanded their work to other metal centres, reporting in 2017 the structural data of other compounds involving the **ppz-bdtc** ligand and Ce^{3+}, Sm^{3+}, Eu^{3+}, Gd^{3+} and Tb^{3+}, isostructural to the previously reported with Nd^{3+}.[12] The structure of the framework $(H_3O)[Sm(\text{ppz-bdtc})_2] \cdot 1.5H_2O \cdot 2.5CH_3NO$ (**ppz-bdtcSm**) is reported in **Figure 73** and it is characterised by a tetracoordinated lanthanoid centre having a H_3O^+ group as counterion: the four **ppz-bdtc** ligands act in fact as a bidentate, chelating and bridging ligands that coordinate to adjacent metal ions, forming a 3D coordination network. The supramolecular packing of **ppz-bdtcSm** shows that 1D channels develop along the *c* axis, with a channel diameter of 1.0 nm. The group explored the luminescence properties of these lanthanoid-based materials, and consequently used a codoping approach to tailor their emission properties.[12] To date, these are the only two works that contains the structure of rare earth MOFs constructed with the **ppz-bdtc** ligand.

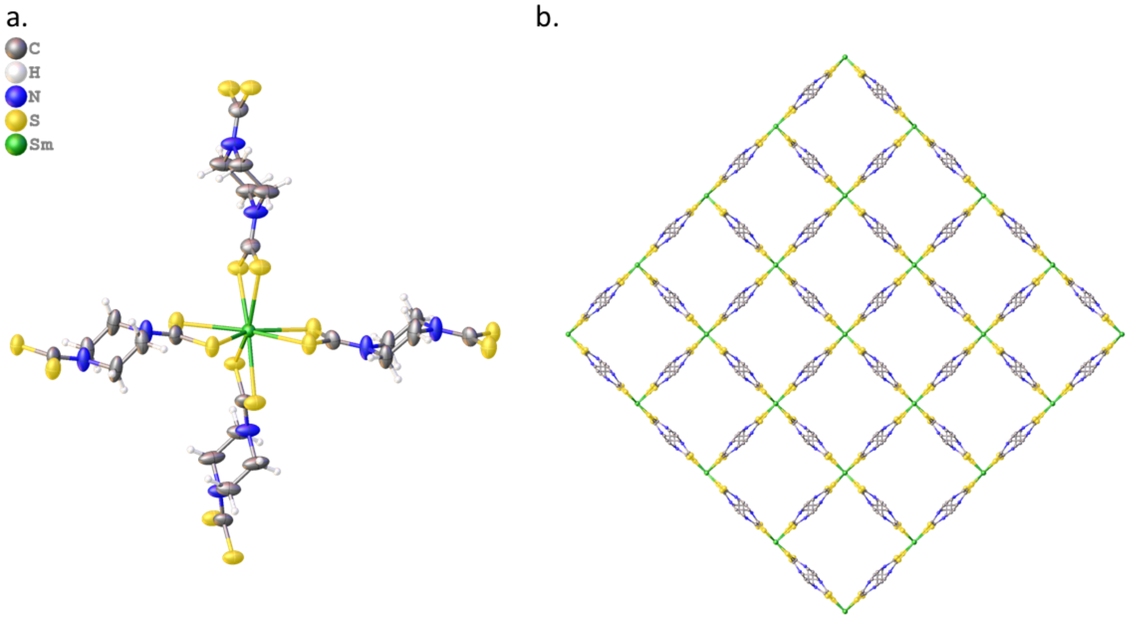

Figure 73: **a.** Coordination sphere of the Sm^{3+} ion in compound **ppz-bdtcSm**; **b.** Supramolecular packing seen along the *c* axis showing the channels that **ppz-bdtcSm** forms. The structure has been drawn isotropically and the hydrogen atoms were removed for clarity. CCDC number: 1503322.[12]

5.1.4 Aims

Important progress has been made in engineering the synthetic procedure to create multifunctional materials usable as chemical sensors. The properties of MOFs with oxygen-donor ligands, such as benzenedicarboxylate (**bdc**), and nitrogen donor ligands, along with their synthesis and numerous applications, have been widely studied and developed by many scientists since these materials have been discovered. However, coordination compounds constructed with sulphur-donor ligands are an underexplored class of materials that has not been thoroughly investigated yet.

The aim of this work is to carry on the study, the design and optimisation of the synthesis of porous lanthanoid coordination compounds using a piperazine-bis-dithiocarbamate (**ppz-bdtc**) ligand. The investigated ligand allows to impart to the final material flexibility that could potentially be fundamental when looking at porous compounds. Additionally, the guest uptake could be used to modulate the luminescence properties of the material, opening up routes to new luminescent sensors.

5.2 Results and discussion

5.2.1 Synthetic approaches

The reactions investigated in this work involved two different approaches: a two-step reaction and a one-step reaction. Initially, the two-step approach was performed, which consisted of the synthesis of the ligand, followed by the reaction of the ligand with various metal centres (**Figure 74**). The procedure followed for the synthesis of the ligand was already reported in the literature,[13] and consisted of the reaction of piperazine with CS_2 in an aqueous NaOH solution performed in a water-bath-cooled vessel. The crystallisation technique that was used to allow the growth of crystals of the product is instead the slow diffusion of the reactants: the metal centres and the ligand were dissolved in different solvents and the two solutions were layered according to the different densities of the solvents.

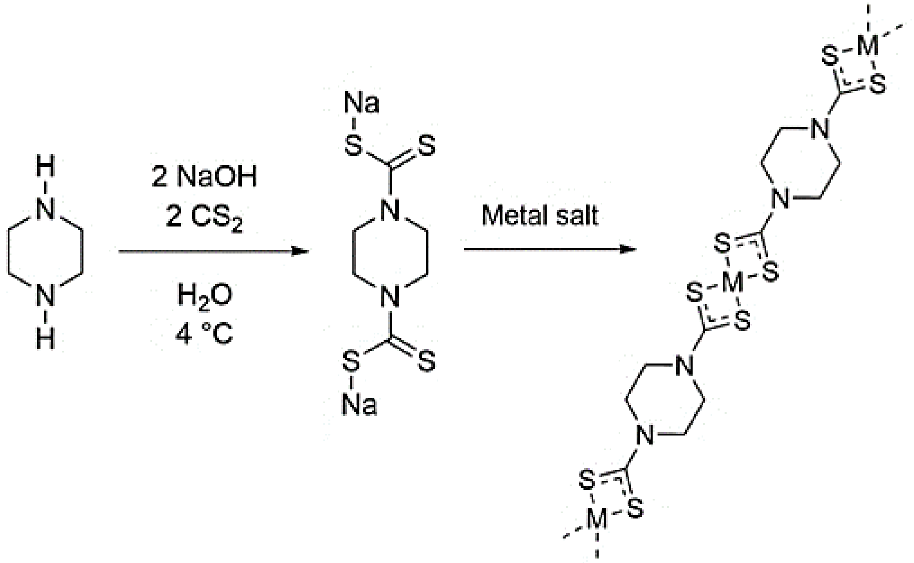

Figure 74: Schematic representation of the two-step MOFs reaction, where the synthesis of the **ppz-bdtc** ligand is followed by the layering of the ligands with the metal salts solution.

The piperazine-bis-dithiocarbamate (**ppz-bdtc**) ligand was successfully synthesised and characterised. In **Figure 75** it is reported the structure that was obtained for the ligand as a sodium salt, Na_2-ppz-bdtc·$2H_2O$ (**Na2-ppz-bdtc**), from SCXRD data. As can be seen below, each ligand bridges with the subsequent ligand through two sodium ions, which further bridge to two water molecules forming a 1D chain coordination motif. Each sodium atom coordinates hence to two sulphur and two oxygen atoms in the equatorial position of a distorted square pyramid. Finally, the apical position of the square pyramid is occupied by another sulphur atom of the adjacent 1D chain, resulting in a more closely packed supramolecular arrangement compared to the one already reported in the literature.[14]

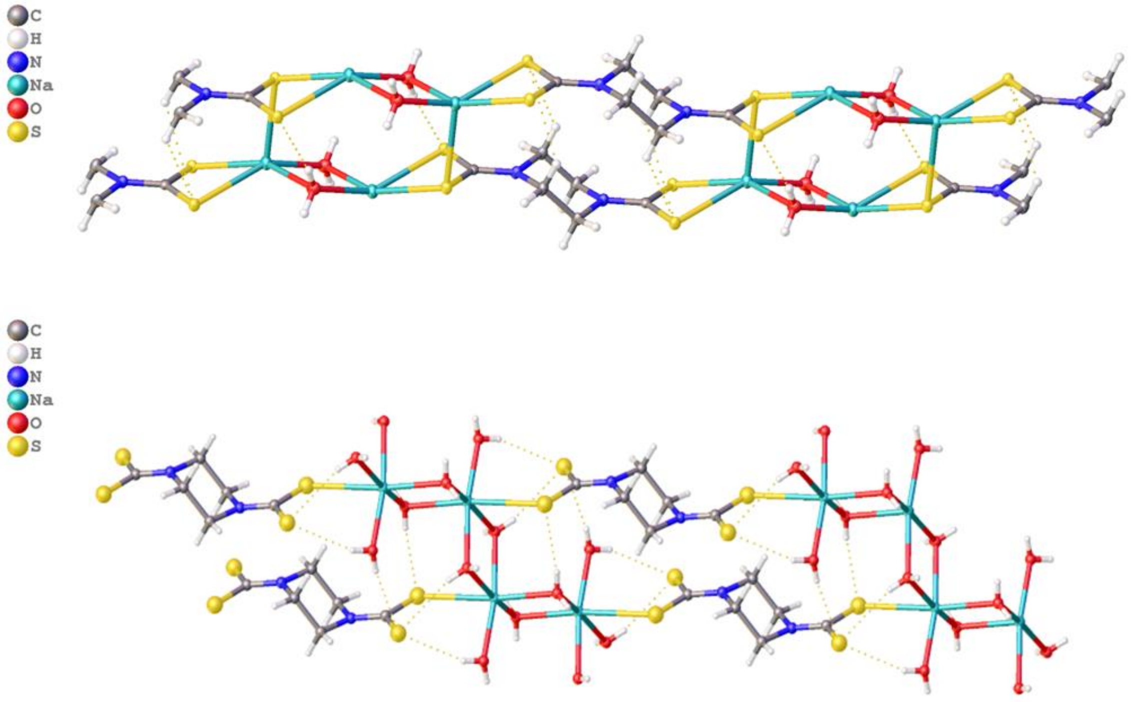

Figure 75: Single crystal structure of the newly synthesised **Na_2-ppz-bdtc** on the top and the solvatomorph of the ligand that is already reported in literature on the bottom. CCDC number: 1124155.[14]

The bulk composition of the ligand has been analysed with powder X-ray diffraction (PXRD). The pattern that was obtained experimentally (**Figure 76**, black line) was compared with the one simulated from the SCXRD data obtained from Na_2-ppz-bdtc·$2H_2O$ (**Figure 76**, blue line) and with the data that are reported in literature for the ligand Na_2-ppz-bdtc·$6H_2O$ (**Figure 76**, red line).[14] By comparing these patterns, it is possible to notice that the ligand is mostly hexahydrated, but some of the diffraction peaks can be assigned to the pattern of the dihydrate form derived from the crystalline structure.

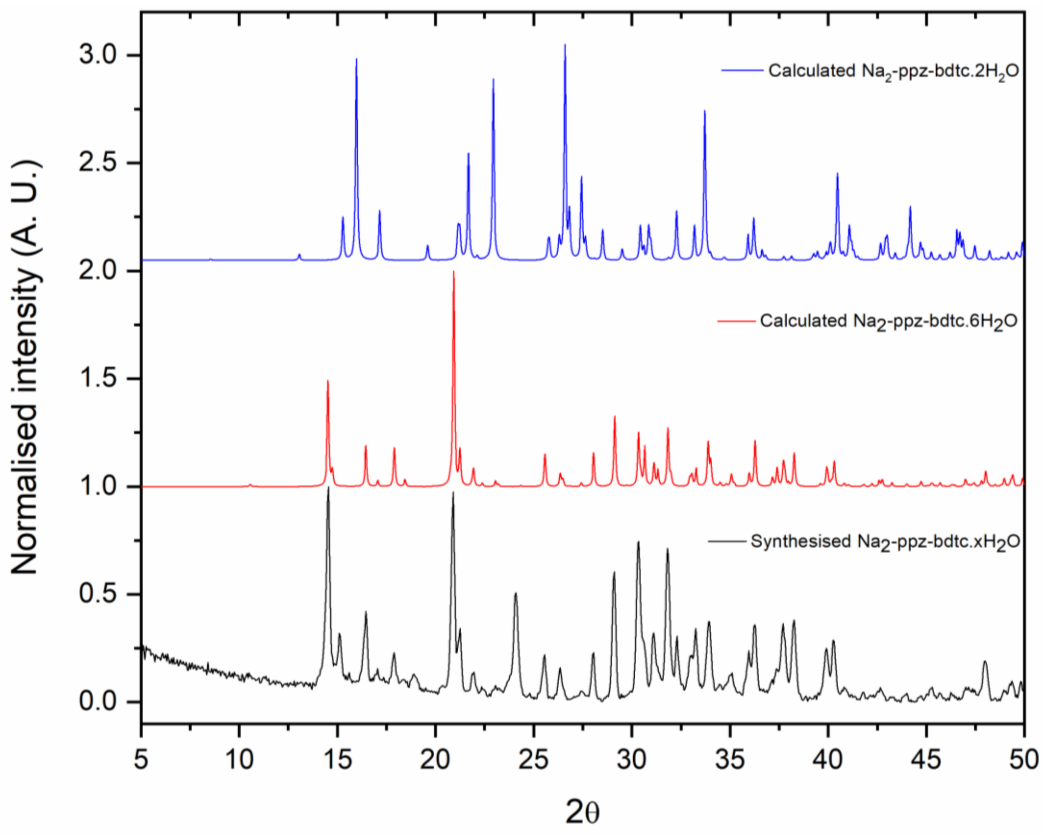

Figure 76: Normalised PXRD pattern of synthesised **Na2-ppz-bdtc** (black line) and the comparison with the calculated patterns. Colour code: blue line, calculated from SCXRD data of **Na2-ppz-bdtc**; red line, simulated from literature data; black line, measured from synthesised ligand powder.

Once the composition of the synthesised ligand was confirmed, the second step of the two-step approach consisted of the layering of the ligand solution with the solutions of metal salts. As already mentioned above, the incorporation of lanthanoid ions in the supramolecular scaffold can be used to induce luminescence to the material and generate sensors that can have real world applications such as in chemical and biological sensing and detection.[15] With the aim of using ions that could generate emission in the region of visible light, the ions that were mostly investigated in this approach were Eu(III) and Tb(III), which exhibit narrow f-f emission bands resulting respectively in a red and a green emission.[9]

Even though different combinations of solvent were used in this approach for the crystallization to occur, only the precipitation of amorphous powders was seen. Meanwhile, the investigation of the one-step approach was carried on. This approach consisted of mixing all the reactants in the same reaction vessel and solvent, favouring the formation of the final material *via* self-assembly of the different building blocks. All the reactants were hence dissolved in the same solvent, but once again upon addition of carbon disulphide (CS_2) as the final reactant, the precipitation of a powder was seen. The powders were analysed with PXRD, showing some broad peaks with a very low intensity, implying that they could be considered poorly crystalline (**Figure 77**).

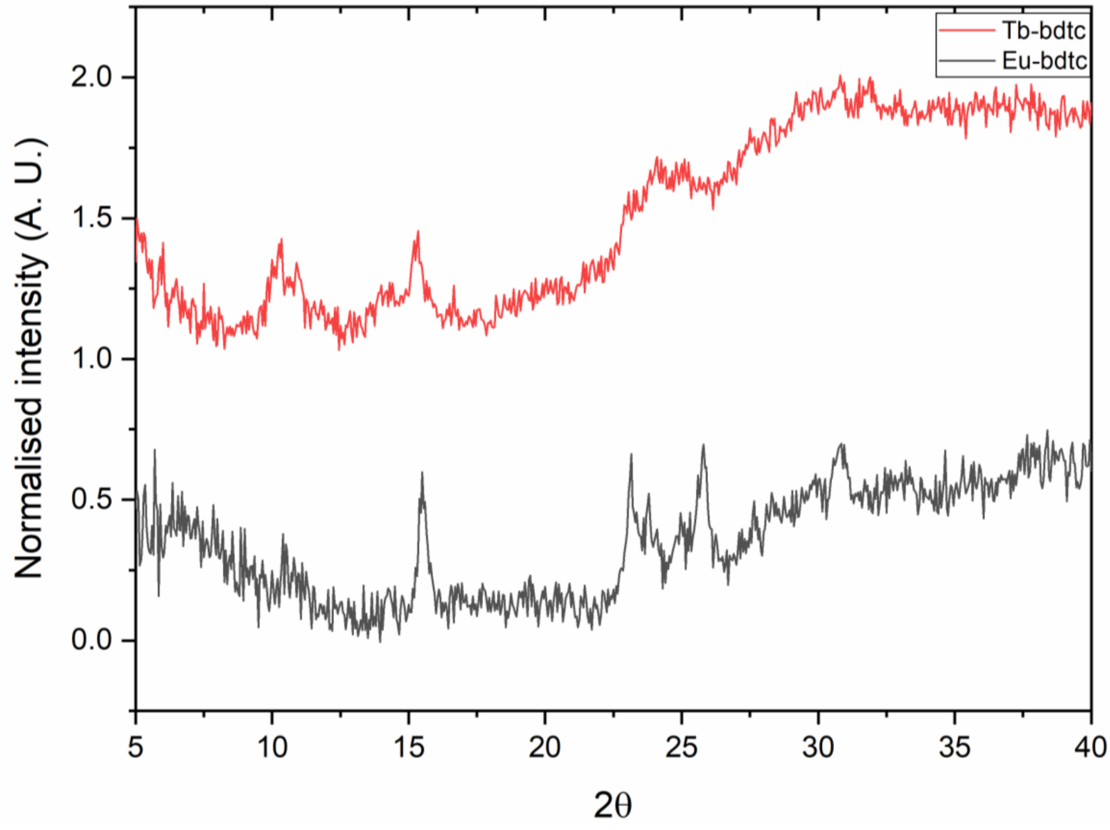

Figure 77: Normalised PXRD pattern of synthesised **ppz-bdtc**-based compounds constructed with Tb^{3+} (top, **Tb-bdtc**) and with Eu^{3+} (bottom, **Eu-bdtc**). Colour code: red line, measured from synthesised terbium-based compound; black line, measured from synthesised europium-based compound.

The one-pot approach was hence optimised changing several conditions such as concentration, solvents used, and metal centres involved. With the aim of growing crystals and achieving information about the atomic and molecular structure of the product, a different experimental setup was finally performed. After mixing piperazine, triethylamine and the metal salt in DMF and placing this solution in a small vial, CS_2 vapours were allowed to slowly diffuse into this solution, favouring a slow diffusion of CS_2 (**Figure 78**). This approach was attempted with all the lanthanoid metal centres available (Ln^{3+} = La^{3+}, Pr^{3+}, Nd^{3+}, Eu^{3+}, Gd^{3+}, Tb^{3+}, Er^{3+} and Yb^{3+}).

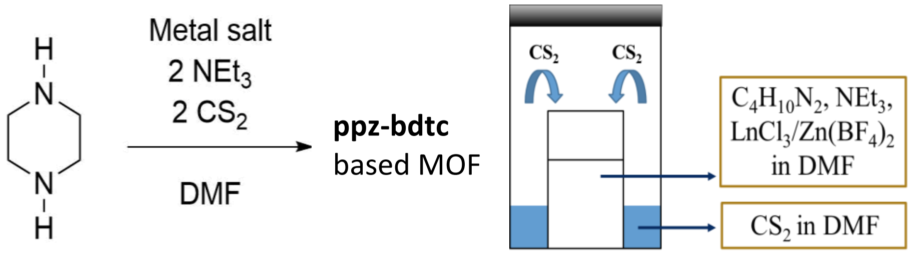

Figure 78: Schematic representation of the one-step MOFs reaction; Ln = lanthanoid ions and experimental setup for the slow diffusion of CS$_2$ vapours.

The slow diffusion approach appeared to be promising and the structure of two isostructural new coordination polymers constructed with **ppz-bdtc** ligand and the metal centres La^{3+} and Pr^{3+} were obtained. Compounds La(ppz-bdtc)$_{1.5}$(DMF)$_2$·DMF (**Figure 79**, **BDTC-1**) and Pr(ppz-bdtc)$_{1.5}$(DMF)$_2$·DMF (**Figure 80**, **BDTC-2**) are isostructural and they crystallise in the triclinic *P-1* space group. As can be seen in **Figure 79a** and **Figure 80a**, the asymmetric units of the coordination polymers contain one lanthanoid ion with 1.5 molecules of the **ppz-bdtc** ligand and two molecules of DMF coordinated to the metal centre, with an additional DMF molecule present as solvent. Two distinct **ppz-bdtc** ligands are hence present in the structure: one that bridges between consecutive Ln^{3+} ions in a bent coordination along one axis; the other that bridges between consecutive Ln^{3+} ions in a linear coordination along the perpendicular axis. The latter ligand appeared to be disordered, a characteristic deriving from the flexibility of the piperazine core of the ligand. The piperazine fragment of the ligand was hence split over two positions, with the two components having a total occupancy of 1. Each of the parts was then freely refined, leading to a percentage of occupancy for the two components of 58 % and 42 %, meaning that the electron density of the core of the ligand is almost split equally between the two components. To further model the disorder of the structure, the ADPs of the piperazine fragment of the ligand were fixed to be equivalent and the same constraint was applied also to the two molecules of DMF coordinated to the metal centre and to the one modelled in the pores, which was kept with a full occupancy of 1.

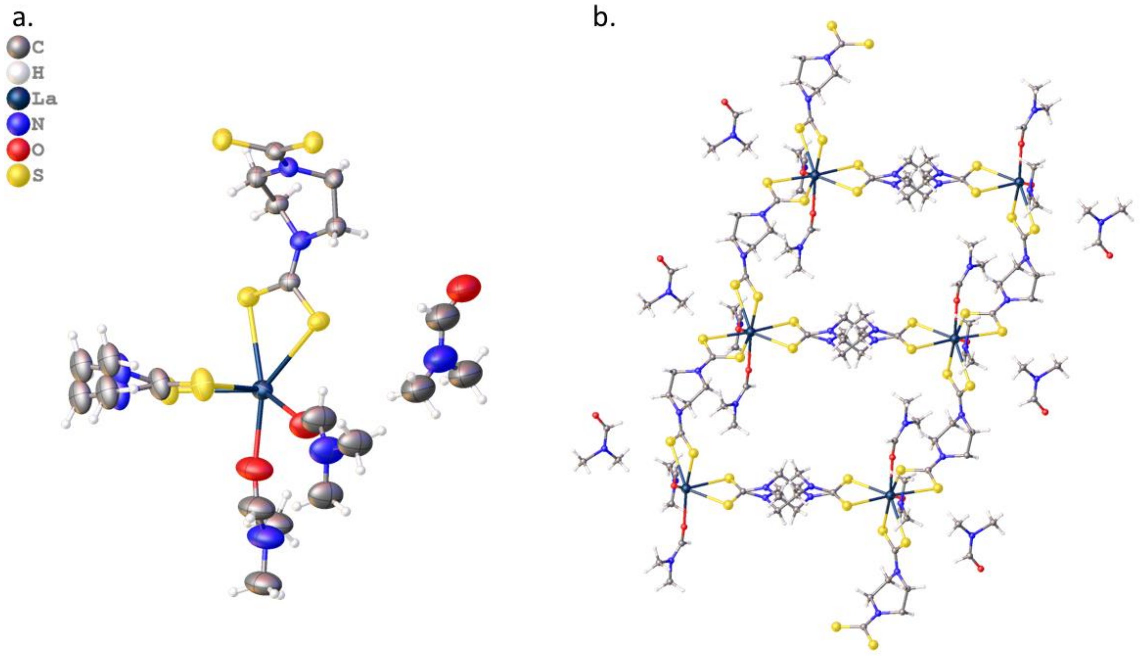

Figure 79: **a.** Asymmetric unit of **BDTC-1** at 150 K. Atomic displacement parameters are drawn at 50 % probability; **b.** Supramolecular packing showing the 1D chains that form compound **BDTC-1**. The structure has been drawn isotropically for clarity.

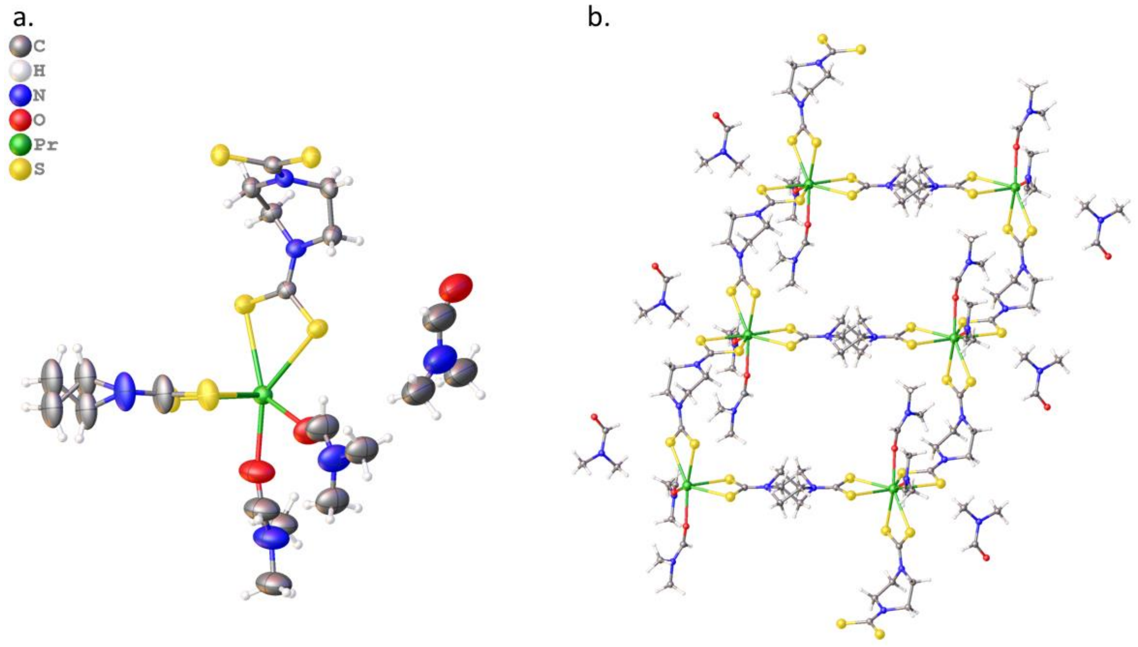

Figure 80: **a.** Asymmetric unit of **BDTC-2** at 150 K. Atomic displacement parameters are drawn at 50 % probability; **b.** Supramolecular packing showing the 1D chains that form compound **BDTC-2**. The structure has been drawn isotropically for clarity.

As seen above, the coordination polymer develops along one dimension, more specifically along the *a* axis. The molecules of DMF solvent are placed in between the distinct 1D chains. An investigation of the solvent accessible volume showed that channels are in fact present along the *b* and the *a* axes, as can be seen in **Figure 81**. From the solvent accessible volume calculation, a value of total solvent accessible volume of 945.6 Å^3 per unit cell was obtained for compound **BDTC-1**, corresponding to the 47.2 % of the unit cell volume, supporting the possibility for porosity of the material. The squeeze routine performed on the structure with the modelled DMF molecules allowed the number of additional electrons that are present in the two pores contained in each unit cell and that could not be modelled to be obtained. A total of 106.0 electrons were calculated to be present within the unit cell, and considering that each DMF molecule carries 40 electrons, this corresponds to at least two and a half molecules of DMF in the void space within the unit cell.

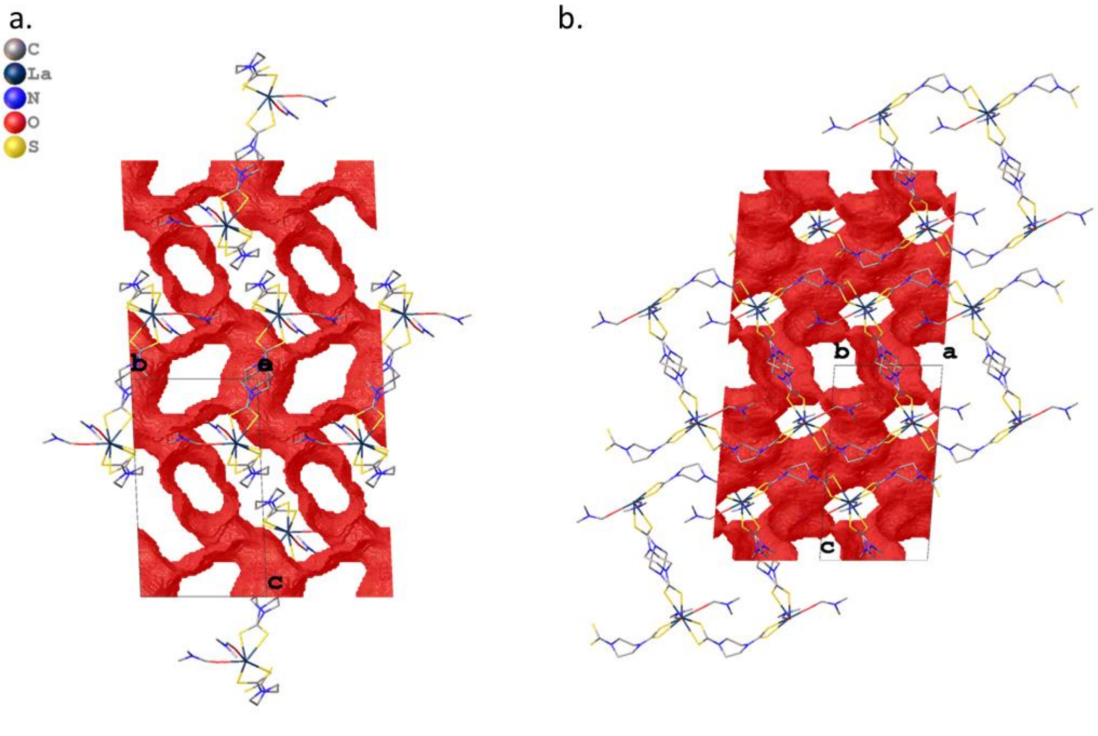

Figure 81: Channels present in compound **BDTC-1** respectively along the *a* and the *b* axis. The red surface is obtained by a calculation that considers a sphere with a 1.2 Å^3 radius rolling within the voids of the structure. The white spaces are hence either occupied by the structure itself, or channels present in the structure.

Even though the slow diffusion approach was attempted with a variety of lanthanoid ions, single crystals suitable for XRD analysis were obtained only with La^{3+} and Pr^{3+}. The bulk composition of the **ppz-bdtc**-based compounds synthesised through this approach was then analysed with PXRD. The measurement was not straightforward because the stability of the compounds appeared to be sensitive to the loss of solvent. In fact, by analysing a dried sample, the diffraction patterns appeared to be noisy and low intensities of the peaks were recorded, as shown in **Figure 82**. Additionally, no peaks comparable to the starting material **Na_2-ppz-bdtc·xH_2O** ligand were seen in the recorded patterns (**Figure 82**).

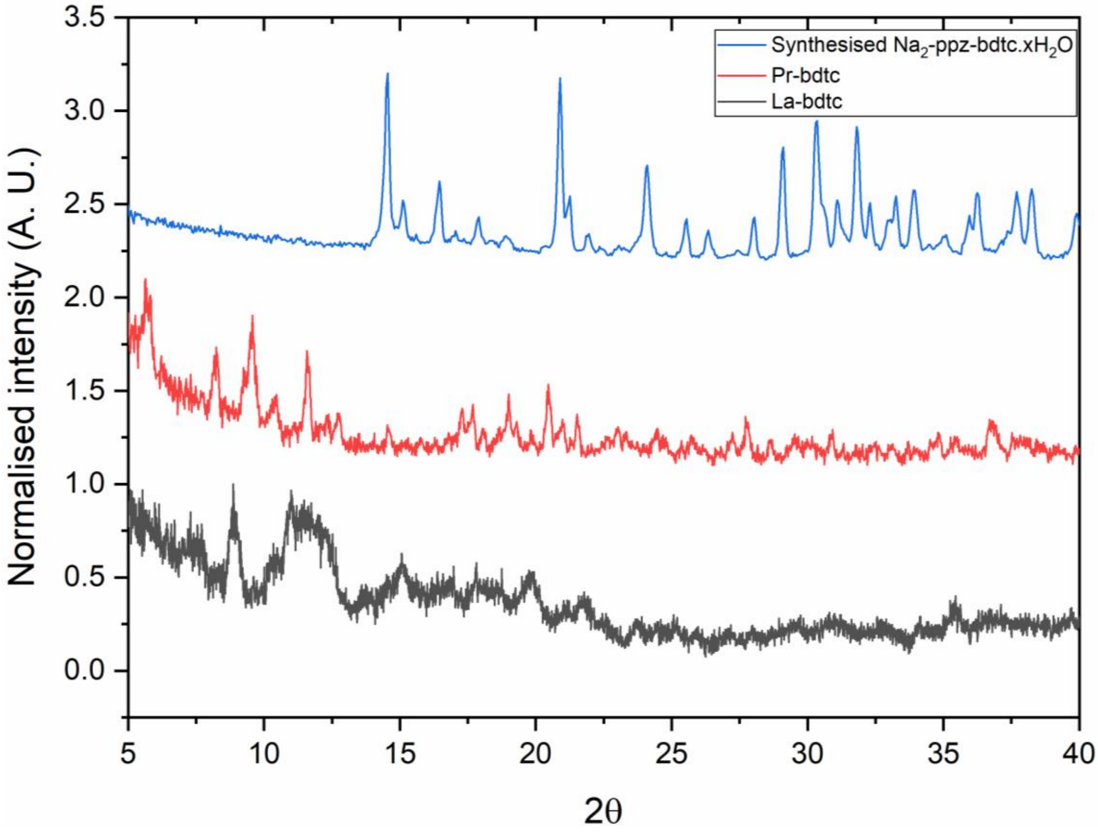

Figure 82: Normalised PXRD pattern of synthesised **Na_2-ppz-bdtc·xH_2O** (top), and of the synthesised **ppz-bdtc**-based compounds constructed with Pr^{3+} (middle, **Pr-bdtc**) and with La^{3+} (bottom, **La-bdtc**) collected from the dried samples. Colour code: blue line, measured from synthesised **Na_2-ppz-bdtc·xH_2O** ligand; red line, measured from synthesised praseodymium-based compound; black line, measured from synthesised lanthanum-based compound.

The patterns appeared instead comparable with the calculated one from the single crystal data of **BDTC-1** when wet samples of the La^{3+} and Pr^{3+} based compounds were used (**Figure 83**). Even in this case, the measurement was not easy to perform, and it required picking up the crystals directly from the solution where they formed and transferring them directly on the sample holder to be analysed. The fact that the sample was not ground could influence the intensities of the diffraction peaks, but these conditions were the only ones that allowed to obtain a representative powder pattern.

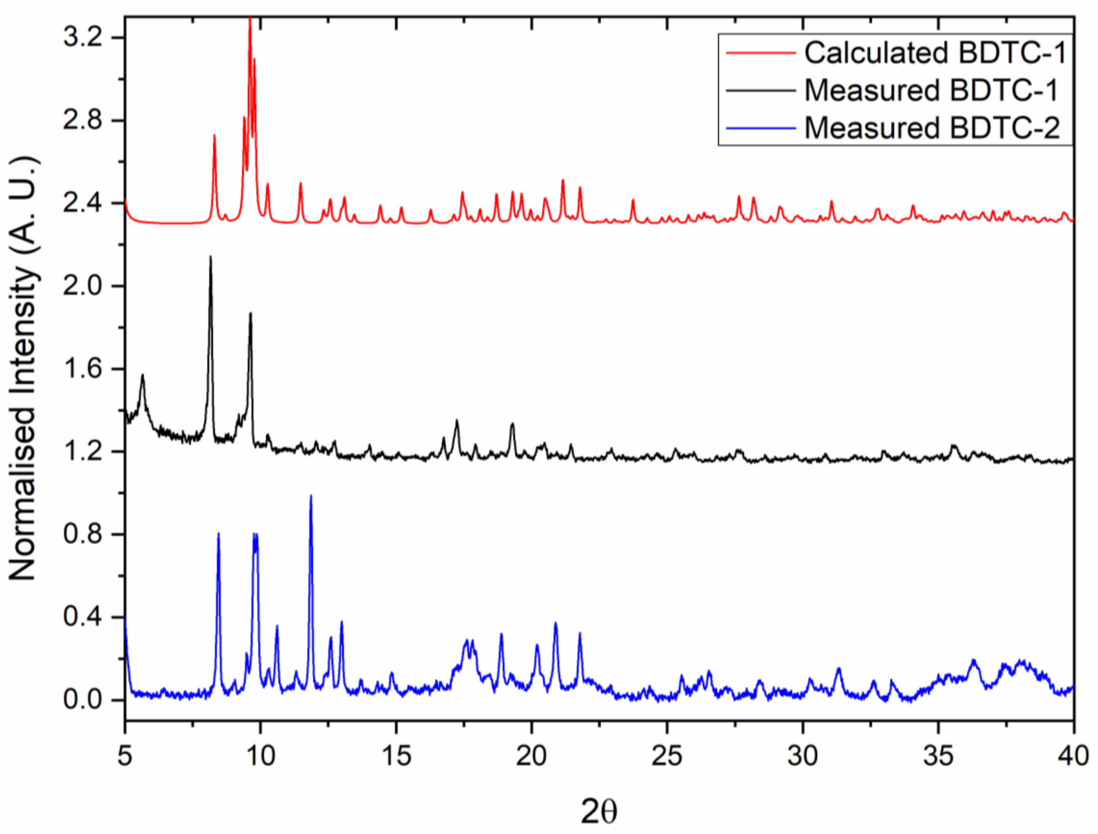

Figure 83: Normalised PXRD pattern of synthesised **BDTC-1** (black line) and of synthesised **BDTC-2** (blue line), and comparison with the calculated pattern from single crystal data of **BDTC-1** (red line). Colour code: red line, calculated from single crystal data of **BDTC-1**; black line, measured from synthesised **BDTC-1**; blue line, measured from synthesised **BDTC-2**.

A final observation that further supports the fact that the amount of solvent has an impact on the crystallinity of the material can be made by looking at the diffraction pattern of the powder of compound **BDTC-1** collected as a function of time. As can be seen in **Figure 84**, the wet powder analysed by taking the crystals directly from the vial (0 minutes, black line) differs from the one analysed after 40 minutes (red line). The latter showed in fact a shift of the peaks to higher angles, probably due to a different amount of solvent present in the pores. Furthermore, a decrease of the intensities due to the degradation of the sample can be seen to occur over the time, with the lowest intensities recorded at 120 minutes (purple line). It should be noted that the measurements reported in **Figure 84** were collected by analysing the same powder sample placed on the same diffraction plate and using the same diffractometer, by collecting a powder pattern every 40 minutes (length of the single PXRD experiment).

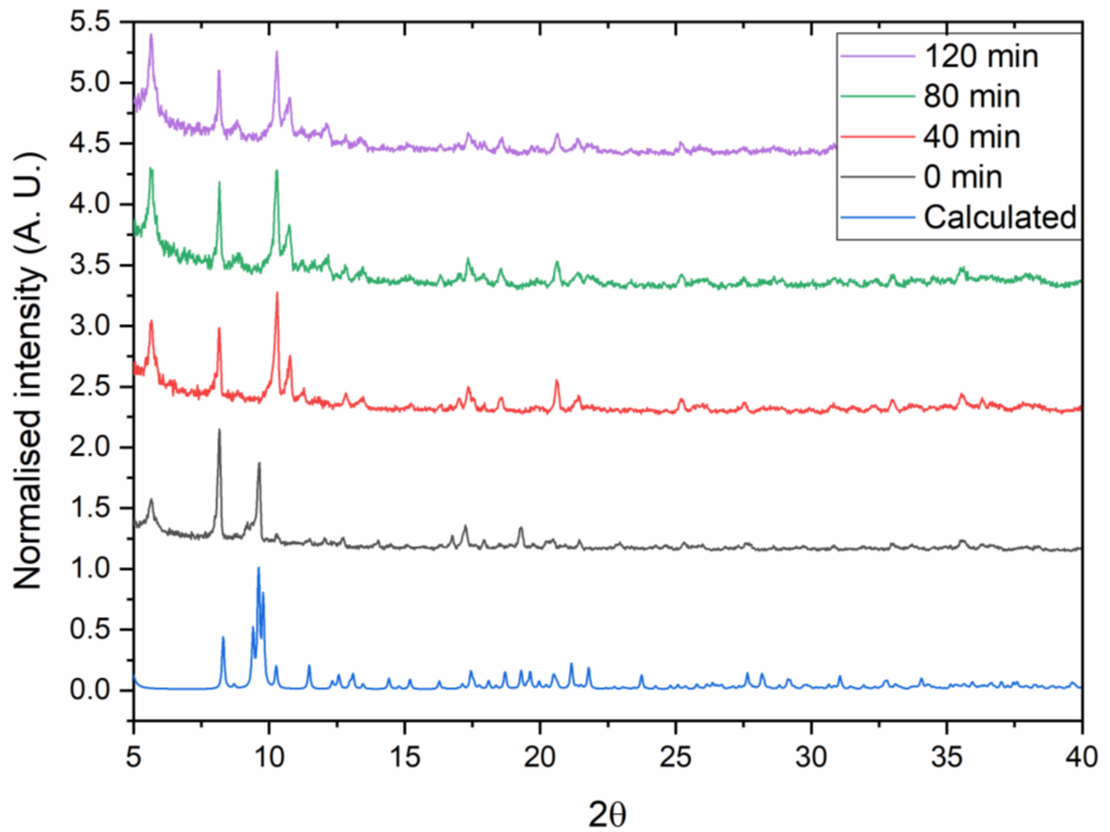

Figure 84: Normalised PXRD pattern of the synthesised **BDTC-1** wet crystals collected over the time and comparison with the calculated pattern from **BDTC-1** (blue line). Colour code: blue line, calculated from single crystal data of **BDTC-1**; black line, measured from synthesised **BDTC-1** taking the crystals directly from the solution (0 min); the same powder was then analysed after 40 min (red line), after 80 min (green line) and after 120 min (purple line).

Unfortunately, the powder patterns reported above for **BDTC-1** and **BDTC-2** obtained from the wet samples were the only two that were comparable to the calculated ones. The rest of the wet powders investigated involving other lanthanoid ions showed once again very noisy patterns with broad peaks (**Figure 85**). The lack of crystallinity of most of the powders analysed, added up to the decrease of the crystallinity over the time for **BDTC-1** and **BDTC-2**, did not allow to perform a full characterisation of the obtained materials. The compounds seem in fact to fall apart when not soaked in the solution they formed from, rendering it impossible to analyse their properties, such as their luminescence, and to use them for real world applications.

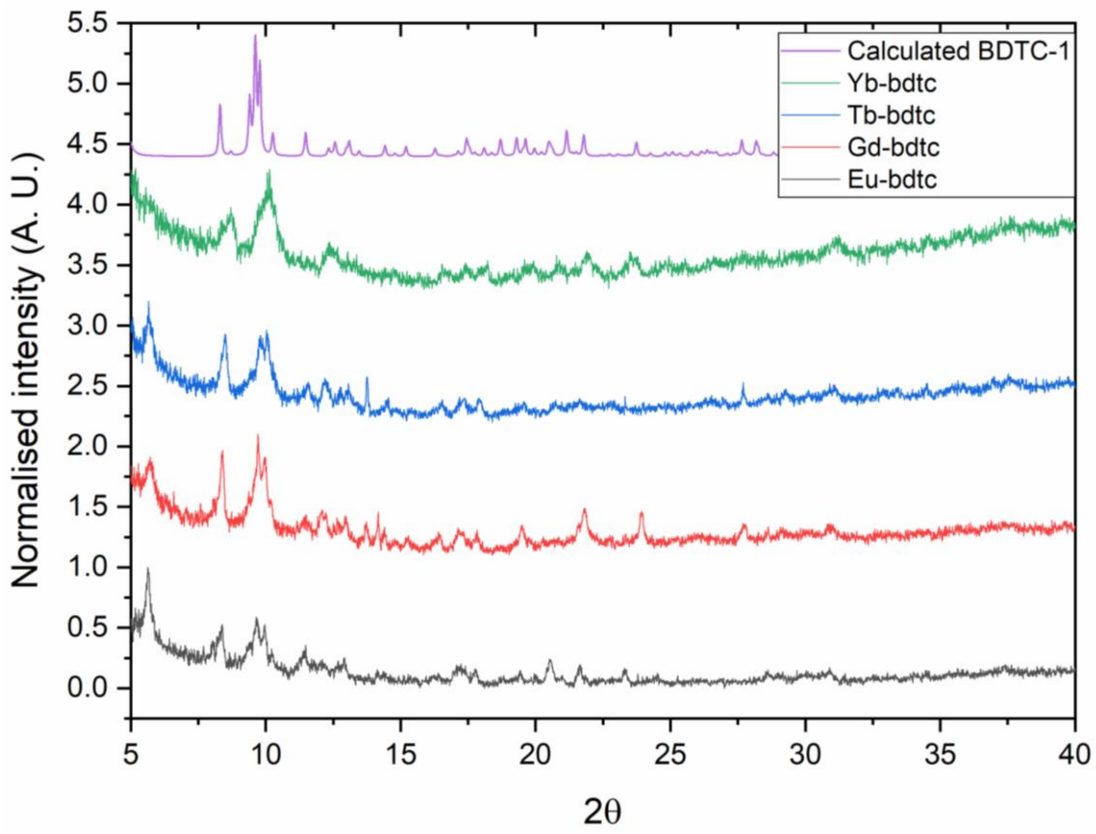

Figure 85: Normalised PXRD pattern of synthesised **ppz-bdtc**-based compounds constructed with Yb^{3+} (green line, **Yb-bdtc**), with Tb^{3+} (blue line, **Tb-bdtc**), with Gd^{3+} (red line, **Gd-bdtc**) and with Eu^{3+} (black line, **Eu-bdtc**) and comparison with the calculated pattern from **BDTC-1** (purple line). Colour code: purple line, calculated from single crystal data of **BDTC-1**; green line, measured from synthesised ytterbium-based compound; blue line, measured from synthesised terbium-based compound; red line, measured from synthesised gadolinium-based compound; black line, measured from synthesised europium-based compound.

5.3 Experimental

5.3.1 Materials

The chemicals piperazine, NaOH, CS_2, $LnCl_3·6H_2O$, $Zn(BF_4)_2·xH_2O$, NEt_3, DMF, EtOH, MeOH and DMSO were obtained commercially (Sigma Aldrich, Thermo Scientific, Fisher Chemical, Strem Chemicals and Acros Organics) and used as received.

5.3.2 Synthesis of Na_2-ppz-bdtc

In a water-bath cooled vessel, piperazine (0.1378 g, 1.6 mmol) was suspended in distilled water (10 ml). The reaction was then performed under nitrogen atmosphere using a Schlenk line. A solution of NaOH (0.1280 g, 3.2 mmol) in distilled water (3 ml) was slowly added, followed by dropwise addition of CS_2 (200 µl, 3.2 mmol) with a 250 µl syringe. The reaction mixture was stirred at room temperature for 2 hrs and then the yellow solution was dried under reduced pressure. The crude white compound was dissolved in MeOH (3 ml ca.), filtrated and the solvent was let evaporate slowly. After a few days, some block-shaped colourless crystals were obtained. SCXRD allowed to identify the structure of the ligand Na_2-ppz-bdtc·$2H_2O$ (**Na2-ppz-bdtc**).

5.3.3 Two-step synthesis of ppz-bdtc-based compounds

A solution of $EuCl_3·6H_2O$ (1.8 mg, 0.005 mmol) in DMF (2 ml) was layered with a solution of ligand **Na2-ppz-bdtc** (5.65 mg, 0.02 mmol) dissolved in different solvents (ethanol, methanol and DMSO, 3 ml). A buffer of pure solvent was added between the two layer and the solutions let diffuse slowly. The same reaction was performed dissolving $EuCl_3·6H_2O$ in DMSO and layering that solution with ligand **Na2-ppz-bdtc** in H_2O. Finally, the analogous layering reactions reported for $EuCl_3·6H_2O$ were set up also with $TbCl_3·6H_2O$.

5.3.4 One-step synthesis of ppz-bdtc-based compounds: direct mixing of reactants

Piperazine (0.0345 g, 0.4 mmol) was dissolved in DMF (2.5 ml) and the metal salt ($EuCl_3·6H_2O$, $TbCl_3·6H_2O$ and $Zn(BF_4)_2·xH_2O$, 0.4 mmol) was dissolved in a separate vial in DMF (2 ml) with the addition of NEt_3 (112 µl, 0.8 mmol). After mixing the two solutions, a water-bath cooled vessel was applied and CS_2 (50 µl, 0.8 mmol) was added dropwise using a 250 µl syringe under nitrogen atmosphere. After 2 hrs, the precipitate was filtered, washed with DMF and dried.

5.3.5 One-step synthesis of ppz-bdtc-based compounds: slow diffusion of CS_2 vapours

Piperazine (0.0177 g, 0.2 mmol) was dissolved in DMF (2.5 ml) and $LnCl_3 \cdot 6H_2O$ (0.1 mmol) was dissolved in a separate vial in DMF (2 ml) with the addition of NEt_3 (55.7 µl, 0.4 mmol). The two solutions were mixed in a small vial. To allow the slow diffusion of CS_2 vapours, that vial was put in a bigger one with CS_2 (25 µl, 0.4 mmol) dissolved in DMF (1 ml) and the CS_2 vapours were let diffuse slowly. After a few days some colourless block crystals of **BDTC-1** and yellow block crystals of **BDTC-2** suitable for SCXRD analysis were obtained. The PXRD analysis was then performed with the wet and dry powders obtained.

5.4 Conclusions

An interesting class of lanthanoid-based coordination polymers constructed with the **ppz-bdtc** ligand was investigated in this chapter through both two- and one-step reactions. The interest arises from the combination of the unexplored characteristics of the sulphur-donor flexible **ppz-bdtc** ligand with the potential luminescence properties deriving from lanthanoid ions, aiming to successfully synthesise new materials that could be used as chemical sensors.

The synthesis of the ligand was successfully performed and its structural composition was confirmed by characterisation with SCXRD and PXRD analyses. Even though different conditions were investigated, the two-step reaction seemed to only lead to amorphous powders rather than to single crystals. The one-step synthesis was optimised too in order to slow down the kinetics of the reaction, going from the direct mixing of the reactants to the slow diffusion of CS_2 vapours. This approach seems to be the most promising, and it allowed to obtain structural information about the isostructural coordination polymers **BDTC-1** and **BDTC-2**.

The coordination polymers **BDTC-1** and **BDTC-2** crystallise with DMF solvent molecules within their pores, and the squeeze routine allowed to confirm that at least another 2.5 molecules of disordered DMF are present in the pores for each unit cell. The porosity of the framework derives possibly from the use of a ligand with a flexible core: within the same structure, the **ppz-bdtc** ligand assumes both a linear and a bent conformation, allowing the channel space to be formed. The use of a flexible ligand is hence a good strategy when aiming to impart flexibility to the final material, but it represents also a limitation for the stability of the structure upon guest removal. **BDTC-1** and **BDTC-2** showed in fact degradation when not soaked in the solution where the crystals grew from, revealing a characteristic of these materials that do not allow most of their properties to be analysed easily. It has also been seen that the quality of the PXRD data is highly dependent on the quantity of solvent that is present in the pores during the analysis. This renders the measurement less straightforward than the expected and also excludes the possibility of performing luminescence studies on the material.

Important progresses were made in this work in engineering the synthetic procedure to create multifunctional materials with enhanced porosity. Even if the initial aim was to obtain a framework-type structure, these structures represent still interesting results. To the best of our knowledge, this is the first example of coordination networks constructed with the **ppz-bdtc** ligand, where both the ligand and the framework are formed *in-situ* and *via* self-assembly. This work might hence open up further studies of the design and optimization of the construction of other new porous structures constructed from the self-assembly of the ligands as well as the frameworks themselves.

5.5 References

1 J.-C. G. Bünzli, J. Coord. Chem., 2014, 67, 3706–3733.

2 J.-C. G. Bünzli and C. Piguet, Chem. Soc. Rev, 2005, 34, 1048–1077.

3 J. Zhou, J. L. Leaño, Z. Liu, D. Jin, K.-L. Wong, R.-S. Liu and J.-C. G. Bünzli, Small, 2018, 14, 1801882–1801910.

4 W. H. Melhuish, Pure Appl. Chem., 1984, 56, 231–245.

5 J.-C. G. Bünzli, Eur. J. Inorg. Chem., 2017, 2017, 5058–5063.

6 J. R. Li, R. J. Kuppler and H. C. Zhou, Chem. Soc. Rev., 2009, 38, 1477–1504.

7 L. E. Kreno, K. Leong, O. K. Farha, M. Allendorf, R. P. Van Duyne and J. T. Hupp, Chem. Rev., 2012, 112, 1105–1125.

8 M. D. Allendorf, C. A. Bauer, R. K. Bhakta and R. J. T. Houk, Chem. Soc. Rev., 2009, 38, 1330–1352.

9 J. Heine and K. Müller-Buschbaum, Chem. Soc. Rev, 2013, 42, 9232–9242.

10 E. J. Mensforth, M. R. Hill and S. R. Batten, Inorganica Chim. Acta, 2013, 403, 9–24.

11 J. Xu, T. Liu, X. Han, S. Wang, D. Liu and C. Wang, Chem. Commun, 2015, 51, 15819–15822.

12 S. Wang, A. Jin Xu, J. Wang, K.-Y. Wang, S. Dang, S. Song, D. Liu and C. Wang, J. Mater. Chem. C, 2017, 5, 6620–6628.

13 C. Bolzati, M. Cavazza-Ceccato, S. Agostini, F. Refosco, Y. Yamamichi, S. Tokunaga, D. Carta, N. Salvarese, D. Bernardini and G. Bandoli, Bioconjugate Chem., 2010, 21, 928–939.

14 J. P. Legros, D. Troy and J. Galy, Acta Crystallogr. Sect. C Cryst. Struct. Commun., 1984, 40, 801–804.

15 G. E. Florence and W. J. Gee, Analyst, 2018, 143, 3789–3792.

Chapter 6: A supramolecular peptide framework: guest adaptable porosity

6.1 Introduction

6.1.1 Porous framework materials

Porous framework materials have widely attracted the interest of researchers in the last decades for their numerous potential applications in a variety of fields like molecular storage and separation.[1] Zeolites represent the first porous compounds discovered, which are inorganic materials with high crystallinity and regular channels or cavities.[2] Later on, MOFs were then discovered from the combination of organic and inorganic moieties, exhibiting higher porosity compared to zeolites and forming highly designable frameworks.[2,3,4,5] It is only from 2013 that the research on porous materials opened up also to organic-oriented polymeric compounds which were inspired by MOFs.[4]

Porous organic frameworks became of significant interest due to their high solubility, low density deriving from the use of light elements such as C, N, O, H, and low toxicity, along with the ability to maintain a structural control *via* crystal engineering.[1] This family of compounds includes covalent organic frameworks (COFs), which are crystalline materials constructed through covalent bonds, amorphous porous organic polymers and supramolecular organic frameworks (SOFs).[6] SOFs are defined as porous materials that are constructed from organic moieties which assemble *via* supramolecular interactions such as hydrogen bonds, π-π stacking, CH$\cdots\pi$ and van der Waals interactions.[1,6] They are characterised by a soft and flexible nature deriving from their molecular interactions, which allow easy manipulation of the organic components. At the same time, they maintain guest selectivity deriving from the possibility to introduce or functionalize the building blocks used, which can impart preferential interactions with guest molecules.[1,7] An additional characteristic of SOFs is that they exhibit high solubility and homogeneity when in solution phase.[8] The first SOF that showed solubility and stability in aqueous solution was obtained by Zhao, Lui and Li in 2013.[9] The group synthesised a honeycomb-shaped SOF in water deriving from the self-assembly of an extended derivative of 1,3,5-triphenylbenzene bearing three 4,4'-bipyridin-1-ium units on the peripheral benzene rings with cucurbit[8]uril, building blocks that can be seen in **Figure 86**.

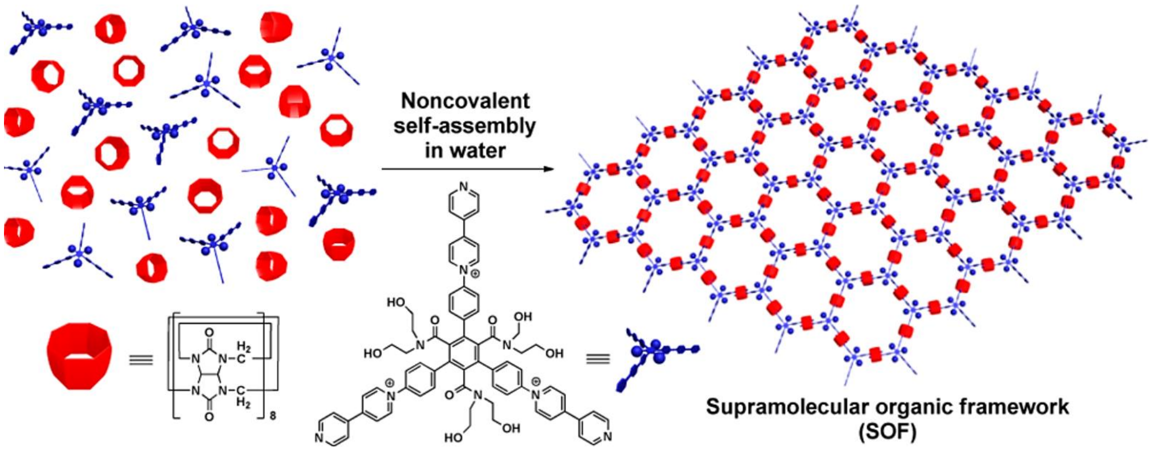

Figure 86: Building blocks used for the SOF synthesis and schematic representation of the structure of the final material. Reprinted with permission.[9]

Peptide-based porous frameworks are a specific class of compounds that found interesting applications as adaptive[10] and reversibly tuneable[11] porous materials which can be used in different fields ranging from the capture of greenhouse gases,[12] to separating chiral drugs.[13] They can be constructed with[10,11,13] or without[12] metal centres, and they are based on the use of amino acids within their structures. This imparts not only enhanced biocompatibility to the material, but also the intrinsic chirality of the amino acids and hence of the peptides imparts the possibility for chiral selectivity of the final material. Even if effort has been put in the investigation of post-functionalization as a tool to induce chiral selectivity in MOFs by grafting amino acids or helical peptides inside the cavities,[14] it still remains a challenge to synthesise peptide-based porous compounds constructed *via* supramolecular interactions. To date, only a few examples are present in the literature involving the full characterization of supramolecular peptide frameworks (SPFs) based on cyclic peptides and on the self-assembly of dipeptides.[12,15,16,17] This field needs hence to still be explored in order to be able to exploit the stability of the secondary structures of peptides as building blocks for the construction of new SPFs.

6.1.2 Choice of the building block

The building block investigated in this chapter is a polyproline, which is a peptide that is formed by repeating units of the proline amino acid, forming a helix-like secondary structure. Polyprolines can interconvert between two different conformations as a consequence of stimuli such as temperature, solvent polarity and pH: polyproline I (PPI), where the compact, right-handed helix presents all the amide bonds in the *cis* conformation and polyproline II (PPII), where the extended, left-handed helix presents instead all the amide bonds in the *trans* conformation.[18] The interest in this peptide as an SPF building block derives from the possibility to have access to rigid secondary structures that can at the same time be stimuli sensitive.[19] PPII helices have a well-defined and rigid conformation that allows them to be used as molecular scaffolds.[20] In addition to this, polyprolines are also resilient to diverse functionalization, retaining their conformation also when formed by a small amount of amino acids.[21]

The first structural characterization of a tetraproline was reported by Matsuzaki in 1974, presenting several of the proline units deviating from the typical conformation of a PPII.[22] Wennemer's group reported then in 2014 the first crystal structure of a polyproline hexamer showing the PPII conformation, which presented a fundamental insight into the stability of the polyproline helix,[20] and was then followed by the work of Hanessian who published the structure of a 4,5-methanoproline tetramer in the PPII conformation.[18] To date, no structural data of other polyprolines are present in the literature. The tetraproline shown in **Figure 87** was investigated during this work.

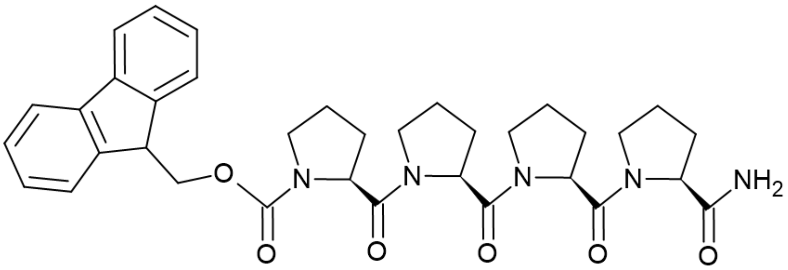

Figure 87: Schematic structure of the tetraproline helix used in this work as a building block for the construction of novel SPF.

6.1.3 Aims

The aims of this chapter are to explore the use of bio-inspired building-blocks for the synthesis of novel supramolecular frameworks and to study their potential to undergo dynamic processes upon guest inclusion. In particular, the use of synthons that can induce specific supramolecular interactions allows to impart control in the self-assembly of the building-blocks, and to perform a rational design of the final material. The impact of supramolecular interactions on the stability and dynamicity of a new supramolecular peptide framework (SPF) will hence be investigated along with the possibility to expand the study of porosity also to this type of compounds. Porosity and guest uptake are in fact a recognised benefits of robust, porous materials like MOFs, but molecular materials like SPF can potentially exhibit similar characteristics when constructed through interactions that are strong enough to be compared to the ones in MOFs.

6.1.4 Declaration

The present chapter is based on the results deriving from a collaboration started from Dr Aniello Palma (A.P.) and the Palma research group members: Dominic F. Brightwell (D.B.), Kushal Samanta (K.S.), Elliott J. Fenn (E.F.) with Dr Helena J. Shepherd (H.J.S.), Professor Simon J. Holder (S.J.H.) and Dr Chris S. Hawes (C.H.). Most of the results that will be presented were collected and analysed by Giada Truccolo (G.T.) and Dr Helena J. Shepherd, but any additional datasets that were obtained by other authors will be clearly stated throughout the document. The full document can be found at the DOI: 10.1002/chem.202202368.

6.2 Results and discussion

6.2.1 Structural characterisation of a porous supramolecular peptide framework

The synthesis of the oligoproline tetramer Fmoc-(Pro)$_4$-NH$_2$ (Pro = proline; **PP$_4$**) was performed by D.B. using solid phase peptide methodology. Single crystals of **PP$_4$** were grown *via* slow cooling of a hot solution containing the synthesised tetramer in ethanol from super-saturated conditions, and were analysed by G.T., D.B. and H.J.S.

The structure of **PP$_4$** is composed of an Fmoc carbamate group that acts as a platform for π-stacking interactions, and four proline units (Pro1-Pro4), forming the peptide reported in **Figure 88**. The C-terminus of **PP$_4$** was amidated so that it could act as a hydrogen bond donor.

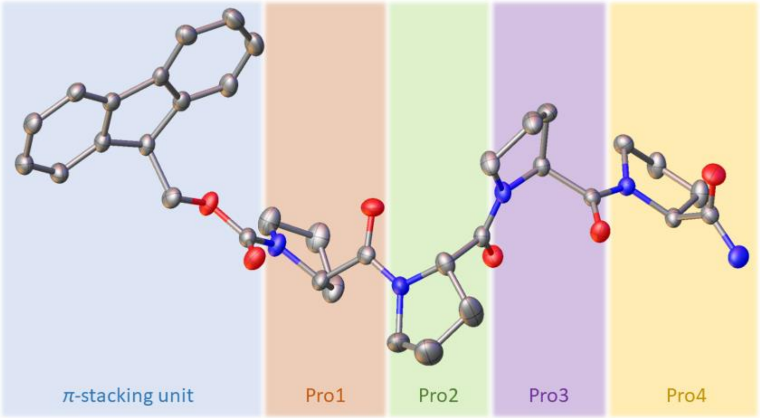

Figure 88: Structure of **PP$_4$** with different parts of the structure highlighted in different colours.

The compound crystallises in the monoclinic *P2$_1$* space group and was analysed at 150 K. As can be seen in **Figure 89a**, the asymmetric unit of **PP$_4$** (CCDC N° 2127750) contains one peptide and a disordered molecule of ethanol. Each peptide interacts with the adjacent ones to form antiparallel rows *via* hydrogen-bonding and *via* Fmoc-Fmoc interactions forming a supramolecular peptide framework (SPF). The formation of hydrogen bonding occurs between the N-H bond of the amide of Pro4 of a peptide with the carbonyl group of Pro2 and of Pro3 of two distinct neighbouring peptides (2.1478(19) Å and 2.1930(18) Å, **Figure 89b**). Each peptide acts hence both as a hydrogen bond donor and acceptor, forming extended 2D layers laying on the [001] plane and developing parallel to the *b* axis. By looking at **Figure 89c**, where the structure is seen along *b*, it is in fact possible to see one of these 2D layers seen from the side, while

Figure 89d, seen along the same axis, shows how adjacent 2D layers pack together, suggesting that the interactions between the Fmoc moieties might be the second aspect that drives the self-assembly process. Channels are present along the *b* axis, with a total solvent accessible volume of 226.19 Å^3 corresponding to the 12.8 % of the unit cell volume.

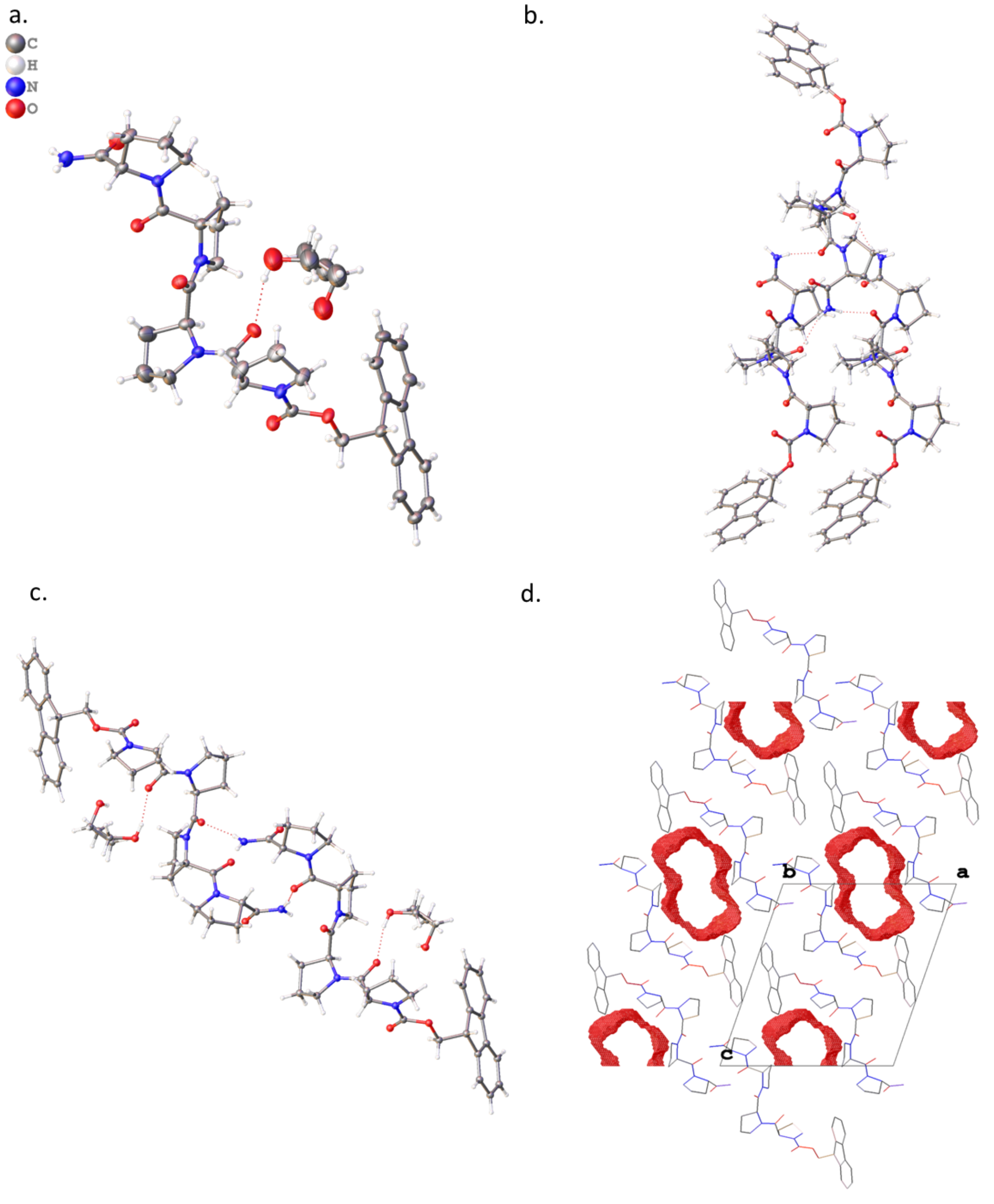

Figure 89: **a.** Asymmetric unit of **PP$_4$**; **b.** Fragment of the packing seen along the *c* axis showing the hydrogen-bonding interactions between neighbouring peptides; **c.** Packing seen along the *b* axis showing a 2D layer from the side and **d.** channels that develop along *b*. The red surface is obtained by a calculation that considers a sphere with a 1.2 Å^3 radius rolling within the voids of the structure. The white spaces are hence channels present in the structure.

As already mentioned above, the molecule of ethanol present within the pores of **PP$_4$** was disordered. In order to model this disorder, the ethanol molecule was split into two components with a total occupancy of 1. The distances between the oxygen-carbon and carbon-carbon atoms were set to the expected values of 1.43 Å and 1.51 Å respectively. Upon refinement, these distances were then fixed to be the same value between the two components and the anisotropic displacement parameters were set to be equivalent within the molecule.

It is worth mentioning that a reversible single crystal to single crystal transition was seen in the unit cell parameters of **PP$_4$**, whereby the Pro2 puckering switches from *exo* to *endo* (**Figure 90**). The transition occurs when the crystals are flash frozen by mounting them directly at the temperature of 150 K (**PP$_{4\text{-flash}}$**, CCDC N° 2127751), and it causes the reduction in the length of the *a* axis and a slight elongation of the *b* and *c* axes, while retaining the same monoclinic *P2$_1$* space group. The original unit cell and conformation of Pro2 is reversibly restored upon returning at room temperature. This behaviour was instead not seen upon slow cooling: in that case, the volume of the unit cell was slightly reduced, but no significant conformational changes were seen.

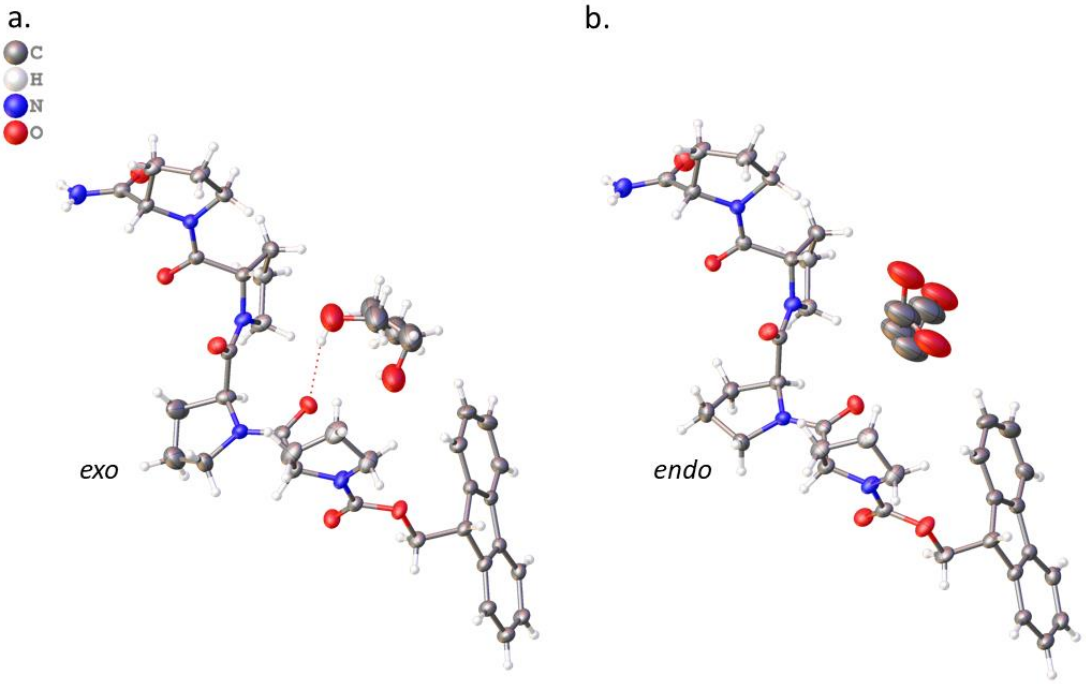

Figure 90: Comparison between the structures of **a. PP$_4$** obtained by slowly cooling down the crystal to 150 K and of **b. PP$_{4\text{-flash}}$** obtained by flash freezing it mounting it directly at 150 K. The Pro2 puckering switching from *exo* to *endo* is highlighted.

As it can be seen above, the molecule of ethanol present in the structure of **$PP_{4\text{-flash}}$** is also disordered. The same restrains and constraints applied for **PP_4** were applied for **$PP_{4\text{-flash}}$** too, with the two components of the ethanol molecule set to 0.75 and 0.25. The oxygen atom of the most abundant component was further split into two, and the total occupancy for its two components was set to sum up to 0.75. A further restrain between the CH_3- carbon and the oxygen atom was necessary to model this component, whose distance was set to be 2.4 Å.

6.2.2 Porosity studies on PP_4

The channels that form within the framework of **PP_4** are filled with molecules of ethanol. The porosity of the material opened up the possibility of activating it by removing the solvent present within the pores and hence allowing the introduction of other guest species. For these reasons, gas adsorption studies were performed by C.H. on the crystalline bulk material in order to investigate their porosity properties.

The activation of freshly isolated **PP_4** crystals was done by degassing them at 45 °C for 29 hours under dynamic vacuum, and it was followed by the measurement of the volumetric uptake of N_2 (77 K) and CO_2 (280 K). In both the cases, no significant adsorption was observed across the loading range $P/P_0 = 10^{-7} – 1.0$ (N_2) or 0 – 1 bar (CO_2), supporting the observation that the adsorption occurred only on the surfaces of the particles without penetration onto the material. With the aim of investigating the change in porosity upon guest removal, SCXRD analysis was carried out by C.H. on an activated crystal (**$PP_{4\text{-act}}$**, CCDC N° 2156434). Even though the crystal showed very poor crystallinity, with no reflections observed beyond 1 Å resolution, the diffraction data could at least be solved to give a connectivity model and accurate unit cell parameters. It should be pointed out that the poor data quality does not allow any meaningful refinement of anisotropic displacement parameters, hence the structure reported below is represented isotropically. By comparing the connectivity model of **$PP_{4\text{-act}}$** with the structure of **PP_4**, it is possible to see that the porous structure collapses as a consequence of a shift of the 2D hydrogen bonded layers such that the Fmoc group fills the pore space (**Figure 91**). These findings were in agreement with the observations obtained through the gas adsorption studies, where the gas uptake was negligible due to the collapse of pores upon solvent removal.

The reversibility of this phenomenon was then proved by D.B. upon analysing *via* PXRD the activated material after soaking in the ethanol mother liquor. This behaviour was further confirmed by placing a sample of **$PP_{4\text{-act}}$**, after being analysed with PXRD and while still on the mount, in a chamber with saturated ethanol vapours for 26 hours. Both the analysis showed a change in phase on the powder pattern coherent with the change seen from the single crystal data when going from **$PP_{4\text{-act}}$** to **PP_4**. Other molecules were then analysed to investigate if the phenomenon would apply to other guests. As the soaking of crystals of **$PP_{4\text{-act}}$** in hexane did not lead to any change in phase on the PXRD pattern, this solvent was used as a diluent for the other guest molecules. The framework was hence soaked in a 5 % solution of various guests (acetone, toluene, THF, 1-bromohexane, (±) 1-phenylethanol and ethyl acetate) in hexane, while for the guest iodine, a saturated iodine solution in hexane was used. All these guests allowed the reinflation of the framework by exhibiting a change in phases from the activated to the original phase. The framework showed hence the capability to reversibly reinflate as a consequence of the shifting of the 2D hydrogen bonded layers of peptides against one another, exhibiting a dynamic porosity behaviour (**Figure 91**). It should be pointed out that even though the present behaviour was not followed on a single crystal, a good match of the PXRD patterns allowed to confirm the dynamicity of the reinflation and its reversibility.

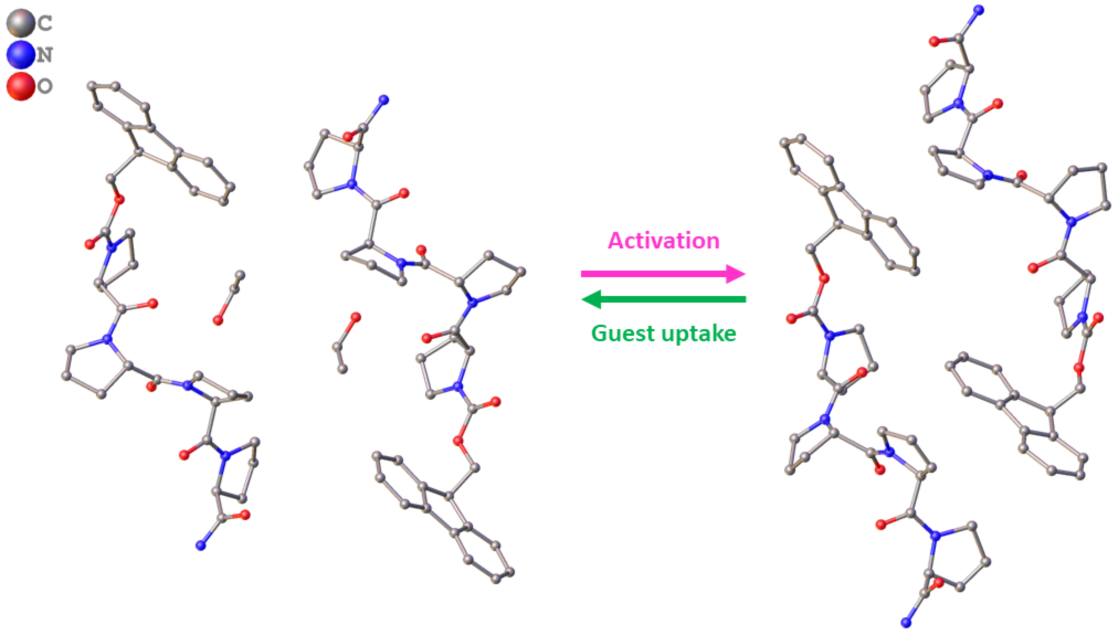

Figure 91: Structure of $\mathbf{PP_4}$ on the left and $\mathbf{PP_{4\text{-}act}}$ on the right showing how the pores collapse upon activation and reinflate upon guest uptake. The structure of $\mathbf{PP_{4\text{-}act}}$ was collected by C.H.

In order to allow the visualization of the guest within the reinflated pores *via* SCXRD even at low guest loadings, iodine was chosen as guest for its high electron density and for its capability to allow a change in colour of the crystals upon guest adsorption. Additionally, the reversibility of the guest adsorption was also investigated upon heating with the aim to explore the potential for the material to be thermally responsive. Crystals of the activated framework were hence soaked by D.B. in a solution of iodine in hexane for one week and then analysed by G.T., D.B. and H.J.S.

A colour change of the crystals from colourless to orange-yellow was observed over time. A SCXRD experiment was set up on one of the crystals exposed to iodine. The crystal was mounted at 290 K, then cooled down to 150 K with a cooling rate of 290 K/h and analyzed *via* SCXRD, giving the structure of $\mathbf{PP_4@I_2}$ (**Figure 92**). From this data it is possible to see that the framework reinflated after exposure to iodine, allowing the absorbed guest within its pores to be modelled. Additionally, the distance between the iodine and the Pro1 carbonyl oxygens (2.813(13) Å) indicated the formation of a halogen bond between the host and the guest.

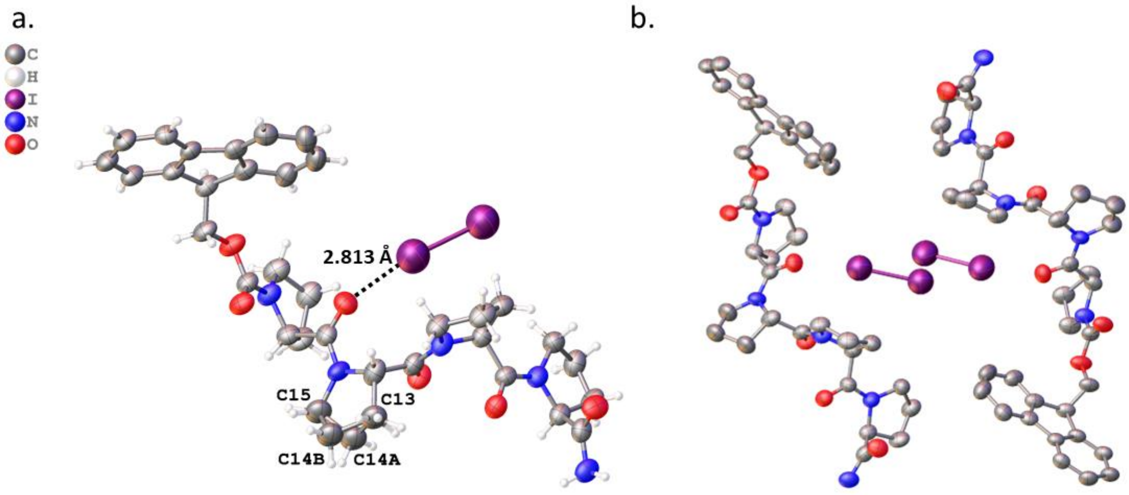

Figure 92: **a.** Asymmetric unit of **PP$_4$@I$_2$** highlighting the halogen bond present between the iodine molecule and the framework and **b.** two parallel peptide units forming the channel for the iodine guest.

A second data collection was performed after heating the same crystal directly in the mount at 323 K with a flow of N$_2$ for 3 hours and cooling it down to 150 K with the same rate used for the previous collection. The whole experiment was carried out by mounting the crystal without using Paratone oil to maximize the guest loss in this step. The structure collected after the thermal treatment (**PP$_4$@I$_{2\text{-heated}}$, Figure 93**) allowed once again to model the iodine guest inside the pores of the framework. The guest molecules present in the structure before and after the thermal treatment were modeled for each of the two sets of data in the same way: the occupancies of the iodine atoms were allowed to freely refine while keeping the atoms isotropic and fixing the atomic displacement parameters to the same value. The analogous treatment of the two data sets allowed to obtain the values of 12.3 % and 5.8 % for the chemical occupancies of the iodine molecules respectively before and after the thermal treatment. This indicates that the chemical occupancy for the iodine guest was reduced by 50 % upon thermal treatment, while the crystallinity was retained, demonstrating the potential for the framework **PP$_4$** to perform thermally responsive guest release.

In the final deposited structures of **PP$_4$@I$_2$** (CCDC N° 2127749) and **PP$_4$@I$_{2\text{-heated}}$** (CCDC N° 2127748), the iodine atoms were instead treated anisotropically and their anisotropic displacement parameters were kept equivalent. Additional disorder present in the structure was treated slightly differently for the two data sets. For the **PP$_4$@I$_2$** structure the carbon atom C14 of the ring of Pro2 was split into two components with a total occupancy of 1 (**Figure 92**). The anisotropic displacement parameters were set to be equivalent for this atom and for the nearest carbon atoms. For the **PP$_4$@I$_{2\text{-heated}}$** structure, three carbon atoms (C13, C14 and C15) of the ring of Pro2 were split into two components with a total occupancy of 1 (**Figure 93**). The anisotropic displacement parameters were set to be equivalent for these atoms in both the components. Within the Pro2 ring, both the N-C and C-C distances were fixed to be the same between the two components.

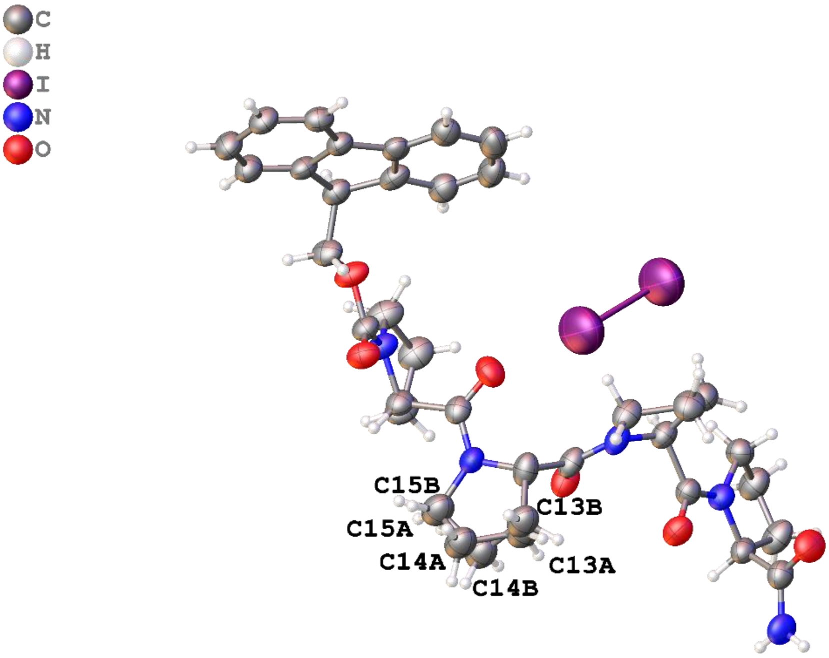

Figure 93: Asymmetric unit of **PP$_4$@I$_{2\text{-heated}}$** highlighting the disorder present within the Pro2 ring.

6.3 Conclusions

This chapter presents the work done in investigating the use of bio-inspired building-blocks for the synthesis of a novel supramolecular framework. More specifically, a tetraproline helix adopting the polyproline II conformation was used for the self-assembly of a porous, crystalline supramolecular peptide framework (SPF). The formation of the compound is driven by strong hydrogen bonding interactions that allow the framework to reversibly collapse and reinflate upon guest inclusion as a consequence of the shifting of the 2D hydrogen bonded layers of peptides against one another. The activation of single crystals of **PP$_4$** and the consequent exposure to iodine, allowed to visualize the guest inside the pores after the reinflation of the framework occurred, which further supported the dynamic process already confirmed *via* PXRD analysis.

The guest-induced dynamic porosity seen in **PP$_4$** represent an outstanding characteristic of this material, being the first reversibly porous SPF formed by the self-assembly of tetraproline peptide. **PP$_4$** has the remarkable capability of reversibly hosting guest molecules in the pores through a guest-induced reinflation from the collapsed de-solvated state. This work represents hence the proof that a framework does not necessarily need to be metal-based in order to exhibit interesting porosity features. On the contrary, the rational design of a material can allow to exploit the strength and directionality of supramolecular interactions to form strong and resilient porous molecular compounds.

6.4 References

1 J. Lü, C. Perez-Krap, M. Suyetin, N. H. Alsmail, Y. Yan, S. Yang, W. Lewis, E. Bichoutskaia, C. C. Tang, A. J. Blake, R. Cao and M. Schröder, *J. Am. Chem. Soc.*, 2014, **136**, 12828–12831.

2 R. Kitaura, S. Kitagawa and S. Noro, *Angew. Chemie - Int. Ed.*, 2004, **43**, 2334–2375.

3 H. Li, M. Eddaoudi, M. O'Keeffe and O. M. Yaghi, *Nature*, 1999, **402**, 276–279.

4 G. Maurin, C. Serre, A. Cooper and G. Férey, *Chem. Soc. Rev.*, 2017, 46, 3104–3107.

5 C. Janiak and J. K. Vieth, 2010, **34**, 2337–2684.

6 W. Yang, A. Greenaway, X. Lin, R. Matsuda, A. J. Blake, C. Wilson, W. Lewis, P. Hubberstey, S. Kitagawa, N. R. Champness and M. Schröder, *J. Am. Chem. Soc.*, 2010, **132**, 14457–14469.

7 J. Tian, L. Chen, D. W. Zhang, Y. Liu and Z. T. Li, *Chem. Commun.*, 2016, **52**, 6351–6362.

8 S. Y. Jiang and X. Zhao, *Chinese J. Polym. Sci. (English Ed.*, 2019, 37, 1–10.

9 K. Da Zhang, J. Tian, D. Hanifi, Y. Zhang, A. C. H. Sue, T. Y. Zhou, L. Zhang, X. Zhao, Y. Liu and Z. T. Li, *J. Am. Chem. Soc.*, 2013, **135**, 17913–17918.

10 J. Rabone, Y. F. Yue, S. Y. Chong, K. C. Stylianou, J. Bacsa, D. Bradshaw, G. R. Darling, N. G. Berry, Y. Z. Khimyak, A. Y. Ganin, P. Wiper, J. B. Claridge and M. J. Rosseinsky, *Science (80-.).*, 2010, **329**, 1053–1057.

11 A. P. Katsoulidis, K. S. Park, D. Antypov, C. Martí-Gastaldo, G. J. Miller, J. E. Warren, C. M. Robertson, F. Blanc, G. R. Darling, N. G. Berry, J. A. Purton, D. J. Adams and M. J. Rosseinsky, *Angew. Chemie - Int. Ed.*, 2014, **53**, 193–198.

12 A. Comotti, S. Bracco, G. Distefano and P. Sozzani, *Chem. Commun.*, 2009, 284–286.

13 A. Saito, T. Sawada and M. Fujita, *Angew. Chemie - Int. Ed.*, 2020, **59**, 20367–20370.

14 J. Bonnefoy, A. Legrand, E. A. Quadrelli, J. Canivet and D. Farrusseng, *J. Am. Chem. Soc.*, 2015, **137**, 9409–9416.

15 V. N. Yadav, A. Comotti, P. Sozzani, S. Bracco, T. Bonge-Hansen, M. Hennum and C. H. Görbitz, *Angew. Chemie - Int. Ed.*, 2015, **54**, 15684–15688.

16 S. Mehrparvar, C. Wölper, R. Gleiter and G. Haberhauer, *Angew. Chemie - Int. Ed.*, 2020, **59**, 17154–17161.

17 C. H. Görbitz, *Chem. - A Eur. J.*, 2007, **13**, 1022–1031.

18 G. Berger, M. Vilchis-Reyes and S. Hanessian, *Angew. Chemie - Int. Ed.*, 2015, **54**, 13268–13272.

19 M. R. Aronoff, J. Egli, A. Schmitt and H. Wennemers, *Chem. - A Eur. J.*, 2020, **26**, 5070–5074.

20 P. Wilhelm, B. Lewandowski, N. Trapp and H. Wennemers, *J. Am. Chem. Soc.*, 2014, **136**, 15829–15832.

21 S. Kakinoki, Y. Hirano and M. Oka, *Polym. Bull.*, 2005, **53**, 109–115.

22 T. Matsuzaki, *Acta Crystallogr. Sect. B Struct. Crystallogr. Cryst. Chem.*, 1974, **30**, 1029–1036.

Chapter 7: Conclusions and prospects

7.1 Conclusions and prospects

This work presents the development and study of new multifunctional coordination polymers, MOFs and an SPF exhibiting promising structure-property correlations. The synthetic approach based on rational design of materials allowed specific structural features to be imparted to the obtained compounds, which were investigated *via* X-ray diffraction techniques. The XRD studies performed allowed properties such as the SCO behaviour, porosity of the frameworks, and host-guest capabilities of the coordination networks to be investigated. This strategy demonstrates the importance of choosing suitable building blocks to tune specific properties.

The first aspect that was investigated in this work is the use of ligands that are less commonly reported in the literature to construct new coordination polymers and framework materials exhibiting interesting structural diversity and a variety of topologies. Eleven new compounds were synthesised while designing new Hofmann-clathrate structures, six of which exhibited the expected topology. The Hofmann-clathrate topology represents in fact the optimal structural arrangement of the building blocks used in this work to favour an effective transmission of the SCO phenomenon. Ligands with different chemical functionalities and conformational flexibility were hence involved in the synthesis, allowing five new 3D Hofmann-clathrates to be obtained when using bidentate ligands, and one new 2D Hofmann-clathrate when using a monodentate ligand. Among them, **AZO-1** and **NICO-1** showed no SCO activity, staying in the HS state within the temperature range 250 K – 100 K, while compound **ISO-2** exhibited a phase transition upon cooling, but no SCO activity was detected. **BPA-2** showed a spin transition within the 200-290 K temperature range, being in the LS state at 200 K and in the HS state at 290 K. The severe disorder seen in the ligand within the structure at 290 K raised the hypothesis that the rotation of the pyridyl rings in **bpa** might be related to the SCO properties of **BPA-2**. Upon cooling, the rings might be locked in a specific orientation that allowed the transition from HS to LS to occur, or *vice versa* the spin transition might be the responsible for locking the rings in a specific position. Either way, this compound represents a very interesting achievement for two main reasons. Firstly, its formation derived from the mixed-ligand approach with **azo** and **bpa**, demonstrating a way to perform topological control in constructing Hofmann-type compounds using a flexible ligand and a template, which was not seen before in the literature. Secondly, this approach allowed tuning of the SCO properties of the **bpa**-based materials, going from a structure that did not exhibit SCO activity when only **bpa** was used (**BPA-1**), to a SCO active material when the **bpa** ligand and the template were simultaneously used (**BPA-2**). Finally, compounds **PINA-1** and **PINA-2** also showed an interesting SCO behaviour, where the two isostructural 3D Hofmann-clathrates exhibited two different SCO curves according to the different amount of solvent present within the pores of the frameworks: an abrupt transition with 15 K hysteresis was reported for **PINA-1** when a lower amount of solvent was present in the pores; a gradual and incomplete transition with no hysteresis was instead reported for **PINA-2** when the quantity of solvent was higher. The results seen with **pina** represent hence an example of how the SCO properties of a material can be influenced by the degree of porosity of a framework, and consequently by the quantity of guest incorporated within it.

The variety of functional groups and heteroatoms that are present in the investigated ligands, allowed new compounds deriving from the *in-situ* self-assembly of the ligands to be obtained. SCO materials, as well as new porous and potentially luminescent compounds with possible application in the field of sensing were constructed following this approach. The reactivity of the hydrazide group of **iso** ligand was the responsible for the unexpected self-assembly of two ligand molecules that formed the dimeric **di-iso** ligand seen in compound **ISO-2**. This further expands the structural diversity when using this ligand, but renders the structural control less straightforward. On the other hand, the known reactivity of amides towards ketones was exploited in **ISO-3**, where the modification of **iso** to **iso-hy** was performed *in-situ* and in a controlled way. The self-assembly approach allowed also to obtain two new porous coordination polymers, compounds **BDTC-1** and **BDTC-2**, from the reaction between the flexible **ppz-bdtc** ligand formed *in-situ*, and lanthanoid ions. Even if the aim of this part of work was to obtain a framework with potential luminescence properties, these results still represent promising findings. **BDTC-1** and **BDTC-2** are in fact the first coordination polymers constructed with the **ppz-bdtc** ligand *via* the self-assembly of the ligand *in-situ* as well as the formation of the framework, opening up the possibility of using this approach to construct a variety of other frameworks and coordination polymers.

In conclusion, the use of bidentate ligands with conformational flexibility allowed much more diverse network topologies than that which have been reported using rigid bridging ligands. Additionally, increasing the chemical functionality of the ligands allowed for self-assembly of larger bridging ligands *in-situ*. While increasing conformational and chemical flexibility of these ligands makes rational design of final products more challenging, it also opens up exciting new directions for these materials with the possibility for substantial structural diversity from the systems that have been reported to date. Future directions should hence aim to expand even more the structural variety in new coordination polymers and frameworks by further extending the self-assembly approach to other ligands with potential active sites, as well as the possibility for templating the network formed while using a more flexible ligand. A systematic and extended study of these aspects, which in this work were demonstrated to be possible, could potentially allow to use them as a rational strategy for the design and synthesis of coordination polymers and frameworks with specific properties tailored to a particular application.

A second aspect that was analysed in this thesis is the porosity of the synthesised compounds, which was exploited both to observe dynamic processes, and to modify the properties of the final materials. The porosity of a known crystalline framework was in fact used as a tool to explore the solid-state behaviour of the photoswitching mechanism of DASAs, a family of photoswitchable molecules. The crystalline sponge framework **tptZn·*x*G** is known for its capability to accommodate guests within the pores and to adapt to the guest's size and shape. Despite the variety of conditions and approaches attempted to analyse the DASAs as guests, only structures of the **tptZn·*x*G** framework including the different solvents used were obtained. Therefore, either no incorporation of the guests occurred, or the amount of incorporated guest was not sufficient to be analysed *via* SCXRD. In addition to this, the porosity of SCO materials has already been mentioned above to explain why the two isostructural 3D Hofmann-clathrates compounds **PINA-1** and **PINA-2** exhibited two different SCO behaviours. It was in fact proved that the different amount of solvent incorporated within the pores of the frameworks influenced the SCO properties of the material, representing an additional way to tune the properties of the final compound. Future studies should hence further investigate the role of host-guest interactions in MOF materials to potentially allow both the incorporation of more guest molecules within the pores of crystalline sponges by further stabilising them, and to allow to use these interactions as a tool to influence the properties of dynamic materials, such as SCO compounds, in a controlled way.

The last aspect treated in this work regards a more recent class of porous frameworks that uses supramolecular interactions to stabilise its structure rather than the more directional metal-ligand coordination bond. A new porous, crystalline supramolecular peptide framework was obtained by self-assembly of a tetraproline helix adopting the polyproline II conformation. Compound **PP_4** exhibited a robust structure stabilised by the presence of strong hydrogen bonding interactions, which allow also the framework to reversibly collapse and reinflate upon guest inclusion. This material represents hence not only the first reversibly porous SPF constructed by the self-assembly of tetraproline peptide, but it also proves that the strength and directionality of supramolecular interactions can be exploited to construct robust and resilient molecular compounds without the use of any metal centre. Future work in this field should once again aim to further investigate the role of supramolecular interactions in the construction of SPFs, to then be able to impart a structural control when designing them.

Appendix A:

Introduction to the book chapter on forensic applications of lanthanides and rare earths

From the collaboration with Dr William Gee:

Forensic applications of rare earths: Anticounterfeiting materials and latent fingerprint developers, G. Truccolo, R. E. Boseley, S. W. Lewis, W. J. Gee, *Handbook on the Physics and Chemistry of Rare Earths, Elsevier*, 2020.

Rare earth elements and their emissive nature

There is more than one way through which a material can luminesce. Photoluminescence (PL) is intended as the luminescence deriving from the direct photoexcitation of the species that emit. When a high-energy photon is absorbed, the material can emit one low-energy photon, giving rise to a downconversion luminesce (DCL) process; the absorption of a low-energy photon, instead, can lead to the emission of a high-energy photon by a non-linear pathway, through a process called upconversion luminescence (UCL).[1] In addition to these modes, novel luminescence paths have been recently studied by Sang *et al.*, with the main aim of developing more complicated and advanced anticounterfeiting technologies.[2] The idea behind their work is that the emission of light can be activated by different external stimuli: a mechanical action on a solid, leading to the so called mechanoluminescence (ML); an increase in the temperature, which generates a thermoluminescence (ThL) process.[2] Finally, a material can also spontaneously luminesce after the removal of the irradiation source through persistent luminescence (PersL), or stored energy can be released from a trapped carrier by irradiation with light through photostimulated luminescence (PSL).[2] In conclusion, more than one of these luminescence modes can be used simultaneously to develop multimodal devices with unconventional and innovative anticounterfeiting properties.

Down-conversion emission

As reported below, the process of downconversion luminescence consists in the conversion of higher energy photons into lower energy photons, with an energy difference between the absorption and the emission that is known as the Stokes shift.[1]

The DCL process involves generally two components of the material: the first is a lanthanide-based host lattice (e.g. vanadate, oxides, phosphate compounds *etc.*), that has the role of absorbing and transferring the energy; the second is a trivalent lanthanide ion, also called activator, to which the energy is transferred from the host, that is a dopant in the lattice and induces the luminescence.[1] More specifically, the ion that is incorporated into the host structure that transfers the energy to the activator is called sensitizer. Two examples are the O^{2-} ion in the Y_2O_3 host lattice, or the VO_4^{3-} in

$GdVO_4$ that act as sensitizers in the materials.[1] The photoluminescence intensity of this process is usually high because the energy transfer is efficient, but the emission can be tuned and enhanced by optimizing the dopant concentration, or by changing the host composition or the synthetic procedure.

Although it is true that a suitable sensitizer enhances the emission intensity of a material, another important process must be taken into consideration: the non-radiative de-activation process. In fact, the smaller is the gap between the lowest excited state and the highest ground state of the metal centre, the easier a non-radiative de-activation process can occur.[3] When it comes to developing a material with high emission properties, that phenomenon has preferentially to be minimised: the ions that are more suitable in that regard are therefore the one with the bigger energy gap, such as Eu^{3+} (12 300 cm^{-1}, $^5D_0 \rightarrow {}^7F_6$), Gd^{3+} (32 200 cm^{-1}, $^6P_{7/2} \rightarrow {}^8S_{7/2}$) and Tb^{3+} (14 800 cm^{-1}, $^5D_4 \rightarrow {}^7F_0$).[3] While Gd^{3+} emits in the UV region, Eu^{3+} and Tb^{3+} have abundant and intense emission peaks in the visible region upon UV excitation, more specifically in the red and green region respectively, and for this reason they are frequently used as activators for the DC process.[4]

It has been mentioned already that the concentration of the dopant plays an important role for enhancing the emission intensity of the material. Scientists reported that the process of embedding a Ln^{3+} ion in the host matrix leads initially to a progressive increase of the photoluminescence with the increase of the dopant concentration.[4] That trend reaches a maximum when the optimal concentration is gained, followed by a decrease that is caused by a concentration quenching, which is the result of the energy transfer between luminescent metal centres that are adjacent.[4] An interesting example of this behaviour, and of how the intensity of the emission can be tuned within a phosphor is reported in literature for the Eu^{3+} and Tb^{3+} doped sesquioxide of yttrium (Y_2O_3).[5]

Y_2O_3 is widely used as host lattice to enhance the luminescence of Ln^{3+} ions. It is important to notice that the unit cell of the host structure has to be maintained after introducing the dopant ions, to confirm that no other phases deriving from impurities are present. With the aim of analysing the doping and codoping effects on the luminescence of this material, Liu and co-workers synthesised Y_2O_3 nanorods with a different percentage of Eu^{3+}, of Tb^{3+}, and of Eu^{3+}/Tb^{3+} as dopants.[5] The emission spectra of Y_2O_3:Eu (λ_{ex} = 254 nm) and Y_2O_3:Tb (λ_{ex} = 307 nm) have been analysed within the range of 2 % and 8 % of dopant percentage. A sensitive enhancement of the photoluminescence intensity has been found when the 5 % of Eu^{3+} has been used as dopant. In these conditions the maximum intensity of the main emission lines is obtained. Among these, the strong peak at 610 nm ($^5D_0$-$^7F_2$) that is due to electric-dipole transition, and the less intense peaks at 589 nm ($^5D_0$-$^7F_1$) and 629 nm ($^5D_0$-$^7F_3$) are included. For Y_2O_3:Tb, instead, the maximum luminescence intensity has been obtained by using the 4 % of Tb^{3+}, which is appreciable from the peaks at 482 nm ($^5D_4$-$^7F_6$), 545 nm ($^5D_4$-$^7F_5$), 586 nm ($^5D_4$-$^7F_4$) and 623 nm ($^5D_4$-$^7F_3$).[5]

In regards to the co-doped samples, different proportions of ions have been analysed, including 7:5, 1:1, 3:5 and 1:5 of Eu^{3+}:Tb^{3+} respectively. As expected, when the percentage of Eu^{3+} is higher or equal to the one of Tb^{3+}, the emission lines deriving from Eu^{3+} are very strong, so the emission colour is mainly red. However, by increasing the relative intensity of Tb^{3+} and reducing the overall percentage of codoping ions in the Y_2O_3 framework, the emission colour goes from orange-red to yellow-white. The fact that different emission colours can be obtained, allows these compounds to be excellent candidates for optical display materials.[5] This example shows a promising approach that can be used to tune the luminescence properties of a material by changing its composition.

Up-conversion emission

Upconversion luminescence occurs when two or more low energy photons are sequentially absorbed by a luminescent centre and consecutively converted into higher energy photons. This non-linear process converts long wavelength light into short wavelength light, with a difference between the emitted and the absorbed photons that is called the anti-Stokes emission.[1]

UC phosphors generally involve an inorganic host lattice doped with multiple trivalent lanthanide ions as emitters, which are known to possess excited states that have relatively long lifetimes.[6] In fact, the peculiarity of this process is that it involves an intermediate excited state that is metastable, thus the choice of a dopant that can maintain a high population of this state is essential for the second excitation to occur.[7]

The upconversion processes can be divided into two main mechanisms: the excited state absorption and the energy transfer upconversion. The first one can be seen in **Figure 94a**, where a lanthanide ion is excited to the higher energy level E3 via the absorption of two photons, passing through the metastable state E2. This approach is limited to certain LN ions (Er^{3+}, Tm^{3+}, Ho^{3+} and Nd^{3+}) that possess regular, well-spaced energy gaps from E1 → E2 and E2 → E3 which enables sequential jumping between energy levels in this manner. The energy transfer upconversion mechanism involves four possible scenarios that are shown in **Figure 94b-e**. In each case, a sensitizer LN ion(s) is required to absorb photons and transfer their energy to a neighbouring activator ion in order to induce luminescence.[1] In two instances (**Figure 94b,c**), the activator must have already attained the metastable E2 state, and the additional energy supplied by the sensitizer promotes that state to a higher energy level at E3, allowing UC emission. In process (b) energy transfer occurs from the E2 state of the sensitizer to the E2 state of the activator, whereas in process (c) the E3 level of the sensitizer acts as a cross-relaxation pathway to E3 of the activator, provided it has adopted the metastable E2 state. An alternate UC process involves a single sensitizer absorbing and transferring the energy of two photons to a spectating activator ion, thereby raising it from the ground to the excited state E3, shown as process (d). Finally, instances where multiple sensitizer ions work in concert to enhance the luminescent emission of neighbouring ions are termed cooperative energy transfer processes. One such pathway, cooperative sensitized up-conversion, is shown as process (e).[1] Thus, in cases where the activator and sensitizer are different LN ions, the ratio of each dopant during synthesis will be important for creating a certain UC process. Cooperative sensitisation for example will benefit from a greater excess of sensitizer LN ions, relative to other energy transfer processes, and as opposed to the excited state absorption process.

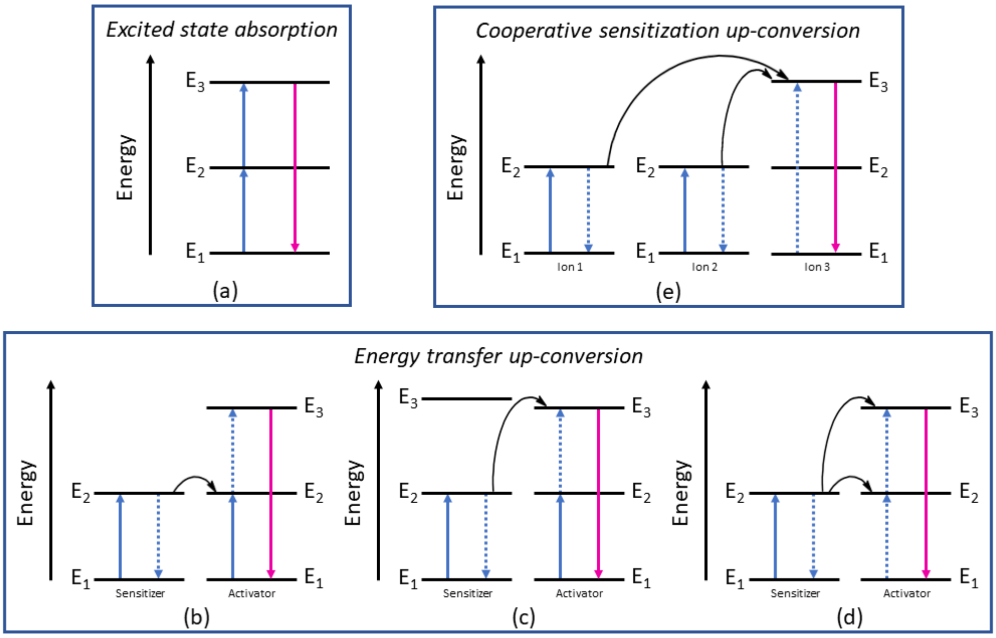

Figure 94: Schematic diagrams for the up-conversion mechanisms, including: (a) excited state absorption; (b-d) energy transfer up-conversion processes; (e) cooperative sensitization up-conversion. Solid blue and pink arrows represent the absorbed photons and the up-conversion emission, respectively. Black arrows show the energy transfer. Dotted blue arrows represent possible non-radiative emission or energy transfer. E1 = ground state; E2 and E3 = excited states.

To date, the most popular host that has been used for upconversion nanophosphors is $NaYF_4$. Its popularity derives from the fact that this material exhibits a minimal nonradiative loss and maximizes the radiative emission, allowing it to be an efficient framework for UC luminescence.[7] Within the host structure, Er^{3+}, Ho^{3+} and Tm^{3+} are the RE ions that are commonly employed as activators because of their large anti-Stokes shifts, sharp emission profiles, long upconversion luminescence lifetimes and high photostability.[6] As explained above, another important component of these materials is the sensitizer, which enhances the upconversion emission. Yb^{3+} is often introduced in the structure as co-dopant with Er^{3+}, Ho^{3+} or Tm^{3+} and employed as sensitizer. The reason why this specific RE ion has been chosen is related to its adsorption cross section being larger than the one of the activators, and to its $^2F_{7/2} \rightarrow {}^2F_{5/2}$ emission line that is resonant with some of the transitions of the aforementioned activators: this facilitates the energy transfer from the Yb^{3+} ion to the activator ions.[7]

One interesting aspect of UC compounds is that their emission wavelength can be tuned by choosing more than one ion as dopants. Xie et al. synthesised β-$NaYF_4$ upconversion hollow microtubes (UCHMs) with different theoretical molar ratio of dopants to induce the emission of the three primary colours red, green and blue.[8] More specifically, they obtained a red emission when the molar ratio for Y^{3+}, Er^{3+}, Tm^{3+} used was 88 : 10 : 2. By using ytterbium instead of thulium as dopant, the material showed a green emission when Y^{3+}, Yb^{3+}, Er^{3+} have been included in the framework with a molar ratio of 78 : 20 : 2. Finally, a blue emission can be gained if Y^{3+}, Yb^{3+}, Tm^{3+} are used as dopant ions, with a molar ratio of 74.7 : 25 : 0.3. This example shows how the UC luminescence properties of this well-known framework can be modified by easily changing the dopant elements and their relative quantities. The three-primary-colour emission of this material allows it to be a suitable candidate for forensic applications in anti-counterfeiting materials or tools for evidence collection.

References

1 P. Kumar, S. Singh and B. K. Gupta, *Nanoscale*, 2016, **8**, 14297–14340.

2 J. Sang, J. Zhou, J. Zhang, H. Zhou, H. Li, Z. Ci, S. Peng and Z. Wang, *ACS Appl. Mater. Interfaces*, 2019, **11**, 20150–20156.

3 J.-C. G. Bünzli and C. Piguet, *Chem. Soc. Rev*, 2005, **34**, 1048–1077.

4 S. Gai, C. Li, P. Yang and J. Lin, *Chem. Rev*, 2014, **114**, 2343–2389.

5 Z. Liu, L. Yu, Q. Wang, Y. Tao and H. Yang, *J. Lumin.*, 2011, **131**, 12–16.

6 W. J. Gee, *Aust. J. Chem.*, 2019, **72**, 164–173.

7 J. Zhou, Q. Liu, W. Feng, Y. Sun and F. Li, *Chem. Rev.*, 2015, 115, 395–465.

8 S. Xie, C. Tong, H. Tan, N. Li, L. Gong, J. Xu, L. Xu and C. Zhang, *Mater. Chem. Front.*, 2018, **2**, 1997–2005.

Appendix B:

Crystallographic tables

Identification code	**ISO-1**	**ISO-2**	**ISO-3**
Empirical formula	$C_{11.5}H_{17}FeN_7O_{5.5}Pt$	$C_{17}H_8FeN_8O_{3.5}Pt$	$C_{30}Fe_3N_{18}O_5Pt_3$
Formula weight	592.26	631.25	526.40
Temperature/K	249.98(11)	249.98(11)	150.00(10)
Crystal system	monoclinic	monoclinic	monoclinic
Space group	$P2_1/n$	P2/m	$P2_1$
a/Å	7.3287(3)	6.9847(4)	7.6065(2)
b/Å	15.1255(8)	7.5871(4)	13.8416(4)
c/Å	18.7440(8)	13.6681(11)	23.9734(10)
α/°	90	90	90
β/°	94.702(3)	93.029(6)	97.857(3)
γ/°	90	90	90
Volume/Å^3	2070.78(16)	723.31(8)	2500.37(14)
Z	4	1	1
ρ_{calc}g/cm^3	1.900	1.449	1.049
μ/mm^{-1}	7.485	5.359	4.637
F(000)	1132.0	298.0	725.0
Crystal size/mm^3	0.152 × 0.075 × 0.033	0.124 × 0.084 × 0.034	0.131 × 0.098 × 0.028
Radiation	MoKα (λ = 0.71073)	Mo Kα (λ = 0.71073)	Mo Kα (λ = 0.71073)
2Θ range for data collection/°	6.718 to 59.768	7.936 to 59.548	6.586 to 59.802
Index ranges	$-9 \le h \le 9$, $-14 \le k \le 19$, $-21 \le l \le 25$	$-9 \le h \le 6$, $-9 \le k \le 10$, $-18 \le l \le 17$	$-10 \le h \le 9$, $-19 \le k \le 18$, $-33 \le l \le 30$
Reflections collected	11108	3655	90419
Independent reflections	4975 [R_{int} = 0.0290, R_{sigma} = 0.0429]	1852 [R_{int} = 0.0304, R_{sigma} = 0.0505]	13153 [R_{int} = 0.1020, R_{sigma} = 0.0638]
Data/restraints/ parameters	4975/0/248	1852/2/100	13153/1/138
Goodness-of-fit on F^2	1.245	1.104	2.829
Final R indexes [I>=2σ (I)]	R_1 = 0.0440, wR_2 = 0.0959	R_1 = 0.0320, wR_2 = 0.0765	R_1 = 0.1515, wR_2 = 0.3746
Final R indexes [all data]	R_1 = 0.0532, wR_2 = 0.0982	R_1 = 0.0339, wR_2 = 0.0782	R_1 = 0.1608, wR_2 = 0.3833
Largest diff. peak/hole / e Å^{-3}	2.31/-4.13	1.16/-0.75	32.28/-13.10
Flack parameter			0.501(6)

Identification code	**NICO-1**	**PINA-1**	**PINA-2**
Empirical formula	$C_{16}H_{12}FeN_8O_2Pt$	$C_{15}H_9FeN_7OPt$	$C_{15}H_9FeN_7OPd$
Formula weight	599.28	554.23	465.54
Temperature/K	100.00(10)	250.01(17)	250.0(3)
Crystal system	triclinic	monoclinic	monoclinic
Space group	P-1	$P2_1/c$	$P2_1/c$
a/Å	7.3496(5)	7.4200(9)	7.3820(5)
b/Å	7.4164(4)	14.6026(17)	14.8746(11)
c/Å	9.0983(6)	27.222(3)	27.171(3)
α/°	75.689(5)	90	90
β/°	70.407(6)	95.449(10)	95.343(7)
γ/°	89.262(5)	90	90
Volume/$Å^3$	451.38(5)	2936.2(6)	2970.5(4)
Z	1	4	4
ρ_{calc}g/cm^3	2.205	1.254	1.041
μ/mm^{-1}	8.574	5.264	1.104
F(000)	284.0	1040.0	912.0
Crystal size/mm^3	0.035 × 0.024 × 0.016	0.057 × 0.04 × 0.038	0.166 × 0.084 × 0.033
Radiation	Mo Kα (λ = 0.71073)	Mo Kα (λ = 0.71073)	Mo Kα (λ = 0.71073)
2Θ range for data collection/°	7.878 to 59.628	6.63 to 59.572	6.484 to 59.578
Index ranges	$-10 \le h \le 10$, $-10 \le k \le 10$, $-11 \le l \le 11$	$-10 \le h \le 7$, $-11 \le k \le 20$, $-37 \le l \le 33$	$-8 \le h \le 10$, $-14 \le k \le 20$, $-35 \le l \le 34$
Reflections collected	5993	15638	15080
Independent reflections	2197 [R_{int} = 0.0785, R_{sigma} = 0.0989]	7054 [R_{int} = 0.1007, R_{sigma} = 0.1730]	6997 [R_{int} = 0.0519, R_{sigma} = 0.0896]
Data/restraints/ parameters	2197/0/112	7054/0/100	6997/0/100
Goodness-of-fit on F^2	0.984	1.050	1.558
Final R indexes [I>=2σ (I)]	R_1 = 0.0380, wR_2 = 0.0610	R_1 = 0.0957, wR_2 = 0.2368	R_1 = 0.1283, wR_2 = 0.3890
Final R indexes [all data]	R_1 = 0.0428, wR_2 = 0.0621	R_1 = 0.1600, wR_2 = 0.2795	R_1 = 0.1527, wR_2 = 0.4187
Largest diff. peak/hole / e Å^{-3}	3.37/-1.31	4.86/-2.73	4.75/-2.80

Identification code	**PINA-3**	**AZO-1**	**BPA-1**
Empirical formula	$C_{32}H_{24}FeN_{14}O_6Pt_2$	$C_{24}H_{16}Ag_2FeN_{12}$	$C_{17.4}H_{12}Ag_{2.4}FeN_6$
Formula weight	1146.62	496.05	947.76
Temperature/K	150.00(10)	293.0(2)	290.0(2)
Crystal system	triclinic	monoclinic	monoclinic
Space group	P-1	$P2_1/n$	C2/c
a/Å	7.1506(3)	9.1493(2)	10.1742(3)
b/Å	7.9380(3)	10.9199(3)	20.2372(9)
c/Å	16.8186(7)	13.6807(3)	10.6212(3)
α/°	79.710(3)	90	90
β/°	87.345(3)	96.897(2)	95.336(3)
γ/°	76.504(4)	90	90
Volume/$Å^3$	913.35(7)	1356.94(6)	2177.40(13)
Z	1	2	4
ρ_{calc}g/cm^3	2.085	1.821	1.897
μ/mm^{-1}	8.096	16.013	22.588
F(000)	544.0	728.0	1193.0
Crystal size/mm^3	0.154 × 0.105 × 0.056	0.13 × 0.061 × 0.044	0.118 × 0.033 × 0.029
Radiation	Mo Kα (λ = 0.71073)	Cu Kα (λ = 1.54184)	Cu Kα (λ = 1.54184)
2Θ range for data collection/°	6.978 to 59.632	10.394 to 143.834	8.74 to 144.186
Index ranges	$-9 \le h \le 9$, $-10 \le k \le 10$, $-20 \le l \le 21$	$-10 \le h \le 7$, $-13 \le k \le 12$, $-16 \le l \le 13$	$-7 \le h \le 12$, $-24 \le k \le 23$, $-13 \le l \le 12$
Reflections collected	8231	5299	6119
Independent reflections	4308 [R_{int} = 0.0484, R_{sigma} = 0.0675]	2589 [R_{int} = 0.0239, R_{sigma} = 0.0318]	2113 [R_{int} = 0.0281, R_{sigma} = 0.0264]
Data/restraints/ parameters	4308/0/245	2589/0/178	2113/18/103
Goodness-of-fit on F^2	1.008	1.031	1.045
Final R indexes [I>=2σ (I)]	R_1 = 0.0313, wR_2 = 0.0622	R_1 = 0.0290, wR_2 = 0.0753	R_1 = 0.0834, wR_2 = 0.2365
Final R indexes [all data]	R_1 = 0.0396, wR_2 = 0.0652	R_1 = 0.0319, wR_2 = 0.0776	R_1 = 0.0943, wR_2 = 0.2542
Largest diff. peak/hole / e Å^{-3}	1.71/-1.96	0.93/-0.53	2.83/-0.76

Identification code	**BPA-2**	**BPA-3**	**TPT-1**
Empirical formula	$C_{56}H_{36}Ag_{12}Fe_3N_{22}$	$C_{17}H_{16}Ag_2FeN_6O$	$C_{37}H_{25}Cl_3I_6N_{12}Zn_3$
Formula weight	1239.53	591.95	567.18
Temperature/K	290.1(6)	293(2)	149.99(10)
Crystal system	orthorhombic	triclinic	orthorhombic
Space group	Pbca	P-1	Pnma
a/Å	18.0990(5)	7.3971(3)	13.2724(2)
b/Å	13.5826(6)	10.9888(4)	29.4085(5)
c/Å	31.0662(10)	13.5180(6)	12.7855(2)
α/°	90	78.686(4)	90
β/°	90	78.698(4)	90
γ/°	90	73.370(4)	90
Volume/$Å^3$	7637.1(5)	1020.90(8)	4990.45(14)
Z	4	2	4
ρ_{calc}g/cm^3	2.156	1.926	2.265
μ/mm^{-1}	28.873	21.017	32.639
F(000)	4672.0	576.0	3160.0
Crystal size/mm^3	0.08 × 0.03 × 0.029	0.081 × 0.065 × 0.035	0.075 × 0.067 × 0.031
Radiation	Cu Kα (λ = 1.54184)	Cu Kα (λ = 1.54184)	Cu Kα (λ = 1.54184)
2Θ range for data collection/°	7.5 to 143.866	8.492 to 144.072	7.54 to 138.024
Index ranges	-21 ≤ h ≤ 22, -11 ≤ k ≤ 16, -37 ≤ l ≤ 38	-8 ≤ h ≤ 9, -9 ≤ k ≤ 13, -16 ≤ l ≤ 16	-15 ≤ h ≤ 15, -35 ≤ k ≤ 27, -15 ≤ l ≤ 13
Reflections collected	81113	10964	25006
Independent reflections	7478 [R_{int} = 0.0785, R_{sigma} = 0.0246]	3912 [R_{int} = 0.0332, R_{sigma} = 0.0316]	4662 [R_{int} = 0.0402, R_{sigma} = 0.0220]
Data/restraints/ parameters	7478/30/274	3912/3/251	4662/19/307
Goodness-of-fit on F^2	1.062	1.034	1.102
Final R indexes [I>=2σ (I)]	R_1 = 0.0787, wR_2 = 0.2895	R_1 = 0.0274, wR_2 = 0.0684	R_1 = 0.0416, wR_2 = 0.1134
Final R indexes [all data]	R_1 = 0.1421, wR_2 = 0.3531	R_1 = 0.0310, wR_2 = 0.0710	R_1 = 0.0438, wR_2 = 0.1154
Largest diff. peak/hole / e $Å^{-3}$	1.19/-1.49	0.44/-0.79	1.63/-0.90

Identification code	**BDTC-1**	**BDTC-2**	**PP4**
Empirical formula	$C_{18}H_{33}LaN_6O_3S_6$	$C_{18}H_{33}N_6O_3PrS_6$	$C_{36}H_{41}N_5O_{6.5}$
Formula weight	711.76	714.77	647.74
Temperature/K	149.99(10)	149.97(12)	149.99(10)
Crystal system	triclinic	triclinic	monoclinic
Space group	P-1	P-1	$P2_1$
a/Å	10.21870(10)	10.1728(3)	16.4182(3)
b/Å	10.68970(10)	10.6764(4)	6.27740(10)
c/Å	18.4835(2)	18.4198(4)	18.2112(3)
α/°	92.1750(10)	91.970(2)	90
β/°	94.1980(10)	94.195(2)	109.152(2)
γ/°	95.0680(10)	94.957(2)	90
Volume/$Å^3$	2003.75(3)	1986.06(10)	1773.03(6)
Z	2	2	2
ρ_{calc}g/cm^3	1.180	1.195	1.213
μ/mm^{-1}	11.350	12.548	0.689
F(000)	718.0	724.0	688.0
Crystal size/mm^3	0.169 × 0.101 × 0.082	0.093 × 0.076 × 0.049	0.217 × 0.063 × 0.054
Radiation	Cu Kα (λ = 1.54184)	Cu Kα (λ = 1.54184)	Cu Kα (λ = 1.54184)
2Θ range for data collection/°	8.312 to 140.47	8.32 to 144.08	8.84 to 146.496
Index ranges	$-12 \le h \le 12$, $-13 \le k \le 12$, $-19 \le l \le 22$	$-10 \le h \le 12$, $-13 \le k \le 12$, $-22 \le l \le 21$	$-16 \le h \le 20$, $-7 \le k \le 7$, $-22 \le l \le 19$
Reflections collected	57996	21497	20144
Independent reflections	7567 [R_{int} = 0.0524, R_{sigma} = 0.0238]	7626 [R_{int} = 0.0475, R_{sigma} = 0.0465]	6929 [R_{int} = 0.0225, R_{sigma} = 0.0217]
Data/restraints/ parameters	7567/6/242	7626/60/230	6929/3/427
Goodness-of-fit on F^2	1.077	1.057	1.076
Final R indexes [I>=2σ (I)]	R_1 = 0.0801, wR_2 = 0.2533	R_1 = 0.0821, wR_2 = 0.2486	R_1 = 0.0562, wR_2 = 0.1726
Final R indexes [all data]	R_1 = 0.0815, wR_2 = 0.2554	R_1 = 0.0852, wR_2 = 0.2529	R_1 = 0.0576, wR_2 = 0.1749
Largest diff. peak/hole / e $Å^{-3}$	2.67/-1.99	2.43/-1.96	1.19/-0.24
Flack parameter			0.02(5)